RADC-TR-87-10, Vol II (of two) In-House Report February 1987



PROCEEDINGS OF THE 1986 ANTENNA APPLICATIONS SYMPOSIUM

Daniel T. McGrath, Capt, USAF



Sponsored by
ELECTROMAGNETIC SCIENCES DIVISION
ROME AIR DEVELOPMENT CENTER
HANSCOM AFB, BEDFORD MASS, 01731
AIR FORCE SYSTEMS COMMAND

APPROVED FOR PUBLIC RELEASE; DISTRIBUTION UNLIMITED

ROME AIR DEVELOPMENT CENTER
Air Force Systems Command
Griffiss Air Force Base, NY 13441-5700

This report has been reviewed by the KADC Public Affairs Office (FA) and is releasable to the National Technical Information Service (NTIS). At NTIS it will be releasable to the general public, including foreign nations.

RADC-TR-87-10, Vol II has been reviewed and is approved for publication.

APPROVED:

JOHN K. SCHINDLER

Chief, Antennas & Components Division

Directorate of Electromagnetics

Jan K Selindle

APPROVED:

PAUL J. FAIRBANKS, Lt Col, USAF

Call Falons

Acting Chief

Directorate of Electromagnetics

FOR THE COMMANDER:

JOHN A. RITZ

Directorate of Plans & Programs

If your address has changed or if you wish to be removed from the RADC mailing list, or if the addressee is no longer employed by your organization, please notify RADC (EEAA) Hanscom AFB MA 01731-5000. This will assist us in maintaining a current mailing list.

Do not return copies of this report unless contractual obligations or notices on a specific document requires that it be returned.



COMPONENT PART NOTICE

THIS PAPER IS A COMPONENT PART OF THE FOLLOWING COMPILATION REPORT:			
TITLE: Proceedings of the Antenna Applications Symposium Held in Urbana,			
Illinois on 17-19 September 19	86. Volume 2.		
TO ORDER THE COMPLETE COMPILATION REPORT, USEAD_A181 537			
THE COMPONENT PART IS PROVIDED HERE TO ALLOW USERS ACCESS TO INDIVIDUALLY AUTHORED SECTIONS OF PROCEEDING, ANNALS, SYMPOSIA, ETC. HOWEVER, THE COMPONENT SHOULD BE CONSIDERED WITHIN THE CONTEXT OF THE OVERALL COMPILATION REPORT AND NOT AS A STAND-ALONE TECHNICAL REPORT.			
THE FOLLOWING COMPONENT PART NUMBERS COMPRISE THE COMPILATION REPORT:			
AD#: P005 410 thru P005 424	AD#:		
AD#:	_ AD#:		
AD#:	_ AD#:		



Acces	on For	T
DTIC	ounced	
By Distrib	ution/	
A	vailability (Codes
Dist	Avail and Specia	
A-1		

DISTRIBUTION STATEMENT A
Approved for public release
Distribution Unlimited

DTIC FORM 463

OPI: DTIC-TID

ECURITY	CLASSIFICA	ATION OF	THIS PAGE

REPORT DOCUMENTATION PAGE					
14 REPORT SECURITY CLASSIFICATION		16. RESTRICTIVE MARKINGS			
Unclassified		<u> </u>			
26 SECURITY CLASSIFICATION AUTHORITY		3. DISTRIBUTION/A	VAILABILITY O	F REPORT	
		Approved for	r public re	lease;	
25. DECLASSIFICATION/DOWNGRADING SCHE	DULE	Distributio	n Unlimited	l .	
4. PERFORMING ORGANIZATION REPORT NUM	ABER(S)	5. MONITORING OF	GANIZATION R	EPORT NUMBER(S)	
RADC-TR-87-10 (Volume II)					
64 NAME OF PERFORMING ORGANIZATION	St. OFFICE SYMBOL	74 NAME OF MONI	TORING ORGAN	ZATION	
Rome Air Development Center	(If applicable) EEAA				
He. ADDRESS (City, State and ZIP Code)		7b. ADDRESS (City,	State and ZIP Cod	le)	
Hanscom AFB					
Massachusetts 01731-5000					
So NAME OF FUNDING/SPONSORING	Sb. OFFICE SYMBOL	9. PROCUREMENT	INSTRUMENT ID	ENTIFICATION NU	MBER
organization Rome Air Development Center	(If applicable) EEAA				
Sc. ADDRESS (City, State and ZIP Code)		10. SOURCE OF FU	NDING NOS.		
Hanscom AFB		PROGRAM	PROJECT	TASK	WORK UNIT
Massachusetts, 01731-5000		ELEMENT NO.	NO.	NO.	NO.
11. TITLE (Include Security Classification) Proce	odings of the	62702F	4600	14	01
1986 Antenna Applications Symp		•		1 -	
12. PERSONAL AUTHOR(S)		<u> </u>		<u> </u>	
13a TYPE OF REPORT 13b. TIME (COVERED	14. DATE OF REPO	RT (Yr., Mo., Day)	15. PAGE CO	DUNT
In-House FROM	to	1987 Februar	.	340	
16. SUPPLEMENTARY NOTATION Volume	I consists of pa	ges 1 through	366; Volum	e II consist	s of
bases 201 rittoria 039			•		
Daniel T. McGrath, Contract Mc					
17. COSATI CODES	18. SUBJECT TERMS (C Antennas 7	ontinue on reverse if no Microst			
09 03	Satellite Ante				m Antennas,
	······································	nnas, HF. VHF, UHF			
19. ABSTRACT (Continue on reverse if necessary an	d identify by block number	r)			
The Proceedings of the 1986 A	ntenna Applicatio	ons Symposium	is a colle	ction of sta	te-of-the-
art papers relating to phased	array antennas,	multibeam and	tennas, sat	ellite anten	nas.
microstrip antennas, reflector	r antennas, HF,	VHF, UHF and v	various oth	er antennas.	
					.1
		1			
	N	,	. (
	N.				
20. DISTRIBUTION/AVAILABILITY OF ABSTRA	СТ	21. ABSTRACT SECURITY CLASSIFICATION			
UNCLASSIFIED/UNLIMITED 🗆 SAME AS RPT	💆 DTIC USERS 🗔	Unclassifi	.ed		
22a. NAME OF RESPONSIBLE INDIVIDUAL	226. TELEPHONE N		22c. OFFICE SYM	BOL	
DANIEL T. MCGRATH, Captain, US	AF	(Include Area Co		RADC/EEAA	
, , , , , , , , , , , , , , , , , , , ,	·	1 (021) 311-40	-50	L KADO/EEAA	

PREFACE

The Antenna Applications Symposium, held at the University of Illinois' Robert Allerton Park, was cosponsored by Rome Air Development Center's Electromagnetics Directorate (RADC/EEAA), Hanscom AFB, MA and the University of Illinois' Electromagnetics Laboratory under Contract F19628-86-M-0004. Professor Paul Mayes if UI was the symposium chairman. Captain Daniel McGrath of RADC/EEA was the symposium manager for the Air Force.

BALLA	NTIS ODTIC Unanno Justifica	CRA&I TAB		
MSPECTED	By Dist ib:	.tio::/	y Code	s
	Dist	Avail a Spe	ind for	
	A-1			

Contents

Volume 1

Ke	note: "A Centennial of Electromagnetics," H. Schrank	
	Wednesday, September 17, 1986	
	Session 1	
	EHF Antennas	
	Chairman: R. J. Mailloux, Rome Air Development Center	
1.	"V-band Space-Based Radar Antennas," J. A. Kinzel	23
2.	"An Antenna System for an EHF Satellite Earth Terminal and its Calibration," L. W. Rispin	37
3.	"EHF/SHF Satcom Antenna and Radome Test Results," A. L. Johnson and W. O. Fischbach	63
4.	"Simplified MMIC Active Aperture Feeding," J. L. Poirier	93
5.	"APS-Workshop on Characterization of MMIC Devices for Array Antenna," J. Smetana and R. Mittra	119
	Session II	
	Conformal Antennas	
	Chairman: W. C. Chew, University of Illinois	

	Co	cutents
6.	"Aperture Coupled Patch Antennas and Arrays," D. H. Schaubert and D. M. Pozar	135
7.	"Phased Array Antenna Pattern Optimization with Failed Elements," B. F. Collins II, Z. H. Lewantowicz, and A. J. Terzuoli	155
8.	"Wideband, Double-Tuned Microstrip Elements," D. Tanner and P. Mayes	173
9.	"Practical Examples of Integral Broadband Matching of Microstrip Antenna Elements, D. A. Paschen	199
10.	"Printed Dipole Radiating Elements for Monolithic Millimeter Wave Phased Arrays," D. B. Rees and B. J. Edward	219
11.	"A Design Concept for an MMIC Microstrip Phased Array," R. Q. Lee, J. Smetana, and R. Acosta	239
12.	"Mutual Admittance Between Slots in Cylinders of Arbitiary Cross Section Shape," A. F. Peterson and R. Mittra	253
	Thursday, September 18, 1986	
	Session III	
	Arrays and Reflectors	
	Chairman: J. L. Poirier, Rome Air Development Center	
13.	"A Technique for Low Sidelobes in Monopulse Planar Array Antennas," A. Derneryd	275
14.	"Phased Array Antenna for Space Shuttle Orbiter," S. E. Davidson	291
15.	"A Hemispherically Scanning X/Ka Band Mirror Antenna," K. Hollenbeck	30 7
16.	"A Lightweight Constrained Lens for Wide Angle Scan in Two Planes," D. T. McGrath	343
		Volume II
17.	"A High Power Phased Array for Sub-Scale Aerial Target Applications," J. DeVries, K. Doi and F. Lauriente	367
18.	"Design Considerations for the Beamwaveguide Retrofit of a Ground Antenna Station," T. Veruttipong, J. Withington, V. Galindo-Israel, W. Imbriale and D. Bathker	387

Session IV

Broadband Antennas

Chairman: J. D. Dyson, University of Illinois

	· · · · · · · · · · · · · · · · · · ·	
19.	"A Wideband Ridge Array Feed," C. J. Favoloro and G. Ledonne*	
20.	"An Inexpensive, Relatively Broadband Multi-Purpose Antenna," S. C. Kuo and W. M. Shelton	.411
21.	"A Log-Periodic Array of Monopole-Slot Elements," D. J. Tammen and P. E. Mayes	425
22.	"A Shallow-Cavity Unity Gain Notch Radiator," G. J. Monser	457
23.	"Ultra-Broadband Impedance Matching Using Electrically Small Self-Complimentary Structures," K. G. Schroeder	469
24.	"Impedance Inverting Feed Designs for Broadband Endfire Complementary Pairs Using Thin Wire Elements," K. G. Schroeder	491
25.	"Pattern Prediction of Broadband Monopole Antennas on Finite Groundplanes Using the BOR Moment Method," D. E. Baker and L. Botha	521
	Friday, September 19, 1986	
	Session V	
	Analysis, Dasign and Measurement	
	Chairman: F. Rupp, Hughes Aircraft Company	
26.	"Polarization Measurement," D. L. Hawthorne	547
27.	"Review of Spherical Near-Field Measurements," D. W. Hess	581
28.	"Swept Frequency Technique for Dispersion Measurement of Microstrip Line," R. Q. Lee	597
29.	"Evaluation of Localized Inhomogeneities in the Reflectivity of Planar Absorber Panels," D. E. Baker and C. A. Van Der Neut	615
30.	"Results of Optimization of Yagi-Uda Arrays of Shaped	631

Contents

655

31.	"Results of Numerical and Physical Modelling of Airborne Adcock Arrays for VHF DF Applications," D. C. Baker, L. Botha, D. McNamara and G. W. Reed	655
32.	"Matrix Formulation of Vector Operations in Electromagnetics	687

A HIGH POWER PHASED ARRAY ANTENNA FOR SUB-SCALE AERIAL TARGET APPLICATIONS

James De Vries and Kaz Doi Pacific Missile Test Center Point Mugu, California 93042

Fred Lauriente Figrowave Applications Group 3030 Industrial Parkway Santa Maria, California 93455

ABSTRACT

The simulation of airborne radars place special requirements on antenna systems used in sub-scale targets. Typical airborne radar antennas are steerable in azimuth and elevation and provide gains on the order of 30 dB. The simulation of these antennas on a sub-scale target has been a difficult task. Low gain non-steerable antennas provide good coverage but suffer from marginal ERP.

Gimballed antenna systems are steerable and provide high gain but not without the attendant problems of excessive weight, large size and high cost. In an effort to find a practical solution, a limited scan prototype phased array antenna has been developed. The prototype phased array effectively utilizes the available aperture to provide a high gain antenna that is steerable over small angles in azimuth and elevation.

The phased array antenna described herein is ideal for this application due to its compact size, light weight, and low cost.

NAMES OF CONTROL OF THE PROPERTY OF THE PROPER

1.0 Introduction

A steerable phased array antenna system was designed and developed for aerial subscale target testing. The principal purpose of this design effort was to increase the effective radiated power (ERP) by a factor of 9 dB over fixed beam antennas. The antenna system fully utilizes the limited available space in subscale targets. A microprocessor control subsystem derives steering commands from analog navigational and altimeter data, and provides drive signals to steer the antenna. The operational requirements for the antenna system of ±20 degrees in azimuth and ±10 degrees in elevation were satisfied by using only eight elements. This minimal number of elements reduces system complexity while providing a low cost antenna system.

The phased array system is comprised of the following components: a two by four array of horn elements, eight high accuracy rotary field phase shifters, an eight-way equal line length waveguide power divider and a beam steering computer. Each of these components can be seen in the photograph of Figure 1-1 and is discussed individually.

2.0 Horn Radiator

The horn radiator is an E-plane sectoral horn fed by a six element slotted waveguide standing wave array. An exploded view of the horn is shown in Figure 2-1. The slotted waveguide array is center fed through a series tee junction with three radiating slots on either side of the junction. With an impedance matching structure, consisting of a resonant iris and dielectric plug in the input arm, an impedance match of better than 17 dB was achieved over the 14.0 to 15.2 GHz bandwidth for each horn, as shown in Figure 2-2.

The sectoral horn contains dielectric mode launching obstacles attached to the broad walls for the purpose of correcting the phase curvature in the E-plane. A similar set on the side walls provides control in the H-plane. The use of this technique has been described in the literature (1,2). The radiation patterns of the horn are shown in Figure 2-3 at 14.4 GHz. The measured gain was 20.7 dB corresponding to an aperture efficiency of approximately 80.2 percent.

The horn radiator was subjected to high power testing at 15 KW peak and 15 watts average power at an altitude of 45,000 feet without evidence of corona or voltage breakdown.

3.0 Power Divider Network

The power divider network consists of commercially available waveguide components. Seven folded H-plane WR-62 waveguide magic tees are used as shown in Figure 3-1. The series port of each tee is terminated in a short profile slab load, capable of dissipating one watt of RF power. The power divider was tested for loss, equality of power split and relative phase. These data are shown in Figures 3-2 and 3-3.

4.0 Rotary Field Phase Shifters

The eight phase shifters used in this array are high accuracy rotary field ferrite phase shifters. These phase shifters are the magnetic analog of the Fox rotary vane phase shifter. Typical performance data is shown in Figures 4-1 through 4-3.

5.0 Beam Steering Controller

The Beam Steering Controller inputs are in the form of three analog voltages corresponding to target range, bearing, and altitude as measured from a shipboard TACAN.

The computer receives the analog signals through an A/D converter.

The Z80 based computer with CP/M and Fortran software generates the appropriate 8-bit sine and cosine data. The eight pairs of drivers receive the data sequentially and latch it into D/A converters.

The power stage of the driver donsists of 2 parts: a precision current sink and polarity switching network. The current sink employs a single power transistor and differential current sensing to eliminate crosstalk. The polarity switching network which receives polarity information from the 8-bit sine or cosine word, uses semiconductor switches to effectively switch the phase shifter coil orientation in the circuit. This design insures good bi-polar symmetry and eliminates the need for a negative power supply.

The beam steering controller block diagram is shown in Figure 5-1.

6.0 Array System Tests

System evaluation tests included radiation patterns and gain measurements throughout the angular coverage at frequencies of 14.0 GHz and 14.4 GHz and 15.2 GHz. A composite of the H-plane scanned patterns is shown in Figure 6-1 and a composite of the E-plane scanned patterns is shown in Figure 6-2.

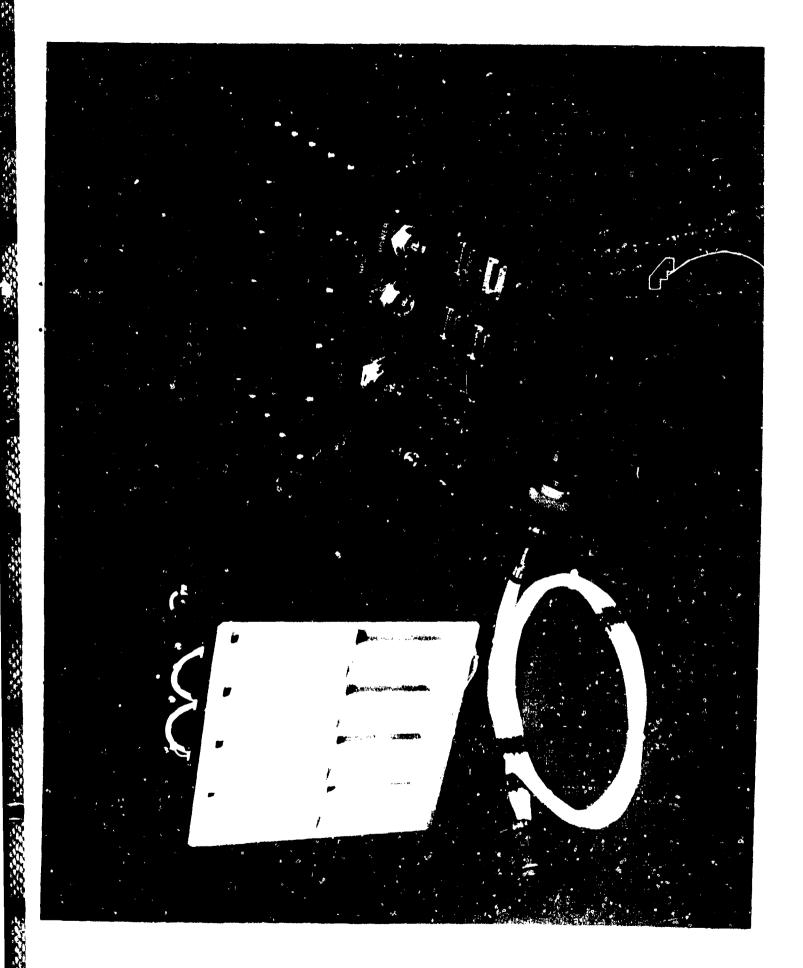
References

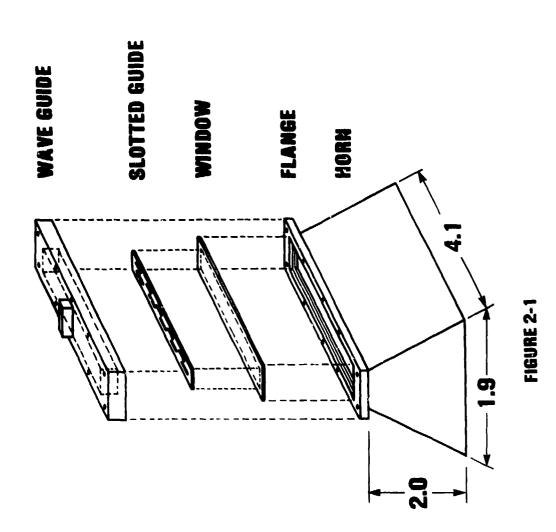
- 1. Sato, T. (1972) Dielectric-Loaded Horn Antenna, <u>IEEE</u>

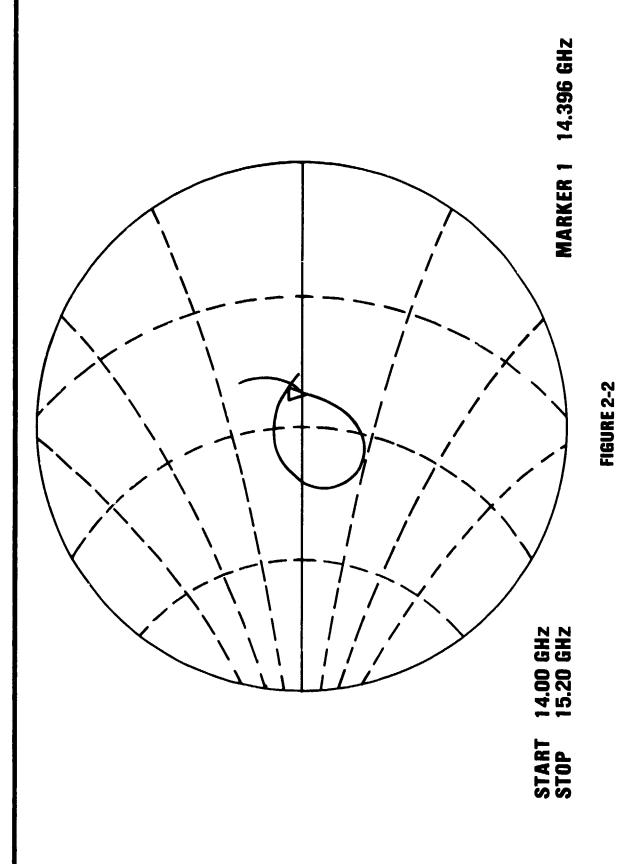
 Transactions on Antennas and Propagation, T-AP Jan '82, 157-161.
- 2. Tsandulas, G. N. and W. D. Fitzgerald (1972) Aperture

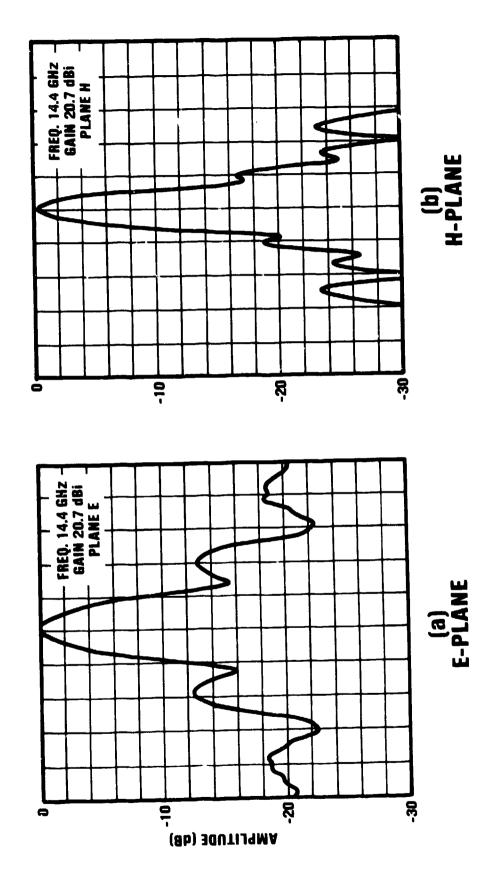
 Efficiency Enhancement in Dielectrically Loaded Horns, <u>IEEE</u>

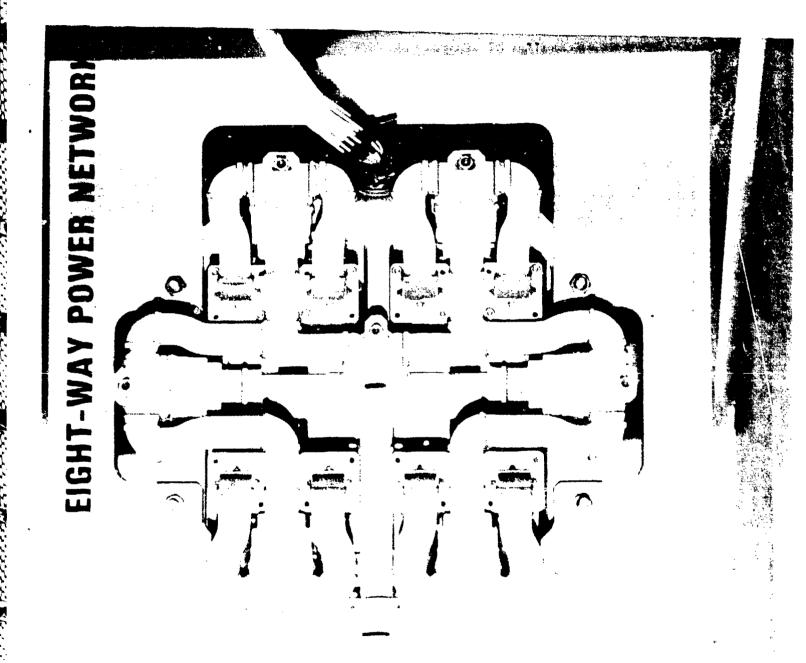
 <u>Transactions on Antennas and Propagation</u>, T-AP Jan '72, 69-72.











POWER SPLIT EQUALITY OF 8-WAY POWER DIVIDER NETWORK

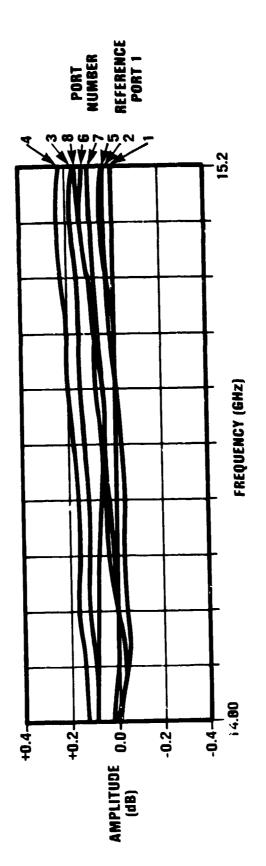


FIGURE 3-2

PHASE BALANCE OF 8-WAY POWER DIVIDER NETWORK

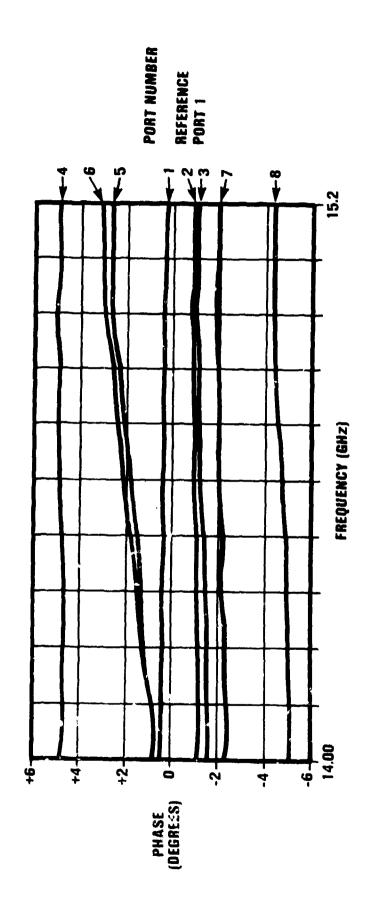


FIGURE 3-3

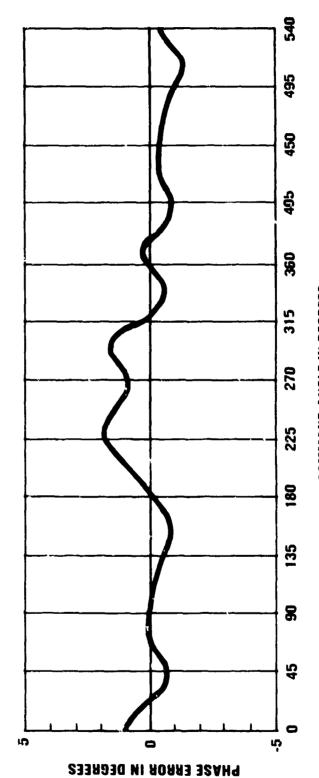
PHASE ACCURACY OF ROTARY FIELD PHASE SHIFTER

KU-BAND ROTARY FIELD PHASE SHIFTER

MAG PART NO. 11F012-001 SERIAL NO.: 4 TEMPERATURE: 25C

MEAN HYSTERESIS	9.63
ASING ERROR RMS	1.07
DECREASING PHASE ERROR PEAK RMS	4.33 1.07
SING ERROR RMS	90
INCREASING PHASE ERROR PEAK RMS	3.76
TEST FREQUENCY	14.6 GHz

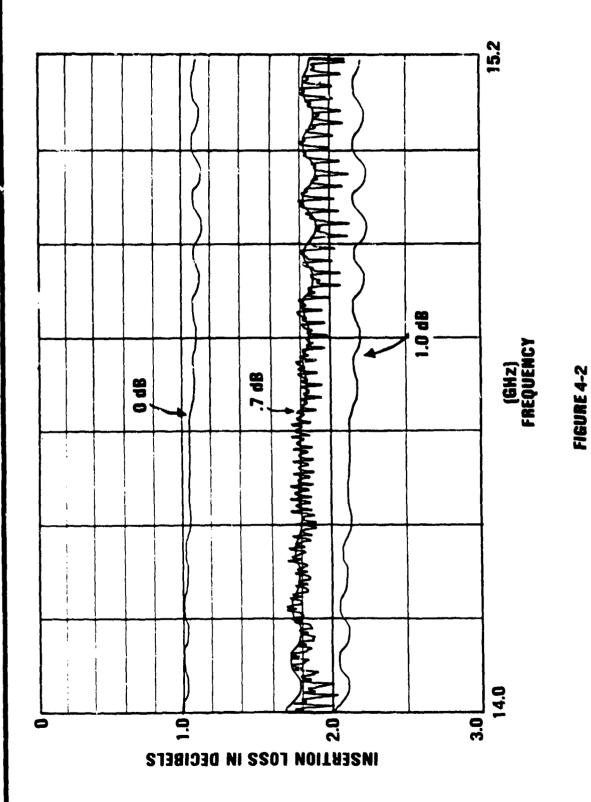
INSERTION PHASE AT 14.6 GHz: -12.31



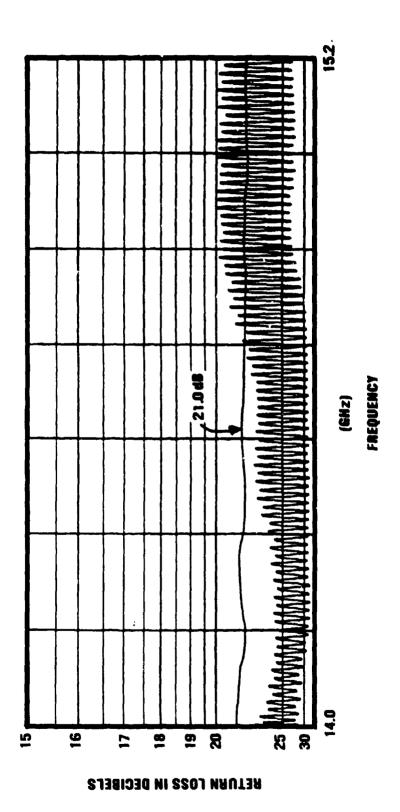
COMMAND ANGLE IN DEGREES PHASE SHIFTER ACCURACY CHARACTERISTICS

FIGURE 4-1

INSERTION LOSS OF ROTARY FIELD PHASE SHIFTER



ROTARY FIELD PHASE SHIFTER



IGURE 4-3

BEAM STEERING CONTROLLER BLOCK DIAGRAM

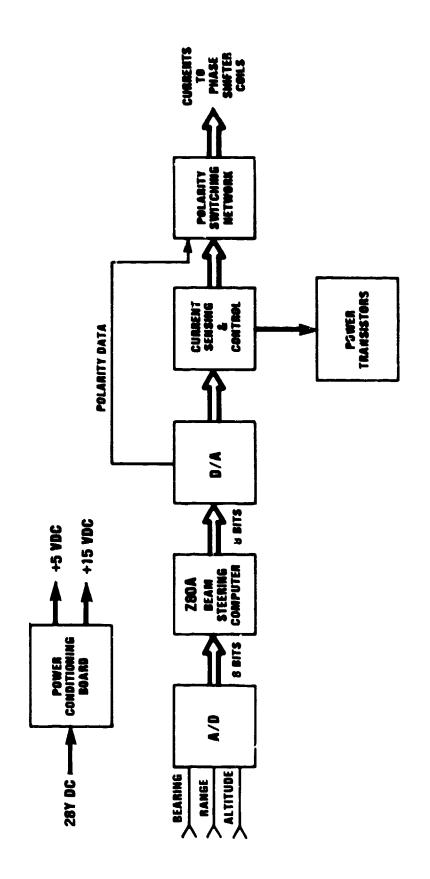


FIGURE 5-1

H-PLANE COMPOSITE

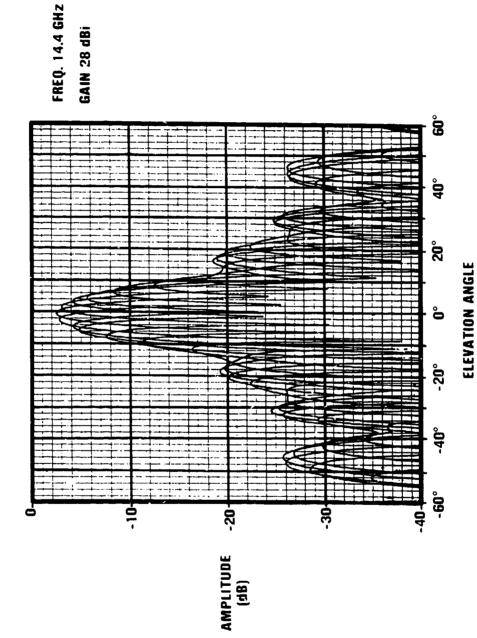


FIGURE 6-1

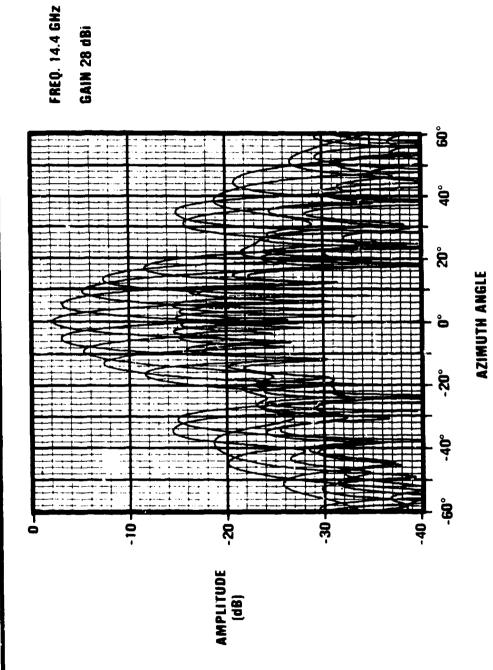


FIGURE 6-2

DESIGN CONSIDERATIONS FOR THE BEAMWAVEGUIDE RETROFIT OF A GROUND ANTENNA STATION*

by

T. Veruttipong, J. Withington, V. Galindo-Israel, W. Imbriale, D. Bathker

Jet Propulsion Laboratory California Institute of Technology

1. / INTRODUCTION

A primary requirement of the NASA Deep Space Network (DSN) is to provide for optimal reception of very low signal levels. This requirement necessitates optimizing the antenna gain to the total system operating noise level quotient. Low overall system noise levels of 16 to 20 K are achieved by using cryogenically cooled preamplifiers closely coupled with an appropriately balanced antenna gain/spillover design. ~ Additionally, high-power transmitters (up to 400 kW CW) are required for spacecraft emergency command and planetary radar experiments. The frequency bands allocated for deep space telemetry are narrow bands near 2.1 and 2.3 GHz (S-band), 7.1 and 8.4 GHz (X-band), and 32 and 34.5 GHz (Ka-band). In addition, planned operations for the Search for Extraterrestrial Intelligence (SETI) program require continuous low-noise receive coverage over the 1 to 10 GHz band. To summarize, DSN antennas must operate efficiently with low receive noise and high-power uplink over the 1 to 35 GHz band.

Feeding a large low-noise, ground-based antenna via a beamwaveguide system has several advantages over directly placing the feed at the focal point of a dual-shaped antenna. For example, significant simplifications are possible in the design of high-power, water-cooled transmitters and low-noise cryogenic amplifiers, since these systems do not have to rotate as in a normally fed dual reflector. Furthermore, these systems and other components can be placed in a more accessible location, leading to improved service and availability. Also, the losses associated with rain on the feedhorn radome are eliminated because the feedhorn can be sheltered from weather.

Many existing beamwaveguide systems use a quasi-optical design, based on Gaussian wave principles, which optimizes performance over an intended operating frequency range. These designs can be made to work well with relatively small reflectors

* The research in this paper was carried out by The Jet Propulsion Laboratory, California Institute of Technology, under contract with the National Aeronautics and Space Administration.

(a very few tens of wavelengths), and may be viewed as "bandpass," since performance suffers as the wavelength becomes very short as well as very long. The long wavelength end is naturally limited by the approaching small D/λ of the individual beam reflectors used; the short wavelength end does not produce the proper focusing needed to image the feed at the dual-reflector focus. In contrast, a purely geometrical optics (G.O.) design has no upper frequency limit, but performance suffers at long wavelengths. These designs may be viewed as "highpass." Considering the need for practically sized beam reflectors and the high DSN frequency and performance requirements, the G.O. design is favored in this application.

Retrofitting an antenna that was originally designed without a beamwaveguide introduces special difficulties because it is desirable to minimize alteration of the original structure. This may preclude accessing the center region of the reflector (typically used in conventional beamwaveguide designs), and may require bypassing the center region. A discussion of the mechanical tradeoffs and constraints is given herein, along with a performance analysis of some typical designs. In the retrofit design, it is also desirable to image the original feed without distortion at the focal point of the dual-shaped reflector. This will minimize gain loss, reflector design, and feed changes.

To obtain an acceptable image, certain design criteria are followed as closely as possible. In 1973, Mizusawa and Kitsuregawa [1] introduced certain G.O. criteria which guarantee a perfect image from a reflector pair (cell). If more than one cell is used (where each cell may or may not satisfy Mizusawa's criteria), application of other G.O. symmetry conditions can also guarantee a perfect image. The problems and opportunities associated with applying these conditions to a 34-m dual-shaped antenna are discussed.

The use of various diffraction analysis techniques in the design process are also discussed. Gaussian (Goubau) modes provide important insight to the wave propagation characteristics, but Geometrical Theory of Diffraction (GTD), FFT, Spherical Wave Expansion (SWE), and Physical Optics (PO) have proven more accurate and faster. GTD and FFT algorithms are particularly necessary at the higher frequencies. PO and S'E have been necessary at the lower frequencies.

2. <u>DESIGN CONSIDERATIONS</u>

2.1 Highpass Design Feed Imaging

For a 2.4-m (8-foot) reflector beam waveguide operated over 1 to 35 GHz with near perfect imaging at X-band and Ka-band and acceptable performance degradation at L-band and S-band, a highpass type beamwaveguide should be used. This type of design

is based upon G.O. and Mizusawa's criteria. Mizusawa's criteria can be briefly stated as follows:

For a circularly symmetric input beam, the conditions on a conic reflector pair necessary to produce an identical output beam are:

- (1) The four loci (two of which may be coincident) associated with the two curved reflectors must be arranged on a straight line.
- (2) The eccentricity of the second reflector must be equal to the eccentricity or the reciprocal of the eccentricity of the first reflector.

Figures 1a, b, and c show some of the orientations of the curved reflector pair that satisfy Mizusawa's criteria. We term a curved reflector pair as one cell.

For the case of two cells where at least one cell does not satisfy Mizusawa's criteria, a perfect image may still be achieved by imposing some additional conditions, described below.

Let S_1 , S_2 , S_3 , and S_4 be curved surfaces of two cells as shown in Figure 2. Each surface can be an ellipsoid, hyperboloid, or paraboloid. Keeping the same sequence order, the surfaces are divided into two pairs [first pair (S_2, S_3) ; second pair (S_1, S_4)] as shown in Figure 2.

For a circularly symmetric input pattern, an identical output pattern (in the G.O. limit) can be obtained if Mizusawa's criteria are satisfied for both pairs in the following manner: First pair (S_2, S_3) satisfies Mizusawa's criteria; second pair (S_1, S_4) satisfies Mizusawa's criteria after eliminating the first pair.

It is noted that the first pair can be eliminated because the input is identical to the output. Also, this concept can be applied to cases with more than two cells. Examples of an extension of Mizusawa's criteria for a multiple-reflector beamwaveguide are given in Figures 3 and 4.

Figure 5 shows a geometrical optics field reflected from each reflector of a beamwaveguide system (refer to Figure 3a). It is clear from Figure 5 that the distorted pattern from the first cell is completely compensated for by the second cell and yields an output pattern identical to the input pattern.

2.2 Bandpass Design Feed Imaging

For many systems, a single-frequency or bandpass design can be advantageously employed. The design considerations can best be described with reference to Figure 6, where the center frequency is given as f_0 , and L_2 is the spacing between two

curved surfaces. A bandpass beamwaveguide system is usually composed of two non-confocal (shallow) ellipsoids (eccentricity close to one). Again from Figure 6, F_{A1} and F_{A2} are G.O. foci of ellipsoid A, while F_{AP} is the phase center of the scattered field from surface A (evaluated at frequency = f_0) in the neighborhood of surface B. Similarly, F_{B1} , F_{B2} , and F_{BP} are for ellipsoid B. The distances from F_{A2} and F_{AP} from surface A are very large compared to L_1 and L_2 . The locations of F_{AP} and F_{BP} depend on frequency as well as surface curvature, L_1 , and L_2 . For example, with a 2.4-m reflector with eccentricity = 0.97 at f = 2.3 GHz and L_2 = 8 m (26 feet), F_{AP} is about 120 m (400 feet) to the left of ellipsoid A, as shown in Figure 6a. In the G.O. limit, F_{AP} and F_{A2} are at the same location, to the right of ellipsoid A.

It is desirable to have two identical surfaces for low cross-polarization and a symmetrical system. Trial and error is needed in order to determine surface parameters for the desired operating frequency and bandwidth within specified losses.

Figure 7 shows the input and output patterns from a bandpass beamwaveguide system where F_{AP} and F_{BP} are chosen to be at the same locations as F_{B2} and F_{A2} , respectively (the choice may not be the optimum condition). The two identical ellipsoids are designed at $f_{\rm O}$ = 2.3 GHz. The results show good agreement between the input feed and the imaged feed. Bandpass beamwaveguide systems appear useful when a limited band coverage is required, using modestly sized (D = 20 to 30%) reflectors. However, these systems do not perform well as the wavelength approaches either zero or infinity. In contrast, a highpass (G.O.) design focuses perfectly at zero wavelength and focuses very well down to $D \sim 40 \, \lambda$. The performance then decreases monotonically as D becomes smaller in wavelengths.

3. APPLICATION CONSIDERATIONS FOR THE DSN

The DSN presently operates three 34-m high efficiency (H.E.) dual-shaped reflector antennas with a dual-band (2.3/8.4-GHz) feed having a far-field gain of +22.4 dBi that is conventionally located at the Cassegrain focal point. The structures were designed prior to beamwaveguide requirements, and feature a continuous elevation axle and a carefully designed elevation wheel substructure. The elevation wheel substructure, shown in Figure 8, plays a key role in preserving main reflector contour integrity as the antenna rotates in elevation. To maintain contour integrity at 8 GHz and above is of prime concern for RF efficiency performance as well as retrofit costs. Figure 9 shows a centerline beamwaveguide approach which, although it is a compact and straightforward RF design, severely impacts retrofit costs and the contour integrity of the main reflector (hence RF efficiency at 8 GHz and above). Figure 10 shows an unconventional approach and represents attempts to reduce structural impacts. Figure 10 is a six-reflector beamwaveguide (eightreflector antenna) based on our extension of Mizusawa's criteria.

Although several detailed options are possible, most options use two cells (four curved reflectors) with two flat reflectors. Some of the options make use of the flexibility afforded by allowing each cell to be distorting (of itself), but then compensated for by the second cell as described in Figures 3, 4, and 5.

Our goal is therefore to perfectly image a feed located perhaps 15 to 25 m (50 to 80 feet) below the main reflector to the original Cassegrain focus. This goal applies over the 1 to 35-GHz frequency range, using a beamwaveguide housing limited to about 2.4 m (8 feet) in diameter. The image should be a 1:1 beamwidth transformation of the original +22.4 dBi feed, permitting reuse of that feed and no changes to the subreflector or main reflector contour. Lastly, the goal includes minimal structural impacts, particularly to the integrity of the main reflector contour. The generalized solution to these goals is reflected in the approach shown in Figure 10, termed the bypass beamwaveguide.

4. ANALYTICAL TECHNIQUES FOR DESIGN AND ANALYSIS

The software requirements for the study and design of beamwaveguides are extensive. These include the capability for G.O. synthesis, Gaussian wave analysis, and high and low frequency diffraction analysis. These requirements are discussed below.

4.1 Geometrical Optics Synthesis Capability

This capability includes software which synthesizes as well as analyzes reflectors satisfying the Mizusawa-Kitsuregawa conditions [1] for minimum cross-polarization and best imaging.

In the high-frequency domain (8 to 35 GHz for the designs considered herein), the focused system shown in Figure 11 is desired. Of course, two paraboloids or mixtures of various conic-section reflectors can be synthesized. Optimization at lower frequency bands generally is accomplished by appropriate defocusing.

4.2 Gaussian Wave Analysis Capability

The required defocusing for the lower bands can be determined by using various beam imaging techniques [2] which are based on Gaussian beam analysis methods first developed by Goubau and Schwering [3]. While Gaussian mode analysis is useful at high as well as low frequencies for "conceptual" designing, conventional diffraction analysis methods are found to be more suitable.

One consideration is that Gaussian mode analysis does not supply spillover losses directly with as great an accuracy as

conventional diffraction analysis methods. The Gaussian modes supply the discrete spectrum, whereas the spillover losses are directly related to the continuous spectrum [4]. Spillover for Gaussian modes is computed by a method more suitable in terms of computational efficiency for a great number of reflection (refraction) elements [3]. The antenna systems considered here rarely contain more than four curved reflectors. Further, spillover losses must be reliably known to much less than a tenth of a decibel for high performance systems.

4.3 Low Frequency Diffraction Analysis Capability.

Because of the large bandwidth of operation (1 to 35 GHz), there is no single diffraction analysis method which will be both accurate and efficient over the entire band.

Efficiency, in the sense of speed of computation, is critical, since in a constrained design many different configurations may be analyzed before an optimum beam waveguide configuration is selected.

In the region of 2.3 GHz (for the 34-m antenna considered herein), the reflector diameters are generally about 20λ . Since a very low edge taper illumination, at least -20 dB, is used to reduce spillover loss, the "effective" reflector diameters are very small in this frequency range.

A comparison between three diffraction algorithms: PO, GTD, and Jacobi-Bessel (JB) leads to the conclusion that:

- (1) GTD is not sufficiently accurate at the low frequencies.
- (2) JB is very slowly convergent in many cases and gives only the far-field in any case. We must determine near-field patterns.
- (3) PO is both accurate and sufficiently fast below 3 GHz.

The above results are illustrated in Figures 12 and 13 when an actual +22.4 dBi corrugated feedhorn is used. It can be seen from Figure 13 that PO and JB agree perfectly to $\sim \pm 20^{\circ}$.

There are two general PO computer algorithms useful at the low frequencies. One is a straightforward PO algorithm which subdivides the reflectors into small triangular facets. This is essentially a trapazoidal integration of the near-field radiation integral and is a very flexible algorithm.

A second algorithm is based on a Spherical Wave Expansion (SWE) and is also a PO technique. It has two useful characteristics: (1) when a high degree of circular symmetry exists in the scattered fields, then the two-dimensional radiation integral is reduced to a small number of one-dimensional integrals with a

resultant marked decrease of computational speed; and (2) an (r) interpolation of the scattered field (at different radial distances from the coordinate origin) is done very accurately.

The PO (direct-trapezoid) and SWE algorithms are useful for cross-checking results. Near-field and far-field computations and comparisons in both amplitude and phase are shown in Figures 14, 15, and 16. Figure 14 contains near-field PO and SWE results for scattering from one paraboloid reflector. Figure 15 contains the results for far-field scattering from two reflectors. Figure 16 contains the near-field scattering for two reflectors and a comparison of the "imaging" with the feed pattern. At higher frequencies (>8 GHz), the feed pattern will be virtually perfectly imaged over an angle of $\pm 15^{\circ}$.

4.4 High Frequency Diffraction Analysis Capability

For reflector diameters of 70 or more wavelengths (>8 GHz), including a -20 dB edge taper, PO analysis methods become too expensive and time consuming. (The SWE may still be useful if a high degree of rotational symmetry exists.) An alternative approach is to use GTD analysis. The GTD computation speed does not increase with increasing reflector diameters, but the accuracy of the analysis does increase.

In order to test the accuracy of GTD at 8 GHz, comparisons were made between GTD and PO. Results for diffraction of a single ellipsoid are shown in Figure 17. The results for the phase of the scattered field were equally as good. GTD was determined to be accurate at 8 GHz and higher.

Analysis of two or more reflectors by GTD involves some manipulation of the fields scattered between any two reflectors. The fields scattered from one reflector must be placed in a format suitable for GTD scattering from the next reflector. This is accomplished by computing the vector-scattered field in the vicinity of the next reflector and then interpolating as follows:

- (1) Use of an FFT for ϕ -variable interpolation.
- (2) Use of a second-order Lagrangian local interpolation for θ interpolation (for a z-axis along the axis of the reflector, ϕ and θ are spherical coordinates).
- (3) For the r (of [r, θ , ϕ] spherical coordinates) interpolation, an approximation consistent with the GTD approximation was to assume a 1/r variation in amplitude and a kr variation in phase. This approximate interpolation should be checked against exact computations of the near fields.

By the method described above, multiple reflector computations, even with a large number of reflectors, can be calculated

with both great speed and accuracy at frequencies above ${\sim}8$ GHz for reflectors of >70 λ in diameter.

A typical result is shown in Figure 18 for a pair of ellipsoids which satisfy the Mizusawa-Kitsuregawa criteria. The object is to perfectly image the input feed over about $\pm 20^{\circ}$. This is accomplished with great accuracy and virtually no loss at X-band frequencies and higher.

5. CONCLUSIONS

A generalized solution has been achieved for retrofitting a large dual-shaped reflector antenna for beamwaveguide. The design is termed bypass beamwaveguide. Several detailed options within the bypass category remain to be studied, and work continues.

With the analysis capability available, we are gaining some valuable views of the RF performance behavior of some of the many options. It appears fairly clear for the 1 to 35-GHz requirement that highpass (pure G.O.) designs are necessary in contrast to a bandpass (non-confocal ellipsoids) approach. It appears that deep confocal ellipsoids satisfying the Mizusawa-Kitsuregawa criteria operate (focus) well with reflector diameters of about 70λ and larger but may not be tolerable at longer wavelengths.

As a part of this activity, an important extension of the Mizusawa-Kitsuregawa criteria has been revealed. The principle revealed shows how a two-reflector (cell), although in itself distorting, may be combined with a second cell which compensates for the first and delivers an output beam which is a good image of the input beam.

REFERENCES

- 1. M. Mizusawa and T. Kitsuregawa, "A Beamwaveguide Feed Having a Symmetric Beam for Cassegrain Antennas," <u>IEEE Trans.</u>
 <u>Antennas and Propagat.</u>, pp. 844-886, November 1973.
- 2. T. S. Chu, "An Imaging Beam Waveguide Feed," <u>IEEE Trans.</u>
 <u>Antennas and Propagat.</u>, pp. 614-619, July 1983.
- 3. G. Goubau and F. Schwering, "On the Guided Propagation of Electromagnetic Wave Beams," <u>IRE Trans. Antennas and Propagat.</u>, pp. 248-256, May 1961.
- 4. R. E. Collin, "Field Theory of Guided Wayes," McGraw-Hill, N.Y., pp. 474-475, 1960.

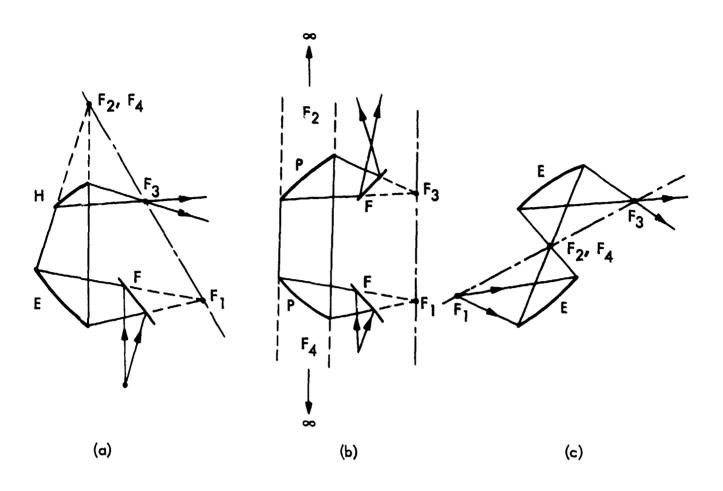


Figure 1. Possible Two-Curved Reflector Beamwaveguide Configurations; E = Ellipsoid, H = Hyperboloid, P = Paraboloid, F = Flat Plate

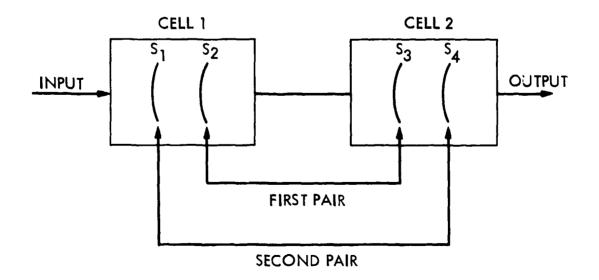
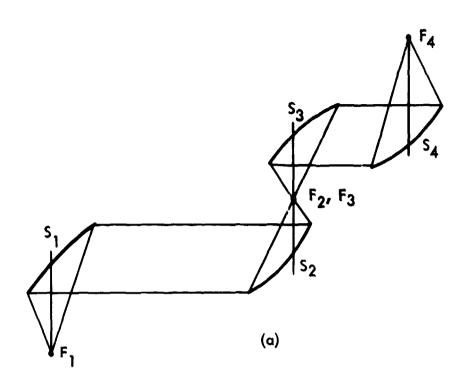


Figure 2. Multiple Curved Reflector Beamwaveguide System; S_i = Ellipsoid, Hyperboloid, or Paraboloid





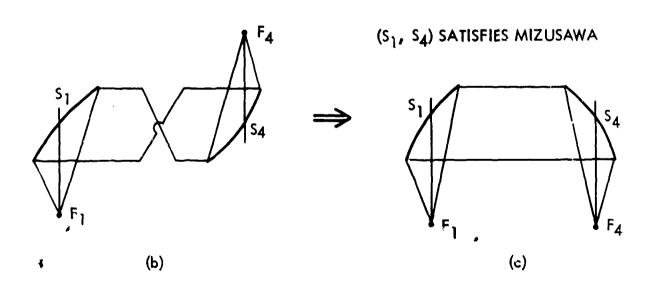
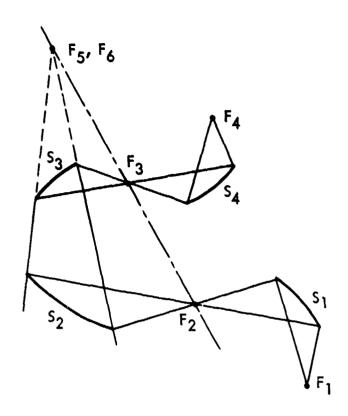


Figure 3. Demonstrating an Extension of Mizusawa's Criteria for a Multiple Reflector Beamwaveguide (Paraboloids)





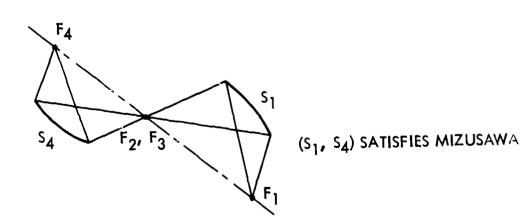


Figure 4. Demonstrating an Extension of Mizusawa's Criteria for a Multiple Reflector Beamwaveguide (Ellipsoids/Hyperboloids)

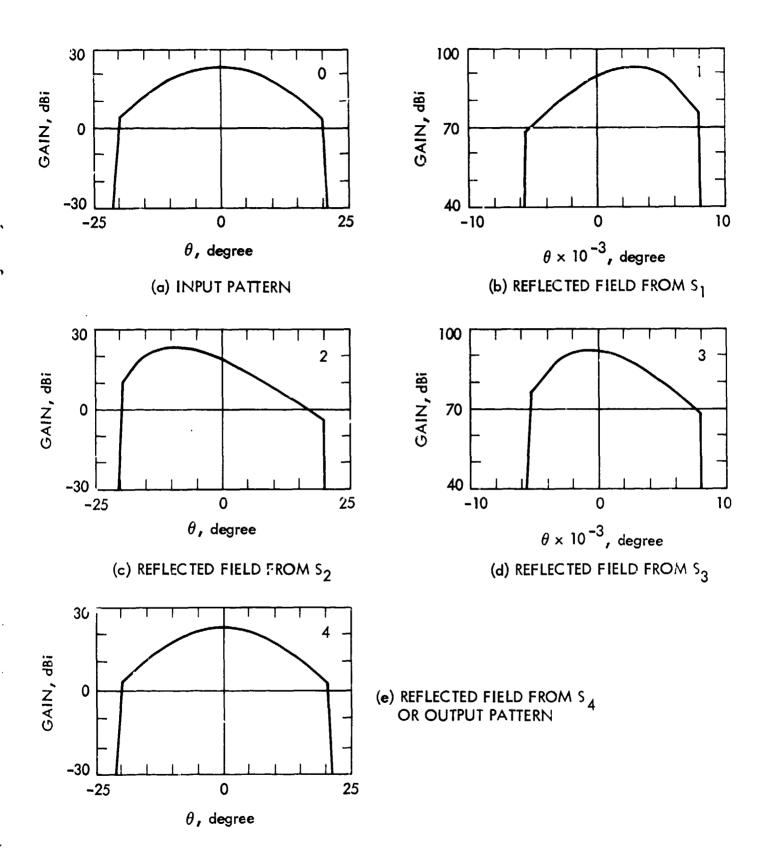
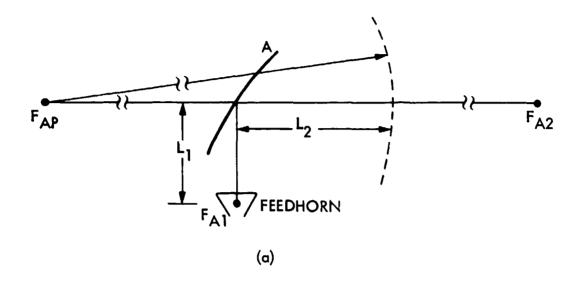


Figure 5. Geometrical Optics Field Reflected from Each Surface of a Beamwaveguide System (Shown in Figure 3a)



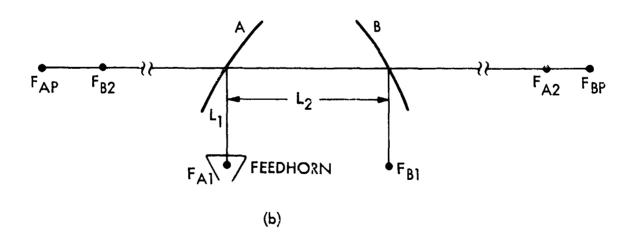


Figure 6. Bandpass Feed Imaging Configuration

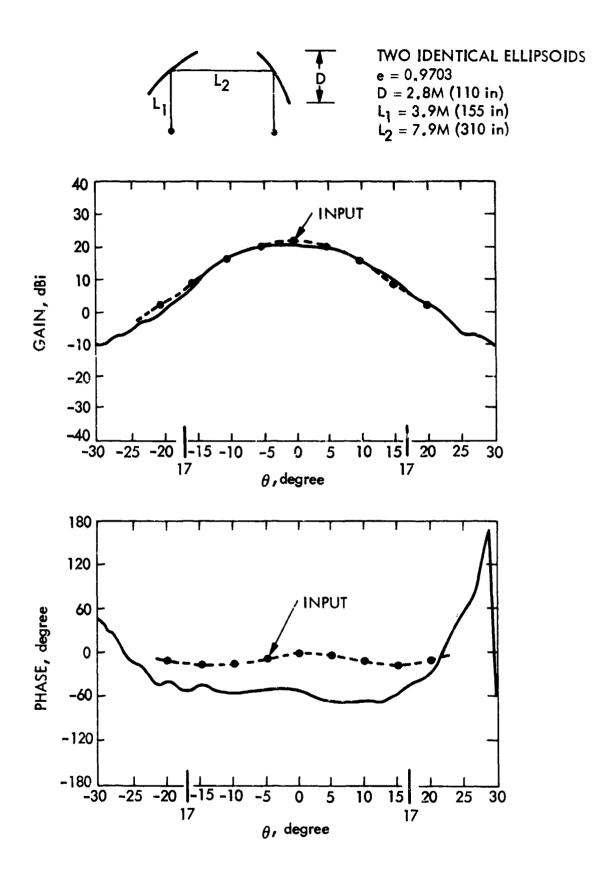


Figure 7. Comparison Between Input Feed Pattern and Feed Image from a Bandpass Beamwaveguide System at Center Frequency = 2.3 GHz

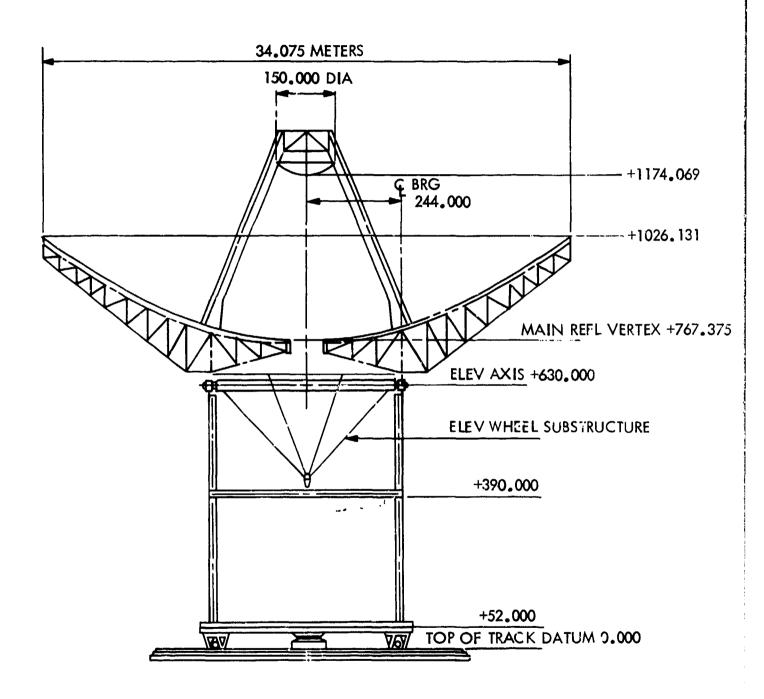


Figure 8. 34-m H.E. Existing Structure

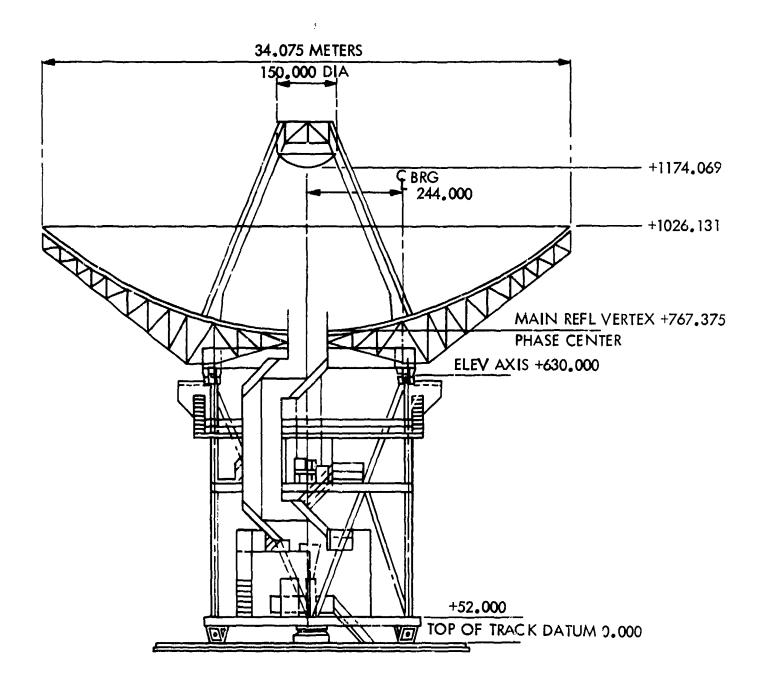


Figure 9. 34-m H.E. Centerline Beamwaveguide

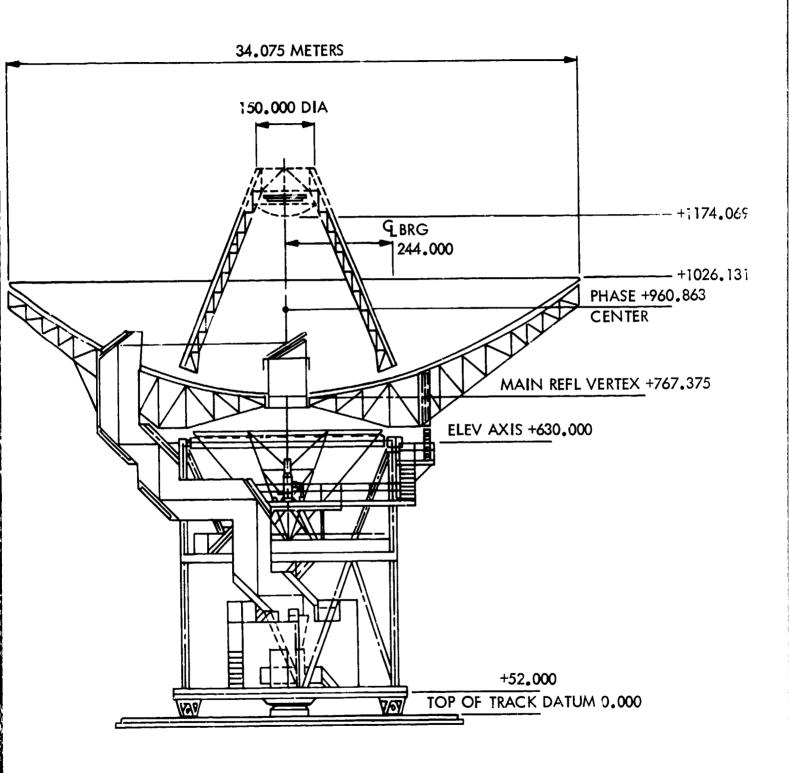


Figure 10. 34-m H.E. Bypass Beamwaveguide

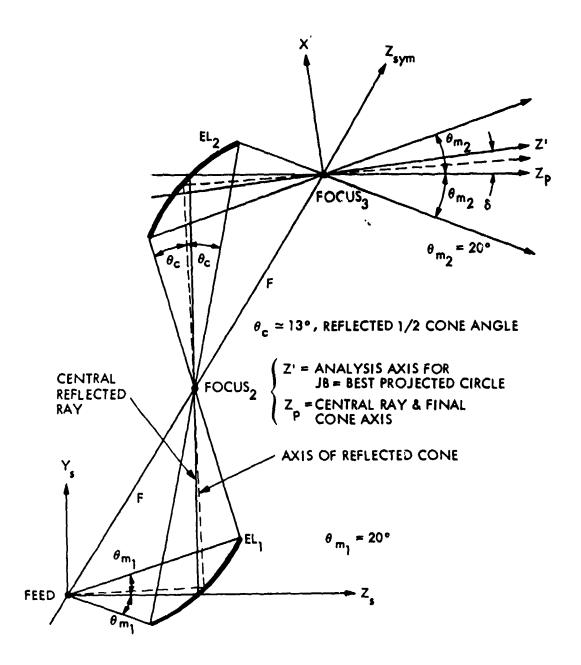


Figure 11. Analysis Geometry for Ellipsoid Pair (EL $_1$, EL $_2$)

THE RESERVE OF THE PROPERTY OF

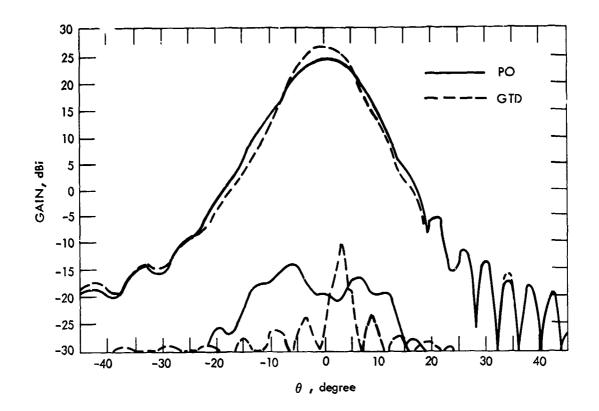


Figure 12. Near-Field, One 2.4-m Ellipse Diffraction Patterns (RCP, 2.3-GHz, Offset Plane)

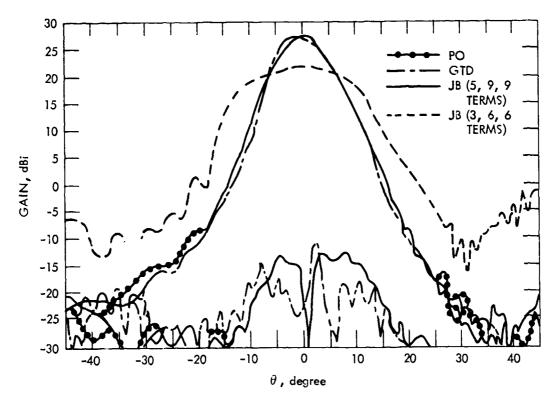


Figure 13. F :-Fi . One 2.4-m Ellipse Diffraction Patterns (RCP: 2.3-GHz, Offset Plane)

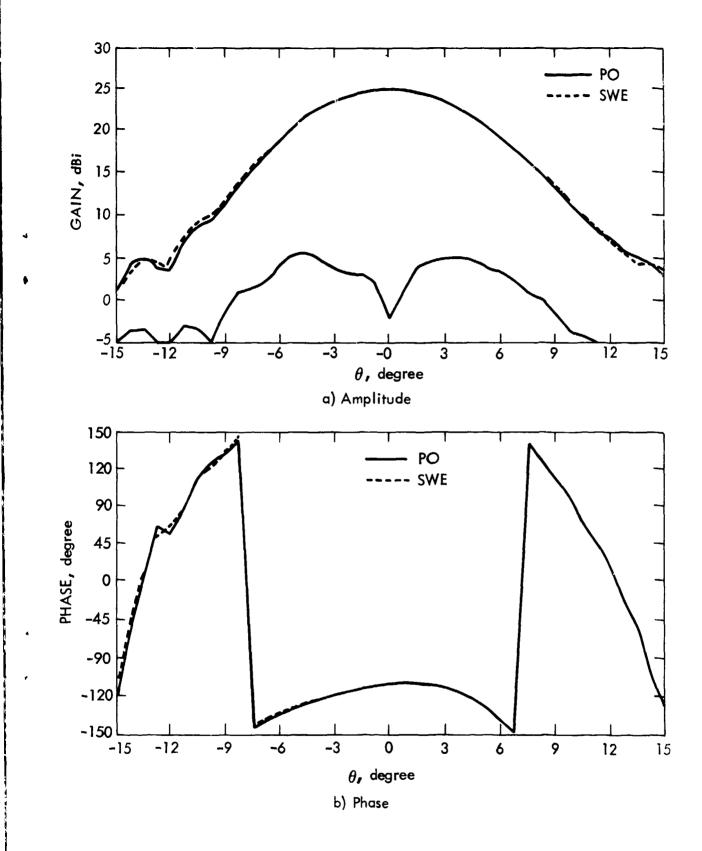


Figure 14. PO and SWE Near-Field Scattering from a Single 2.4-m Paraboloid at 2.3 GHz

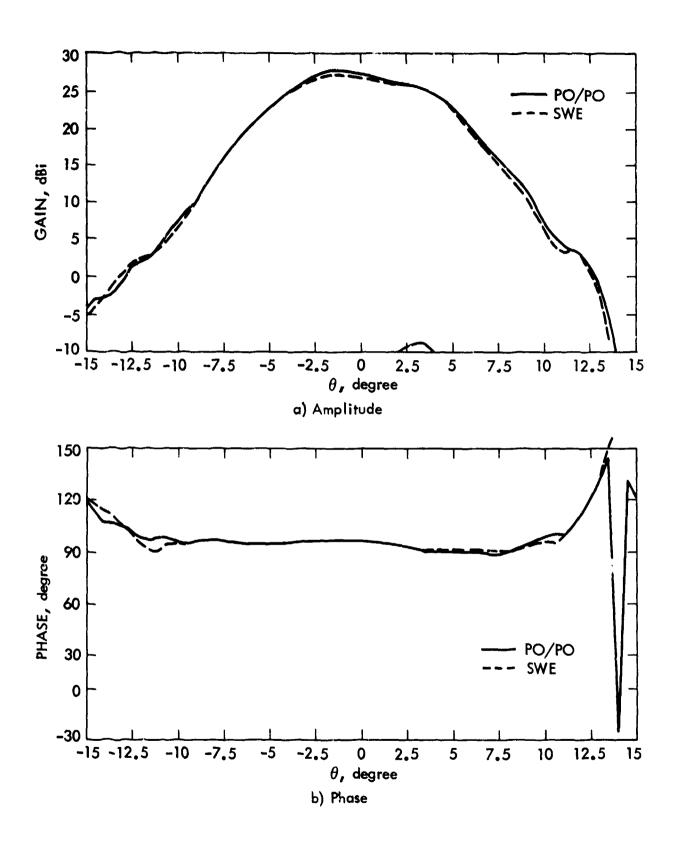


Figure 15. PO and SWE Far-Field Scattering from Two 2.4-m Paraboloids at 2.3 GHz

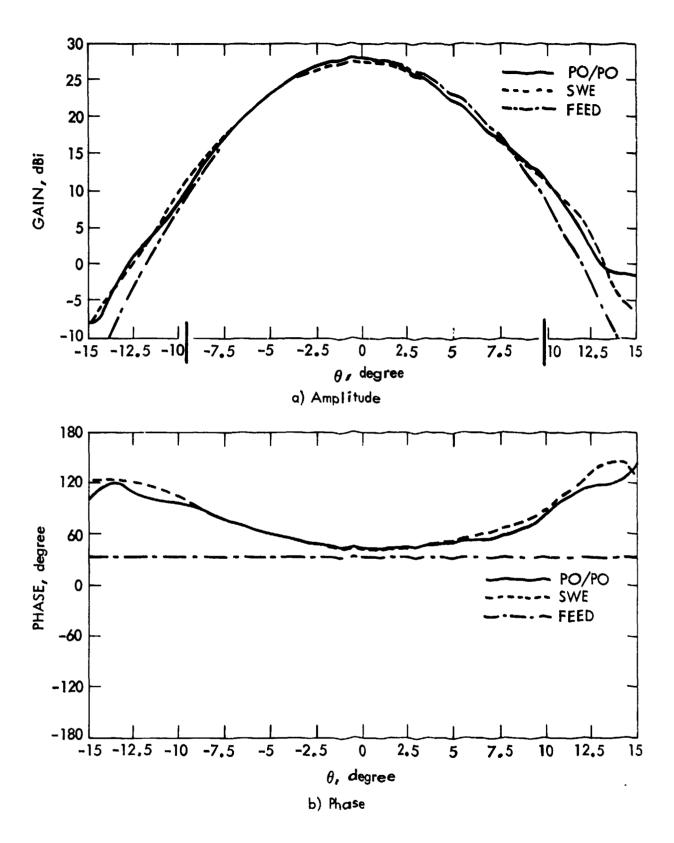


Figure 16. PO and SWE Near-Field Scattering from Two 2.4-m Paraboloids at 2.3 GHz (Comparison with Feed Pattern)

AND CHARLES AND CONTROL OF THE CONTR

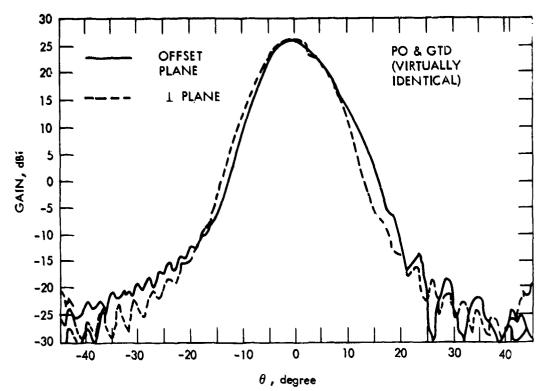


Figure 17. Near-Field, One 2.4-m Ellipse Diffraction Patterns (RCP, 8.4 GHz, Offset and 1 Plane Cuts)

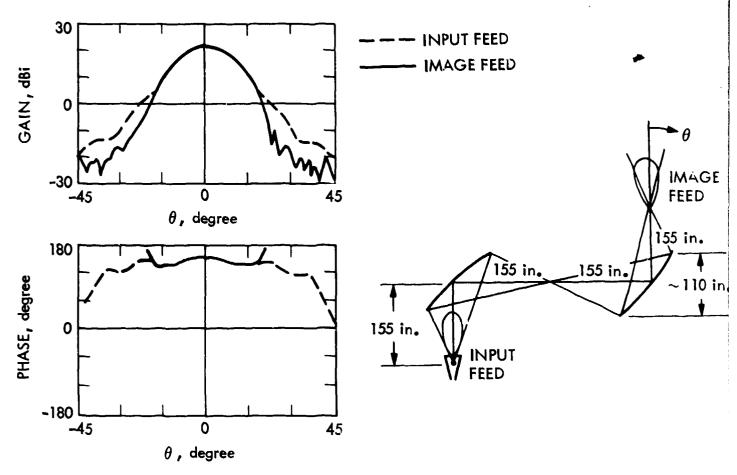


Figure 18. GTD Scattering for Two 2.4-m Ellipses, RCP at 8.4 GHz

THE PROPERTY OF THE PROPERTY O

AN INEXPENSIVE RELATIVELY BROADBAND MULTI-PURPOSE ANTENNA

Samuel C. Kuo and Warren M. Shelton GTE Government Systems, Western Division

The one-wavelength loop antenna has been widely used in the HF and low VHF range by amateur radio operators in the form of the Quad antenna ever since it was introduced in the late 1940's by Moore. \mathcal{A} Three types of the one-wavelength loop antennas are shown in Figure 1-a through 1-c. In (a) and (b) the sides of the square loops are equal to 1/4 wavelength and the sides of the triangular loop in (c) are equal to 1/3 wavelength. The relative direction of current flow is also shown in the drawing to demonstrate the polarization of these antennas. When the input terminals are on the bottom and are excited with equal amplitude and out-of-phase currents, these antenna provide horizontally polarized radiation. The original Quad antennas introduced by Moore, shown in Figure 1-d and 1-e, consisted of two one-wavelength loops; one as the driven element, and the other as the reflector. Subsequent development added more loops as directors and the antenna with directors added was called a Quagi antenna which is claimed to have a gain of approximately 2 dB over a Yagi of the same array length.

Various types of the Quad and Quagi antennas have been developed through the years, and they have always been used as rela-

Figure 2-a has better characteristics in terms of VSWR, gain, and bandwidth than the two other types, it was selected for bandwidth comparison with a single loop.

A Bi-loop antenna, as shown in Figure 2-a, was fabricated with each side of the loop antenna approximately 4 inches long and was mounted 3 inches above a 14 by 18 inches ground plane. Using a VSWR of 3.0:1 as the criteria, this antenna has a bandwidth of approximately 2.4:1, while a single loop of the same dimension and configuration as one-half of the Bi-loop has a bandwidth of approximately 2.0:1. The swept gains of the two antennas from .55 to 1.2 GHz, shown in Figure 3, shows the gain of the Bi-loop antenna to be approximately 2 dB higher than that of a single loop antenna.

The bandwidth of a dipole or monopole antenna depends a great deal on the diameter of the radiator. The same is also true for the loop antenna. The Bi-loop antenna, snown in Figure 4, was made of relatively large diameter tubing. The bandwidth of this particular antenna is, however, limited by the balun. Subsequent antennas built were fed with coaxial cables as shown in Figure 5. Since the characteristic impedance of this antenna is approximately 75 ohms, a 50/75-ohm transformer was included in the feed line for impedance transformation. When a Bi-loop antenna with 4-inch sides was built with 0.650 diameter tubing, and fed with 75-ohm coaxial cables and a 50/75-ohm impedance transformer, the

tively narrow band antennas by the amateurs. For instance, a popular version of the antenna, the "Three-band Quad," which has three sets of different sized full-wavelength loops, is used to cover 14.4, 21.1, and 28.1 MHz.

In the high VHF, UHF and microwave frequency range where broad frequency coverage is often desired, the original Quad antenna which has limited broadwidth, can not meet the frequency bandwidth requirements. In Moore's design, one of the two loop antennas is used as a reflector, which is very sensitive to the operating frequency and consequently limits the bandwidth of the antenna. The bandwidth of the Quad antenna can be increased by replacing the reflector loop element with a flat ground plane. The performance of a one-wavelength loop in front of a ground plane is similar to that of a dipole over ground. When the spacing is small in terms of wavelength, the radiation efficiency is very low and the VSWR is high. When the spacing approaches one-half wavelength, a null will appear on the antenna axis.

Further increase of the operating bandwidth of this antenna can be achieved by arraying two one-wavelength loop antennas. The uniqueness of the one-wavelength loop antenna is that the two loops can be arrayed without a RF combiner, and the second loop antenna can simply be paralleled to the first loop antenna at the feed point. The new structures are called Bi-loop antennas, three forms of which are shown in Figure 2. Since the type shown in

bandwidth (3.0:1 VSWR) approached 3.0:1. Unfortunately, the cost of this antenna is very high due to the tubular construction and the cost of the transformer.

An inexpensive version of the Bi-loop antenna was developed which costs less than 10% of the cost of the tubular configuration. This antenna was fabricated using printed-circuit board techniques where the Bi-loop antenna element was etched on one side of the PC board and the impedance transformer etched on the other. The antenna element trace serves as the ground plane for the microstrip transformer which provides the impedance transformation from 50 ohms at the input connector to 75 ohms at the input to the Bi-loop antenna. A sketch of this Bi-loop antenna with its integral impedance transformer is shown in Figure 6. The details of the connector and the feed point configurations are also shown. The material used to fabricate this Bi-loop antenna and its ground plane consist of a piece of G-10 epoxy fiberglass PC board, a panel type connector and a piece of aluminum sheet for ground plane. The total cost is less than \$30.00 including etching the antenna. A slight decrease in bandwidth and gain are the trade-off for the low cost in comparison to the tubular configuration.

One such antenna was fabricated using 1/8-inch G-10 epoxy fiberglass PC board with the following parameters:

Length of each side of the loop 4.0 inches

Width of the loop conductor 0.75 inches

Spacing from ground plane 3.0 inches

Size of ground plane 11 by 14 inches

The performance characteristics of this antenna are shown below, and typical E- and H-plane patterns are shown in Figure 7.

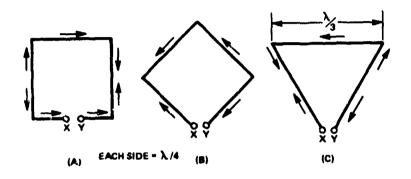
VSWR: 600 - 1300 MHz 2.0 Max.

Gain: 600 - 1200 MHz 7.5 dBi Min. 8 dBi Nom.

3 - dB Beamwidth, E-plane 65° Nom.

H-plane 65° Nom.

Since these antennas are fabricated using PC board etching techniques, they are nearly identical and are good candidates for linear array elements. Figure 8 shows a 10-element linear array using the Bi-loop. Over a 1.6:1 bandwidth, the array can be steered to +/-32° with the VSWR of the antenna elements remaining under 2.0:1. Azimuth radiation patterns of this array measured on axis and with 32° scan, are shown in Figure 9 for low, medium, and high frequencies.



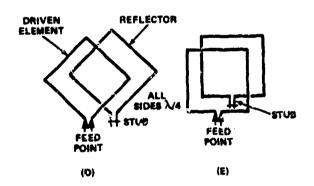


Figure 1. One Wavelength Loop and Quad Antennas.

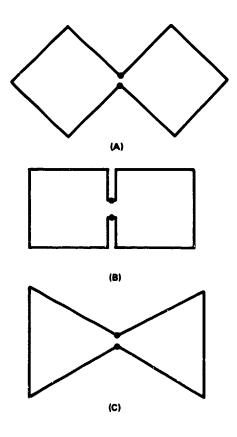


Figure 2. Three Types of Bi-Loop Antennas.

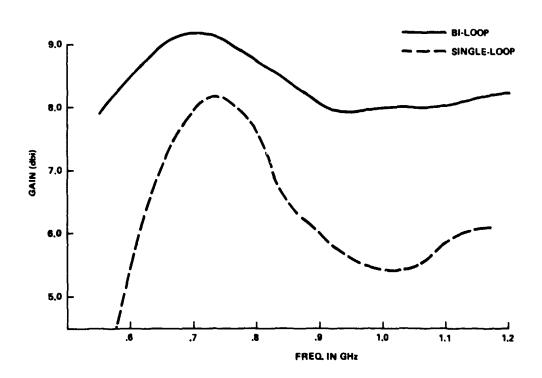


Figure 3. Gain Comparison of A. Bi-Loop and A single-Loop Antenna Over Ground

 $oldsymbol{L}$

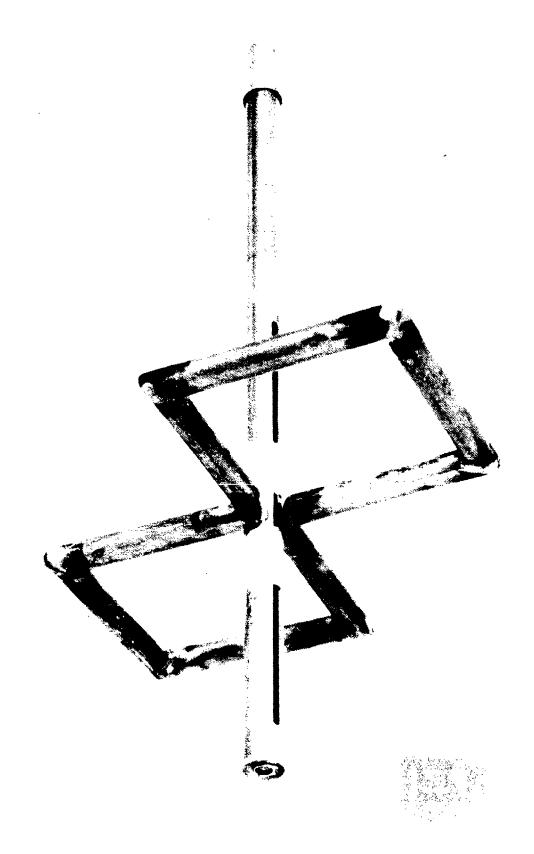


Figure 4. Bi-Loop Antenna

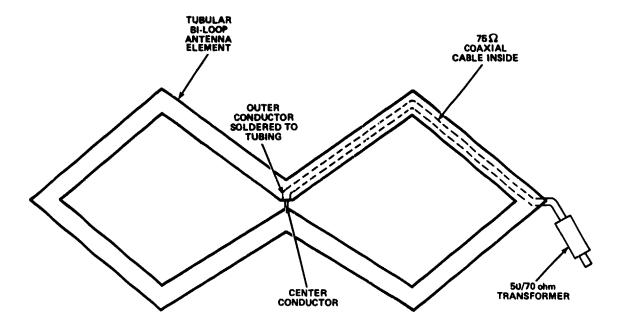


Figure 5. A Tubular Bi-Loop Antenna and Its Feed Construction

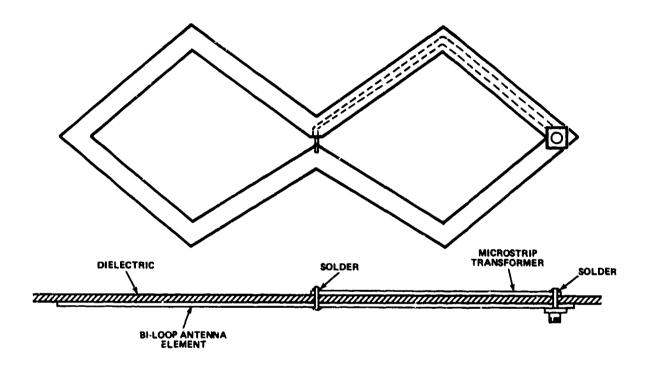


Figure 6. A Bi-Loop Antenna on PC Board with Its Integral Impedance Transformer

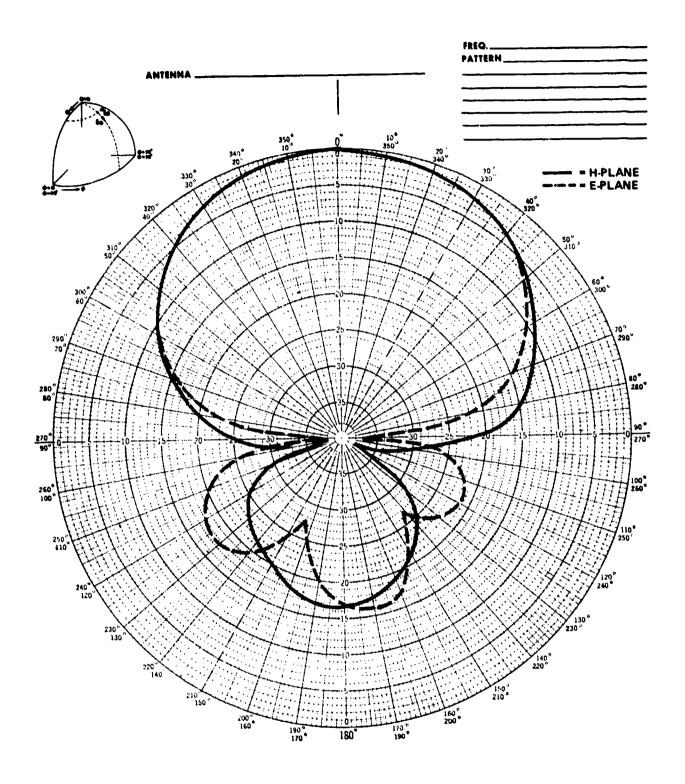


Figure 7. Typical E & H-plane Radiation Patterns of a Bi-loop Antenna

‡.

Figure 8. A 10-Element Linear Array of Bi-Loop Antennas

Radiation Patterns of a 10-Element Linear Array of Bi-Loop Antennas Figure 9.

A LOG-PERIODIC ARRAY OF MONOPOLE-SLOT ELEMENTS

David J. Tammen
Space and Communications Group
Technology Division
Hughes Aircraft Company
El Segundo, California

Paul E. Mayes University of illinois Champaign-Urbana

ABSTRACT

In feeding a log-periodic monopole or slot array, excess line must be used between radiating elements to achieve proper phasing for backfire radiation. Discontinuities presented by the radiating elements, which are approximately one-half wavelength apart on a series feedline, cause additive reflections on the line. There is, therefore, a region on the log-periodic array which behaves similarly to a periodically loaded transmission line operating in a stopband. Reflections occurring in this region inhibit propagation of energy down the feedline. To obtain a frequency-stable impedance, these "structural stopband" regions should be reduced.

One technique that can be used to minimize the stopband region on a series feedline is to reduce the reactive nature of the non-radiating eliments using the principle of complementarity. A two-port monopole-slot antenna has been previously shown to have a relatively constant image impedance below its first resonance.

In the work presented here, a log-periodically scaled array of monopole-slot elements was constructed and tested. The results

demonstrate the elimination of the structural stopband regions without the use of modulation of the feedline impedance. Other performance characteristics such as impedance bandwidth, beamwidth, and front/to-back ratio of the array are also presented.

Ì

1. INTRODUCTION

In the past few years there has been a great deal of interest in broadband, low-profile, surface-mounted antennas. Although microstrip patch and cavity-backed slot antennas satisfy the requirements of low profile and surface mountability, neither structure can be considered broadband. However, log-periodic arrays of cavity-backed slots are able to satisfy the broadband requirement. Theoretically, the operating bandwidth of such an array is limited only by the number of elements used and the size allowed for construction of the array. In practice, however, there is a fundamental problem in the feeding of such an array.

In feeding a log-periodic monopole or slot array, excess line must be used between the radiating elements to achieve proper phasing of the elements for backfire radiation. Ingerson and Mayes ¹ found that the discontinuities presented by slots, which were approximately one-half wavelength apart along a series feedline, cause additive reflections on the line. There is, therefore, a region on the log-periodic array that behaves similarly to a periodically loaded transmission line operating in a stop band. Reflections that occur in this stop region inhibit the propagation of energy down the feedline. To achieve an input impedance that changes little with frequency, "structural stopband" regions between the source and

the active elements should be minimized. Ingerson and Mayes demonstrated that modulating the impedance of the feedline could greatly reduce this stopband phenomenon. The input impedance of the antenna constructed by Ingerson was approximately 150 ohms. This impedance is too high for many applications. With this fact in mind, Ostertag applied the impedance-modulation technique to a shallower cavity with a microstrip feedline and was able to reduce the input impedance to 50 ohms².

Another technique that can be used to minimize the stop band for a series feedline is to reduce the reactive nature of the nonradiating elements using the principle of complementarity. A planar dipole and the corresponding complementary slot are duals of each other. Using Babinet's principle it can be shown that:

$$Z_{s}Z_{d} = -\frac{\mu}{4e} = -\frac{\eta^{2}}{4}$$
 (1)

where \mathbb{Z}_{s} is the slot impedance and \mathbb{Z}_{d} is the impedance of the complentary dipole. Thus it is seen that the input impedance of a slot and a complementary dipole fed together is independent of frequency. This principle was used by Schroeder 3 , Dunlavy 4 , and Itoh and Chen 5 . However, all of these structures required some sort of external feed network for proper operation.

In 1970 Mayes and Weisenmeyer⁶ demonstrated that a two-port monopole-slot antenna can be made to have a relatively constant image impedance for frequencies below its first resonance. A simple microstrip feedline with a cylindrical monopole attached directly above the slot

ASDR: MD86-3/040:511

a registra en control de la co

feedpoint was used with this antenna. Stripline versions of the monopole-slot were later studied by Cwik⁷, Halpern⁸, and Paschen⁹. Paschen also investigated the properties of the monopole-slot with regard to using the antenna as an array element. He found that in addition to having a uniform image impedance (thus minimizing the effect of the structural stopbands), the element also has other characteristics which make it a desirable element for a log-periodic array. He found that the far-field characteristics of the monopole combined with the slot result in an element with a fairly high front-to-back ratio. This allows for easy construction of an array with a high front-to-back ratio. He also demonstrated that this characteristic of the monopole-slot can reduce the mutual coupling between the cascaded elements of a series-fed array.

In the project reported herein, a log-periodically scaled array of monopole-slot antenna elements was constructed and tested. One objective was to demonstrate the elimination of the structural stopbands without the use of modulation of the feedline impedance. Other objectives were to evaluate the performance characteristics of impedance bandwidth, pattern bandwidth, beamwidth, and front-to-back ratio.

2. MEASUREMENTS FOR A SINGLE MONOPOLE-SLOT ELEMENT

Before construction of the complete array could begin, the impedance characteristics of a single representative monopole-slot were needed. The impedance characteristics of a previously constructed cavity-backed slot were determined using a vector network analyzer (Figure 1). Two different techniques were initially used to achieve an impedance

characteristic for the monopole which was complementary to the impedance of the slot: top loading of the monopole to reduce its resonant impedance; and increasing the feedline impedance to 85 ohms, a value closer to the 300 ohm resonant impedance of the slot.

Since it was easier to adjust the monopole length without the top load, the latter method was used in construction of the array. The impedance characteristics of this monopole-slot are shown in Figure 2. Note in this figure that the VSWR is less than 1.5 for frequencies below 1000 MHz and that nearly all of the incident power is radiated between 1100 and 1200 MHz.

3. DERIVATION OF CAVITY AND ARRAY PARAMETERS

The basic cell size and scaling factor had to be determined before construction of the log-periodic array could begin. The cell size of an array of cavity-backed slots is determined by the length-to-width ratio of the largest element. It has been previously found by Mayes¹⁰ that a wider slot results in a significantly lower resonant frequency for a given slot length than does a narrow slot. To minimize the energy coupled into the non-radiating modes it is desirable to have the cavity-backed slot antenna resonate below the lowest order mode (TE₁₁) of the closed cavity. The cavity-backed slot previously mentioned (cavity dimensions 10x3x.125 in., slot length of 9 in.) was found to satisfy this requirement (1180 MHz for the slot vs. 1256 MHz for the cavity mode).

There are two fundamental opposing factors to consider when choosing the scaling factor for an array:

- Physical limitations due to size limitations and material cost and availability
- 2. Operational characteristics such as bandwidth, sidelobes, etc.

 To meet the physical requirements the scaling factor should be as small as possible. To meet the electrical performance requirements the scaling factor should be as large as possible to increase the number of elements operating in the active region of the array. For the array constructed a compromise scaling factor of .89 was chosen. This allowed for an array with a "structural bandwidth" of 4.05:1 and for a nearly uniform distribution of power between 3 elements for most of the operating frequency range.

4. CONSTRUCTION OF THE ARRAY

The cavity-backed slot array was constructed using the scaling factor of .89 and a base cavity size of 11.5x3.375 in. on a single .125 inch thick double copper-clad Rexolite 2200 substrate of dimension 12x24 inch (Figure 3). The cavity walls were constructed using brass screws spaced .5 inches apart for the largest cavity and (.5 inch) (.89)ⁿ⁻¹ for the remaining elements. It has been previously shown that this arrangement of screws is a fairly good approximation for a PEC wall for the frequencies of interest. The Rexolite substrate was mounted on a .125 inch thick aluminum plate for increased structural stability. The slots were formed by removal of the copper cladding in the desired area on the top surface of the substrate. The above array of cavity-backed slots was constructed 2-3 elements at a time starting with the low frequency elements and moving to

higher frequencies with each succeeding cavity. (Cavity and slot dimensions are given in Table 1).

TABLE I
DIMENSIONS OF CAVITY-BACKED SLOTS
(IN INCHES)

CAVITY	CAVITY		SLOT	
NUMBER	LENGTH	WIDTH	LENGTH	HTDIW
1	11.500	3.375	9.750	.200
2	10.235	3.003	8.678	.178
3	9.109	2,673	7.723	.158
4	8.107	2.379	6.873	.141
5	7.215	2.118	6.117	.125
6	6,422	1.885	5,444	.112
7	5,175	1.677	4.846	.099
8	5.087	1.498	4,313	.088

Using a Hewlett-Packard 8510 vector network analyzer each cavity was matched to a monopole of appropriate length. The technique used is as follows:

- The resonant frequency of the slot was determined using the network analyzer and one wavelength 50-85 ohm microstrip tapered feedlines.
- 2. A monopole was cut to a quarter of the free space wavelength corresponding to this frequency.
- The length of the monopole was trimmed to minimize the input reflection coefficient.

S-parameters were taken for each of the 8 monopole-slot elements. A typical set of S-parameters for a monopole-slot (the fourth in the array) is given in Figure 5. It can be seen from the S-parameters shown in Figure 5 that the monopole-slot is well suited for use as an array element. At frequencies below resonance, the element is well matched to the feedline and transfers most of its input energy with a shift in phase to the next element in the array. As the frequency is increased to resonance, the element radiates most of its input energy (represented by the simultaneous low magnitudes of S_{21} and S_{11}).

The lengths of the matching monopoles (3/32 inch brass rod with #0-72 threads on the bottom to fasten to the nuts soldered to the feedline) are given in Table 2.

TABLE 2 LENGTHS OF MONOPOLES

NUMBER LE	ENGTHS (cm)
l	2.87
2	3.46
3	3.80
4	4.07
5	4.44
6	4.96
7	5.49
Q	6 38

The final phase of array construction was building the meandering feedlines and the two corresponding 85-50 ohm linear tapers. Three

feedlines with slightly different interelement spacing were constructed to allow for experimental uncertainties in the individual element responses. Feedline 1 was constructed for proper phasing for the backfire radiating condition. Feedline 2 was 7.5% longer between feedpoints while feedline 3 was 7.5% shorter between feedpoints. The required spacing for the backfire condition is given by Equation 1.

$$d = \frac{(\lambda_0 - l)}{(\epsilon_{eff}) \cdot 5}$$
 (1)

where λ_0 = free space wavelength corresponding to the resonant frequency of the larger element (cm)

 ℓ = the physical separation between the elements (cm)

 ϵ_{eff} = effective permittivity of the microstrip feedline (ϵ_{eff} = 2.048 for this 85 line)

Equation (1) was solved for the section of line between the first and second largest elements. For this condition of line $\lambda_0 = 27.78$ cm and $\ell = 8.10$ cm. Using Equation (1) results in the following:

$$d = 13.75 \text{ cm} = 5.413 \text{ in}$$
 (feedline 1)

$$d^+ = d + (0.075)d = 5.819 in,$$
 (feedline 2)

$$d^{-} = d - (0.075)d = 5.006 in$$
 (feedline 3)

The resulting lengths of feedlines between elements are shown in Table 3.

The three feedlines were constructed on .125 inch copper-clad Rexolite 2200 substrates using the values given in Table 3. #0-72 nuts were soldered to the feedline above the point where the feedline crossed over the slot to allow for connection of the monopoles to the feedline. Two 85-50 ohm tapers to match the 85 ohm feedlines to the 50 ohm measurement

system were also constructed on .125 inch Rexolite substrate. Using a time-domain reflectometer, the whole feedline assembly was trimmed for minimum discontinuities at the connectors and feedline corners for each of

TABLE 3
LENGTH OF FEEDLINE BETWEEN ELEMENTS
(IN INCHES)

	FEEDLINE 1 FEEDLINE 2				FEEDLINE 3		
SECT.	<u>d</u>	EXCES	<u>65</u> <u>d+</u>	EXCESS	<u>d-</u>	EXCESS	
1	5,413	2,223	5.819	2,629	5.007	1.818	
2	4.817	1.979	5.179	2.340	4.456	1.618	
3	4.287	1.761	4.609	2.083	3.965	1.440	
4	3.816	1.567	4.102	1.854	3,530	1.281	
5	3.396	1.395	3.651	1.650	2.824	1.140	
6	3,022	1.240	3.249	1.468	2.513	1.015	
7	2.690	1.105	2.892	1.307	2,237	.903	

three meandering feedlines. After the lines were trimmed, the bottom ground plane of the feedlines was removed in the area of the feedlines above the slots to allow for coupling of energy to the slots. See Figure 6 for the arrangement of the array complete with feedlines.

5. ELECTRICAL MEASUREMENTS

The two basic types of measurements made on the complete array were S-parameter measurements and E-field pattern measurements.

The S-parameter measurements were made with the Hewlett-Packard 8510 network analyzer using feedline 3. The input VSWR for the array is shown from 500 MHz to 4 GHz in Figure 7. S_{11} is shown in Figure

8. The magnitude of the transmission coefficient is shown from 500 MHz to 2.5 GHz in Figure 9.

It is seen from Figure 7 that the input VSWR of the antenna is less than 2 for all frequencies below 1950 MHz and is less than 3 for all frequencies below 3 GHz. Thus it is seen that the structural stopband in regions observed for other series fed log-periodic slot arrays have been effectively eliminated by using the monopole-slot element. This antenna, therefore, represents a stable load for most sources. Note also in Figure 8 the periodic nature of the impedance as expected for a log-periodic array. Looking at Figure 9 it is seen that above 1 GHz very little energy reaches the second port. This and the low input VSWR of the array below 1980 MHz show that the antenna radiates nearly all of the energy presented to its input. Since very little energy is left on the feedline after passing through the array few if any large-end truncation effects should be observed when using this array above 1 GHz.

E-field measurements were made on 20x20 foot ground plane pattern range. For all measurements the antenna under test was used as the transmitting antenna. For the azimuth patterns a vertically polarized log-periodic monopole array was used for the receiving antenna. Elevation patterns were taken using a dipole mounted in a corner reflector attached to a fiberglass boom and positioned so that it was vertically polarized. The patterns measured for feedline 3 are shown in Figures 10 and 11.

Half-power beamwidths and front-to-back ratios were found from the patterns and are given in Figures 12 and 13 respectively. In computation of the front-to-back ratios, the size of the backlobe was assumed to be that of the largest lobe in the back plane defined by 180 $\pm 40^{\circ}$.

From the patterns it is seen that the front-to-back ratio never deteriorates significantly over the whole range of frequencies measured. This is not a surprising result since the monopole-slot has a fairly high front-to-back ratio as an individual element (see Figure 14). Therefore, a significant degradation of the front-to-back ratio cannot be used as a valid limiting factor in determining the pattern bandwidth for this array.

The half-power beamwidth for this antenna is relatively stable for frequencies below 2.5 GHz. Above 2.5 GHz the pattern "balloons" out to be a nearly 180° sector pattern. Thus it is seen that the upper frequency limit for this array is approximately 2.5 GHz. However, if a higher directivity and main beam on axis are desired the upper frequency limit is approximately 1.7 GHz. Even within this frequency range the half-power beamwidth does vary as a function of frequency (Figure 12). Some of this variation is due to unequal power distribution among elements. Figure 15 and Table 4 show the power distribution of each of the elements as a function of frquency. From the figure and the Table it is seen that generally the narrowest beamwidths were measured at frequencies where at least 3 elements were each radiating at leat 20% of the total power and that the distribution between these elements was fairly uniform. This is not surprising since element power "hogging" reduces the effectiveness of using the elements in an array environment.

It is informative to look at the power distribution graph shown in Figure 15 and the data in Table 4 to define limits on the active region of

the array. The most active element is seen to shift as the frequency is changed. As expected at high frequencies, only the first two or three elements radiate a significant fraction of the power (notice the highly peaked response as the frequency is increased). Looking at Table 4 for

TABLE 4
POWER DISTRIBUTION AMONG ELEMENTS OF ARRAY

FREQ.	FRACT	ION OF I	NPUT P	OWER RA	DIATED	BYEA	ACH EL	EMENT
Mhz]	2	3	4	5	6	7	8
500.0	$\overline{0}.000$.003	.024	.007	.003	.067	.014	.014
600.0	0.000	0.000	0.000	0.000	0.000	.039	.039	.036
700.0	.013	.007	.005	.006	.034	.039	.042	.042
800.0	.008	.008	.010	.003	.018	.065	.078	.111
900.0	0.000	0.000	0.000	0.000	0.000	.084	.124	.221
1000.0	0.000	.007	.004	.012	.055	.090	.223	.351
1100.0	.016	.026	.040	.044	.080	.155	.289	.349
1200.0	.010	.033	.076	.173	.125	.243	.331	.006
1300.0	.012	.043	.079	.132	.227	.344	.142	.009
1335.0	.019	.058	.085	.145	.259	.362	.054	.006
1415.0	.056	.080	.141	.198	.379	.137	.004	.001
1456.0	.125	.091	.184	.213	.348	.033	.003	.001
1500.0	.084	.112	.230	.253	.320	.001	.000	.000
1544.0	.097	.162	.245	.286	.200	.006	.002	.002
1590.0	.103	.215	.268	.305	.092	.010	.003	.001
1685.0	.150	.269	.355	.224	.001	.000	.000	.000
1700.0	.188	.308	.351	.153	.000	.000	.000	.000
1800.0	.207	.461	.322	.007	.001	.000	.000	.000
1900.0	.333	.589	.071	.004	.001	.001	.000	.000
2000.0	.475	.517	.006	.001	.000	.000	.000	.000
2100.0	.793	.174	.018	.006	.007	.001	.000	.002
2200.0	.992	.005	.001	.001	.001	.000	.000	-000
1 200.0	.925	.037	.014	.009	.004	.002	.002	.001
2400.0	.732	.111	.059	.068	.005	.002	.019	.000
2500.0	.652	.131	.083	.083	.009	.008	.005	.004

frequencies above 1.7 GHz., it is seen that one element is radiating well over 40% of the power incident on the array. Therefore, one would expect

to see the pattern shapes degrade above 1.7 GHz. Looking at the patterns given in gigure 10, this is seen to be the case. At frequencies near the middle of the operating band (1.2 GHz - 1.7 GHz), the power distribution is more uniform than at higher or lower frequencies. Consequently, one would expect to see well defined patterns in this range. Looking at the patterns given in Figure 10, it is seen that this is also the case. At low frequencies the higher frequency elements do not radiate a significant fraction of the power (as expected). Hence, when frequencies below the resonant frequency of the largest element are approached, little power is radiated by any of the elements. Thus, the radiation efficiency of the whole array is decreased significantly. However, as previously mentioned, well-formed beams are still observed due to the relatively good patterns for each element when the element is operated below its resonance. Thus, it is seen that the patterns for this array degrade gracefully at frequencies beyond both ends of its operating bandwidth.

6.0 CONCLUSION

In this project a log-periodic array of monopole-slot elements was constructed and tested. It was found that using the monopole-slot antenna in the array does indeed eliminate the structural stopband regions normally associated with a series fed log-periodic array. In fact, the antenna had an input VSWR below 2:1 for most of its operating range. Thus, an antenna constructed similar to the one built in this project should not present loading problems for most sources. The front-to-back ratio was found to be fairly high for the total operating range of the antenna. The half-power

bearnwidth and pattern shape were found to be the limiting factors in determination of the upper frequency limit for this array. Radiation efficiency for the array was found to establish the low frequency limit. Using these two limitations, the array was found to operate quite effectively between 1100 MHz - 1800 MHz. If a wider half-power beamwidth is acceptable, the high frequency limit can be extended to approximately 2500 MHz.

Use was also made of the wider element bandwidth inherent with the monopole-slot in lowering the value of the scaling factor required for proper operation of the array. This lowering of the scaling factor allows for use of physically smaller arrays to cover the same frequency range. If narrower and more uniform beams are desired, the scaling factor should be increased from the value of 0.89 used in this array to allow for a more uniform distribution of power between elements. If a wider operating bandwidth is desired, this can be easily accomplished by adding more elements to the array.

REFERENCES

Ingerson, Paul G. and Mayes, Paul E., "Log-periodic Antennas with Modulated Impedance Feeders," IEEF Trans. Antennas Propagat.,

Volume AP-16, Number 6, November, 1968, pp. 633-642.

See also

- Ingerson, Paul G., "Analysis of Some Closed Log-periodic Structures with Applications to Log-periodic Antennas," Ph.D. Thesis, Department of Electrical Engineering, University of Illinois, Urbana, Illinois, 1968.
- Ostertag, Edward L., "Experimental Study of a Log-periodic Cavity-backed Slot Array with Computer Synthesized 50 Ohm Modulated Impedance Feeder, M.S. Thesis, Department of Electrical Engineering, University of Illinois, Urbana, Illinois, 1973.
- Schroeder, K., "A New Class of Broadband Antenna Using
 Complementary Pair Element Groups," IEEE Int. Conv. Rec., Vol. 5, 1965, pp. 159-171.
- 4. Dunlavy, J., "New High Frequency Antenna: The Passive Network Array," Electronics, January, 1964.
- 5. Itoh, K. and Cheng, D., "A Novel Slots-and Monopole Antenna with a Steerable Cardioid Pattern," IEEE Trans. Aeros. Electron. Syst., March 1972, pp. 221-223.

CALLACTIC CONTRACTOR C

6. Mayes, P.E., and Wiesenmeyer, F.M., "The Monopole-slot - An Electrically Small DF and Communications Antenna," Abstracts of the Twentieth Annual Symposium, USAF Antenna Research and Development Program, AFAL, Wright-Patterson AFB, Ohio, and University of Illinois, Urbana, Illinois, 1970.

See also

- Mayes, P.E., Warren, W.T., and Wiesenmeyer, F.M., "The Monopoleslot: A Small Broad-band Unidirectional Antenna," IEEE Trans.

 Antennas Propagat., Vol. AP-20, July 1972, pp. 489-493.
- 7. Cwik, T.A., "The Hybrid Slot Antenna," M.S. Thesis, Department of Electric Longineering, University of Illinois, 1981.

See also

Mayes, P.E. and Cwik, T.A., "The Hybrid Slot, a Low-profile Energy-density Antenna," Abstracts of the International Conference on transportation Electronics, Detroit, Michigan, 1980.

and

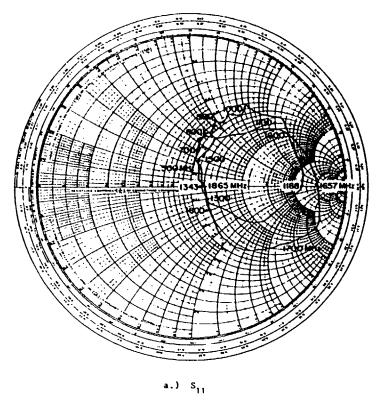
Mayes, P.E. and Cwik, T.A., "The Hybrid Slot, a Versatile Low-profile Radiator with Small Reflection Coefficient," Abstracts of the Antenna Applications Symposium, Deputy for Electronic Technology, Rome Air Development Center, Electronic Systems Division, Air Force Systems Command, and Electromagnetics Laboratory, Department of Electrical Engineering, University of Illinois, Urbana, Illinois, 1980.

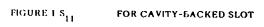
- 8. Halpern, B.M., "The Monopole-slot as a Two-port Diversity Antenna for Mobile Radio," M.S. Thesis, Department of Electrical Engineering, University of Illinois, Urbana, Illinois, 1981.
- Paschen, D.A., "The Stripline Fed Monopole-slot as an Array
 Element," M.S. Thesis, Department of Electrical Engineering,
 University of Illinois, Urbana, Illinois, 1982.
- 10. Mayes, P.E., "Very Wide Band Antennas for Missile Fuze

 Applications," Final Report Part I, Electromagnetics Laboratory,

 University of Illinois, Urbana, Illinois, Navy Contract Requn. No.

 3313-0052-00-81, Contract No. N60530-81-c-0304, 1984.





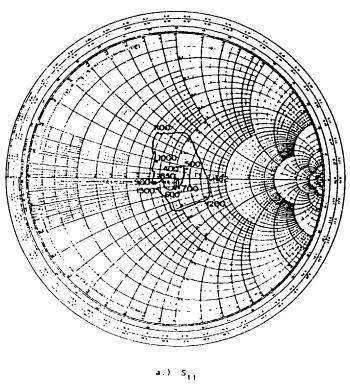


FIGURE 2 $\mathbf{S}_{14}^{}$ — FOR MONOPOLE-SLOT WITH 85 OHM FEEDLINE

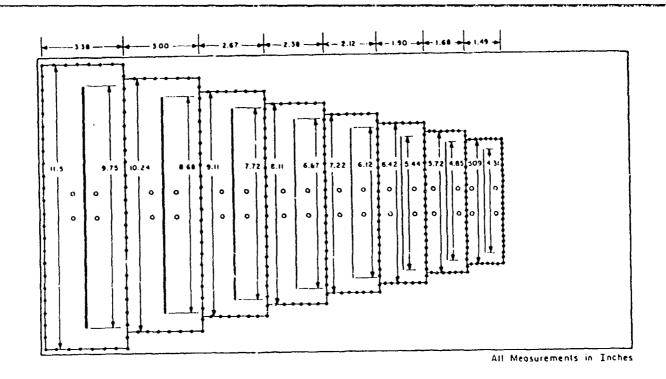
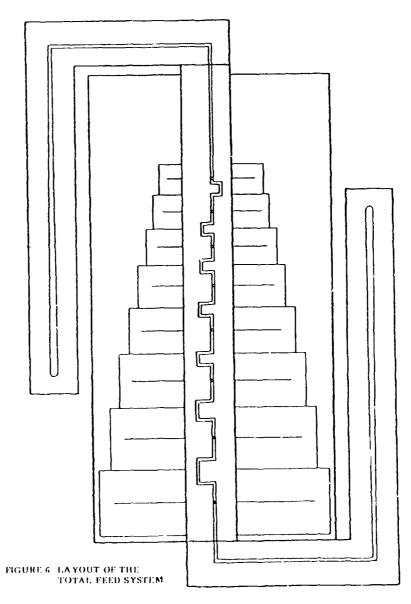
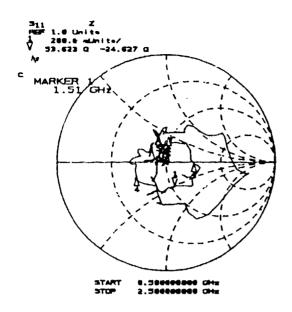
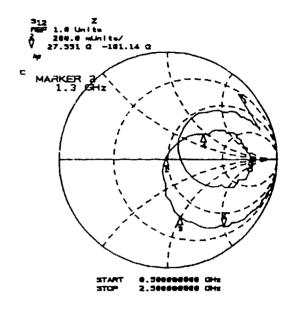
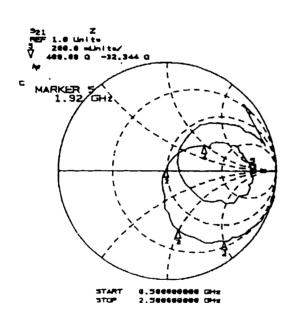


FIGURE 3 DIMENSIONS OF CAVITY-BACKED SLOT ARRAY









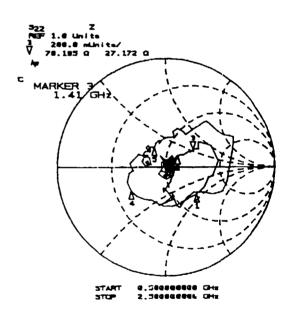
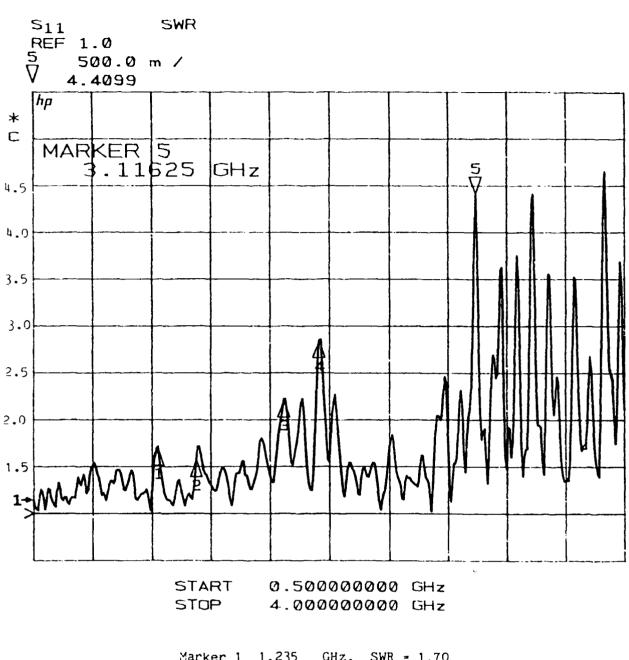


FIGURE 5 S-PARAMETERS FOR THE FOURTH MONOPOLE-SLOT ELEMENT



Marker 1 1.235 GHz. SWR = 1.70 Marker 2 1.4625 GHz. SWR = 1.58 Marker 3 1.97875 GHz. SWR = 2.20 Marker 4 2.18875 GHz. SWR = 2.85 Marker 5 3.11625 GHz. SWR = 4.41

FIGURE 7 INPUT VSWR FOR ARRAY (500 MHz - 4 GHz)

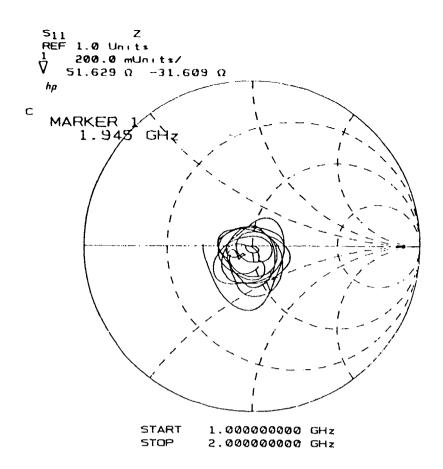


FIGURE 8 S_{11} FOR ARRAY (I GHz - 2 GHz)

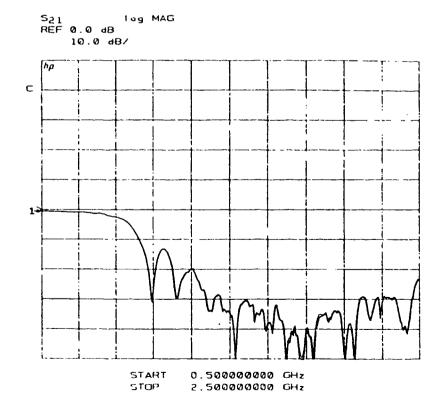


FIGURE 9 S_{21} FOR ARRAY (500 MHz - 2.5 GHz)

MANAGEM PROPERTY OF THE STATE O

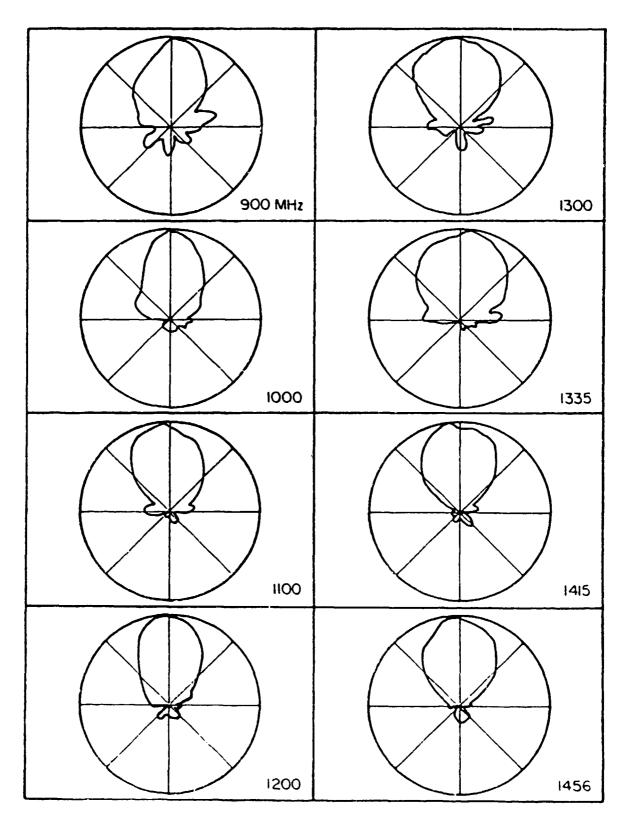


FIGURE 10 AZIMUTH E $_{\mbox{\scriptsize 6}}$ PATTERNS FOR FEEDLINE 3

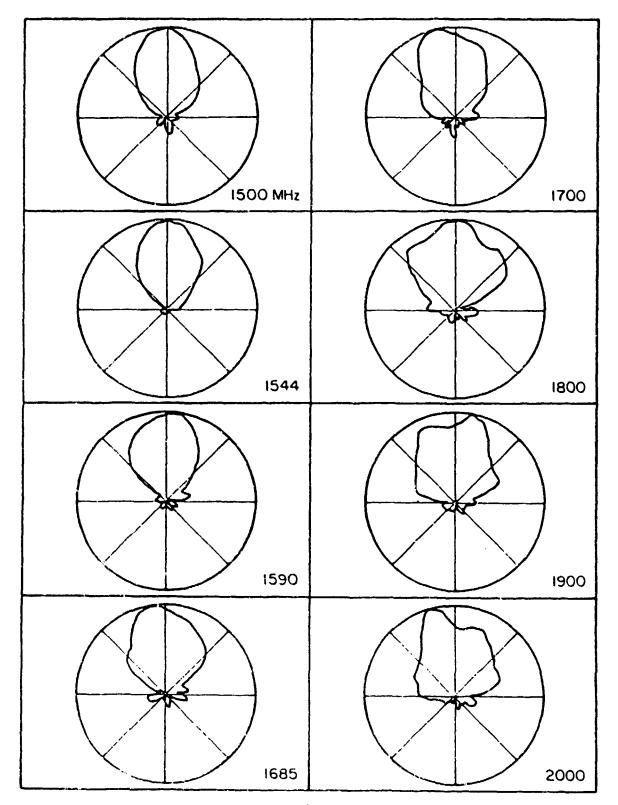


FIGURE 10 (CONTINUED)

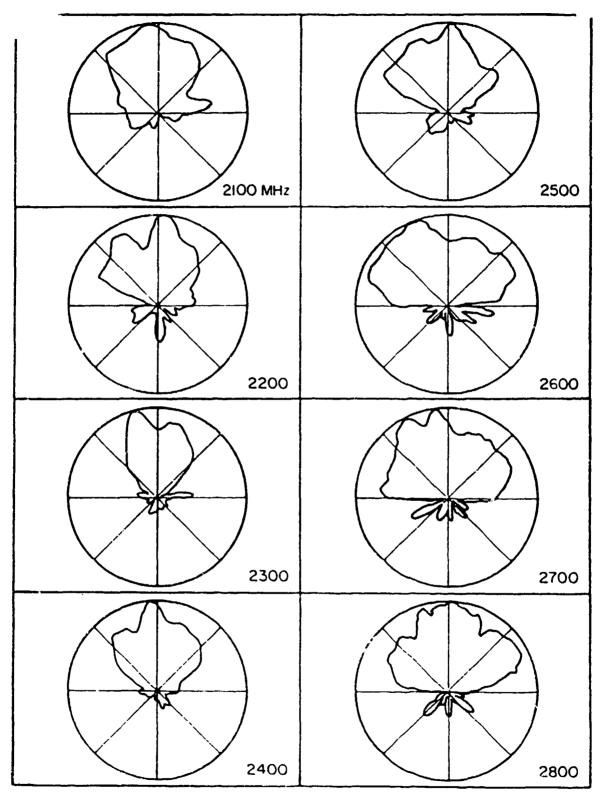


FIGURE 10 (CONTINUED)

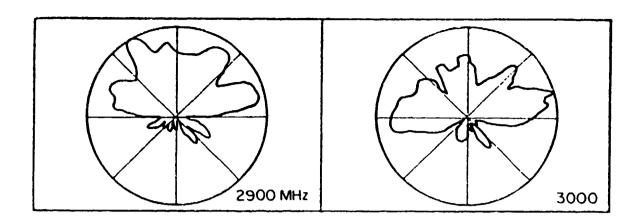


FIGURE 10 (CONTINUED)

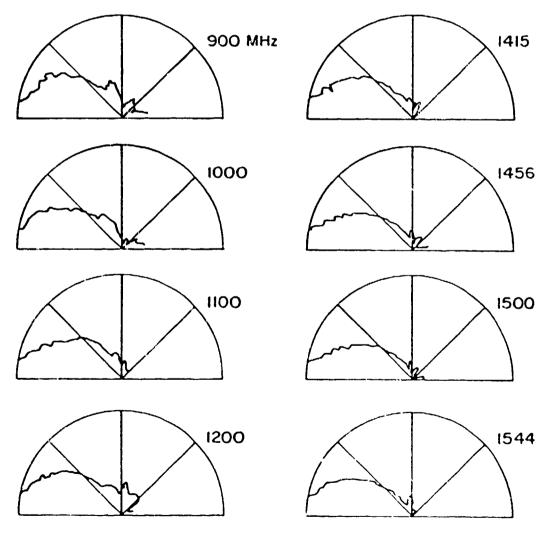


FIGURE 11 ELEVATION E $_{\pmb{\theta}}$ PATTERNS FOR FEEDLINE 3

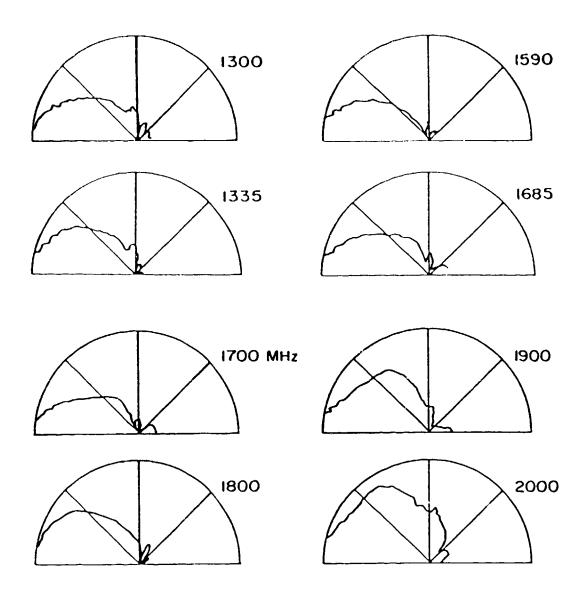


FIGURE 11 (CONTINUED)

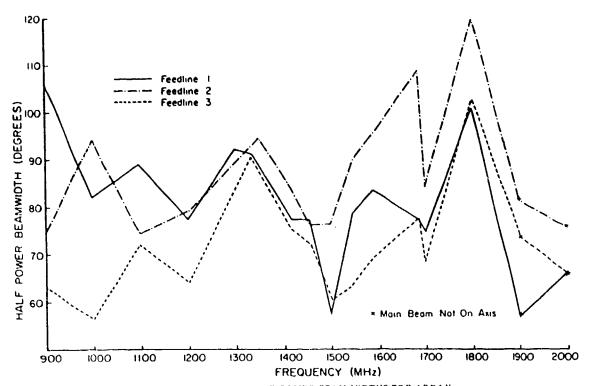


FIGURE 12 HALF-POWER BEAM WIDTHS FOR ARRAY

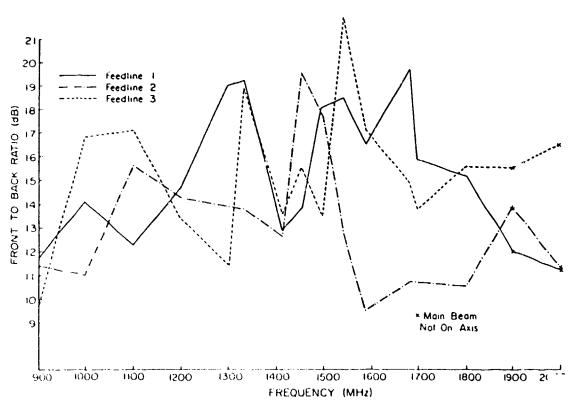


FIGURE 13 FRONT-TO-BACK RATIOS FOR ARRAY

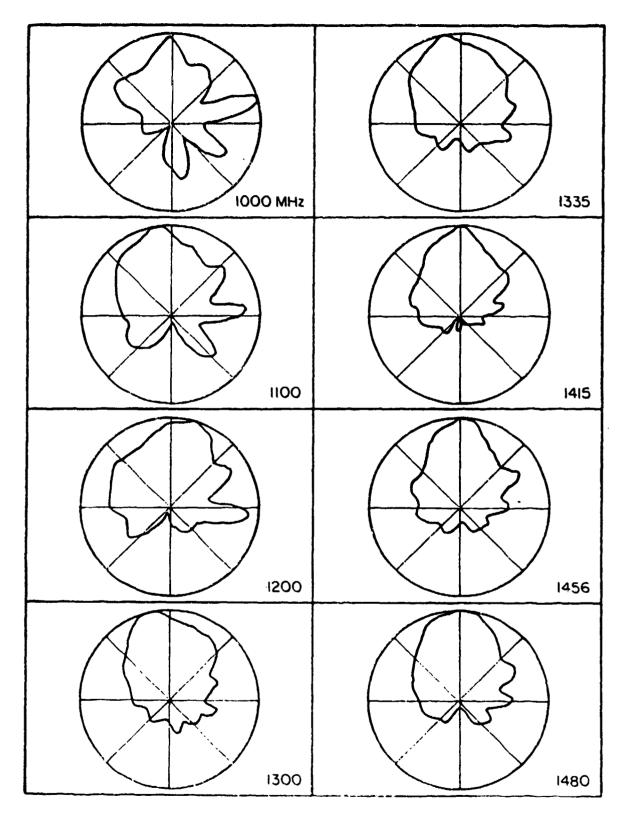


FIGURE 14 AZIMUTH E $_{\theta}$ PATTERNS FOR FOURTH MONOPOLE-SLOT ELEMENT

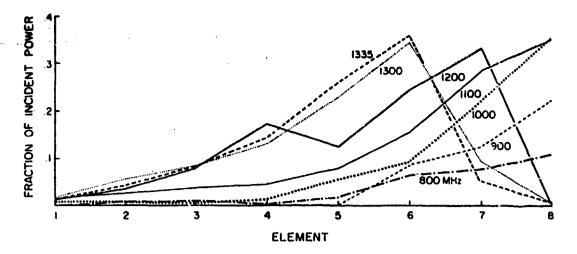


FIGURE 15 POWER DISTRIBUTION AMONG ARRAY ELEMENTS

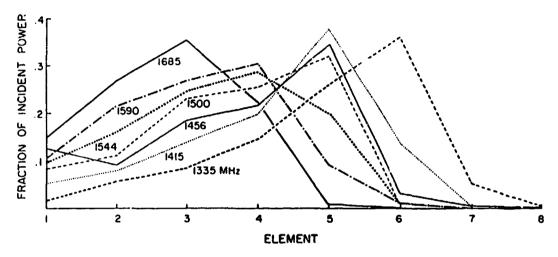


FIGURE 15 (CONTINUED)

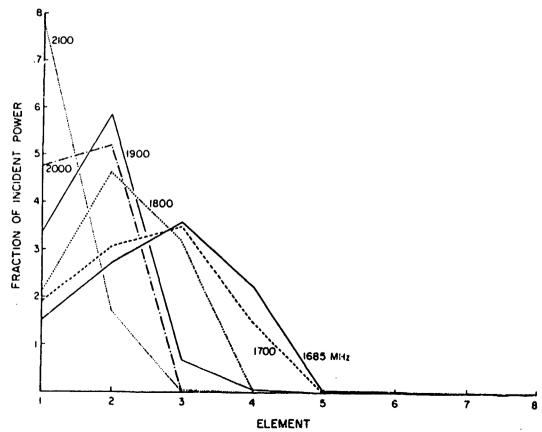


FIGURE 15 (CONTINUED)

A SHALLOW-CAVITY UNITY

GAIN NOTCH RADIATOR

by: George J. Monser Consulting Engineer

Raytheon Company
Electromagnetic Systems Division
Goleta, California

1986 Antenna Applications Symposium 17-19 September Monticello, Illinois

Sponsored by

Electromagnetic Science Division
Rome Air Development Center
USAF Systems Command
and
Electromagnetics Laboratory
University of Illinois

ABSTRACT

A Shallow-Cavity Unity Gain Notch Radiator
by: George J. Monser

This paper presents the results of an empirical approach for designing shallow-cavity (0.080 wavelengths deep) notch radiating elements for use in greater than octave bandwidth applications. Three different size models were built and evaluated. It was concluded that nearly unity gain could be achieved over an octave with excellent pattern characteristics over greater than a 3/1 bandwidth.

A SHALLOW-CAVITY UNITY GAIN NOTCH RADIATOR

By: George J. Monser

SUMMARY

This paper describes a shallow-cavity (0.080 wavelengths deep) notch radiating element* with a peak gain of unity, operable over greater than one octave in bandwidth. Based upon three different size antennas excellent pattern characteristics were measured over a 3/1 frequency band when flush-mounted in a small ground plane.

1.0 INTRODUCTION

The notch radiating element is a wide bandwidth efficient antenna which has been used in many applications since first reported by Johnson [1]. These applications have used Johnson's notch (or nitch) in generic form. That is, as a simple radiating discontinuity. This paper extends the technology to radiating notches over shallow cavities where the plane defining the notch is parallel to the cavity base. Efficient radiating structures with cavity depths of a few hundred's of wavelengths are attainable offering an alternative to patch antennas [2].

2.0 ANTENNA CONFIGURATION

Figure 1 shows the basic elements of the notch/cavity antenna. In this figure the input micro-strip line couples energy to

^{*} Patented by author and Raytheon Company.

the slot which, in turn, excites the notch. Without the cavity in place radiation would occur with a maximum along the axis of the slot. Adding the cavity changes the radiation patterns, yielding a maximum normal to the plane containing the slot and notch. Two elements contribute to the far field pattern: the microstrip line and slot/notch.

3.0 TEST MODELS

Three models were built for evaluation:

Model A 1.3 x 1.5 x 0.29 inches.

Model B $2.7 \times 3.0 \times 0.50$ inches.

Model C $3.1 \times 3.8 \times 0.62$ inches.

The first two values pertain to aperture size. The last value pertains to the cavity depth.

Model A was tested and evaluated over the 2.0 to 5.0 GHz range. Model B was evaluated over 1.0 to 3.0 GHz range. Model C was evaluated over the 0.75 to 2.0 GHz band.

Because of space constraints the cavity depths were not scaled in proportion to notch sizes.

A photograph of the Model A antenna is shown in Figure 2.

4.0 TEST RESULTS

Figures 3 through 6 show typical pattern characteristics.

Broad, smooth patterns were measured in both planes (i.e., along

and normal to the microstrip line) with the broader patterns in the plane of the microstrip line.

Figure 7 shows gain versus cavity depth expressed in fractions of a wavelength. On the order of unity gain is displayed over approximately one octave commencing with a cavity depth of approximately 0.06 wavelengths.

Figure 8 shows transmission loss versus cavity depth. Again good transmission efficiency (50 percent or better) is shown over nearly an octave, except for Model B with the deeper cavity.

5.0 DISCUSSION OF RESULTS

Data displayed in Figures 7 and 8 showed similar trends almost independent of aperture (slot/notch) size. By computing directive gain (i.e., $4\pi A/\lambda 2$) and deducting the mismatch loss, the reported gains (Figure 7) were substantiated.

One anomaly in data was observed in Figure 8, where Model B showed a narrower transmission band for 50 percent efficiency than the models. This occurrence is believed to be attributable to the deeper cavity. Since the primary effort was to achieve a shallow cavity design, the phenomenon was not investigated.

6.0 CONCLUDING REMARKS

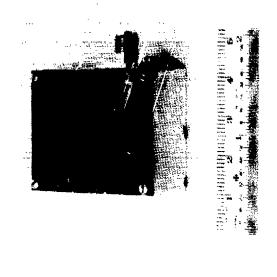
Based upon an empirical study, it is felt that notches over shallow cavities can be used in applications requiring broad coverage and unity gain over octave bandwidths.

If the restriction of unity gain is removed, then the full pattern bandwidth 3/1 can be realized.

As configured, this type of antenna offers a viable solution for flush-mounted applications requiring very little depth for installation.

References

- W.A. Johnson (1955). The Notch Aerial and Some Applications to Aircraft Radio Installations, <u>Proc. IEE</u>, March 1955, pp 211-218.
- 2. A. Henderson, et al (1986). Bandwidth Extension Techniques in Printed Conformal Antennas, Military Microwaves (86), Microwave Exhibitions and Publishers, Ltd., Kent TN 1 1LE, England, pp 329-334.



Copper Circuit

Mounting Holes

-0.07x Mid

Figure 1. Notch Circuit Board (Basic Details)

Copper Far Side

> No Copper Far Side



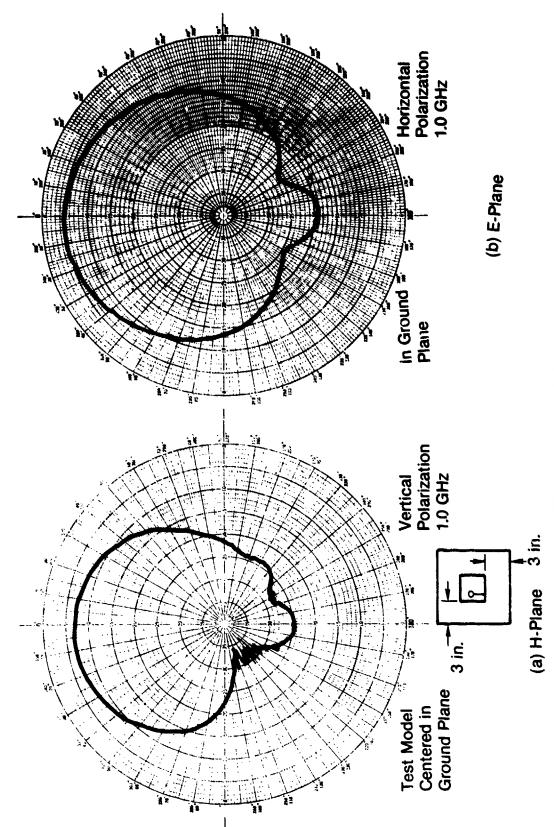
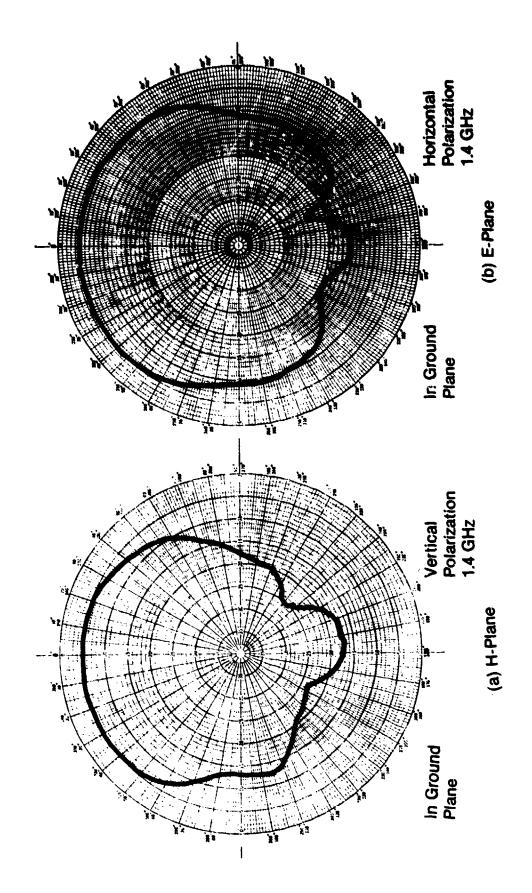
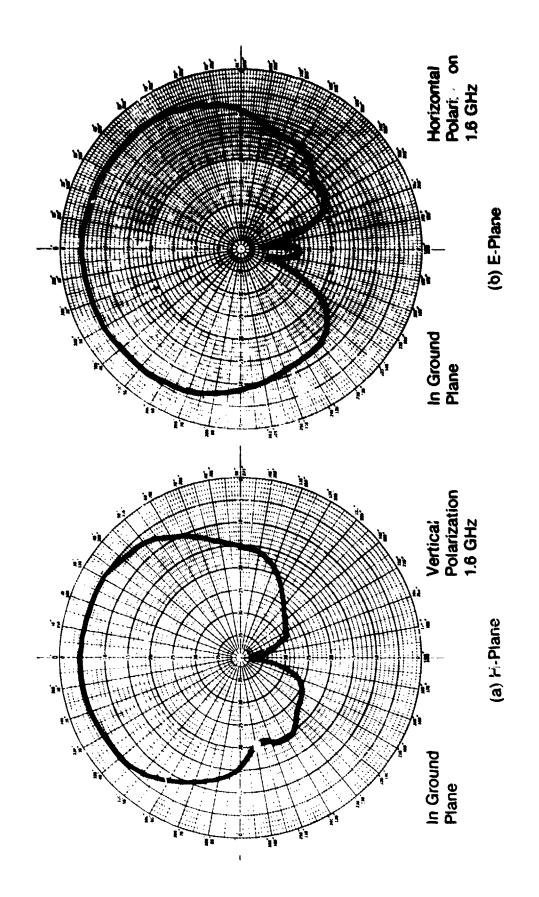
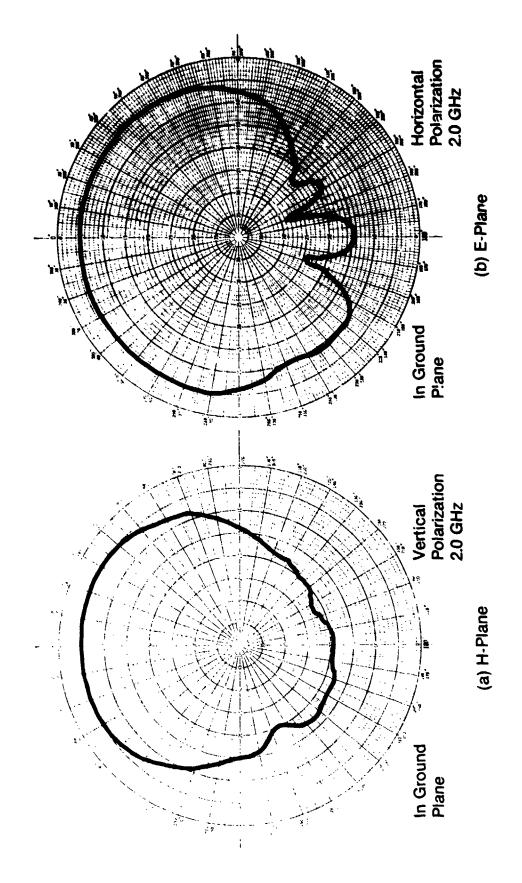
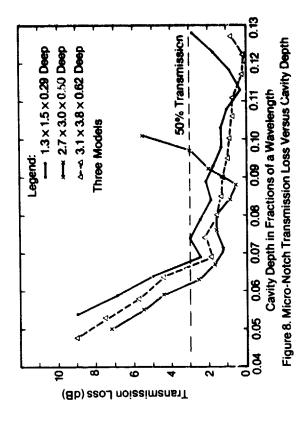


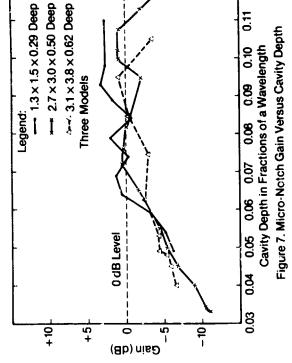
Figure 3. Model B Patterns











0.12

ULTRA-BROADBAND IMPEDANCE MATCHING USING ELECTRICALLY SMAIL SELF-COMPLEMENTARY STRUCTURES

K. G. Schroeder

American Electronic Laboratories, Inc. Lansdale, Pa. 19446

ABSTRACT Sauchas

A number of self-complementary structures are investigated with the goal of providing frequency-independent matching of the inductive reactance of the other element. Impedance bandwidths of up to 50:1 are found to be achievable with very small (H approximately 0.006 %) element heights. Efficiencies are determined by achievable loss resistances in the radiating structure itself, rather than the (limited) quality of an external loading coil, and by energy channeled into the difference port of the feed hybrid, which is used to match two complementary impedances.

1.0 INTRODUCTION

The ultra-broadband self-complementary pair of elements described here is based on the general concept first formulated in 1963. It basically uses a 180-degree hybrid to match two radiators which are closely spaced and enhance each other's radiating properties and which have impedances which are complementary. In the past, mutual coupling between closely spaced radiators has prevented the physical realization of such a pair, except for

the vertical monopole/slot combination described by P. Mayes, which did not use a hybrid feed. The evolution of a monopole/half-loop combination is now described, which both overcomes the mutual coupling problem and, at the same time, results in more practical monopole structure for mobile applications. The complementary pair impedance matching concept is now discussed in more detail.

2.0 GENERAL IMPEDANCE MATCHING PRINCIPLE

The complementary matching approach is based on the impedance averaging properties of a magic-tee or 180-degree hybrid. Fig. 1 shows the generalized impedance relations at the outputs of a 180degree hybrid used in the complementary pair, and Fig. 2 shows typical locations of complementary impedances on a Smith Chart, where Z and 2 🛵, etc. are located on the same VSWR circle, but on opposite sides with respect to the center of the Smith Chart. It can be shown that the sum-port impedance is always the center point of a straight line connecting two impedances on a Smith Chart, even if this line does not go through the center, i.e., even if the two impedances are not exactly complementary. Physical embodiments of a self-complementary pair of small elements consist of loops (half-loops) and monopoles; slots and monopoles (dipoles); dipoles and folded dipoles, etc. The end-fire complementary pair is formed by using two identical elements (e.g. monopoles, see Fig. 3) and externally complementarizing one of them by a network, such as a delay line. This end-fire pair is now not only matched with respect to the self-impedances of the two elements, but also with respect to mutual impedances in a phased array environment. However, the bandwidth of the complementarizing network generally

limits the total pair bandwidth to about 4:1.* For applications where 10:1 total bandwidth or more is required, the self-complementary approach currently offers a better solution, and is described below in more detail.

3.0 SELF-COMPLEMENTARY MONOPOLE-PLUS-HALF-LOOP PAIR

Fig. 4 shows a basic self-complementary pair consisting of a short monopole (whip) and a grounded half-loop. One is an open circuit at very low frequencies, and the other a short circuit. This means that at these frequencies, when connected to a feed hybrid as shown in Fig. 5, the sum-port impedance should be matched.

Fig. 6 shows the measured sum-port impedance from 1.2 to 115 MHz for a whip and a half-loop with 0.002 wavelength height and stretched length (half-circumference), respectively, at 2 MHz. The impedance is not as good as it should be at the low end, since the hybrid impedance deteriorates below approximately 5 MHz, and the ground plane was too small for frequencies below approximately 5 MHz.

Above approximately 30 MHz (model frequency), the impedance match was suspected not to be as good as possible because the whip was too thin. Remembering that a fat conical monopole has a good high-frequency performance, one might try to improve the high-frequency performance by using a conical monopole. However, the mutual coupling between the loop and the fat monopole will then be

^(*) See Companion Paper: "Feed Designs for Broadband End-Fire Complementary Pairs Using Thin-Wire Elements"

too strong, upsetting the self-complementarity. Hence, a new radiator approach was evolved, which is described below, and which is capable of optimizing electrically small, self-complementary structures.

4.0 EVOLUTION OF THE SELF-COMPLEMENTARY SCHROEDER ANTENNA

Fig. 7 shows the well-known equivalency between a fat cylindrical monopole with conical feed section and a flat sheet of a width equal to twice the diameter of the cylinder diameter. For the frequencies involved in most HF and VHF systems, the dimensions of the radiator are still too bulky and do not lend themselves to easy installation and deployment. The next step in simplifying the structure is now shown in Fig. 8. Instead of using a continuous metal surface or sheet, one can simulate this sheet by building an outline of the actual radiating structure. This can be done, because the radiating currents essentially travel up the extreme edges of the radiator. The center portion does have some effect, particularly at the high frequency end, by virtue of the capacitive field lines connecting to the surrounding plane. Because of this. the optimum angle β is almost zero degrees. That is, the optimum equivalent sheet radiator a flat (instead of angled) bottom is most nearly equivalent to the optimized conical section of the cylindrical conical monopole, where the included cone angle is about 60 degrees and α also equals 60 degrees. This angle can be found empirically by varying a until the impedance plot is most ideally centered around the 50-ohm point on the Smith Chart

for the widest frequency range. This new equivalent-sheet, wireoutline monopole can now be used in combination with a half-loop
to form a self-complementary pair, where the interaction (through
mutual coupling) between the loop and the monopole is minimized
by the symmetry and orthogonality of the current-carrying parts
of the structure. A further attempt in improving symmetry can be
made by using four whips instead of two, which allows the use of
orthogonal loops also. This is shown in Fig. 9, except that only
one of the two orthogonal half-loops is shown. The reason for
the second loop will be explained below when discussing patterns.

5.0 TEST RESULTS

A VSWR plot of the four-whip arrangement is shown in Fig. 10 for a small pattern model built at a 50:1 scale factor so that good patterns could be measured swith a limited-size ground plane. The impedance match is obviously excellent (better than 2:1) over a more than 20:1 bandwidth. From 100 to 1000 MHz (full-scale equivalent e.g. 3 to 30 MHz) the azimuth patterns (Fig. 11 to 16) show astoundingly good front-to-back ratios, averaging better than 10 dB. The explanation for this directivity is the fact that, over the entire band where the half-loop is electrically shorter in circumference than the resonant length, the electrical current vector of the half-loop is pointing upward at the feed point, thus enhancing the electrical vector of the monopole which is also pointing up. The electrical vector of the half-loop points downward at the grounded end, and therefore cancels out the monopole

contribution. This forms a directional pattern in the direction of the half-loop feed point. This performance is also present when only two whips are used, which are orthogonal in their feed arrangement (e.g., using a center feed bar going underneath the center of the half-loop). With four whips, two orthogonal loops can be installed with four feed points that are alternately switched to the hybrid output or to ground, so that the directional pattern can be switched into four major directions spaced 90 degrees apart (0, 90, 180, and 270 degrees).

6.0 CONCLUSION AND SUMMARY

A new embodiment of self-complementary pairs has been described which shows very wide impedance and directional pattern bandwidths. This antenna has also a small physical size in comparison to product-line HF antennas. The "hybrid-fed, wire-outline, equivalent-sheet-monopole plus half-loop, electrically small, self-complementary pair", (short: self-complementary Schroeder antenna) warrants further detailed investigations in the form of model and full-scale experiments. Already, impedance bandwidths in excess of 50:1 have been measured, and ultimate bandwidths could be as high as 100:1, with the only limitation being given by acceptable efficiency.

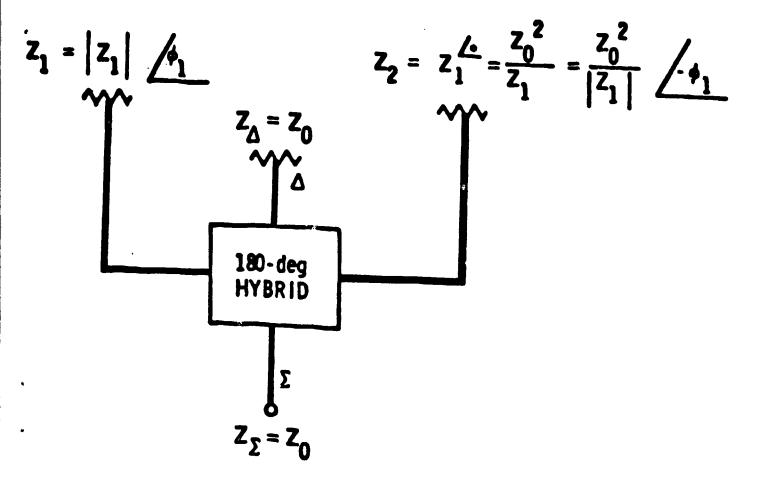


Fig. 1: Impedance Relations of a Complementary Pair

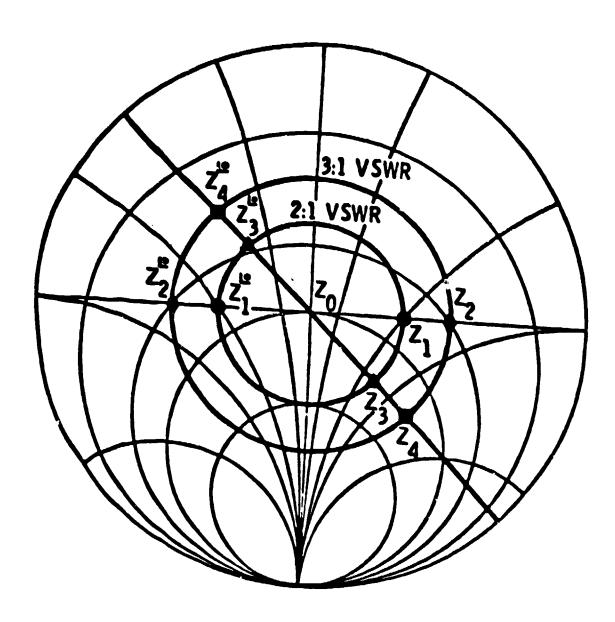


Fig. 2: Complementary Impedances on the Smith Chart

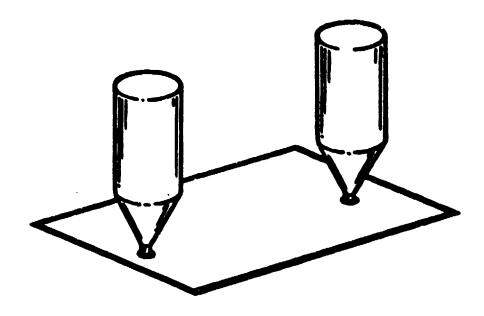


Fig. 3: Endfire Complementary Pair of Conical Monopoles (Approximately 4:1 bandwidth)

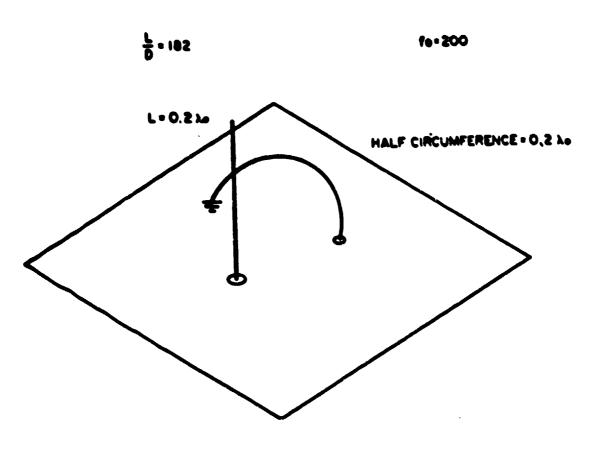


Fig. 4: Self-Complementary Impedance Matching System Using Whip and Half-Loop (Element Layout)

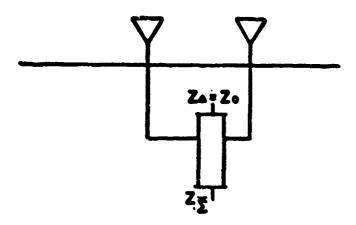


Fig. 5: Self-Complementary Impedance Matching System Using Whip and Half-Loop (Feed Circuit)

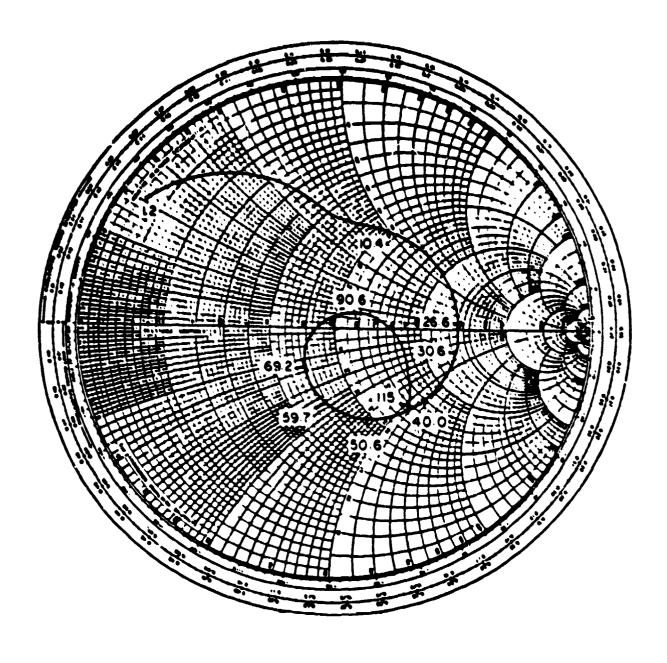
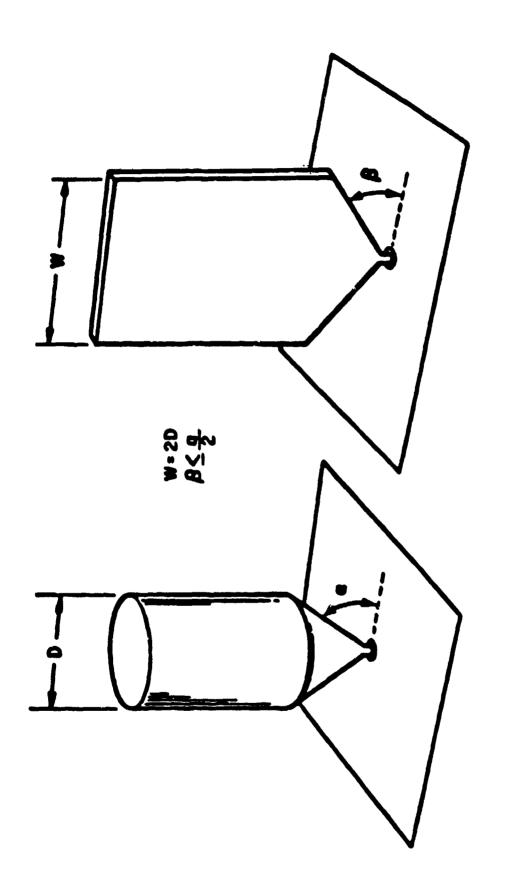


Fig. 6: Self-Complementary Impedance Matching System Using Whip and Half-Loop (sum-Port Input) Impedance



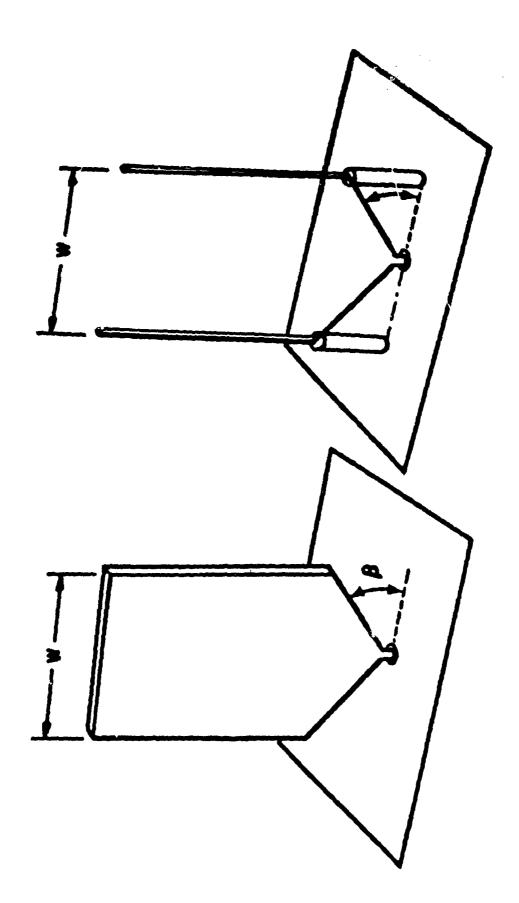


Fig. 8: Evolution of Equivalent-Sheet Wire Outline Monopole

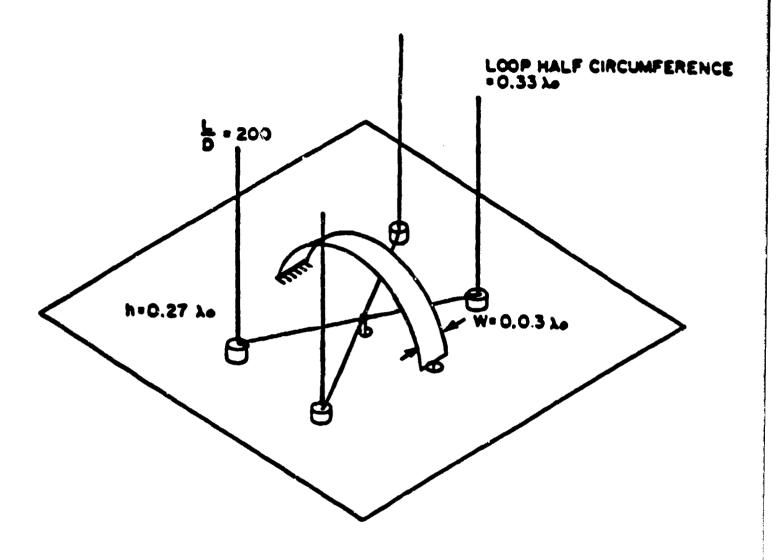


Fig. 9: Self-Complementary Pair of Equivalent Conical Monopole Wire-Outline Radiator and Fat Strip Half-Loop

Fig. 10: Impedance Match of Pattern Model for Self-Complementary Pair

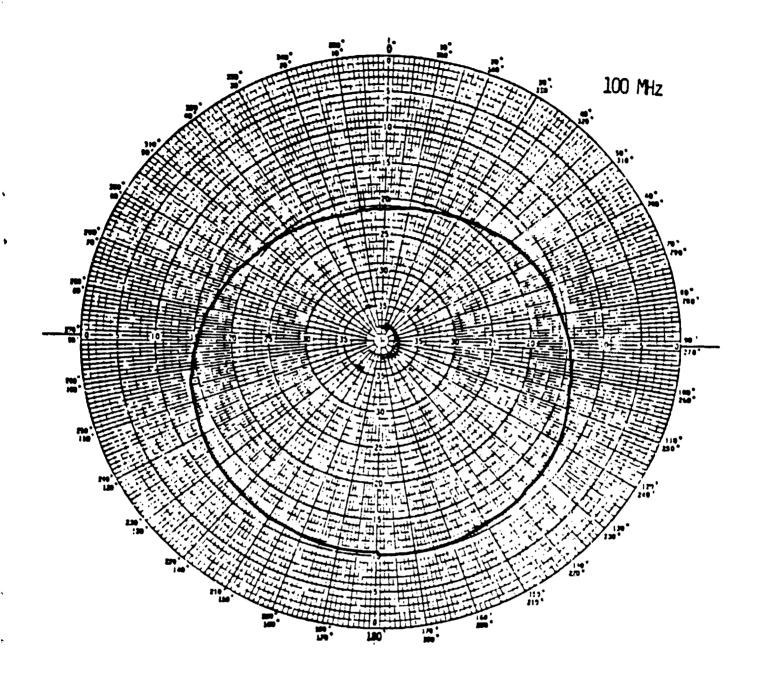


Fig. 11: Azimuth Pattern of Self-Complementary Pair of Monopole and Half-Loop, 100 MHz

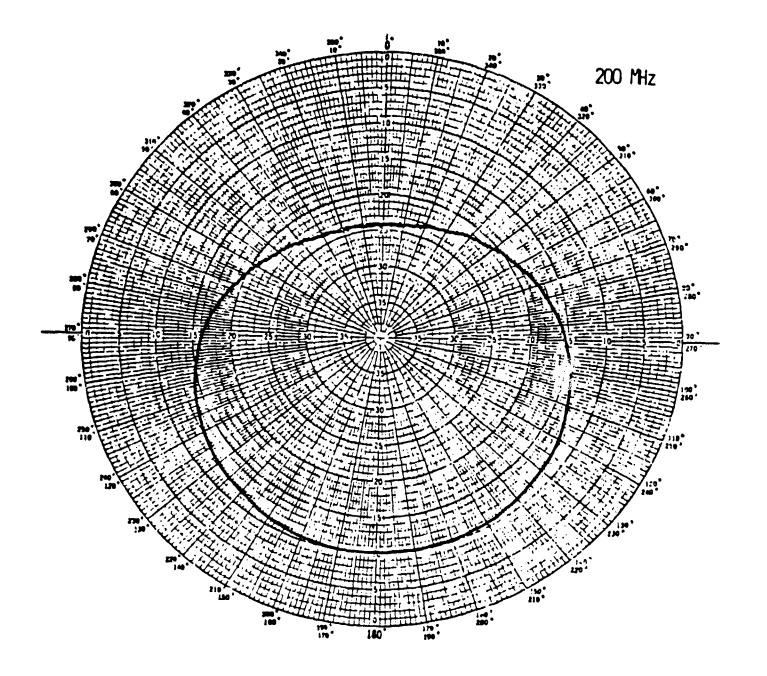


Fig. 12: Azimuth Pattern of Self-Complementary Pair of Monopole and Half-Loop, 200 MHz

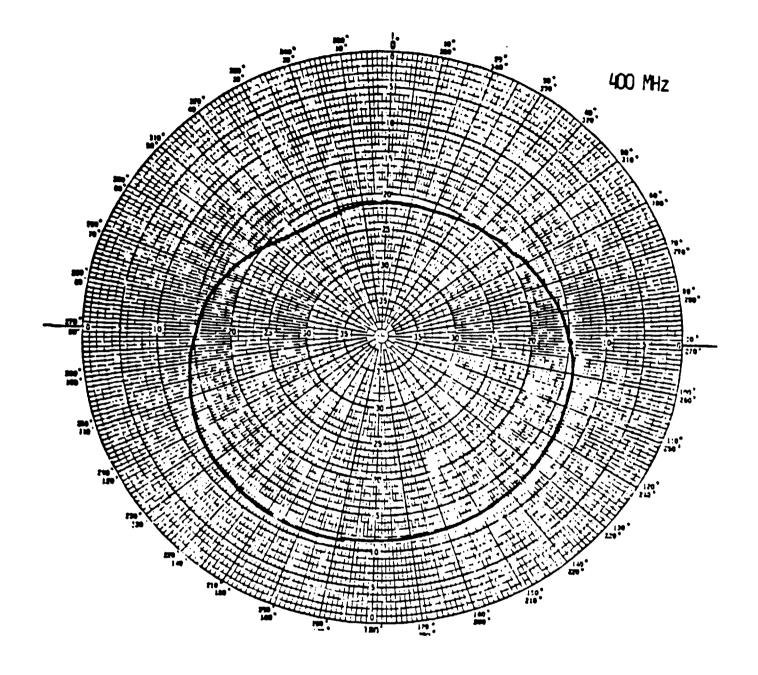


Fig. 13: Azimuth Pattern of Self-Complementary Pair of Monopole and Half-Loop, 400 MHz

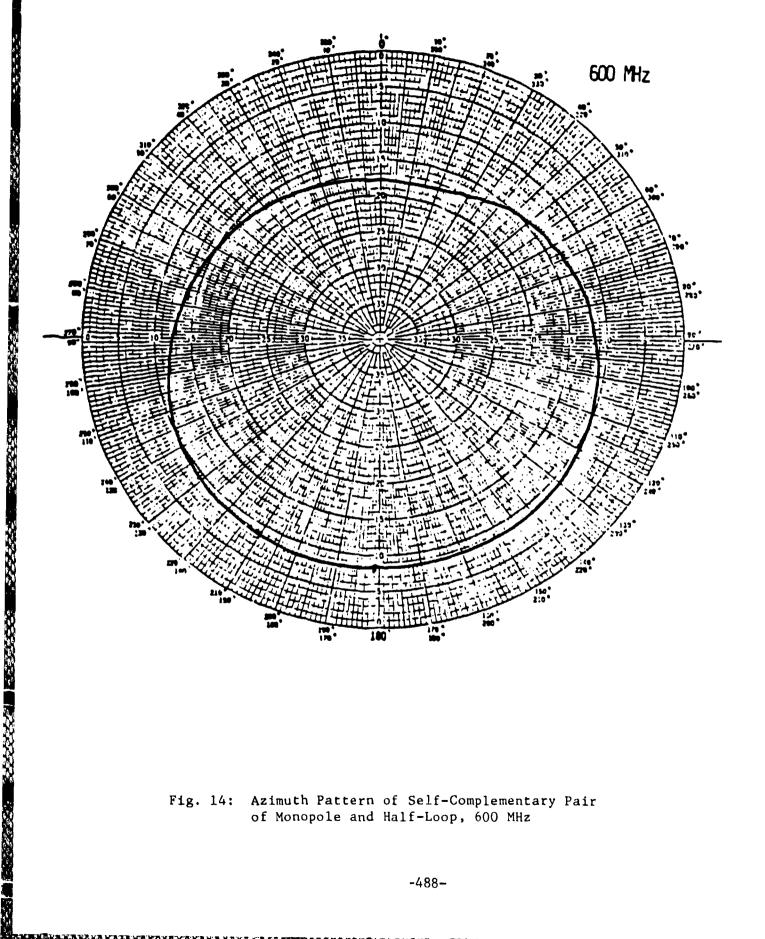


Fig. 14: Azimuth Pattern of Self-Complementary Pair of Monopole and Half-Loop, 600 MHz

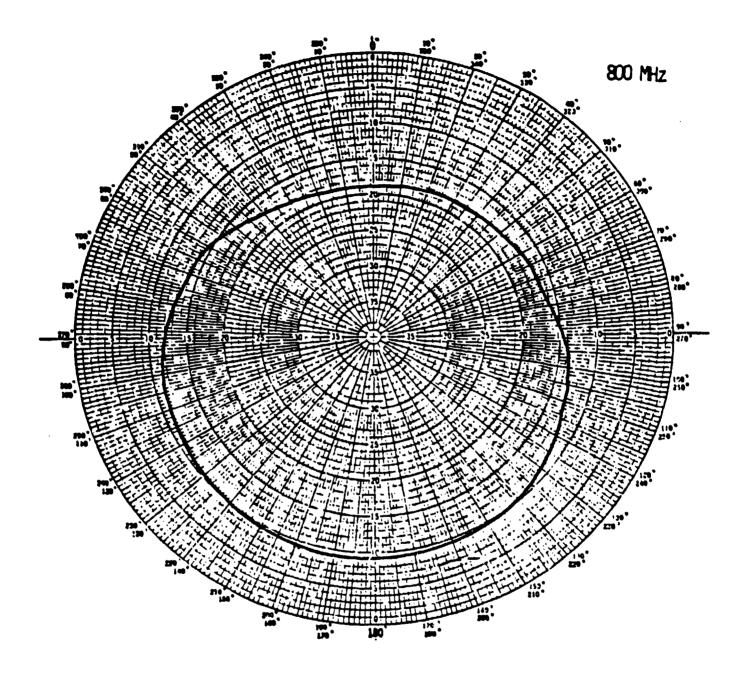


Fig. 15: Azimuth Pattern of Self-Complementary Pair of Monopole and Half-Loop, 800 MHz

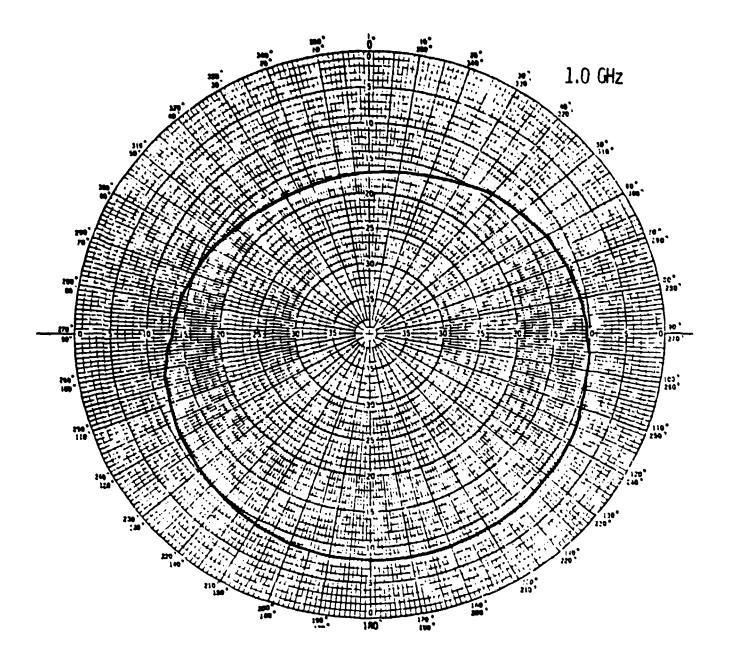


Fig. 16: Azimuth Pattern of Self-Complementary Pair of Monopole and Half-Loop, 1000 MHz

IMPEDANCE-INVERTING FEED DESIGNS FOR BROADBAND ENDFIRE COMPLEMENTARY PAIRS USING THIN WIRE ELEMENTS

K. G. Schroeder

American Electronic Laboratories, Inc. Lansdale, Pa. 19446

ABSTRACT

Broadband impedance matching of externally complementarized endfire monopole pairs is described, where the radiating elements consist of thin wires. Broadband impedance loci are achieved for the thin radiators by impedance inverters placed prior to the complementarizing circuit. Impedance matching is then accomplished in a standard broadband hybrid or "Magic Tee".

1.0 INTRODUCTION

From Ref. 1, it is known that fat monopoles, arrayed in endfire, can be impedance- matched over at least a 3:1 frequency range. (Fig. 1). The conical monopoles required for this performance typically have included cone angles of 60 degrees and length-to-diameter ratios of less than approximately 4:1. Solid monopole complementary pair arrays, however, are not very practical for HF and VHF, particularly in mobile applications. A standard

way to build conical monopoles at those frequencies is the wire-cage construction.

To implement a quasi-short monopole (height between one-sixth of a wavelength and a half a wavelength) in wire-cage construction, typically eight to six wires are required, which shape the outline of the cone and attached cylinder. Keeping in mind that this provides one monopole, a second wire-cage structure has to be added to the first one to form a pair. This then leads to 12 wires minimally in an endfire complementary pair of conical wire-cage monopoles. (Fig. 2).

These wire-cage structures now have to be supported somehow, which leads either to an almost impractical complex array and support structure, or the need for 12 individual self-supporting whips forming the wire-cage outlines in the verical direction.

The desire clearly exists to further reduce the number of vertical radiators. It is known that the conical cylindrical monopoles can be replaced by their equivalent flat sheet monopoles provided the width of the sheet is twice the diameter of the cylinder. (Fig. 3). Figure 4 shows an endfire pair using solid sheets of conducting material. (See also companion paper entitled: "Ultra-Broadband Impedance Matching Using Electrically Small Self-Complementary Structures".)

Such solid-sheet "equivalent" arrays offer no advantage, of course, unless the sheets are also configured in thin-wire construction technique. The flat sheet monopoles, however, can

be simulated by using just two wires or two whips, thus reducing the total number of elements to four. No connection is required between the tops of the whips. (Fig. 5) Another way of explaining the horizontal connecting bar of the wire-outline equivalent — sheet radiator is that it constitutes an impedance inverter. The thin-wire monopole impedance is inverted about the characteristic impedance of the open-wire transmission line leading from the whip endpoint to the center (feed) point.

2.0 MODEL DESIGN

In order to be able to investigate the impedance matching performance of the equivalent-sheet whip array concept, an impedance test model was constructed and various locations on a ground plane were tested using an end-fire beam-forming network. The elements were located on a square and on a rectangle. The full-scale whips are envisioned to be standard fiberglass whips with conducting braid embedded in fiberglass, mounted on a spring and base insulator.

3.0 IMPEDANCE MATCHING TEST RESULTS

A single thin monopole (whip) was shown to be poorly matched, and its impedance locus on the Smith Chart generally not useful for complementary matching. Fig. 6 shows the measured impedance plot for a thin wire with about $0.12~\lambda$ height at the lowest frequency. The wire was mounted in a ground plane location as shown in Fig. 6. The sum-port impedance for a rectangular array phased into the front/aft direction of the ground plane is shown in Fig. 7. This was one of the earlier test results, and was aimed at proving the general concept. The basic idea is, of course, that two of the whips con-

nected together, as shown in Fig. 5 will behave impedance-wise like a fat conical monopole.

Fig. 8 and 9 show the input impedances of two whips with a height of 0.16 λ when fed in parallel with impedance-inverting horizontal members. Fig. 8 is the front pair and Fig. 9 the back pair. Fig. 8 and 9 show that the horizontal feed circuits indeed transform the center of the whip impedance locus towards the center of the Smith Chart, which is a prerequisite for complementary matching. The sum-port input impedances for a fore/aft phasing condition are shown in Fig. 10. It is seen that the impedance match at the very low end had deteriorated somewhat, the 3:1 VSWR circle being penetrated above a frequency of approximately 220 MHz instead of 200 MHz. The spacing between whips was a constant 0.12λ at the lowest frequency. The same is true for the left/ right phasing condition (Fig. 11), the two impedance plots being very similar. This implies that the dimensions between the whips are more critical than the ground plane conditions in front of the forward radiating element, i.e., the whole array is matched together as an entity, and independent of ground plane extensions. The patterns, of course, may show more gain reduction in the left/ right direction.

4.0 DIFFERENCE PORT POWER

One of the many design aspects of a broadband antenna system is the matching network efficiency. In the case of the complementary pair, there is an immediate measure in the power lost in the difference port. That power is shown versus frequency in Figures 12 through 16. As one would expect, a significant amount

is lost in the difference port at the lowest frequency, where much impedance matching has to be achieved in the inversion and complementarization process. A secondary peak appears between 700 and 900 MHz. In both cases, however, the power is down more than 5 dB from the input, meaning that the matching efficiency is better than 50%. Obviously, some additional losses will occur and absolute gain measurements will have to be made. Preliminary gain measurements have confirmed a gain of not less than 0 dBi, and up to 6 dBi.

5.0 PATTERN TEST RESULTS

Figures 17 through 20 show representative azimuth patterns at 210, 400, 600, and 800 MHz model frequencies for an array phased in the left/right direction. It can be seen that even at the lowest frequency there is a front-to-back (i.e., left side-to-right side) ratio of approximately 3 dB, which increases to 6 dB at 400 MHz, 10 dB at 600 MHz, and averages better than 10 dB at 800 MHz. The associated elevation patterns, in the plane of the main beam, are shown in Figures 21 through 24. The roll-off varies from about 3 dB over most of the band to about 7 dB at the highest frequency. (The peak of the main beam is pointing to the right side of Figures 21 through 24.)

6.0 REFERENCES

1.0 K. G. Schroeder and K. M. Soo Hoo, IEEE Transactions on Antennas and Propagations, Vol. AP-24, No. 4, July 1976, pp. 411-418.

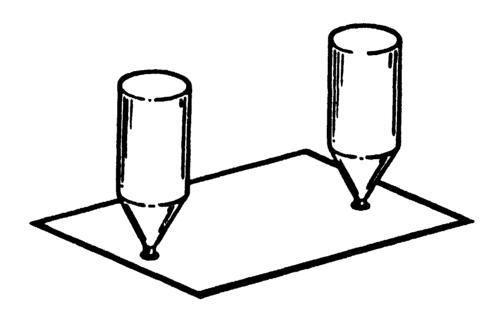


Fig. 1: End-Fire Complementary Pair of Conical Monopoles (Approximately 4:1 Bandwidth)

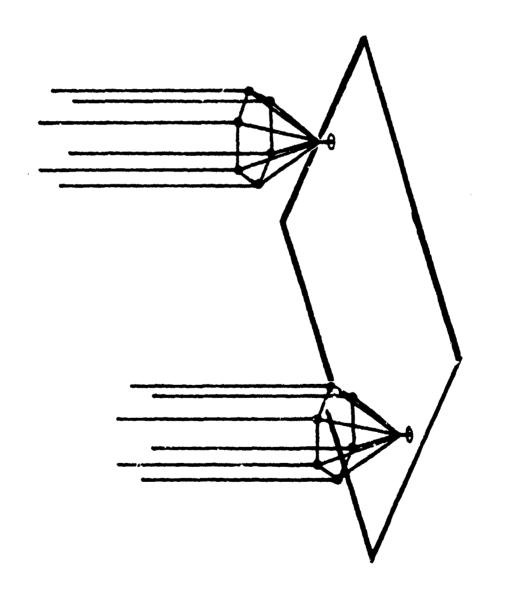


Fig. 2: End-Fire Complementary Pair of Conical Monopoles in Six-Wire-Cage Construction

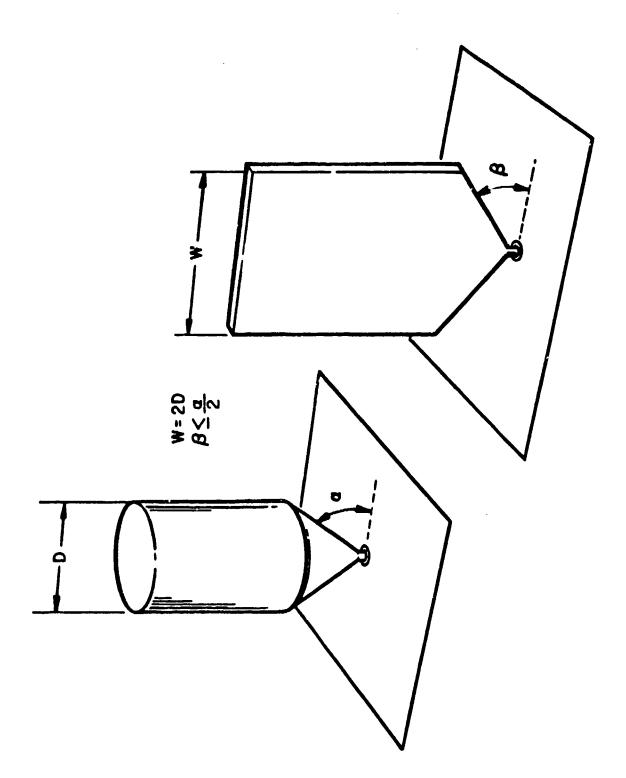
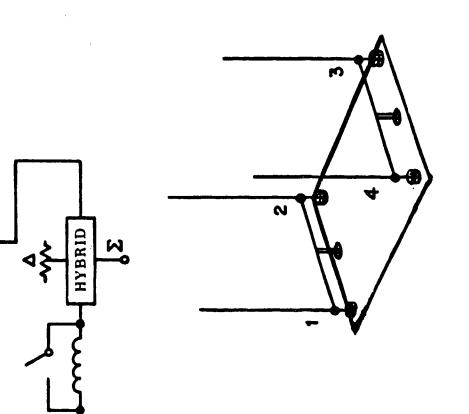


Fig. 3: Equivalency Between Cylindrical and Flat Monopoles

Fig. 4: End-Fire Complementary Pair of Equivalent-Sheet Monopoles



(B) FEED BAR AND WHIP LAYOUT

End-Fire Complementary Pair of Equivalent-Sheet Monopoles Simulated by Dual Whips Fed from Impedance-Inverting Feed Bar Fig. 5:

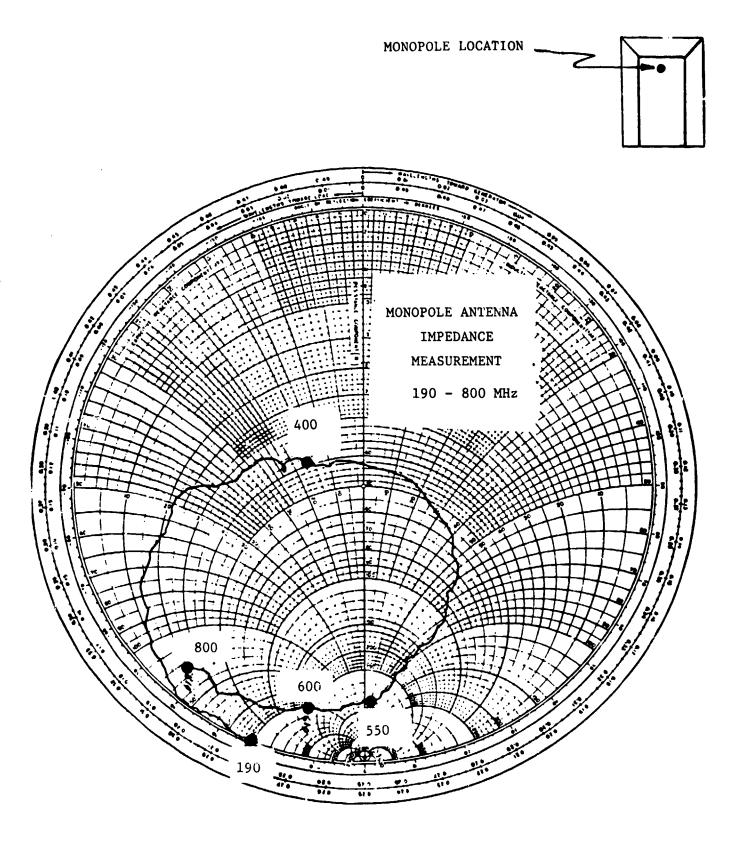


Fig. 6: Individual Thin Whip Model Impedance Plot from 190 to 800 MHz

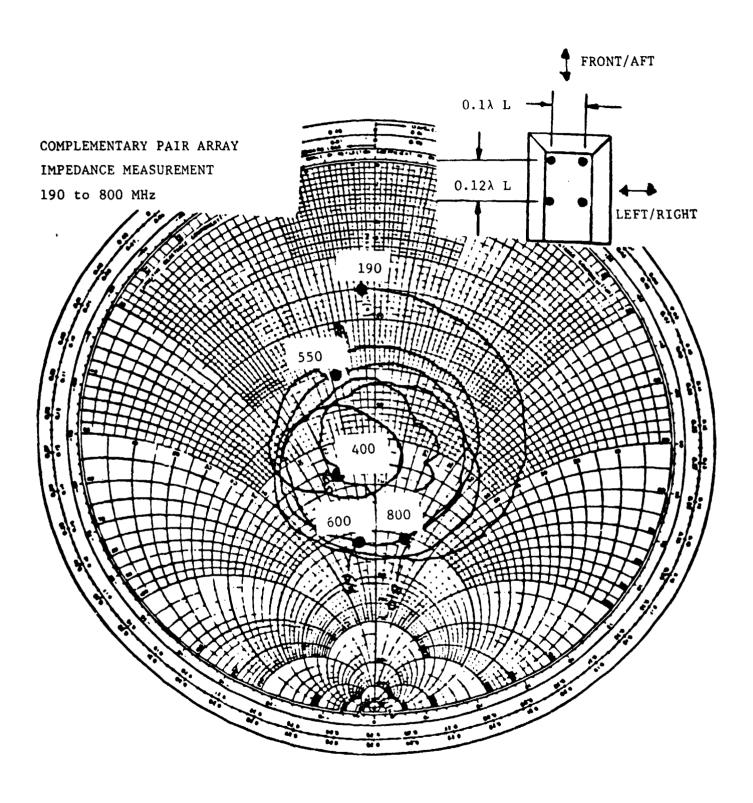


Fig. 7: Matched Sum-Port Model Impedance for Four-Whip Array with Unequal Spacing

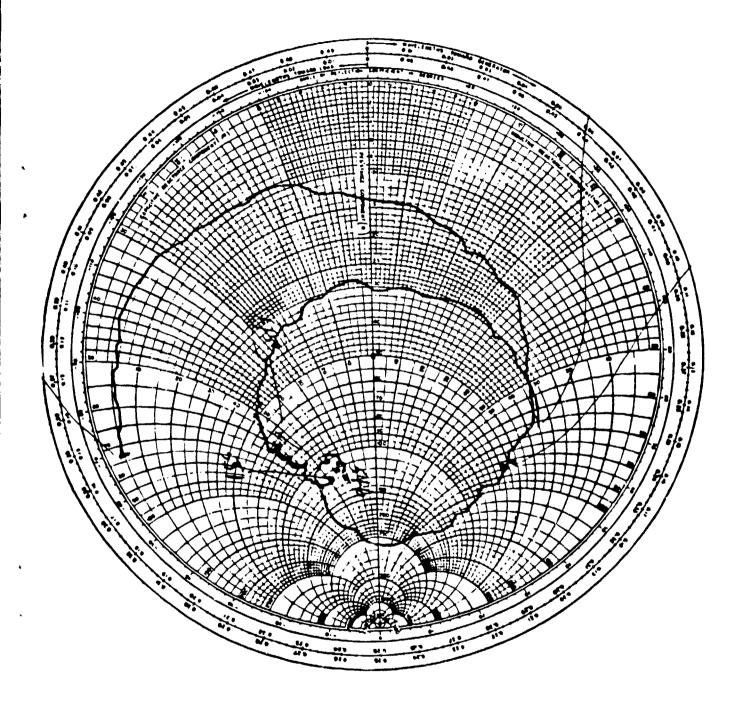


Fig. 8: Combined Input Impedance of Two Whip Antennas with Horizontal Impedance Inverter

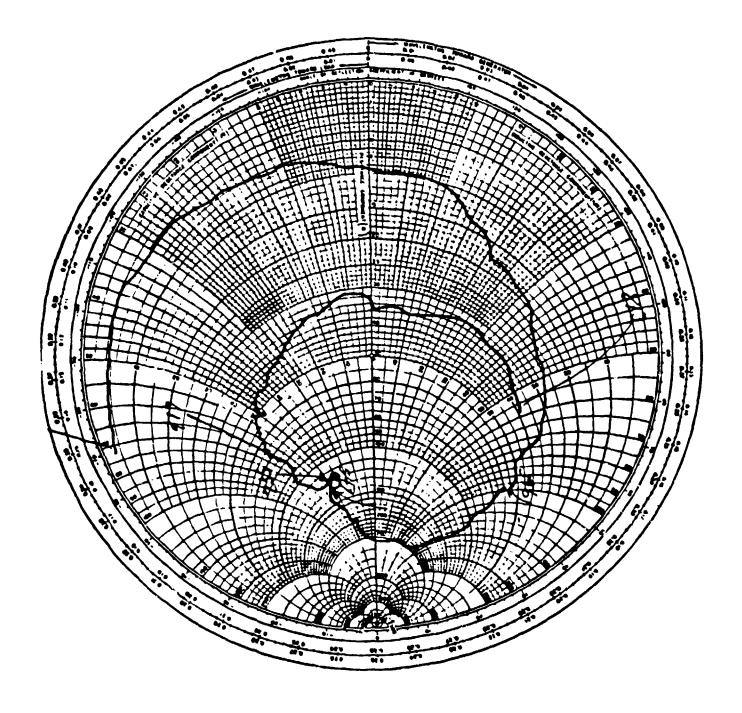


Fig. 9: Combined Input Impedance of Two Whip Antennas with Horizontal Impedance Inverter

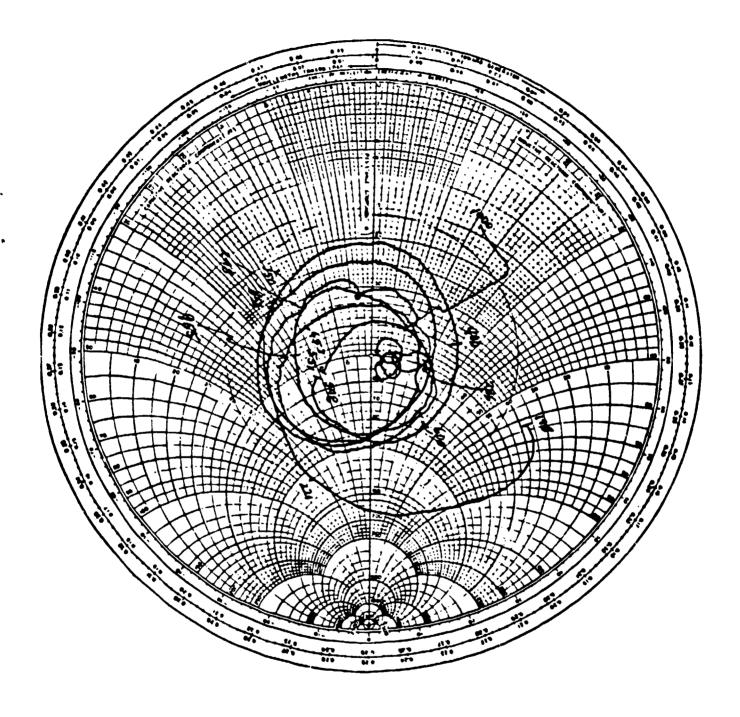


Fig. 10: Sum-Port Input Impedance of Four-Whip Array System with Phasing in the Fore/Aft Direction

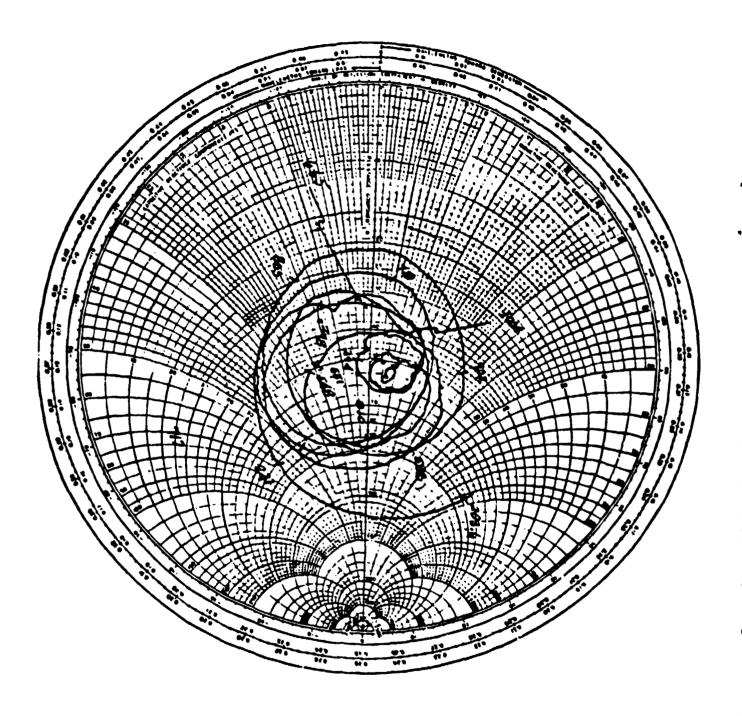
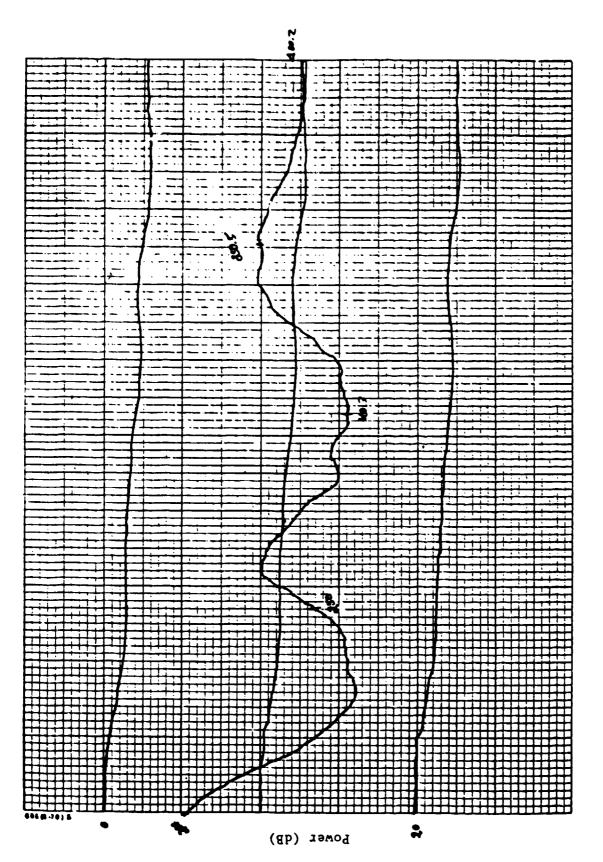
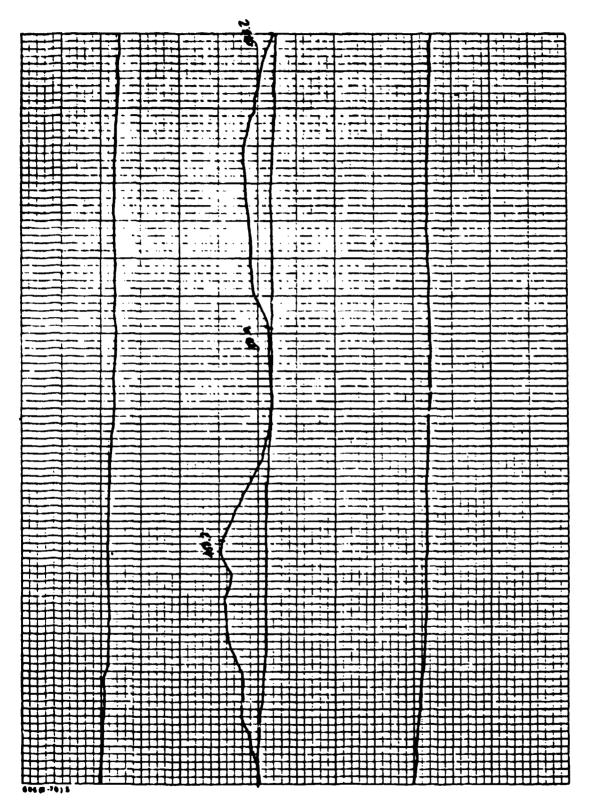


Fig. 11: Sum-Port Input Impedance of Four-Whip Array System with Phasing in the Left/Right Direction



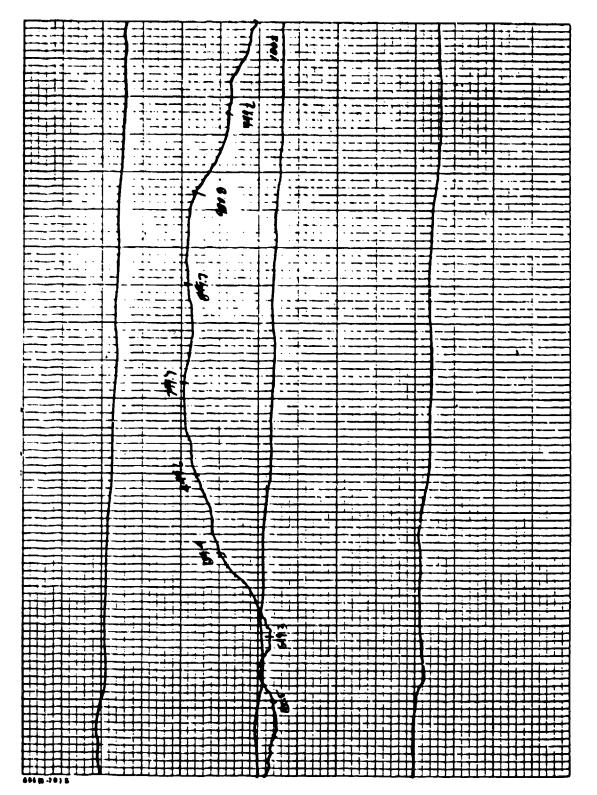
Frequency MHz

Fig. 12: Difference Port Relative Power for Broadside Beam Position (200 to 400 MHz)



Frequency MHz

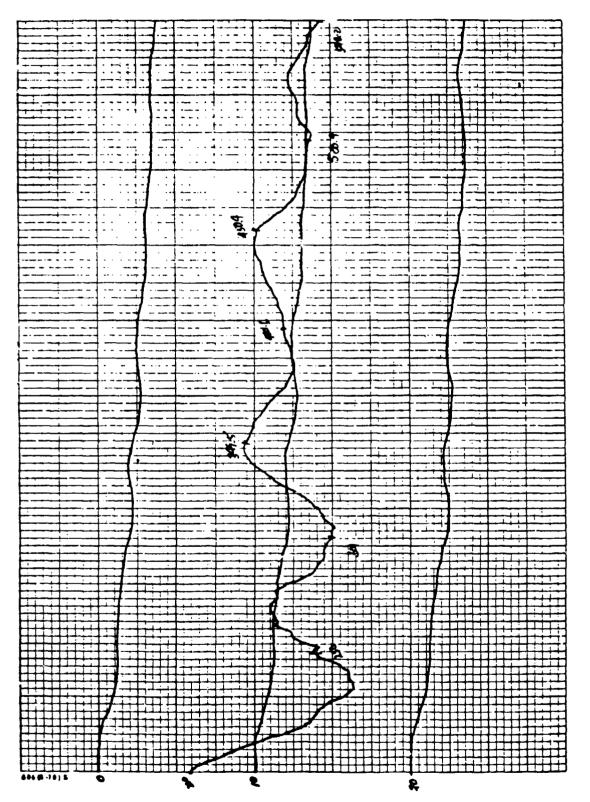
.g. 13: Difference Port Relative Power for Broadside Beam Position (400 to 550 MHz)



Power (dB)

Frequency MHz

Difference Port Relative Power for Broadside Beam Position (550 to 1000 MHz)

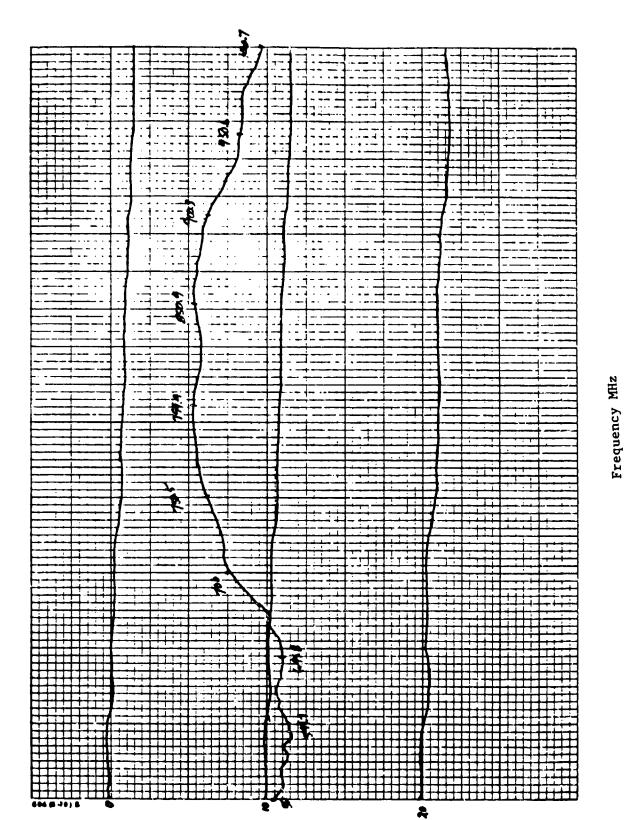


100

Frequency MHz

Difference Port Relative Power for Endfire Beam Position (200 to 550 MHz)

Power (dB)



Power (dB)

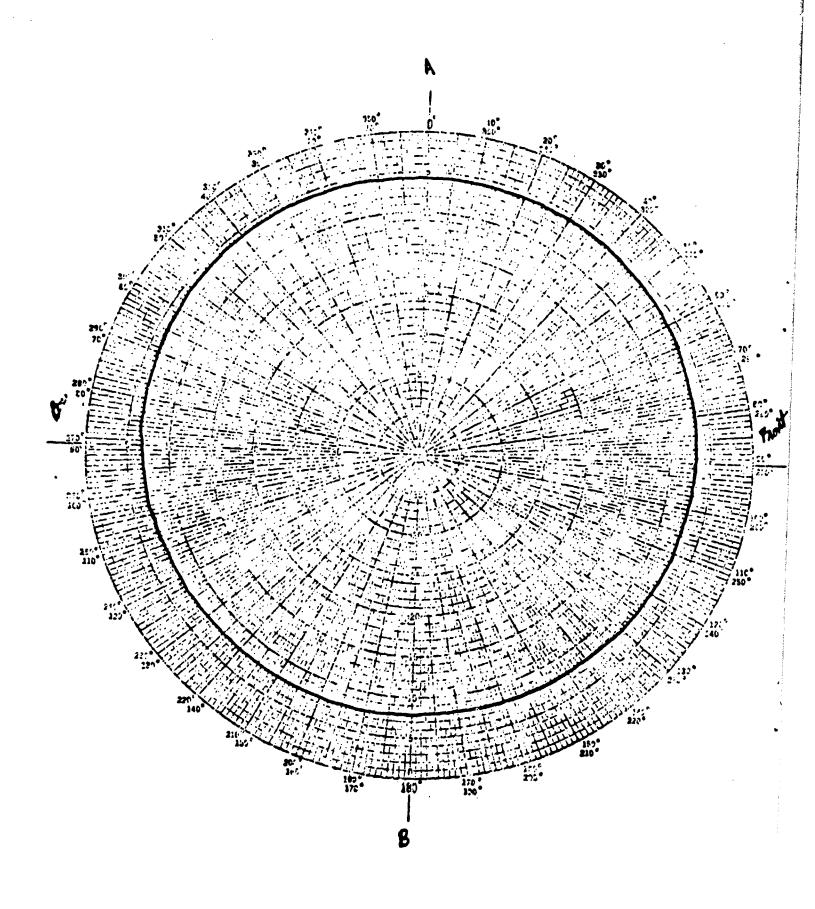


Fig. 17: Azimuth Pattern of Vehicular Array (210 MHz)

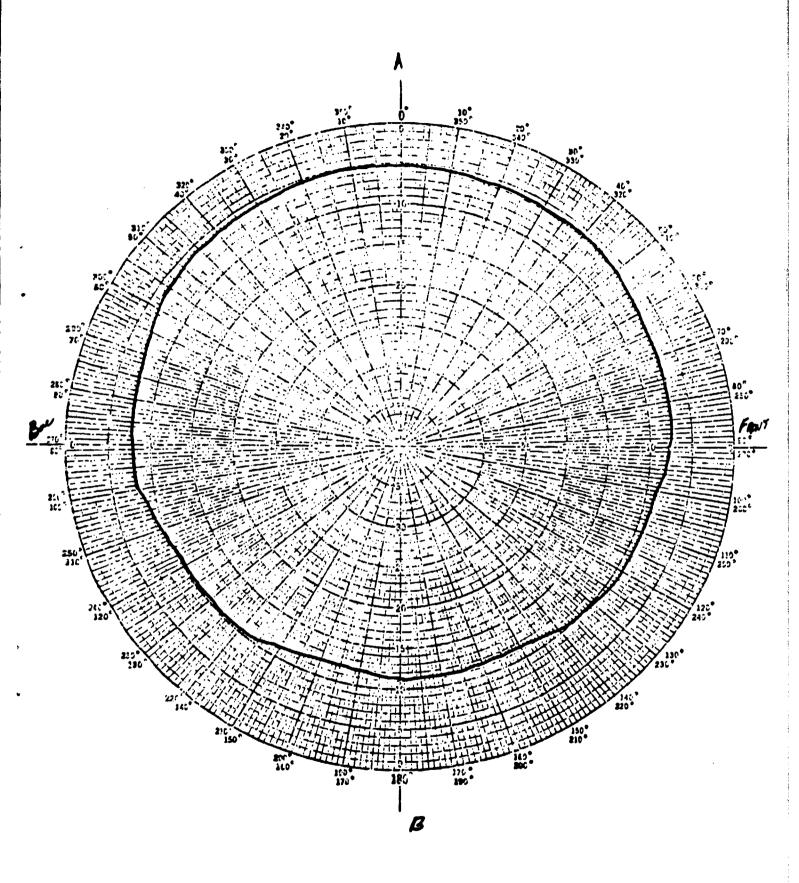


Fig. 18: Azimuth Pattern of Vehicular Array (400 MHz)

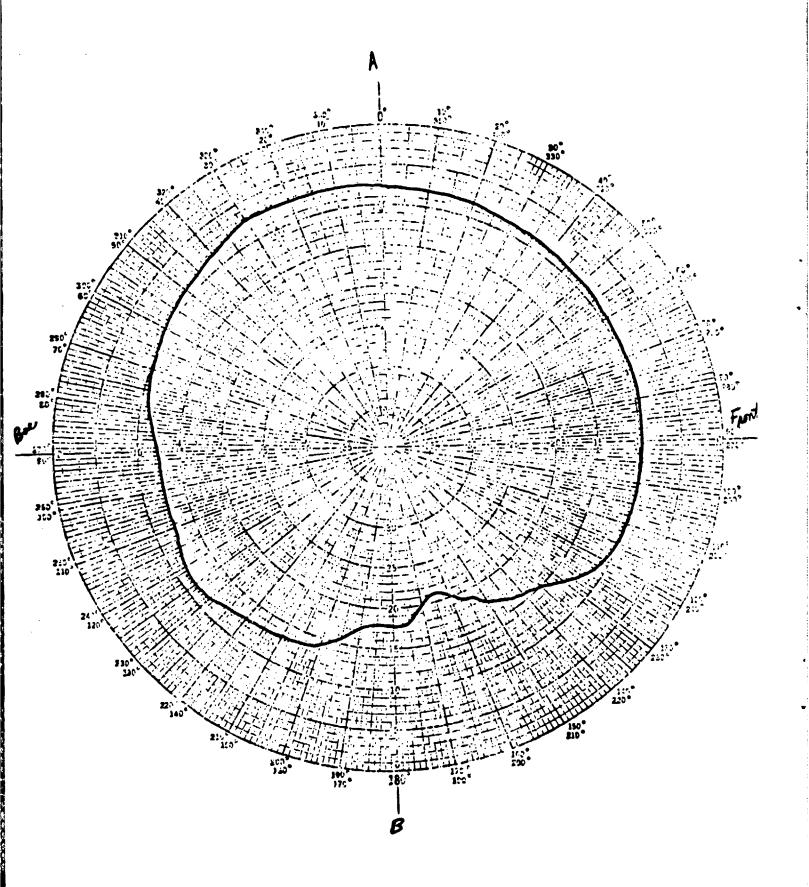


Fig. 19: Azimuth Pattern of Vehicular Array (600 MHz)

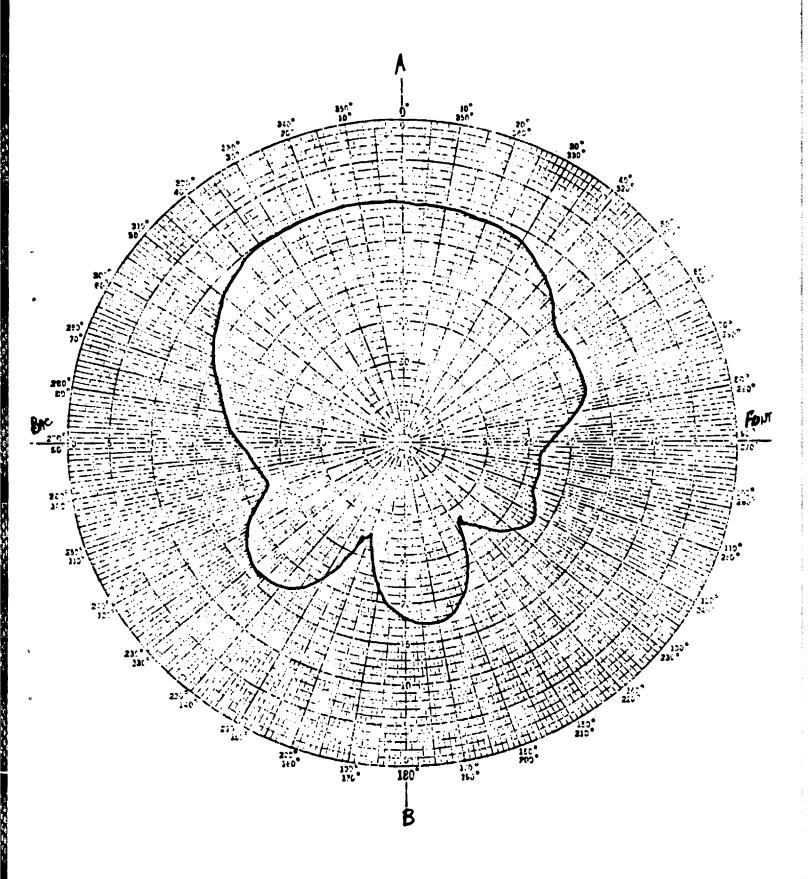


Fig. 20: Elevation Pattern of Vehicular Array (210 MHz)

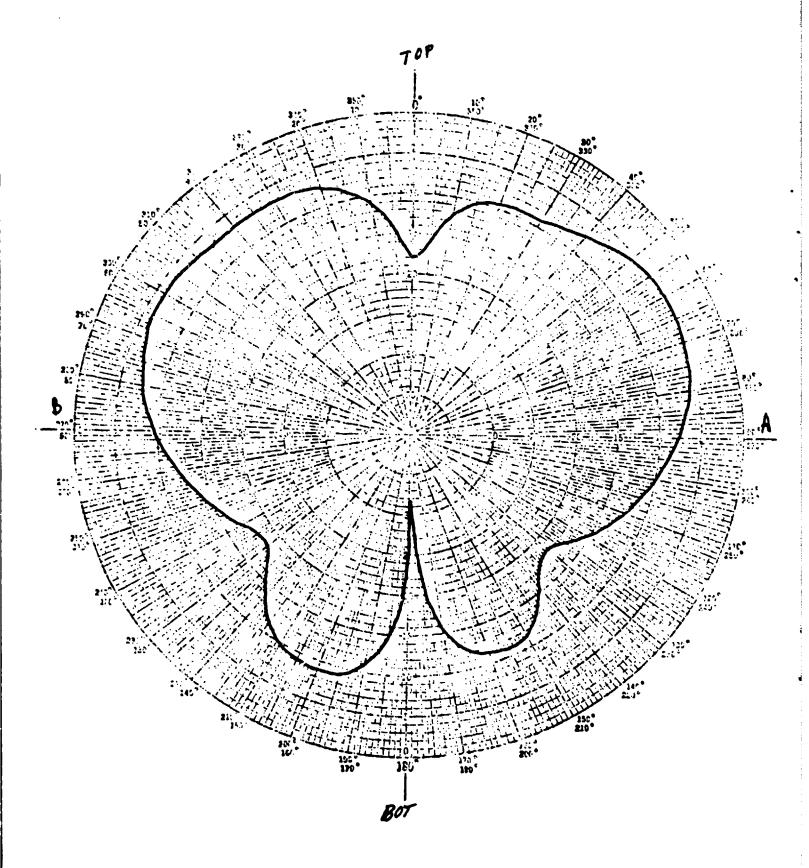


Fig. 21: Elevation Pattern of Vehicular Array (210 MHz)

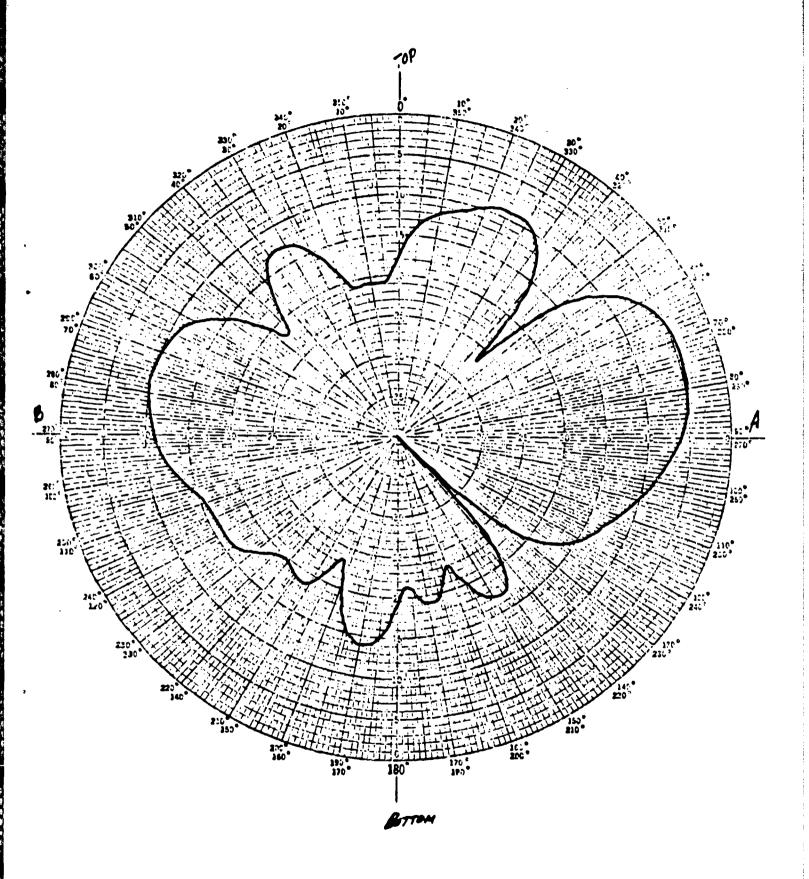


Fig. 22: Elevation Pattern of Vehicular Array (400 MHz)

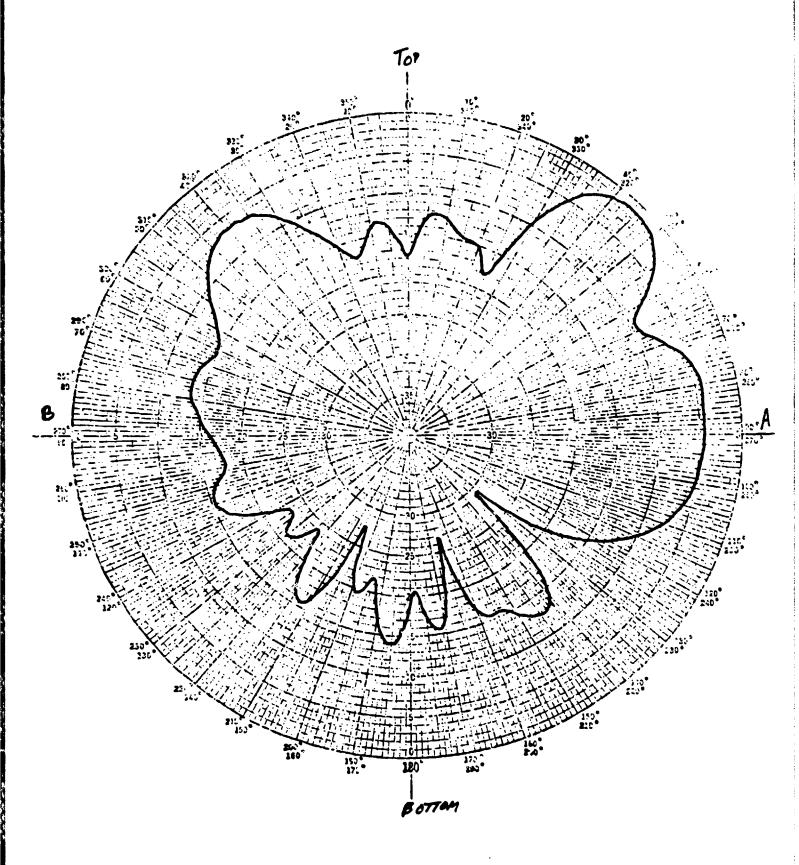


Fig. 23: Elevation Pattern of Vehicular Array (600 MHz)

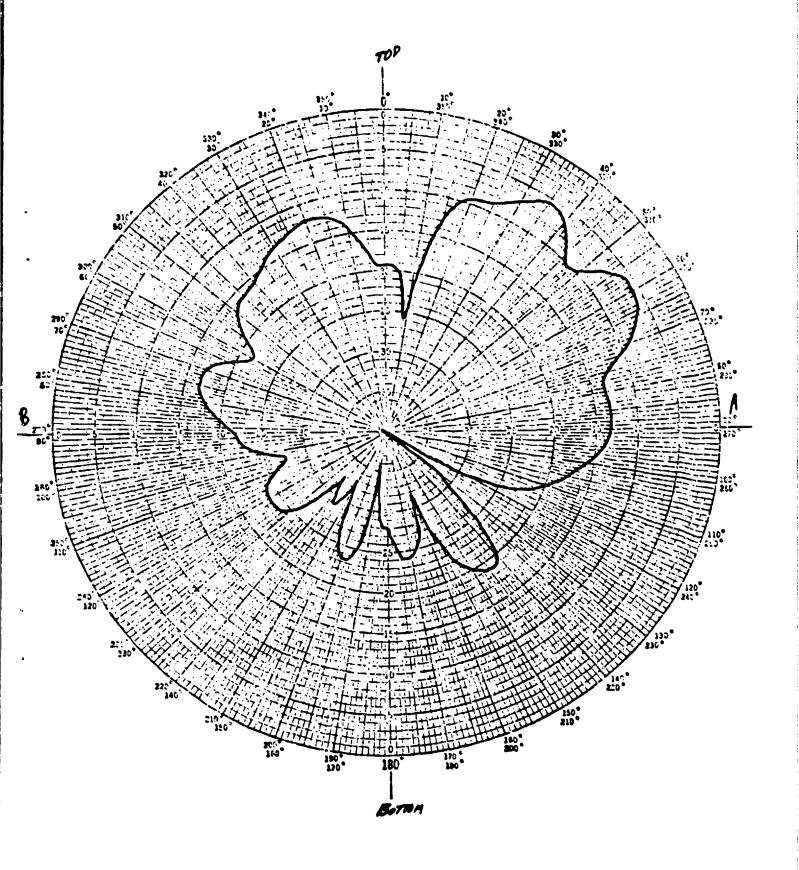


Fig. 24: Elevation Pattern of Vehicular Array (800 MHz)



PATTERN PREDICTION OF BROADBAND MONOPOLE ANTENNAS ON FINITE GROUNDPLANES USING THE BOR MOMENT METHOD

DIRK E BAKER AND LOUIS BOTHA

COUNCIL FOR SCIENTIFIC AND INDUSTRIAL RESEARCH P.O. BOX 395, PRETORIA, SOUTH AFRICA 0001

ABSTRACT

This paper describes the design and measured performance of very thick cylindrical monopole antennas (length-to-diameter ratios These very thick monopole antennas exploit the physical dimensions of common coaxial connectors to achieve 3:1 frequency bandwidths with VSWR less than 2:1 in the 2 to 20 GHz frequency range. The antenna patterns of the very thick monopole differ significantly from antennas those of their thin counterparts. The body of revolution moment method technique is used to predict the E-plane patterns of the very thick cylindrical monopoles as well as those of conical monopoles at the center of finite circular groundplanes. Agreement between measured and predicted patterns is excellent.

1. INTRODUCTION

There is continuing interest in finding accurate methods for predicting the patterns and impedance of monopole antennas on finite groundplanes 1,2 . Both the moment method 3 and the geometrical theory of diffraction $(\text{GTD})^{1,4,5}$ have been used to predict the patterns of thin cylindrical monopoles at the center of circular groundplanes. Generally the monopoles are about a quarter wavelength long which considerably simplifies the

problem. This is especially true for the GTO where the dipole pattern in the absence of the groundplane (the geometrical optics field) must be known.

Thin monopoles are generally narrow band antennas resonating at a length a little shorter than a quarter wavelength. It has been known for a very long time that the impedance variation of thick monopoles is significantly less than that of thin monopoles 4,6,7 . Thick cylindrical monopoles have been studied in some detail 8,9 but these thick monopoles were usually driven by low impedance coaxial cables (about 10 ohms).

At microwave frequencies, above about 2 GHz, it becomes possible to make very thick monopoles (length-to-diameter ratio L/D=2) by exploiting the dimensions of commonly used coaxial connectors (N, TNC, PTNC and SMA). Figures 1(a) to 1(c) show the progression to a very thick monopole antenna. The diameter of the monopole conductor does not extend beyond the dielectric of the 50 ohm coaxial line. This significantly reduces the excess base capacitance resulting in monopole antennas with 3:1 frequency bandwidth for a VSWR less than 2:1. Monopoles with $L/D \approx 2$ are much thicker than those treated in 4,6,7.

At the high-frequency end, these very thick monopoles are more than a half wavelength long and their patterns differ significantly from those of their thin counterparts. The patterns of the conical monopole antenna of Figure 1(d) can be quite complex and no simple solution exists although extensive measured data 10 and theoretical results for a 60° conical monopole 11 exist.

This paper describes the design and VSWR performance of very thick monopole antennas having 3:1 bandwidth when fed directly by a 50 ohm coaxial line. The highly efficient body of revolution (BOR) moment method formulation of Mautz and Harrington¹² is used to calculate the patterns of very thick cylindrical as well as conical monopole antennas on finite groundplanes. In most cases the groundplanes are quite small (one to three wavelengths) at the low-frequency limit of the antennas. The predicted patterns are compared to measured patterns to assess the accuracy of the technique.

2. DESIGN AND PERFORMANCE OF VERY THICK MONOPOLES

2.1 Design

To exploit the reduction in impedance variation as the L/D ratio of monopoles decreases, several monopoles were constructed. Figure 2 shows the typical construction of the antennas. The antennas are all based on standard panel mount 50 ohm coaxial connectors. The thick monopoles (L/D=7) are made by cutting the connector center conductor to the desired length while the very thick monopoles (L/D=2) are made by adding a brass bush to the center conductor. The diameter of the brass bush is made the same as that of the dielectric insulator of the panel mount connector. All the monopoles are mounted on finite circular groundplanes whose diameters were chosen somewhat arbitrarily to lie in the one to three wavelength range at the low-frequency end of the antenna bandwidth.

Even though the conductor of the very thick monopole does not extend beyond the connector dielectric, there is some excess base capacitance which must be compensated for. The compensating gap g (see Figure 2) was determined experimentally to achieve the best VSWR performance over a nominal 3:1 bandwidth. It was observed that the compensating gap increased linearly with the diameter of the very thick monopole. Figure 3 shows the compensating gap g as a function of monopole diameter D. This curve can be used to estimate the gap for other monopole diameters but it applies specifically to the case where the monopole and connector dielectric have the same diameter.

Table 1 shows the dimensions of four very thick monopole antennas based on the SMA, TNC, PTNC and N connectors. The symbols are those used in Figure 2.

<u>TABLE 1</u>: Dimensions and frequency limits of very thick monopole antennas.

NO.	TYPE*	D (mm)	L (mm)	L/n -	d (mm)	g (mm)	W (mm)		f _{min} (GHz)	f _{max} (GHz)
1	SMA	4.0	7.8	1.95	1 25	1.6	129.0	1.5	7.1	21.8
2	PTNC	5.3	11.2	2.11	1.62	2.1	76.0	1.5	4.6	14.2
3	TNC	7.0	13.8	1.97	2.14	2.9	129.0	1.5	4.1	11.9
4	N	10.0	22.1	2.21	3.00	4.1	175.0	3.0	2.6	7.5

^{*} Type here refers to the standard coaxial connector.

2.2 Measured reflection coefficient

Figures 4 to 6 show the measured reflection coefficient (VSWR) for three of the very thick monopole antennas. Also shown is the reflection coefficient for thick monopole antennas with $L/D \approx 7$. The thick monopole antennas show the usual resonant behaviour of monopoles while the very thick monopole antennas all exhibit about 3:1 frequency bandwidths at the VSWR = 2:1 points. The frequency limits for each antenna are given in Table 1. The superior bandwidth capability of the very thick monopoles ($L/D \approx 2$) over the thick monopoles ($L/D \approx 7$) is clearly demonstrated in Figures 4 to 6. Only two very thick monopole antennas are required to cover the 2.6 to 21.8 GHz frequency range.

2.3 Comments on measured patterns

It is well known that the antenna patterns of very thick monopoles do not differ too significantly from those of very thin monopoles when the lengths are about 0.25 λ . As the monopole length increases to 0.625 λ the very thick monopole patterns start to deviate from the thin patterns by showing filled in nulls and higher secondary lobes 6 .

Figure 7 shows a set of three measured patterns for antenna number 1 (SMA monopole on 129 mm groundplane) at 10 GHz where L/λ = 0.26. The three antennas have L/D = 1.95 (very thick monopole), L/D = 6.24 (thick monopole) and L/D = 33.9 (thin monopole). The patterns are identical (the peak value at 60° was adjusted to be the same between plots) which confirms the observation about 12 patterns of 0.25 λ monopoles. This result indicates that the assumption of using the thin dipole pattern in

the GTD is valid even for very thick dipoles provided the monopole height is about $\lambda/4$. The result in Figure 7 should be compared to that in Balanis⁵ where the GTD plus ring currents are used to solve for the patterns of a $\lambda/4$ monopole on a 4 λ groundplane. Agreement between Figure 7 and Figure 11.38 of reference 5 is very good.

Antenna number 4 (N-type monopole on 175 mm groundplane) was used to examine the effect on patterns when the very thick (L/D = 2.2) and the thick (L/D = 7.4) monopoles are $0.625~\lambda$ long. Figure 8 shows that there are significant differences between the patterns in the upper hemisphere between 50° and 90°. In the lower hemisphere the sidelobe structure for the two antennas is identical but there is about 10 dB difference between the power levels. The peak values at 38° were adjusted to zero dB; the peak value of the very thick monopole lay only 0.5 dB above that of the thick monopole. At 90° the levels differ by 6.5 dB. Other pattern measurements show that differences are evident when the monopole lengths exceed 0.37 λ .

Because the monopole antennas are very light, they can be supported directly on a 0.141 inch semi-rigid coaxial cable with a swept radius 90° bend. This eliminates the need for test fixtures and structures behind the antenna groundplane. The measured patterns are extremely symmetrical and it is felt that the backlobes are at the correct levels because there are no obstructions (except for the short horizontal section of the 90° bend) behind the antenna. This is a significant improvement over the measurement set-up in where the back mounting structure influences the backlobes.

3. BOR MODELLING PROCEDURE

A body of revolution is a body whose surface is generated by rotating a plane curve around an axis. This leads to a body with perfect rotational symmetry. Examples of bodies of revolution are cylinders, cones and spheres. Mautz and Harrington 12 formulated the BOR moment method technique. This is mathematical procedure which exploits the symmetry of bodies of revolution by using modal expansions of the current around the BOR. These modes are chosen to be orthogonal and are thus uncoupled. Each mode can therefore be solved independently from other modes. This leads to a few small matrices rather than one large matrix. Small matrices are easier and faster to solve than large ones and this gives a significant saving in computer time. For a completely symmetric aperture as considered here, only one mode needs to be solved.

To model an antenna using the BOR technique a generating curve must be defined. Several examples of such generating curves are shown in Figure 9. There is a limitation of 99 on the maximum number of points that can be handled by the BOR moment method program in use. This limits the detail that can be modelled.

Because the moment method calculates the current on the body under consideration, it is very important to put segments at the correct places to ensure the correct current flow on the body. Where large changes in current are expected, more segments must be used for accurate modelling. Figure 9(a) shows that more segments are used on the monopole than on the groundplane. On the groundplane more segments are used close to the monopole than further away.

Figure 9(b) shows an example of a case where there are too few segments available to model all the details of the antenna. The lower portion of the groundplane has been modelled with a few segments which were truncated near the edge. This will account for the radiation from the finite edge of the groundplane.

Figures 9(c), 9(d) and 9(e) show three models of the conical monopole of Figure 1(d). These models were used to demonstrate different effects found in the models. Figure 9(c) shows the normal model of the capped cone which models only the upper side of the groundplane and has a maximum segment length of 2 mm. This gives a segment length of $1/15 \lambda$ at 10 GHz. Figure 9(d) shows a model with the same resolution but modelling both sides of the Figure 10 shows the difference between the predicted patterns for the conical monopole on its 129 mm groundplane using these two models. The bottom side of the groundplane has very little effect on the computed radiation pattern at 10 GHz. This is also true at other frequencies. convergence of the moment method solution, a high resolution model as shown in Figure 9(e) was used. This model has a segment length of 1 mm (1/30 λ at 10 GHz). Figure 11 shows the comparison of the radiation patterns for these two models. There are slight differences between the two models at 10 GHz in the ±120° region. At higher frequencies (18 GHz), the patterns of the two models start to differ by more than a dB showing that the normal resolution model is not valid at these frequencies because there are too few segments.

The antenna feed network is modelled realistically by using the TEM field of a coaxial cable. This is done by defining a constant radial field from the center conductor to the outer conductor of the coaxial line feeding the monopole.

An attempt was made to compute the input impedance of the antennas at different frequencies using the BOR method. This was done by integrating over the field and currents in the feed aperture. The results obtained look promising but more work is needed on this aspect.

4. MEASURED AND PREDICTED RESULTS

The VSWR of the 70° capped cone of Figure 1(d) on a 129 mm groundplane (as for antenna no. 1) was 2.2:1 at 2 GHz and better than 1.5:1 from 2.5 to above 21 GHz. All the predicted patterns were computed using the high resolution model of Figure 9(e).

Figure 12 shows the measured and predicted patterns at 2 GHz where the groundplane is only 0.86λ in diameter. groundplane the agreement is excellent, below the groundplane the measured pattern lies about 2.5 dB below the predicted one. Because the groundplane is so small, currents will creep onto the underside of the groundplane and possibly excite the horizontal section of supporting cable. It was found that the length of the horizontal section of cable did influence the measured patterns indicating that the antenna is not completely isolated from the measurement environment at 2 GHz. There may also be merit in using one of the BOR models which includes the lower portion of the groundplane. Figures 13 and 14 show the patterns at 4 GHz Now the agreement is excellent both as regards the mainlobes above the groundplane and the sidelobes below the groundplane.

Figure 15 shows the measured pattern for antenna no. 4 at 2.7 GHz where the groundplane is $1.58~\lambda$ in diameter. The predictions were made using the model of Figure 9(b). The agreement is good except near the horizon where the measured pattern is about 2.5 dB below the predicted one. It is felt that a more detailed model of the underside of the groundplane and a means to suppress stray currents on the 0.141 inch semi-rigid cable could improve this comparison. Figure 16 shows excellent agreement at 7.9 GHz.

Measured and predicted patterns for antenna no. 1 are shown for 10 GHz in Figure 17. Agreement is excellent. The patterns for the thick cylindrical monopole in Figure 17 should be compared to those of the 70° conical monopole in Figure 14. The backlobe structure of the two sets of patterns is almost identical (as expected since the shape of the backlobe structure is determined almost entirely by the diameter of the groundplane). However, there are significant differences in the upper hemisphere where the maximum of the conical monopole occurs at about 25° while that for the very thick monopole occurs at 60°. This emphasizes the fact that the basic radiator pattern can strongly influence the pattern structure in the upper hemisphere.

5. CONCLUSIONS

Measured reflection coefficient data has been presented to show that broadband very thick monopoles can be made quite simply by exploiting the dimensions of common connector types. Frequency bandwidths of 3:1 can be achieved with VSWR less than 2:1. Because the broadband monopoles are very thick, their basic radiation patterns differ significantly from those of their thin counterparts for L/λ greater than about 0.4. The BOR moment method is a powerful technique for taking into account directly

the radiation characteristics of the thick monopoles. In addition, the more complex conical monopoles can also be modelled. Agreement between measured and predicted patterns is excellent, the main differences occurring for groundplane diameters in the 1 to 1.5 λ region. Additional work is required to refine the BOR model and the measurement technique for these very small groundplanes.

6. ACKNOWLEDGEMENTS

The authors are indebted to the CSIR for permission to publish this work.

REFERENCES

- Bach, H. and Lemanczyk, J.H. (1986) The monopole on a finite groundplane, National Radio Science Meeting, URSI, Philadelphia, PA, p. 233.
- 2. Hassan, M.A. (1986) Solution of a monopole antenna over a circular finite disc, IEEE/AP-S International Symposium Digest, Philadelphia, PA, p. 133 to p. 136.
- 3. Adwalla, K.H. and MacLean, T.S.M (1979) Monopole antennas at center of circular groundplane: Input impedance and radiation pattern, <u>IEEE Trans. Antennas Propagat</u>. AP-27 (No. 2):151-153.
- 4. Johnson, R.C. and Jasik, H. (Eds.) (1984) Antenna Engineering Handbook, McGraw-Hill, New York, p. 4-27 to p. 4-31 and p. 4-4 to p. 4-9.

- 5. Balanis, C.A. (1982) Antenna Theory, Harper and Row, New York, p. 518 to p. 520.
- 6. Reich, H.J. (Ed.) (1946) <u>Very High-frequency Techniques</u>, McGraw-Hill, New York, p. 110 to p. 114.
- 7. Brown, G.H. and Woodward, O.M. (1945) Experimentally determined impedance characteristics of cylindrical antennas, Proc. IRE, 33:257-262.
- 8. Chang, D.C. (1968) On the electrically thick monopole Part II Experimental Study, <u>IEEE Trans. Antennas Propagat</u>. AP-16 (No. 1):64-71.
- 9. King, R.W.P. (1972) Measured admittances of electrically thick monopoles, <u>IEEE Trans. Antennas Propagat</u>. AP-20 (No. 6):763-766.
- 10. Brown, G.H. and Woodward, O.M. (1952) Experimentally determined radiation characteristics of conical and triangular antennas, RCA Rev. 13 (No. 4):425-452.
- 11. Papas, C.H. and King R. (1951) Radation from wide-angle conical antennas fed by coaxial line, Proc. IRE 39:49-51.
- 12. Mautz, J.R. and Harrington, R.F. (1969) Radiation and scattering from bodies of revolution, Applied Sci. Res. 20:405-435.

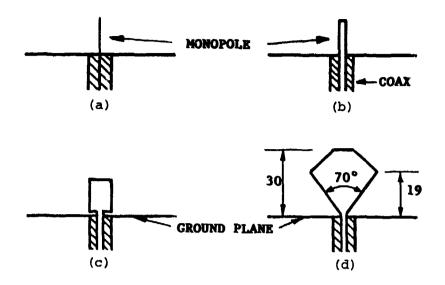


FIGURE 1: Various monopole antennas (a) thin (L/D large), (b) thick (L/D \approx 7), (c) very thick (L/D \approx 2) and 70° conical monopole with truncated 90° cap.

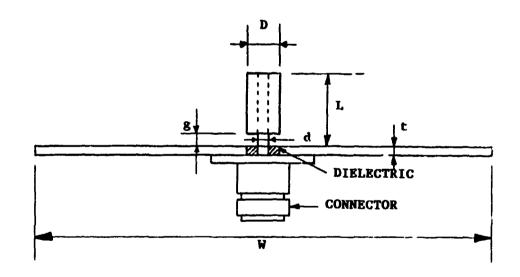


FIGURE 2 : Schematic diagram showing design parameters of the monopole antenna.

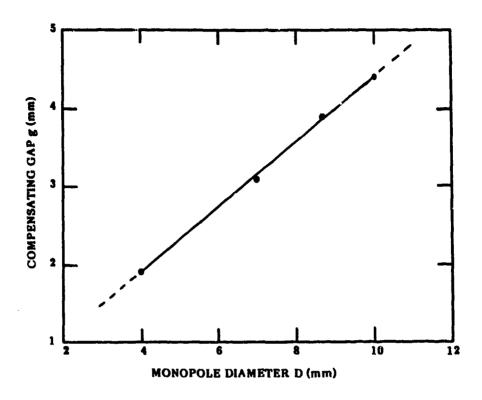


FIGURE 3 : Compensating gap vs. monopole diameter.

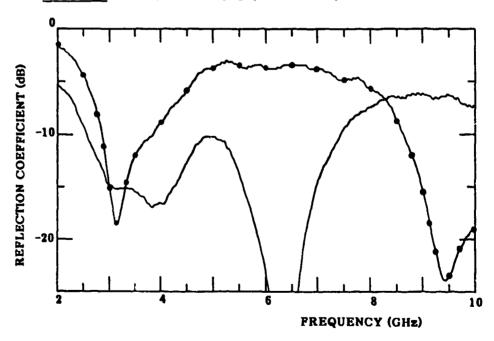


FIGURE 4: Measured reflection coefficient of antenna no. 4 with L/D = 2.21 (——) and monopole with L/D = 7.37 (——).

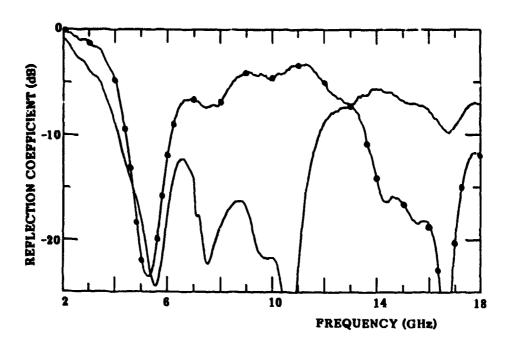


FIGURE 5: Measured reflection coefficient of antenna no. 3 with L/D = 1.97 (----) and L/D = 6.45 (-----).

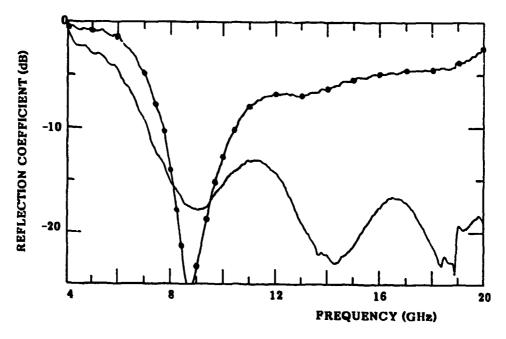


FIGURE 6: Measured reflection coefficient of antenna no. 1 with L/D = 1.95 (----) and L/D = 6.24 (-----).

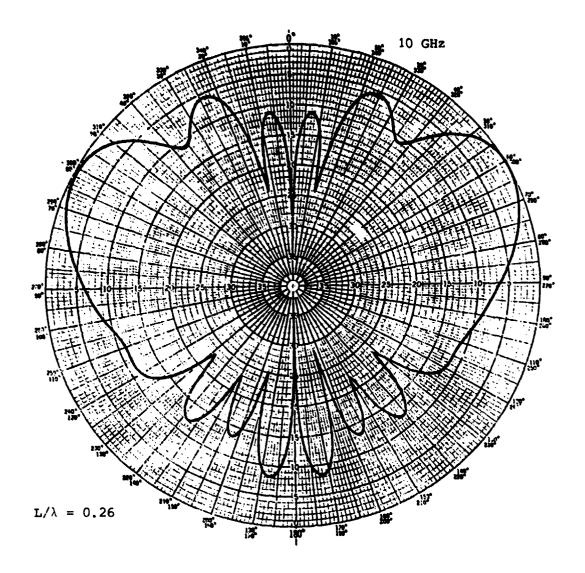


FIGURE 7: Superposition of a set of measured patterns at 10 GHz for three monopole antennas with $L/D \approx 1.95$, L/D = 6.24 and L/D = 33.9 on a 129 mm groundplane (antenna no. 1 with various radiators).

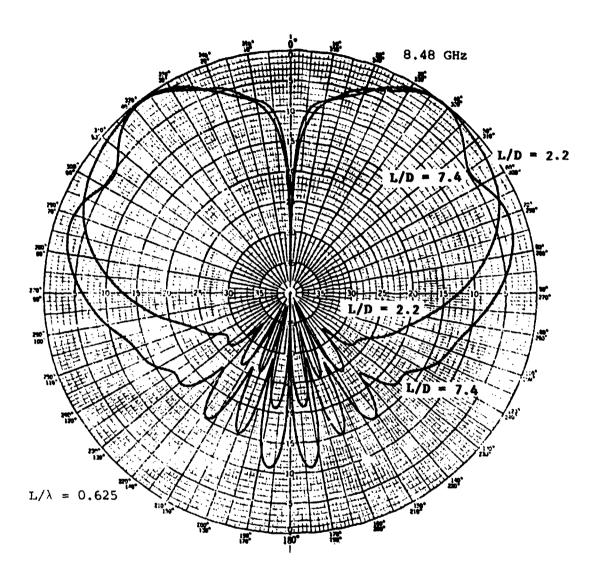


FIGURE 8: Measured patterns at 8.48 GHz for antenna no. 4 with monopole radiators having L/D = 2.2 and L/D = 7.4.

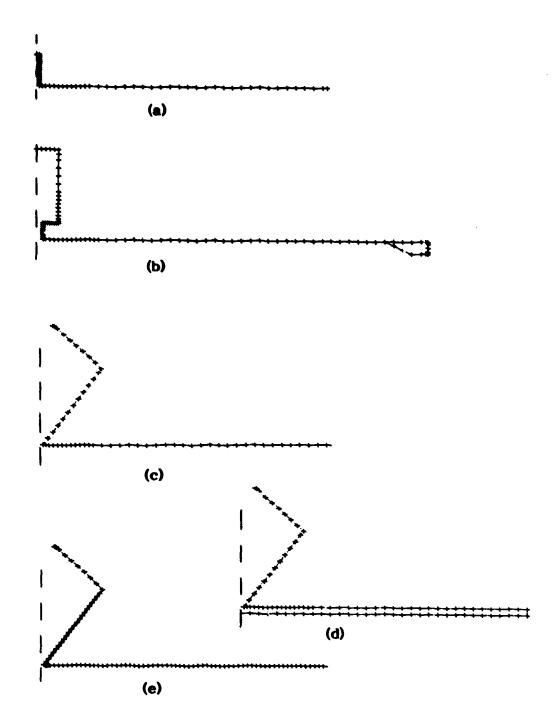


FIGURE 9: Examples of BOR generating curves showing segmentation for (a) antenna no. 1, (b) antenna no. 4 and the conical monopole of Figure 1(d) with (c) normal model, (d) double sided groundplane and (e) high resolution model.

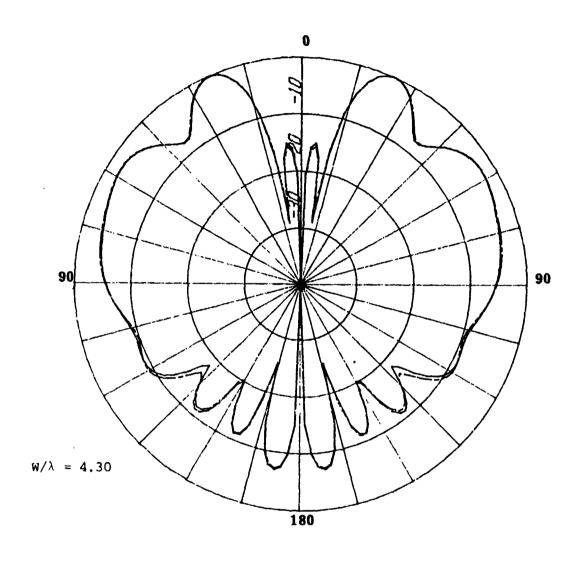


FIGURE 10: Difference Letween the predicted patterns for the normal model (----) and the double sided model (----) of the conical monopole of Figure 1(d) at 10 GHz.

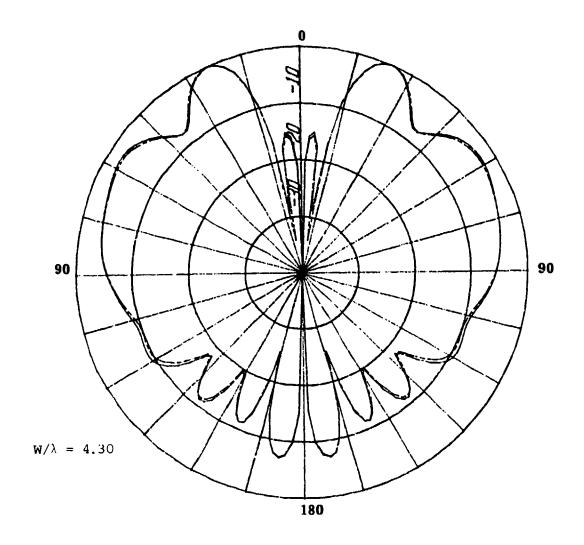


FIGURE 11: Difference between the predicted patterns for the normal model (----) and the high resolution model (----) of the conical monopole of Figure 1(d) at 10 GHz.

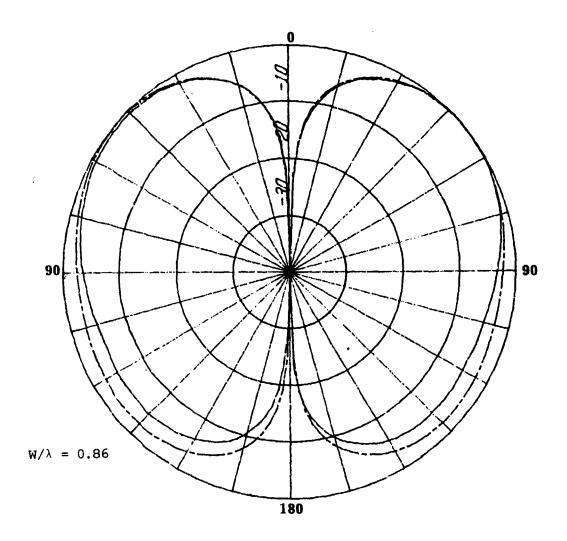


FIGURE 12: Measured (---) and predicted (----) patterns at 2 GHz for the 70° conical monopole.

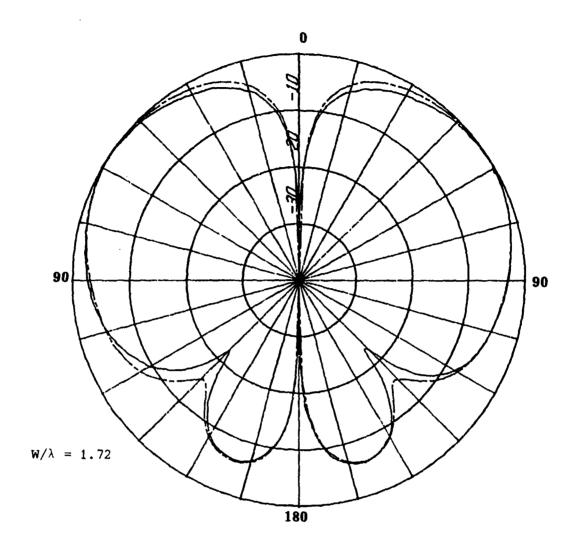


FIGURE 13: Measured (——) and predicted (----) patterns at 4 GHz for 70° conical monopole on 129 mm groundplane.

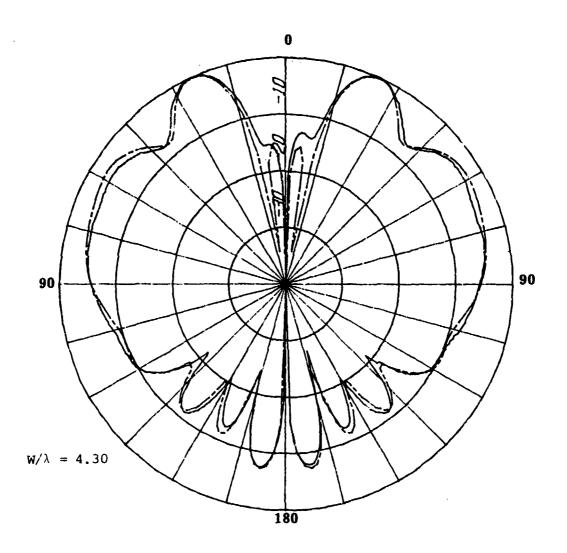


FIGURE 14: Measured (——) and predicted (----) patterns at 10 GHz for 70° conical monopole on 129 mm ground-plane.

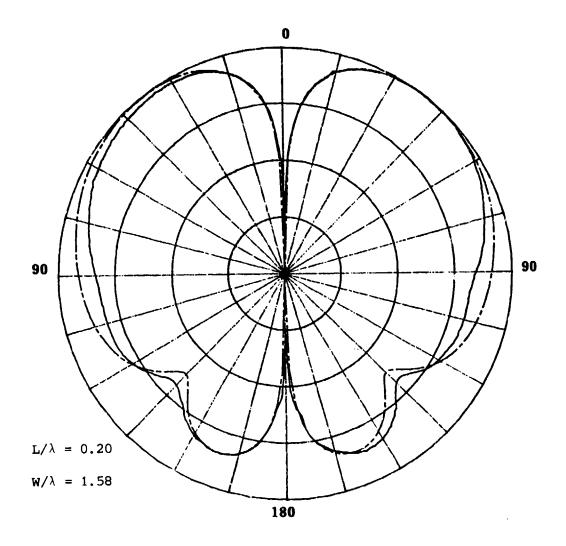


FIGURE 15: Measured (——) and predicted (----) patterns at 2.7 GHz for antenna no. 4 on 175 mm groundplane.

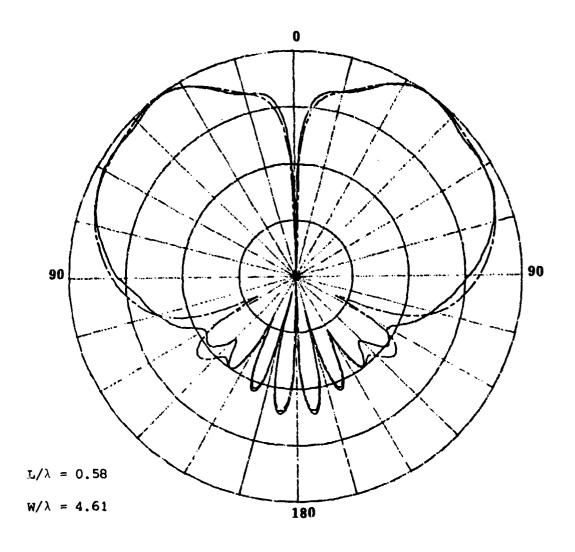


FIGURE 16: Measured (——) and predicted (———) patterns at 7.9 GHz for antenna no. 4 on 175 mm groundplane.

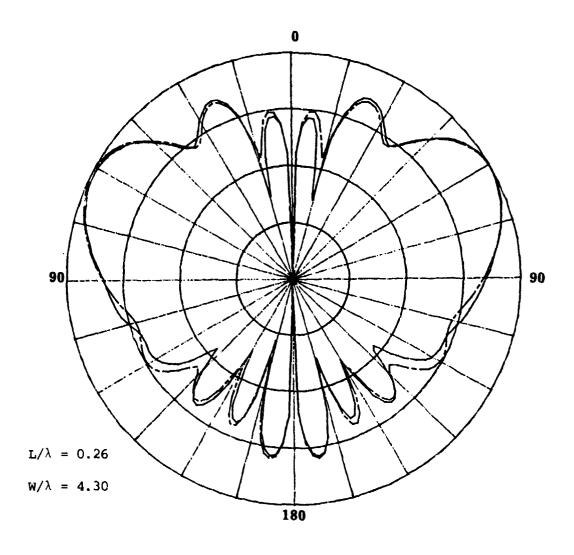


FIGURE 17: Measured (---) and predicted (---) patterns at 10 GHz for antenna no. 1 on 129 mm groundplane.

POLARIZATION MEASUREMENT

David L. Hawthorne
Watkins-Johnson Company

ABSTRACT

Potential applications for a precision, monopulse polarimeter exist in many areas, from ELINT to communications. Many applications require coverage of a broad range of frequencies, rapid processing, and the ability to present measurement results to both human operators and other digital systems. In addition, the form in which measurement results are presented must often be modified to suit a particular application. The need for a powerful, flexible, monopulse polarimeter prompted the development of the Watkins-Johnson Company polarization measurement system.

The polarization state of an electromagnetic wave may be specified in several ways. The interpretation of polarization information in any form, however, requires an understanding of vector theory. In order to visualize polarization relationships the concept of the Poincaré Sphere can be very useful. From the Poincaré Sphere, the polarization box may be derived for use in calculating polarization components. A discussion of these concepts lays the groundwork for evaluation of polarization measurement techniques.

The Watkins-Johson Company polarization measurement system discussed will allow monopulse measurements of the polarization of received signals in the 2 to 18 GHz region. The system utilizes a spread spectrum multiplexing technique that preserves the amplitude and phase relationships of signals from two orthogonal antennas. The ability to simultaneously measure the relative amplitudes and phase of orthogonal signals without the detrimental effects of multiple receivers should greatly improve the accuracy of polarization measurements, while providing the flexibility of broad frequency coverage. In addition, the processing capability incorporated in the system will allow the calculation of polarization parameters as required for presentation to operators or reporting to other systems.

1.0 INTRODUCTION

The area of microwave signal analysis has evolved to the point where systems capable of detailed characterizations of signals are in relatively common use. Signal parameters that are routinely measured include frequency, amplitude, phase, direction of propagation, and modulation type and rate. For pulsed signals, properties such as pulse width and PRI are frequently determined. In addition, the time variance of signal parameters is measured as it contains information about scan patterns, frequency agility, doppler and stagger.

Careful analysis of these properties using digital techniques has produced powerful results, but no system can exploit the full vector nature of E.M. waves while remaining insensitive to polarization. Unfortunately, information regarding the polarization state of an electromagnetic wave has traditionally been ignored, discarded, or simply unavailable in conventional signal analysis systems, although the utilitarian nature of such information has been discussed at great length.

Applications exist in several fields for precision polarization measurement. The most obvious use for such equipment is in the design and testing of antennas, yet polarimetry has the potential to enhance system performance in many ways.

As the demand increases for improved, passive, surveillance capabilities, systems will expand to provide previously unavailable measurement data. Since polarization diversity and agility characteristics can be used to distinguish emitters, ELINT collection systems taking advantage of polarization information could add another dimension to the array of parameters used for signal classification. Passive ESM systems could then utilize received polarization data for purposes of emitter identification, or use pulse by pulse polarization information as a deinterleaving parameter.

Poelman¹ described a method which allows improvement in target detection performance of active radars in clutter and interference environments through adaptive antenna polarizations, when return polarization information is available. Another polarimetry technique² looks promising for improvements in target identification using radar processing that examines the depolarization of back-scattered radiation to obtain geometrical type information relating to target symmetry and orientation in space.

ECM systems can extend their effective range by adapting the polarization of transmitted jamming signals to match that of the received signal. To optimize such a technique, detailed information about the received polarization is necessary.

Earth-space communication links are susceptible to cross-polarized signal interference resulting from depolarization during propagation, and from small changes in orientation of satellite antennas with respect to ground stations. It has been demonstrated that cancellation of residuals through adaptive antenna polarization is desirable³, but is dependent on the availability of polarization information about the received signal.

The use of polarization processing techniques is considered the next logical step in the enhancement of many microwave systems. However, taking the step depends on the availability of equipment

that is capable of precision polarization measurements. The need for such equipment prompted the development of Watkins-Johnson Company's polarization measurement system.

In the following pages, the basic equations for the vector representation of electromagnetic waves shall be discussed. The concepts of polarization and the Poincaré Sphere shall be presented in order to understand the technique used to measure received polarization. The implementation of the measurement technique used in the Watkins-Johnson Company polarization measurement system and the limitations on the accuracy of such systems will be examined.

2.0 COORDINATE SYSTEM AND VECTOR REPRESENTATION

Consider a rectangular, cartesian, coordinate system consisting of three mutually orthogonal axes whose variables are denoted x, y, and z. Unit vectors \vec{a}_x , \vec{a}_y , and \vec{a}_z are oriented as shown in Figure 1. For purposes of analysis we will assume that we are dealing with a plane wave traveling in the z direction. Phase fronts of the wave will be normal to \vec{a}_z .

A plane electromagnetic wave traveling in the z direction is composed of electric and magnetic time-varying fields that lie in the xy plane. The fields are perpendicular to each other, and at a specific time can be represented by orthogonal vectors as shown in Figure 2.

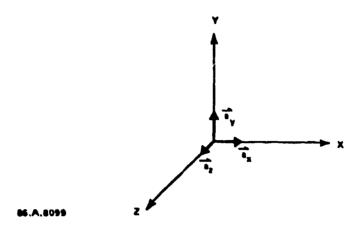


Figure 1. The Rectangular Coordinate System

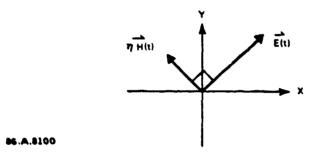
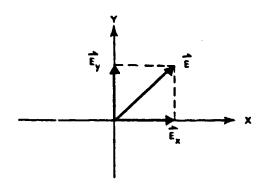


Figure 2. Electric and Magnetic Fields in a Plane Wave

The E and H components of the plane wave vary with time at the same frequency and in the same phase, and the magnitudes are related by a constant. The discussion will therefore deal only with the electric field.

The superposition principle states that the total electric field vector of a wave is the sum of all electric field vectors composing the wave. This means the total field vector for a wave can be decomposed into, or constructed from, two orthogonal vector components, as shown in Figure 3.



86.A.8101

Figure 3. Decomposition of Electric Field Vector into Orthogonal Components

Component vectors \vec{E}_x and \vec{E}_y are related to the total field vector \vec{E} by the equation

$$\vec{E}(t) = \vec{E}_x + \vec{E}_y = E_x(t)\vec{a}_x + E_y(t)\vec{a}_y$$
 (1)

If $\vec{E}(t)$ is a function of a single frequency, the magnitudes of the orthogonal components can be expressed as

$$E_{x}(t) = E_{x} \cos (\omega t)$$
 (2)

and

$$E_{y}(t) = E_{y} \cos (\omega t + \delta)$$
 (3)

where -180 deg $<\delta$ <180 deg.

3.0 POLARIZATION

The polarization of a wave is related to the orientation of the electric field vector with respect to the coordinate system in use.

If an electric field vector always lies in a given plane parallel to the direction of propagation, the wave is said to be linearly polarized. Since \vec{E}_x and \vec{E}_y fit this description, the orthogonal components we have defined can be thought of as linearly polarized fields which differ in time phase by the angle δ .

In general, any electric field can be resolved into orthogonal linear components of appropriate magnitudes and phase. Combining \vec{E}_x and \vec{E}_y to form the total field vector, and plotting the locus described by the tip of the resultant vector over time, will generate an ellipse (Figure 4).

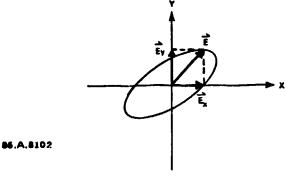


Figure 4. Polarization Ellipse Generated from the Locus of Points at the Tip of \vec{E} over Time

The electric field represented in Figure 4 is said to be elliptically polarized, due to the way the field changes with time. The locus is called the polarization ellipse. If the tip of the electric field vector had traced out a circle, the polarization would be called circular, or, as mentioned above, if the vector remains at a constant angle with respect to the coordinate system, the field is

can be considered elliptical, as the circular and linear polarizations tions are simply degenerate (special) cases of the polarization ellipse.

Discussions of polarization commonly refer to horizontal, vertical, slant-linear, and circular polarizations. These terms refer to the fact that the coordinate system has been defined in relation to a particular (usually earth-bound) frame of reference. However, polarized waves are rarely of a purely linear or circular polarization, due to depolarization during propagation, as a result of reflections, or due to imperfections in the radiating antenna. Most waves are actually elliptically polarized. However, it is instructive to consider the degenerate cases in order to gain an understanding of the relationships between the orthogonal components for different polarizations. The relative amplitudes and phases of \vec{E}_{χ} and \vec{E}_{y} for these cases are given in Table 1, which assumes that the coordinate system has been aligned such that the x axis is parallel to the horizon.

If the components are in phase but have unequal amplitudes the total field is linearly polarized in a direction that makes an angle with the x axis that is given by the equation

angle = arctan
$$(|\vec{E}_y|/|\vec{E}_x|)$$
 (4)

Table 1. Amplitude and Phase Relationships between Orthogonal

Linear Components of Degenerate Polarizations

Polarization	Amplitudes	Phase (δ)
Horizontal	$\left \vec{\mathbf{E}}_{\mathbf{y}}\right = 0$	N/A
Vertical	$\left \vec{\mathbf{E}}_{\mathbf{x}}^{\mathbf{j}}\right = 0$	N/A
+45 Deg Slant	$\left \vec{E}_{x} \right = \left \vec{E}_{y} \right $	0 degrees
-45 Deg Slant	$\left \vec{\mathbf{E}}_{\mathbf{x}}\right = \left \vec{\mathbf{E}}_{\mathbf{y}}\right $	180 degrees
Arbitrary Linear	·	
Polarization	Don't Care	0 or 180 degrees
Right Hand Circular	$ \vec{\mathbf{E}}_{\mathbf{x}} = \vec{\mathbf{E}}_{\mathbf{v}} $	-90 degrees
Left Hand Circular	$ \vec{\mathbf{E}}_{\mathbf{x}} = \vec{\mathbf{E}}_{\mathbf{y}} $	+90 degrees

If δ equals ±90°, the ellipse is oriented with its major and minor axes aligned with the x and y coordinate axes. Under these conditions, if $E_x > E_y$, the major axis is $2E_x$ and the minor axis is $2E_y$. If $E_x = E_y$ the ellipse degenerates into a circle. If phase is negative (positive) the sense of rotation is clockwise (counterclockwise) in the z = 0 plane, looking in the direction of propagation, and is called right-handed (left-handed).

4.0 AXIAL RATIO, TILT ANGLE, ELLIPTICITY ANGLE The ratio of the major axis to the minor axis is called the axial ratio (r), which is a frequently used parameter for characterizing

polarization. The second parameter used in conjunction with the axial ratio to characterize a polarization is the sense of rotation. The final parameter needed to fully define the polarization of a plane wave is the orientation of the major axis with respect to the coordinate system. This parameter is called the tilt angle (r).

Figure 5 shows the major and minor axes of an elliptically polarized field. The tilt angle is also indicated. For consistency, the value of the tilt angle is limited to the range

$$-90 < r < +90$$
 (6)

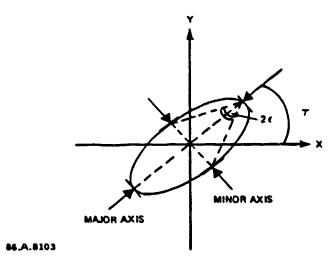


Figure 5. Relationship between Major and Minor Axes, Tilt Angle, and Ellipticity Angle

Figure 5 defines an alternate parameter to the axial ratio. The ellipticity angle (ϵ) is simply

5.0 ORTHOGONAL POLARIZATIONS

Two polarizations are said to be orthogonal if, and only if, their axial ratios are equal and their tilt angles differ by 90 degrees. 9 Any polarization can be thought of as the superposition of two arbitrary, elliptical polarizations. Equations have been derived to describe polarized fields in terms of the following orthogonal pairs:

Left-hand/Right-hand Circular

Horizontal/Vertical

Left/Right Slant Linear (±45 slant)

General Case of Orthogonal Elliptical Polarizations

The following discussion will focus on the horizontal and vertical pair.

6.0 POWER DENSITY AND EFFECTIVE VALUES

If two fields are orthogonal, the sum of the powers contained in the two fields is equal to the total power in the field. Given orthogonal linear polarizations in the x and y directions, the total power density in the wave can be expressed as

$$S_{w} = S_{x} + S_{y} \tag{8}$$

where

$$S_{x} = \frac{E_{x}^{2}}{\zeta} , \qquad (9)$$

$$S_{y} = \frac{E_{y}^{2}}{\zeta}, \qquad (10)$$

and

$$S_{W} = \frac{E_{W}^{2}}{\zeta} \tag{11}$$

 E_{x} , E_{y} , and E_{w} are the effective values of the fields. For linear polarizations the effective value of the field is 0.707 times the peak value. For circular polarizations the effective and peak field values are equal.

7.0 POINCARÉ SPHERE

Poincaré used the relationship in equation (8) to construct the unit sphere shown in Figure 6. The Poincaré Sphere 11 is a very useful graphical aid in visualizing polarization relationships. Poincaré showed that the polarization of a wave can be represented by a unique point on the surface of the sphere. The Poincaré sphere can be used to express the results of a polarization measurement, rather than specifying the shape and orientation of the polarization ellipse.

Orthogonal polarizations are located at opposite poles of the sphere. The sphere in Figure 6 is oriented such that the circular

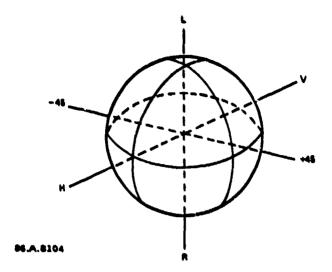


Figure 6. The Poincaré Sphere

polarizations are located at the North and South poles. The family of linear polarizations are located on the equator. The mutually orthogonal axes of the sphere represent the (L,R), (H,V), and (± slant) polarizations,

Defining a point on the surface of the sphere can be done in relation to any of three spherical coordinate systems, although one will be more appropriate for a specific measurement technique than others. The polar angle with respect to each axis is determined by the corresponding polarization ratio. The polarization ratios 12 are defined as

$$\rho = \tan \gamma = \frac{E_R}{E_L}$$
 (circular polarization ratio), (12)

$$\rho_{L} = \tan \alpha = \frac{E_{V}}{E_{H}}$$
 (linear polarization ratio), and (13)

$$\rho_{\rm D} = \tan \beta = \frac{E_{\perp}}{E_{\perp}}$$
 (diagonal polarisation ratio) (14)

where E_R and E_L are the effective values of the right-hand and left-hand circular components of the electric field, E_V and E_H are the effective values of the vertical and horizontal components, and E_- and E_+ are the effective values of the -45 and +45 slant-linear components, respectively. The polarization ratio is an indication of the relative contributions of two orthogonal components of a polarized wave.

The longitude of a point on the sphere about a particular axis is the phase angle by which the component in the numerator of the polarization ratio leads the component in the denominator. The polarization ratio together with the corresponding phase angle uniquely specifies a polarization.

8.0 THE POLARIZATION BOX

The mutual consistency of the three spherical coordinate systems is confirmed by the polarization box, ¹³ which is shown in Figure 7. The polarization box is inscribed inside the Poincaré Sphere. It is a graphical aid to understanding the relationships between the three basic sets of polarization components.

The point W on the surface of the Poincaré Sphere is located at the corner of the polarization box opposite the corner located at

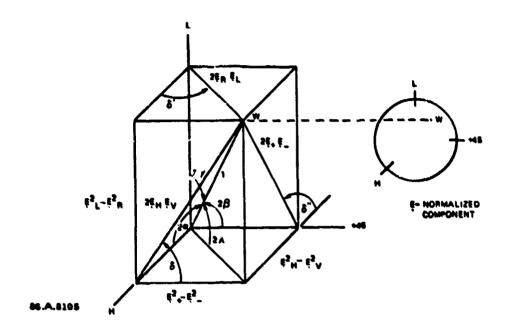


Figure 7. The Polarization Box

the origin. The three axis form the three edges of the box that intersect at the origin. Specifying the dimensions of the polarization box is equivalent to specifying the polarization.

9.0 POLARIZATION MEASUREMENT TECHNIQUES

The polarization box may be described in several ways. The method of description usually depends on the actual technique used to measure the polarization. The first manner in which the box can be defined is by specifying its three dimensions (i.e., length, width, and height). These dimensions are found directly by measuring the normalized, effective values of the six degenerately polarized components. In other words, the lengths of the three sides are given by

$$E_L^2 - E_R^2, \tag{15}$$

$$E_{V}^{2} - E_{H}^{2}$$
, and (16)

$$E_{-}^{2} - E_{+}^{2}$$
 (17)

To measure the contributions of all six cardinal polarizations would require an antenna array with all six receive polarizations available.

Another way to define the polarization box involves specifying the three longitudinal angles about the axes, which are found directly be measuring the phase angles between the same three orthogonal pairs used above. This technique requires the use of the same antenna array with multiple receive polarizations.

Finally, the three polar angles found from the polarization ratios (equations 12, 15, 14) can be specified to define the polarization box, but the direct measurement of the polarization ratios also requires the redundant antenna array described above. Fortunately, it is possible to synthesize the responses of all six cardinal polarizations using only two orthogonal antennus by passing the received signals through the appropriate phase shifting networks. Alternatively, it is possible to calculate the responses of an orthogonal pair of feeds from the amplitude and phase

information extracted from a different orthogonal pair. The inherent relationship between the basic sets of polarization components is represented by the polarization box itself.

To find the lengths of the remaining sides of the polarization box given only the length of one side (which can be measured directly using only two orthogonal antennas) and the longitudinal angle about that side at which the point W exists (which is equal to the phase angle between the responses of the two orthogonal antennas used to measure the length of the side) requires simple geometry. In fact, any of the parameters of the polarization box can be calculated from this information. This allows simplification of the antenna array for purposes of polarization analysis, but increases the requirements of the data processing portion of the polarization measurement system.

The relationship of the polarization box to the tilt angle, sense of rotation, and axial ratio is straightforward. The tilt angle 14 (7) is proportional to the phase (8') between the left and right circular components of the field, as given by the equation

$$\tau = \frac{\delta'}{2} \tag{18}$$

This phase angle can be measured directly or can be calculated using the geometry of the polarization box. The sense of rotation can be found from the circular polarization ratio, which was

defined in equation 12. If the circular polarization ratio is greater than unity, the sense of rotation is clockwise looking in the direction of propagation (right-hand sense). If ρ is less than one, the sense is left-hand. If the orthogonal elements used in the antenna array are not circular, the circular polarization ratio can be calculated from the relationships described above.

The axial ratio is also related to the circular polarization ratio by the equation

$$\mathbf{r} = \frac{\rho + 1}{\rho - 1} \tag{19}$$

10.0 ACCURACY OF POLARIZATION MEASUREMENTS

Jensen¹⁵ derived a general expression for estimating the errors in polarization measurements on the basis of the relative power of an error signal. If the complex vector \vec{E} denotes the electric field of a received wave, and $\Delta \vec{E}$ the limit of error involved with the measurement of \vec{E} , then \vec{E} + $\Delta \vec{E}$ represents the actual measurement result.

If the polarization \vec{E} is represented by a point D on the surface of the Poincaré Sphere, and the polarization of $\vec{E} + \Delta \vec{E}$ by the point T, then the angular distance between D and T reflects the measurement error. Assuming that the power of the error signal $\Delta \vec{E}$ relative to the power of \vec{E} is known to be less than unity and given by

$$p = \frac{|\Delta E|^2}{|E|^2} \tag{20}$$

it can be shown that the upper bound value of V, the angular error, is given by

$$V_{\text{max}} = 2 \arcsin \left(\sqrt{p} \right)$$
 (21)

If D represents the polarization of the wave, then the measured polarization will be represented by a point T on the sphere located within the circular area Ω , which is characterized by a maximum angular deviation from D equal to \mathbf{v}_{max} , as shown in Figure 8.

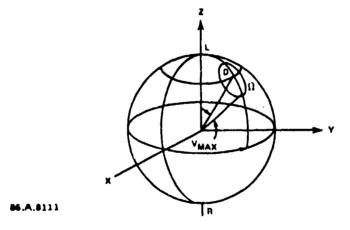


Figure 8. Uncertainty of Polarization Measurements

The size of the circular area Ω on the surface of the Poincaré Sphere can be specified for a particular measurement if the received power level, and the errors in measured parameters, are known. The angular error in a polarization measurement can then

be translated into uncertainties in the reported tilt angle, ellipticity and sense using the geometric relationships of the polarization box.

11.0 POLARIZATION MEASUREMENT SYSTEM

The polarization measurement system discussed in the following pages is based on Watkins-Johnson Company's extensive experience in the design, production, and support of microwave receiving and analysis systems. It provides a powerful, reliable and accurate system in a compact, cost-effective package.

The block diagram of the system is presented in Figure 9. The antenna is a broadband, dual-polarized horn housed in a protective radome. Two orthogonal ports (horizontal and vertical polarizations) collect signals in the 2 to 18 GHz frequency range.

The signals pass through matched RF Distribution paths to a spread-spectrum multiplexer, which is essential to the accuracy of the system. The multiplexing technique incorporated in this system allows signals from both ports to be received and analyzed simultaneously, on a pulse-by-pulse basis without introducing the detrimental effects of separate tuner channels. By encoding the received signals at the antenna output and downconverting through a single tuner, the amplitude and phase relationships of the signals are preserved, allowing a more accurate measurement of polarization than is possible with conventional systems.

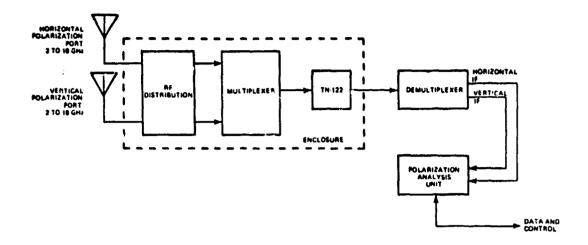


Figure 9. Signal Polarization Measurement System Block Diagram

The RF Distribution components, multiplexer, and wideband superheterodyne tuner are contained in an environmentally protected enclosure. The proximity of the multiplexer and tuner to the antenna permits the simplification of the RF Distribution by eliminating the need for preamplifiers and their inherent tracking problems.

The TN-122 wideband tuner downconverts the multiplexed signal to a 1 GHz IF. The signal travels through a single IF cable to the demultiplexer, thus avoiding the problems of matching a pair of long IF cables and maintaining the match over time. At the demultiplexer the individual channels are recovered for processing by the Polarization Analysis Unit, which is interfaced to the host system computer.

The spread spectrum multiplexing technique was adapted from the WJ-1988 Monopulse DF System. 16 The frequency multiplexing of two channels into one tuner is accomplished by applying a different BPSK modulation code to each of the channels prior to combining. The mixers in the multiplexer unit are driven with a maximally linear sequence similar to that shown in Figure 10. The sequence simulates pseudo-random noise but is repetitive in nature and can be reconstructed at the demultiplexer to recover the information in the individual channels.

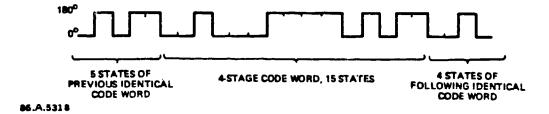


Figure 10. Maximally Linear Sequence

The 31 bit sequence used in this system is generated by a set of shift registers with the appropriate feedback. The circuitry used to generate the code consists of high speed ECL logic. The code rate is 240 MHz.

The autocorrelation property of maximally linear sequences results in noise and spurious signals unless the applied code in the demultiplexer is in time synchronization with the delayed signal.

The resultant channel to channel isolation is proportional to the length of the code, as given by the equation

Isolation =
$$20 \log (code length)$$
 (22)

For a 31 bit code word, the isolation is approximately 30 dB.

The spectrums of the encoded signals are shown in Figure 11. The input signals are displayed in the top photo. After passing through the multiplexer, the bandwidths of the individual channels are many times those of the original signals. The spectral distribution has a $\sin(x)/x$ distribution, with a main lobe width of twice the code rate, or 480 MHz. The spectral line spacing is equal to the code rate divided by the code length. It is interesting to note that the balanced nature of the code sequence results in the suppression of the carrier frequency.

At the multiplexer, the two modulators are driven with timeshifted versions of the same code sequence. As long as the time shift is greater than 1 bit, the two channels are orthogonal and can be combined without unwanted interferometry effects. The combined signals are shown in the center photo of Figure 11.

The 500 MHz bandwidth of the TN-122 tuner is required to support the combined signals. The requirement for a full code word to be applied to a pulse for full isolation sets a limit on the

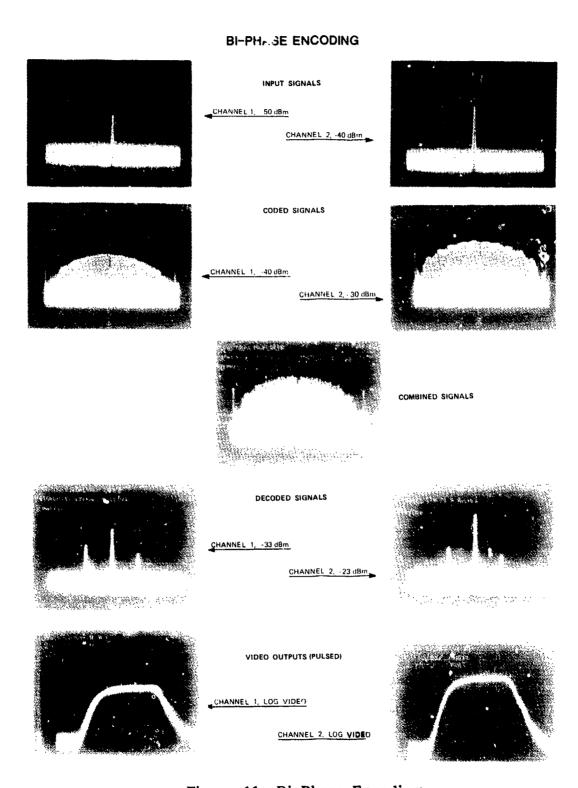


Figure 11. Bi-Phase Encoding

effective bandwidth of the system. The minimum pulse width that the system can process is therefore 135 ns.

The composite signal is downconverted and routed to the demultiplexer. The signal is split and routed to two demodulators. At this point the identical code sequence must be applied to the divided signals in the same time relationship as in the multiplexor to recover the individual channels, as shown in the lower photographs in Figure 11.

The outputs of the demultiplexer are two IF signals with the same amplitude and phase relationships as the original received signals. The preservation of these relationships is critical to the polarization measurement process, as was shown above. The observed performance of the multiplexing/demultiplexing chain is quite good. The gain tracking is on the order of 2 dB, and the phase tracking is 3 degrees RMS.

The Polarization Analysis Unit (Figure 12) converts the IF signals to log video for amplitude measurements and processes the iF to recover the phase information. The CPU accepts control information from the main system as well as information regarding the amplitude and PRI of the signal of interest. The main system directs the TN-122 to the signal frequency and directs the polarization measurement antennas to the correct azimuth. The CPU then adapts its processing threshold accordingly and finds the

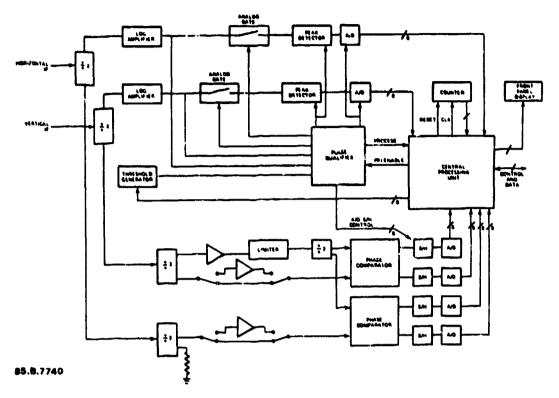


Figure 12. Polarization Analysis Unit

pulse train of interest using the PRI information from the main system.

After locking onto the correct pulse train, the Polarization Analysis Unit begins measuring relative amplitude and phase of each incoming pulse. The measured data is analyzed by the numerical data processor. The polarization data is returned to the main system and presented to the operator via the front panel display.

The Polarization Analysis Unit is capable of returning polarization information in several ways. The tilt angle, axial ratio, and sense

can be returned, or the contributions of the (H,V), (RHC, LHC), (+45, -45) components can be calculated. The degree of polarization can also be calculated for the primary polarization component.

Calculations of the polarization parameters are based on the relationships presented in the preceding paragraphs. Having measured the amplitudes of the horizontal and vertical components and the phase between the two fields allows the calculation of the dimensions of the polarization box. The dimensions of the polarization box in terms of the measured parameters are shown in Figure 13.

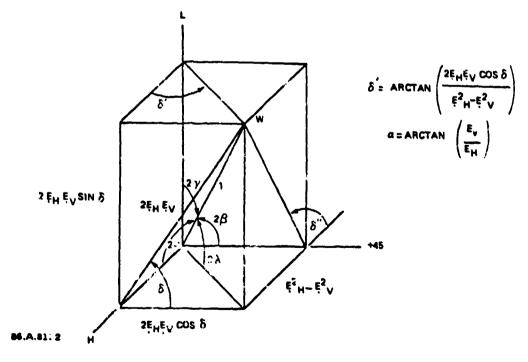


Figure 13. The Polarization Box in Terms of Measured Amplitudes and Phase of Horizontal and Vertical Components

The tilt angle is related to the polarization box by the equation

$$\tau = \frac{\delta'}{2} \tag{23}$$

Unfortunately, the phase angle δ' is not directly measured by this system. However, the angle δ' can be calculated from the equation

$$\delta' = \arctan \left(\frac{2E_{H}E_{V}\cos \delta}{E_{H}^{2} - E_{V}^{2}} \right)$$
 (24)

The axial ratio was defined in equation 19 in relation to the circular polarization ratio. Although ρ is not measured in this system, it is easily calculated 17 using the equation

$$\rho = \left(\frac{1 - X_L \sin \delta}{1 + X_L \sin \delta}\right)^{\frac{1}{2}}$$
 (25)

where

$$X_{L} = \frac{2 \rho_{L}}{1 + \rho_{L}^{2}}$$
 (26)

The sense of rotation depends on whether ρ is greater than or less than unity, as discussed above.

Once the dimensions of the polarization box have been found, it is possible to identify which of the degenerate polarizations (H, V, RHC, LHC, +45, or -45) the received signal most closely resembles. This information can also be presented as output data. The degree to which this component dominates can be calculated. The degree of circular polarization 18 is defined by the equation

$$CP = E_L^2 - E_R^2 = 2E_H E_V \sin \delta$$
 (27)

where CP = +1 for a purely LHC polarized wave and -1 for a purely RHC polarization. The degree of linear polarization can be defined in a similar manner by the equation

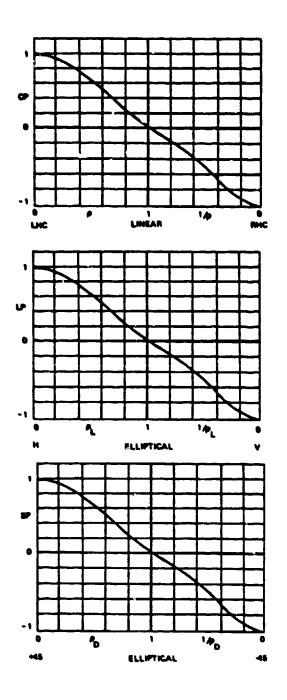
$$LP = E_{H}^{2} - E_{V}^{2} \tag{28}$$

where LP = +1 for a purely horizontal polarization and -1 for a purely vertical polarization. Finally, the degree of slant polarization is given by the equation

$$SP = E_{+}^{2} - E_{-}^{2} = 2E_{H}E_{V} \cos \delta$$
 (29)

where +1 indicates a purely +45 slant linear polarization and -1 indicates a purely -45 slant linear polarization. The astute observer will realize that these quantities are merely the lengths

of the appropriate sides of the polarization box. The curves for the degree of polarization can be plotted as shown in Figure 14.



66.A.8110

Figure 14. Degrees of Polarization versus Polarization Ratio

12.0 SUMMARY

Precision polarization measurements would be impossible without the excellent amplitude and phase tracking characteristics of the orthogonal antennas employed in this system. Combining this performance with careful matching of signal paths to the multiplexor ensures the accuracy of each measurement.

The availability of precision polarization measurement equipment will allow systems designers to exploit all signal parameters in the pursuit of system optimization. However, it is also imperative that systems designers become aware of the potential that polarimetry holds for system enhancement. Research into applications for polarization measurement equipment must continue if strides are to be made in improving the capabilities of microwave systems.

13.0 CITED REFERENCES

- Poelman, A.J. (1976) Reconsideration of the Target Detection
 Criterion Based on Adaptive Antenna Polarizations, <u>AGARD</u>
 <u>Conf. Proc. no. 197 on New Devices, Techniques and Systems in Radar, the Hague, Neth., pp. 30/1-15.</u>
- Cloude, S.R. (1983) Polarimetric Techniques in Radar Signal Processing, <u>Microwave Journal</u> 26 (No. 7):119-127.
- Dintelmann, F. (1981) 12-GHz Slant-path Propagation Measurements, <u>Ann. Telcommun.</u> (France), 36 (No. 1-2): 95-101.

THE STATE OF THE PROPERTY OF THE STATE OF TH

- 4. Dearhold, D.W. and McSpadden, W.R. (1973) Electromagnetic Wave Propagation, McGraw-Hill, NY, pp. 166-189.
- 5. Ibid, pp. 179-182.
- 6. Rao, N.N. (1977) Elements of Engineering Electromagnetics,
 Prentice-Hall, Inc., Englewood Cliffs, NJ, pp. 18-21.
- 7. Hill, J.E. (1979) Antenna Polarization, Watkins-Johnson Company Tech-Notes 6 (No. 4):6-8.
- 8. Hollis, J.S.; Hickman, T.G. and Lyon, T.J. (1970) Microwave Antenna Measurements, Scientific Atlanta, Atlanta, Ceorgia, p. 3-3.
- 9. Ibid, pp. 3-17.
- 10. Ibid, pp. 3-17.
- 11. Poincaré, H. (1889) Theorie Mathematique de la Lumiere, pp. 282-285.
- 12. Hollis, Op Cit, pp. 3-25.
- 13. Hollis, Op Cit, pp. 3-24.
- 14. Hollis, Op Cit, pp. 3-6.
- 15. Jensen, F. (1976) Limits of Accuracy in Antenna Polarization

 Measurements, IEEE Conf. on Precision Electromagnetic

 Measurements, Boulder, CO, July, 1976 pp. 60-62.
- 16. Klaus, D.E. and Hollis, R.P. (1982) Monochannel Direction
 Finding Improves Monopulse Technique, <u>Defense Electronics</u>
 14 (No. 3):35.
- 17. Hollis, Op Cit, pp. 3G-1 5.

- 18. Hollis, Op Cit, pp. 3-29.
- 19. Jasik, H. ed. (1961) Antenna Engineering Handbook,

 McGraw-Hill, NY, pp. 34-28 32.





Doren W. Hess Scientific-Atlanta, Inc.

Abstract

Over the past decade spherical near-field measurements have made the transition from research to application. Based upon spherical modal expansion and a port-to-port transmission equation, the spherical near-field technique utilizes sophisticated mathematical processing to solve the practical problem of obtaining antenna pattern measurements in a confined space. Conventional hardware — consisting of rotary test positioners, signal sources and receivers augmented by digital control electronics and minicomputers — now makes spherical near-field measurements practical by automation.

Recent developments in spherical near-field software architecture have expanded the basic scanning feature to include dual-ported scanning, probe pattern and probe polarization correction, three antenna polarization measurements, gain comparison measurements and correction for thermal drift of the system.

In this presentation I review the theoretical basis for the method and describe these more advanced features.

The text of this article originally appeared in the March 1985 issue of Microwave Systems News entitled "Spherical Near-Field Antenna Measurements Improve Through Expanded Software Features" by myself and co-authors J. R. Jones, C. Green, B. Melson and J. Proctor.

INTRODUCTION

Over the past two years a development program at Scientific-Atlanta has supported work on an expanded software package for performing spherical near-field measurements with the mini-computer based Model 2022A Automatic Antenna Analyzer. In this article we review the features of this expanded software.

The original spherical near-field software package for the Model 2022 Antenna Analyzer was designed to support non-probe-corrected single channel near-field measurements. With the introduction of the Model 1780 three channel receiver and it's inclusion in the Model 2022A Antenna Analyzer, the spherical near-field package was expanded to provide for dual ported near-field probes. Now, as a result of the latest software improvements, the following features are included.

• Gain Comparison Measurement

- Three-Antenna Polarization Measurement
- Probe-Polarization-Corrected Measurements
- Probe-Pattern-Corrected Measurements
- Dual Port Probe Correction by Channel Balancing
- Thermal Drift Corrected Measurements
- Polarization Based Output Presentation

Details of these features are described individually later.

An easy way to understand spherical near-field measurements are is to first think in terms of conventional far-field measurements. On a far-field range a source antenna illuminates an antenna under test with a spherical wave whose phase front is nearly planar and whose amplitude distribution is nearly constant across the aperture.

On a far-field range the test antenna is placed on a two-axis positioner and the source antenna is placed on a single polarization axis. The two-dimensional far-field pattern is recorded as the test antenna is turned in step-scan fashion through its two axes. The angular readout values correspond to the ϕ and θ axes of the standard spherical coordinate system. As the two-axis rotary motion occurs the range source antenna scans over an imaginary

THE REPORT OF THE PROPERTY OF

spherical surface fixed to the test antenna. (The radius of the imaginary surface corresponds to the length of the range). Far-field testing is properly thought of as spherical far-field scanning.

Spherical near-field testing is simply the far-field configuration with the range length collapsed to a small distance, usually about one test antenna diameter. With the range length reduced, measurements can be made indoors in an anechoic chamber where laboratory conditions exist. This gives near-field testing a great practical advantage over far-field testing. The far-field pattern is obtained by a mathematical computation, the near-field to far-field transform.

Spherical near-field testing differs from far-field testing in several important aspects. First, phase measurements must be made; amplitude alone is not adequate. Second, solid-angle scans must be made; principal planes alone measured in the near-field are not adequate to yield the correct principal planes in the far-field. Third, significant signal processing calculations are required to obtain the far-field. These features require the sophistication of automatic data acquisition and data management available in the Scientific-Atlanta 2022A Antenna Analyzer.

THE MATHEMATICAL BASIS OF SPHERICAL NEAR-FIELD SCANNING

The mathematical basis of spherical near-field scanning is the reduced transmission equation, usually written in the following notation:

$$W(kr_{o}; \phi_{o}\theta_{o}\chi_{o}) = \sum_{\substack{smn \\ \sigma\mu\nu}} R_{\sigma\mu\nu}^{i} C_{\sigma\mu\nu,s\mu n}(kr_{o}) D_{\mu m}^{(n)}(\phi_{o}\theta_{o}\chi_{o}) T_{smn}$$

where:

$$W(kr_o;\phi_o,\theta_o,\chi_o) = b_o'/a_o$$

is the relative received phasor at the port of the probe antenna; \mathbf{a}_0 is the input phasor at the port of the antenna under test and \mathbf{b}_0^* is the output phasor from the probe.

The output of the probe depends parametrically on the frequency and the range length:

 $k = 2\pi/\lambda$

r = range length

The output of the probe depends on the position of the probe on the scanning sphere and the orientation of the probe in polarization; these physical quantities are:

- ϕ_{O}^{-} azimuthal angle for probe position
- θ_{a} polar angle for probe position
- χ_{Ω}^{-} polarization angle for probe orientation

(These are in fact the Euler angles that relate the probe and test antenna coordinate systems' rotational orientation).

The two angles ϕ_0 and θ_0 are the turning angles at the test antenna on the two-axis positioner. To within an offset they are the values read on the synchro or encoder display of the test positioner. χ_0 is the polarization angle of the range-source-probe antenna; to within an offset it too is the value of the synchro readout. The right hand side of the transmission equation contains scattering matrix elements for both the probe antenna and the test antenna.

- T = transmitting characteristics of the test antenna's general scattering matrix
- R' = receiving characteristic of the probe antenna's general scattering matrix

These quantities can also be thought of as modal expansion coefficients. They characterize the transfer of excitation to or from the port of their respective antenna to or from free space spherical modes labelled as follows:

- s.g = TE or TM label
- m, p = azimuthal label
- n,v = principal label

The indices n and m occur in the associated Legendre polynomials which appear in the spherical coordinate solutions to the Maxwell equations. The TE, TM index is required to distinguish different vector solutions.

The right hand side of the transmission equation also contains geometrical functions which relate the modal coefficients or scattering matrix elements in different coordinate systems.

$$D_{um}^{(n)}$$
 $(\phi_0, \theta_0, \chi_0)$ = Rotational Transformation Matrix

$$C_{\sigma\mu\nu,s\mu\eta}(kr_0)$$
 = Translational Transformation Matrix

These functions are calculable and are evaluated in the process of the spherical near-field to far-field transform.

If one knows both $R'_{\sigma\mu\nu}$ for the probe antenna and T_{smn} for the test antenna then the response of the probe b_0^r to an input a_0 at the test antenna can be computed using the transmission equation. Unfortunately this can be done for an unknown test antenna only after its characteristic has been determined. To get the transmitting characteristic for an unknown antenna, one measures b_0 as a function of sampled values of ϕ_0,θ_0,χ_0 and by inverting the transmission equation gets the T_{smn} . (It is assumed that $R'_{\sigma\mu\nu}$ for the probe are already known from a preliminary measurement step and that C and D are known from calculation.) Having obtained T_{smn} , b'_0 may be finally calculated for a far-field value of r with a dipole probe.

Thus the necessary ingredients of the spherical near-field measurement process are the capability of measuring and storing the probe output voltage b_0 ' as a function of scanning position ϕ_0,θ_0,χ_0 and of reducing the data thus obtained to yield the equivalent far-field. The probe's far-field pattern can be measured in a preliminary step on the same range on which the test antenna near-field data is measured. Its modal coefficients or receiving scattering matrix elements are obtained from its measured pattern and must be stored until utilized in a test antenna computation.

The features of automatically acquiring spherical coordinate scanning data, of storing data, of performing digital calculations with the data and of presenting the results in usable hardcopy formats are fundamental to the Scientific-Atlanta 2020 Antenna Analyzer design. The implementation of a software system for spherical near-field scanning was straightforward given the pre-existing architecture of the far-field measurement software.

The main addition to the software architecture for the expanded spherical near-field system has been the files for storing spherical scattering matrix transmitting and receiving coefficients. Files have also been added to store data from dual-ported probes' channel balancing procedures, from drift correction procedures, and from gain transfer measurement procedures.

SPHERICAL MEAR-FIELD FEATURES OF THE ANTENNA ANALYZER

Spherical Near-Field Gain Comparison Measurements

Gain measurements in conjunction with near-field scanning can be carried outly either of two methods - the gain standard substitution method or the range insertion loss method. The gain measurement technique implemented in the Scientific-Atlanta Antenna Analyzer is the gain standard substitution method.

The advantages of the gain standard substitution method are that the gain of the probe antenna does not have to be known and that the range does not have to be "short circuited" by use of a long cable to determine its insertion loss. Furthermore, the gain standard method makes use of existing standard

gain antennas whose gains are known to within 0.25 to 0.50 dB. In the range insertion loss method, the insertion loss of the near-field range (typically 20 to 40 dB) must be measured to within the accuracy tolerated by the error budget (usually 0.25dB). This restriction requires additional calibration of a detection or receiving system. The gain standard substitution method, although it usually requires the scanning operation to be carried on the gain standard as well as the test antenna, is readily implemented and bears a strong resemblance to the technique used on far-field ranges.

Recall that for the far-field case, the operating equation for gain measurement by comparison to a gain standard is:

$$G_{AUT} = G_{STD} \frac{P_r^{AUT}}{P_r^{STD}}$$

where $G_{\rm AUT}$ and $G_{\rm STD}$ are the gains of the unknown test antenna and to gain standard, respectively. Here $P_{\rm r}^{\rm AUT}$ and $P_{\rm r}^{\rm STD}$ are the power levels received under polarization matched conditions when the two antennas are illuminated by plane waves of equal power density. (Gain, although it is defined upon the assumption that an antenna is transmitting, is usually measured with the antenna receiving.) To understand how gain comparison measurements are done with spherical near-field scanning, one can simply take the pure far-field case and rewrite it.

The operating equation for spherical near-field gain comparison measurement, written in terms of power quantities is in simplified form:

$$G_{AUT} = G_{STD} \frac{P_r^{AUT-FF}}{P_r^{AUT-NF}} \frac{P_r^{AUT-NF}}{P_{INT}} \frac{P_{INT}}{P_r^{STD-NF}} \frac{P_r^{STD-NF}}{P_r^{STD-FF}}$$

The right hand side consists of the gain of the standard and four, rather than one, gain comparison factors. The second and third of the four factors can be combined into one factor if desired, which is the comparison between the power received under identical near-field illumination by the test antenna and the gain standard; at times it is convenient to use an intermediate reference level to assist in the comparison measurement when one passes between the test antenna and gain standard level comparison. Hence the reason for two terms.

The first and fourth comparison terms relate the power levels received under near-field illumination to those received under far-field illumination; they are the near-field to far-field comparison terms. The equation used for the most general case of polarization correction and impedance mismatch correction is written in terms of field quantities rather than power quantities. In concept, it is identical to this.

In spherical near-field scanning, one augments the scanning operation by making a comparison of the response of the test antenna under illumination by the range-source-probe antenna to an intermediate power level which may be the APC signal level on the receiver. In the 2022A Antenna Analyzer this comparison is stored in a computer disc file. Previously this intermediate level has been calibrated by comparing the response of a gain standard antenna under identical illumination conditions, which result has also been stored in a file.

Scanning operations are carried out on both the gain standard antenna and the antenna under test. The initial points of the scanning operations are identical to the point on the patterns of the test antenna and gain standard where the comparison measurements were made. When identical transforms are computed to both antennas the points of interest in the far-field radiation intensity functions can be compared in level to the initial near-field points. These comparisons yield the near-field to far-field gain comparison terms in the equation. Thus a near-field gain measurement consists of a near-field scan plus a transfer measurement for both the test antenna and the gain standard.

In the 2022A Antenna Analyzer the gain of an unknown antenna is computed by a program that goes back to the data files where the requisite measurement data are stored. The value of the gain of the gain standard, the near-field comparison data, the near-field scanning data and the far-field radiation intensities for both antennas are all available once the procedures are carried out. The gain analysis program brings the data together for calculation in an equation that closely resembles the one above.

Polarization Measurements

Because electric field (and magnetic field) is a vector quantity, no antenna measurement is complete without a determination of the polarization characteristic of the field. Many antenna measurements which do not properly account for polarization suffer a lack of accuracy. Polarization is an important antenna parameter.

The usual method of polarization measurement is the polarization pattern Two antennas in their mutual far-field regions couple via the two orthogonal polarization components of a plane wave propagating along their A polarization pattern is made by rocating a linearly line of sight. polarized sampling antenna about the line of sight in the field of an unknown The peaks and nulls of the familiar pattern determine the axia! ratio and tilt angle of the field of the unknown. However, no sampling antenna is perfectly linear and the peaks and nulls of a polarization pattern are in truth only apparent ones; they are not the true values because of the finite axial ratio of the sampling antenna. To get at the true values from the measured data, one needs the polarization of the sampling antenna from a previous measured result. This process of correcting measured polarization data using the polarization of one antenna to obtain the true polarization of the other is called a two-antenna polarization transfer measurement.

In many cases where accurate polarization measurements are desired, the polarization of the sampling antenna needs to be measured as well. In this case, without a sampling antenna of known polarization, a three-antenna polarization measurement must be made.

The three antenna polarization measurement entails taking three unknown antennas and making three polarization patterns pair wise among the set. The three polarization patterns may then be analyzed for the true polarization characteristic of each of the three members of the set. (The method assumes that none of the three antennas is circularly polarized.) The three-antenna polarization measurement is a far-field measurement and is usually carried out on smaller antennas (such as near-field probe antennas). It is applied one

frequency at a time, although automatic systems make multiple frequency acquisition straightforward.

Once the polarization of a probe antenna is determined it may be utilized to perform a polarization-corrected pattern measurement, in which the polarization of the sampling antenna is taken into account and corrected for.

The expanded spherical near-field software package in the 2022A supports both two and three antenna polarization measurements. An acquisition routine for acquiring polarization patterns and a data reduction routine are included as features of the 2022A; these features are necessary for accurate cross-polarization measurements with spherical near-field scanning. These software routines permit users to calibrate probe antennas for later use in near-field scanning.

Probe-Pattern-Corrected Pattern Measurements

A probe that is used to measure the near-field of an antenna possesses a response which weights the field of the probe over its volume to produce a net signal. The manner in which the rest antenna near field is weighted can be removed from affecting the measured result by a process known as probe correction. Probe correction presumes that one knows the probe antenna characteristic in advance of the test antenna measurement and that this characteristic can be utilized to determine the far-field of the test antenna.

Probe correction in general can be broken into three categories which describe the degree of correction — in the order of increasing sophistication:

Oth order - No Probe Correction

1st order - Probe Polarization Correction

2nd order - Probe Pattern Correction

In the case of no probe correction, the probe is assumed to be an ideal elemental dipole which responds to the field at a point. Here no preliminary knowledge of the probe pattern is assumed. For probes which are highly linear, this is often a very acceptable approach.

In the case of probe polarization correction, the probe's polarization characteristic is assumed known and is modelled as a crossed dipole, as described earlier. The probe's polarization characteristic may have been determined either by a two-antenna or a three-antenna polarization measurement.

In the case of probe pattern correction, the complete pattern of the probe is assumed to be known by a preliminary pattern measurement. Usually the pattern will have been obtained in a polarization corrected measurement with a secondary probe whose polarization has been determined one step earlier.

In general, whether the probe correction is polarization correction only or a pattern correction, the probe pattern is represented by an expansion of spherical modes. The expansion of the probe pattern in modal coefficients is the key element by which pattern correction operates. For polarization correction only, the expansion is truncated abruptly, keeping only the dipole modes. For general pattern correction only enough modes are utilized to give the accuracy desired; too many modes appear to give difficulties. The modal coefficients are determined by applying the near-field to far-field transform in a specialized way, reducing the measured patterns to obtain them. Modal coefficients for the crossed dipole model are obtained by reducing polarization pattern data.

Probe pattern correction (over and above polarization correction) has been useful only for small probes that require only a few modes to represent their fields. It is important only when the probe is very close to the test antenna (within a few wave lengths).

In the 2022A Analyzer, probe patterns are acquired with the same data acquisition routine that is used to acquire test antenna data. A probe

pattern can be used to correct test antenna measurements once the pattern is reduced to receiving coefficients. This is done by the same spherical near-field subroutine that yields far-field transformed data.

Probe-Polarization-Corrected Pattern Measurements

Once the polarization of a probe antenna is known that information may be utilized to correct any pattern measurements made with that probe. This technique is termed probe polarization correction. It is extremely important in measurement of cross-polarized patterns in order to achieve accurate results. Probe polarization correction in spherical near-field scanning has application in the measurement of probe patterns and in the measurement of unknown test antennas.

It is well known that the response of an idealized elemental dipole antenna is directly proportional to the linear component of electric field at the location of the dipole. Furthermore, one knows that an elemental electric dipole produces a perfectly linearly polarized plane wave in its far-field at the peak of its pattern.

Analogously, the response of a coupled pair of crossed dipoles to an electric field will be a superposition of the responses of the crossed dipole elements to two orthogonal linear components of electric field. And, in the far-field of a crossed dipole pair that is transmitting, a superposition of two orthogonal linearly polarized plane waves will be produced. Intuitively, it is clear that the polarization characteristic of a probe antenna can be related to the equivalent exitation amplitudes of a pair of crossed dipoles. This approach is extremely useful in fitting probe polarization correction into the same framework as probe pattern correction to be discussed later.

Since a nonideal probe responds to both linear components of electric field one must utilize polarization correction if a pattern made with a nonideal probe can be modelled as a pair of crossed dipoles, one weakly coupled in comparison to the other. By using this approach, polarization correction of pattern measurements, either near-field or far-field, can be looked upon as a special case of probe correction.

Probe polarization correction is especially important in obtaining the patterns of primary probe antennas used in probe-pattern-corrected measurements. Usually the primary probe and a secondary probe whose polarization is then known can be utilized to make a polarization-corrected measurement of the pattern of the primary probe.

Probe polarization correction can also be applied to spherical near-field scanning measurements by making use of the crossed dipole model of the probe as an approximation to its modal expansion. Very often, polarization correction alone is adequate to give perfectly acceptable far-field patterns of an unknown test antenna.

Dual Port Probe Correction by Channel Balancing

The strict method of near-field scanning requires two scans of the measurement surface (one for each polarization). This approach has always given good results and is theoretically correct. However, electromagnetic technology has provided methods of fabricating dual-ported probe horns (now available in round waveguide) which permit both polarizations to be measured simultaneously in one scan. Probe horns have been developed which permit spherical near-field measurements to be made with dual-ported probe horns over half-octave bandwidths.

Each port of an ideal dual-ported probe couples to only one linear component of the field, and responds equally to equal field strengths. In reality, however, each port has different polarization responses and field strength responses.

Not only is the probe horn slightly imperfect but also the separate channels of the receiving system are imperfect. Different amplifier gains and different phase lengths of connecting cable require matching via a calibration procedure called channel balancing.

Channel balancing is carried out with a single ported utility antenna or a secondary probe whose polarization is known. The channel balancing antenna is mounted on the test positioner with the dual-ported probe mounted on the polarization axis of the range tower.

First the polarization characteristic of each port of the dual-ported probe can be found from a two antenna polarization transfer measurement if they are not already known. Then, since the polarizations of both the utility antenna and the ports of the dual-ported probe are known, the polarization efficiency factors in the far-field transmission equation can be evaluated.

The imbalance between the responses of the ports can be evaluated by copolarizing the utility antenna to each port separately and observing the receiver's response for each channel. The calculated polarization efficiency factors and the observed responses provide the information necessary to correct for the port imbalance and the receiving system imbalance.

In the 2022A Antenna Analyzer's new spherical near-field software this channel balancing procedure with polarization correction is carried out automatically with the measured data recorded and stored and the calibration performed in the process of the near-field to far-field transform.

Thermal Drift Correction

.

of the primary features of near-field scanning is the necessity of making phase measurements. Phase measurements on an antenna range are troubled by the necessity of using long cable runs, as compared with bench measurements. RF cable tends to be sensitive to changes in temperature as small as several degrees Fahrenheit, which causes a drift in the phase measurements. This drift can be removed from the measurement if it is monitored during the scanning process.

The 2022A Antenna Analyzer corrects for thermally induced drift by a method called the return-to-peak method. In this technique the probe is returned periodically during scanning to the near-field peak. The same point is remeasured upon each return and the variation in phase and amplitude of the

peak value is used to produce a correction factor which is applied to each data point of the near-field scan.

The accuracy of the correction is determined by the amount of drift which occurs, the mathematical form of the true drift, the frequency of the returns to the near-field peak and the accuracy with which the peak point can be measured.

Typically one might set up an antenna measurement to record data on a near-field sphere every 1 degree in ϕ_0 and θ_0 , the polar and azimuthal spherical angles respectively. Scanning ϕ_0 and stepping θ_0 gives a raster of data consisting of successive scans each taking several minutes. Provided that the thermal drift can be linearized appropriately over the time required for a few scans, one would choose to return to the peak every five or ten scans. Experience with the particular range often yields the knowledge of how often returns ought to be made.

Polarization-Based Output Presentation

It has long been a frustating fact of life that antenna engineers must deal with the various polarizations that the electromagnetic field offers. Quite often an engineer will wish to make measurements on a circularly polarized antenna on a range equipped with linearly polarized source antennas. Correction for imperfectly polarized source antennas has consistently been a problem for those interested in optimum measurement accuracy. Conversion between different polarization formats has also been a problem.

The 2022A Antenna Analyzer Spherical Near-Field software permits the far-fields to be presented in linear and circular polarization formats. The linear polarization formats can be referred either to the $\theta-\phi$ grid system of reference directions or the Ludwig system of reference directions. Furthermore the far-field radiation intensity function can be presented and plotted just as if it had been measured directly. Also, Poincare' sphere parameters can be plotted versus position on the radiation sphere.

The output presentation features of the spherical near-field software package are sufficiently general that they will be appropriate for any particular antenna.

CONCLUSION

Whereas the original 2022 Antenna Analyzer Spherical Near-Field Software package was restricted to the non-probe-corrected case, the new 2022A software is designed for correction of all recognizable errors for which solutions exist. Among the errors not yet correctable are (1) errors due to unrestricted probe patterns which contain azimuthal index values other than ±1 (2) probe position errors (3) standing waves between the probe and test antenna and (4) extraneous reflection signals. It is likely that correction procedures for these unsolved problems will also be found and implemented in future generations of Antenna Analyzers.

In the meantime the 2022A Antenna Analyzer and the expanded software option -08A for spherical near-field measurements enables industrial users to make use of the advantages of near-field testing.

Swept Frequency Technique for Dispersion Measurement of Microstrip Lines

Richard Q. Lee Lewis Research Center Cleveland, Ohio

Prepared for the 1986 Antenna Applications Symposium cosponsored by the University of Illinois and the Rome Air Development Center Monticello, Illinois, September 17-19, 1986



SWEPT FREQUENCY TECHNIQUE FOR DISPERSION MEASUREMENT OF MICROSTRIP LINES

Richard Q. Lee
National Aeronautics and Space Administration
Lewis Research Center
Cleveland, Ohio 44735

1. SUMMARY

Microstrip lines used in microwave integrated circuits are dispersive. Because a microstrip line is an open structure, the dispersion can not be derived with pure TEM, TE, or TM mode analysis. Dispersion analysis has commonly been done using a spectral domain approach, and dispersion measurement has been made with high Q microstrip ring resonators. Since the dispersion of a microstrip line is fully characterized by the frequency dependent phase velocity of the line, dispersion measurement of microstrip lines requires the measurement of the line wavelength as a function of frequency. In this paper, a swept frequency technique for dispersion measurement is described. The measurement was made using an automatic network analyzer with the microstrip line terminated in a short circuit. Experimental date for two microstrip lines on a 10 and 30 mil. Cuflon substrates were recorded over a frequency range of 2 to 20 GHz. Agreement with theoretical results computed by the spectral domain approach is

good. Possible sources of error for the discrepancy are discussed.

2. INTRODUCTION

Microstrip lines used in microwave integrated circuit network and device designs are very attractive because of low cost and easy fabrication. Unlike ordinary transmission lines of TEM mode, the analysis of a microstrip line is very complex and requires the hybrid mode expansion of both the TE and TM modes to account for the fringing. Furthermore, a microstrip line is more difficult to design because of its dispersion characteristics. The dispersion characteristics of microstrip lines have been investigated experimentally and theoretically. 1,2 Dispersion analysis has commonly been done using a spectral domain approach, 3 and dispersion measurements have been made with a high 0 microstrip ring resonator. This paper describes a swept frequency technique for dispersion measurements. The technique is applied to analyze the dispersion characteristics of an open microstrip structure as shown in Fig. 2. The measured results are compared to the analytical results computed by a spectral domain method.

3. DISPERSION MEASUREMENT

Since the dispersion of an open microstrip line is fully characterized by its frequency dependent phase velocity, dispersion measurement of the microstrip line requires the measurement of the line wavelength as a function of frequency. Troughton²

first proposed a technique for measuring wavelengths and disperison characteristics using a microstrip ring resonator. By capacitively coupling RF power into and out of the ring resonator with 50 Ω transmission test probes, the line wavelength is determined by measuring the transmitted power as a function of frequency. The effective dielectric constant at each resonance frequency, f, is obtained from

$$\epsilon_{eff} = \left(\frac{nc}{2\pi rf}\right)^2$$

where c is the velocity of light and n = 1, 2, 3, ... The mean radius, r, of the ring is approximated from Wheeler's results which are valid for frequencies below 6 GHz. Although the ring resonator approach eliminates errors in determining the electrical length due to fringing, the curvature of the ring and the coupling probes may introduce errors in the resonance frequency measurements. At high frequencies, the validity of Wheeler's theory, for approximating the mean radius r is also questionable. In fact, large discrepancies between calculated and measured results have been reported. The swept frequency technique shown in Fig. 2 is based on the transmission line theory. The dispersion measurement was made using an automatic network analyzer with the microstrip line terminated in a short circuit. Treating the microstrip line like a quarter-wavelength resonant stub, the line wavelength, \(\lambda \), may be calculated by measuring the input dependence as a function of frequency. The

effective dielectric constant, $\epsilon_{\rm eff}$, at each resonance can be determined from the following relations:

$$1 = \frac{n\lambda}{4}$$
 (n = 1,2,3...)

$$\epsilon_{eff} = \left(\frac{nc}{42f}\right)^2$$

where 2 is the electrical length of the microstrip line. All of the measurements were made on 1 in. long microstrip lines on a Cufion substrate (ε_r = 2.1). The line width is chosen to provide a low-frequency characteristic impedance of approximately 50 Ω . A SHA MIC flange mount connector was used to connect the microstrip line to the automatic network analyzer and the short circuit termination.

4. NUMERICAL ANALYSIS

A spectral domain method as outlined in Ref. 3 is utilized to analyze the disperison of an open microstrip structure. In brief, the formulation of the problem yields a hybrid mode solution of linear combinations of TE and TM fields. The hybrid-mode fields in the spectral domain are given by

$$\widetilde{E}_{z1}(\alpha,y,z) = \frac{k_1^2 - k_z^2}{jk_z} \widetilde{\phi}_1^e (\alpha,y) e^{-jk_z z}$$

$$\widetilde{H}_{z1}(\alpha,y,z) \approx \frac{k_1^2 - k_z^2}{jk_z} \widetilde{\phi}_1^h(\alpha,y) e^{-jk_z z}$$

$$\widetilde{E}_{x_1}(\alpha, y, z) = \left(-j\alpha\widetilde{\phi}_1^e(\alpha, y) - \frac{\omega\mu_0\mu_r}{k_z} \frac{\partial\widetilde{\phi}_1^h(\alpha, y)}{\partial y}\right) e^{-jk_z z}$$

$$\widetilde{H}_{x_1}(\alpha, y, z) = \left(\frac{\omega\varepsilon_0\varepsilon_r}{k_z} \frac{\partial\widetilde{\phi}_1^e(\alpha, y)}{\partial y} - j\alpha\widetilde{\phi}_1^h(\alpha, y)\right) e^{-jk_z z}$$

The subscripts i = 1,2 designate the regions 1 (substrate) and 2(air). The Fourier transforms of scalar potentials satisfy the homogeneous Helmholtz equation

$$\nabla^2 \widetilde{\phi}_1 + k_1^2 \widetilde{\phi}_1 = 0$$

or

$$\frac{a^2\widetilde{\phi}_2}{ay^2} - \gamma_1^2\widetilde{\phi}_1 = 0$$

where

$$\gamma_1^2 = \alpha^2 + k_z^2 - k_0^2 \epsilon_r \mu_r$$

$$\gamma_2^2 = \alpha^2 + k_z^2 - k_0^2$$

$$k_0^2 = \omega^2 \mu_0 \epsilon_0$$

By matching tangential components (x and z) of the fields at the air-dielectric interface, and satisfying the radiation condition and appropriate boundary conditions at the conducting strip, two coupled equations of the unknown transformed currents $(\widetilde{J}_{x},\widetilde{J}_{z})$ and the transformed longitudinal fields $(\widetilde{E}_{z2},\widetilde{H}_{z2})$ are obtained.

$$G_{11}(\alpha, k_z) \tilde{J}_{\chi}(\alpha) + G_{12}(\alpha, k_z) \tilde{J}_{\chi}(\alpha) = \tilde{E}_{\chi 2}(\alpha, d)$$

$$G_{21}(\alpha, k_z) \tilde{J}_{\chi}(\alpha) + G_{22}(\alpha, k_z) \tilde{J}_{\chi}(\alpha) = \tilde{H}_{22}(\alpha, d)$$

where the expressions for the Green's functions $G_{11}(\alpha,k_z)$, $G_{21}(\alpha,k_z)$ etc. are given in Ref. 3. To find the unknown propagation constant k_z , Galerkin's method in the spectral domain is applied to reduce the coupled equations to a matrix equation. By expanding the transformed current \widetilde{J}_x and \widetilde{J}_z in terms of some known basis functions \widetilde{J}_{xn} and \widetilde{J}_{zn} , i.e.,

$$\widetilde{J}_{X}(\alpha) = \sum_{n=1}^{M} c_{n} \widetilde{J}_{Xn}(\alpha)$$

$$\tilde{J}_{z}(\alpha) = \sum_{n=1}^{M} d_{n} \tilde{J}_{zn}(\alpha)$$

A matrix equation of the unknown constants $\ensuremath{c_n}$ and $\ensuremath{d_n}$ is obtained.

$$\sum_{n=1}^{M} K_{mn}^{(1,1)} C_n + \sum_{n=1}^{N} K_{mn}^{(1,2)} d_n = 0 \qquad m = 1,2,...N$$

$$\sum_{n=1}^{M} K_{mn}^{(2,1)} C_n + \sum_{n=1}^{N} K_{mn}^{(2,2)} d_n = 0 \qquad m = 1,2,...M$$

where

$$K_{mn}^{(1,1)} = \int_{-\infty}^{\infty} \tilde{J}_{zm}(\alpha)G_{11}(\alpha,k_z) \tilde{J}_{xn}(\alpha)d\alpha$$

$$K_{mn}^{(1,2)} = \int_{-\infty}^{\infty} \mathfrak{I}_{2m}(\alpha) G_{12}(\alpha,k_z) \, \mathfrak{I}_{2n}(\alpha) d\alpha$$

$$K_{mn}^{(2,1)} = \int_{\infty}^{\infty} \mathfrak{I}_{xm}(\alpha)G_{21}(\alpha,k_z) \, \mathfrak{I}_{xn}(\alpha)d\alpha$$

$$K_{mn}^{(2,2)} = \int_{-\infty}^{\infty} \mathfrak{I}_{xm}(\alpha) G_{22}(\alpha,k_z) \, \mathfrak{I}_{2n}(\alpha) d\alpha$$

The unknown propagation constant, $\mathbf{k}_{\mathbf{Z}}$, is calculated numerically by finding the root to the determinant of the matrix equation

$$[K] = 0$$

The root to the determinant is computed by iteration technique. Romberg's numerical integration algorithm has been used to compute K_{mn} . The numerical result is strongly dependent on the choice of the basis functions. Different bases function for \widetilde{J}_{χ} and \widetilde{J}_{Z} have been reported in the open literature. For the work here, the following basis functions have been chosen.

$$J_{\chi}(x) = \sqrt{\frac{2}{\pi}} \frac{J_{\chi 0}}{\sqrt{\left(\frac{W}{2}\right)^2 - \chi^2}} - \frac{W}{2} < x < \frac{W}{2}$$

$$= 0 \qquad \text{otherwise}$$

$$J_{\chi}(X) = J_{\chi 0} \sin \frac{\pi \chi}{0.8W} \quad |x| \le 0.8 \frac{W}{2}$$

$$= J_{\chi 0} \cos \frac{\pi \chi}{0.2X} \quad 0.8 \frac{W}{2} < |X| \le \frac{W}{2}$$

5. COMPARISON OF CALCULATED AND MEASURED VALUES

Figure 3 shows the measured and computed values of the effective dielectric constant, $\epsilon_{\rm eff}$, as a function of frequency for a microstrip line of 0.89 mm line width on a 10 mil Cuflon substrate ($\epsilon_{\rm r}=2.1$). The measured curve exhibits the

usual oscillatory characteristics of the coaxial microstrip transition. 2 If the substrate thickness is increased, the transition effect is enhanced as clearly indicated in Fig. 4 for the 30 mil substrate. The transition effect, if not removed, will obscure the small deviations in impedance and phase velocity due to the dispersion of the microstrip line. To remove the oscillations experimentally requires a broadband, well matched coaxial-microstrip transistion. However, by fitting the measured data to an interpolating polynomial to smooth out the transition characteristics, the measured curves show good agreements with the computed curves. The maximum deviation is approximately 5 percent over a frequency range of 2 to 20 GHz. The discrepancy between the measured and the calculated values can be traced to different sources of error. Since the physical line length is used to determine the line wavelength, the effective dielectric constant, ϵ_{eff} , computed from the measured line wavelength generally has a higher value. The fringing at the end of the line tends to increase the electrical length of the line, and thus, lowers the value of the measured $\epsilon_{\rm aff}$. By including the fringing effect, a closer agreement between the measured and the computed values can be obtained. Also, it has been observed experimentally that the type of short termination has a profound effect on $\varepsilon_{\mbox{eff}}$. By terminating the microstrip line with a SMA coaxial short and by wire bonding the microstrip line to its ground

plane, the measurements can be changed by a few percent. For the latter case, the impact of fringing on the electrical length is significant. Better agreement between the analytical and experimental results are also possible if a more accurate basis function for the unknown current or a better analytical model for the microstrip line is used. Finally, the impedance variation along a short-circuit microstrip line can be obtained by measuring the input impedance as a function of frequency or electrical lengths. Figures 5 and 6 show the variation of the normalized resistance and reactance with frequency. The resistance curve shows an impulse type of response at resonant frequencies, while the reactance curve demonstrates similar characteristics of a lossless short-circuited transmissions line of TEM modes. It is important to point out that because of the dispersion of the microstrip line, the resonant frequencies for the higher order modes do not always occur at exactly the multiple of the fundamental frequency. As a consequence, the phase velocity and the effective dielectric constant are frequency-dependent.

7. CONCLUSION

A swept frequency technique for dispersion measurement of microstrip lines has been described. The technique is easy to apply, and yet, yields fairly accurate results for both thin and thick substrate over a frequency range of 2 to 20 GHz. From this technique, one is able to obtain the impedance variation along a

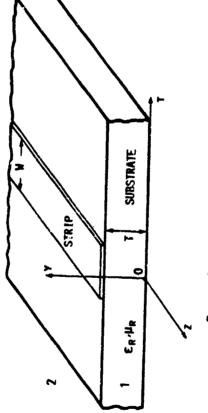
dispersive line, and a better physical understanding of the dispersive characteristics of an open microstrip line.

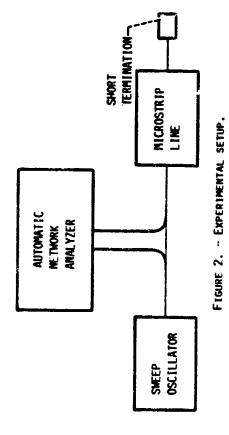
REFERENCES

- Denlinger, E.J. (1971) A Frequency Dependent Solution for Microstrip Transmission Lines, <u>IEEE Trans. Microwave Theory</u> Tech., 19:30-39.
- 2. Troughton, P. (1969) Measurement Techniques in Microstrip.

 Electron. Lett., 5:25-26.
- Itoh, T. and Mittra, R. (1973) Spectral-Domain Approach for Calculating the Dispersion Characteristics of Microstrip Lines, IEEE Trans. Microwave Theory Tech., 21:496-499.
- 4. Wheeler, H.A. (1965) Transmission-Line Properties of Parallel Strips Separated by a Dielectric Sheet, <u>IEEE Trans. Microwave</u>
 Theory Tech., 13:172-185.
- 5. Wolff, I. and Knoppik, N. (1971) Microstrip Ring Resonator and Dispersion Measurement on Microstrip Lines, <u>Electron</u>. <u>Lett.</u>, 7:779-781.

6. Kobayashi, M. (1985) Longitudinal and Transverse Current
Distributions on Microstriplines and Their Closed-Form
Expression, <u>IEEE Trans. Microwave Theory Tech.</u>, 33:784-788.





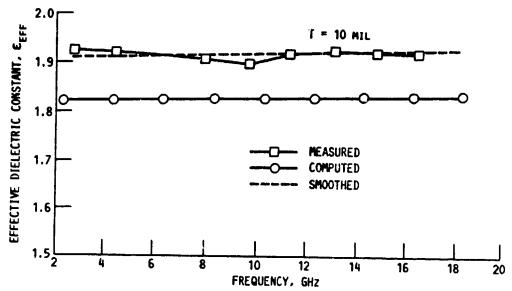


FIGURE 3. - EFFECTIVE DIELECTRIC CONSTANT, ϵ_{EFF} , versus frequency.

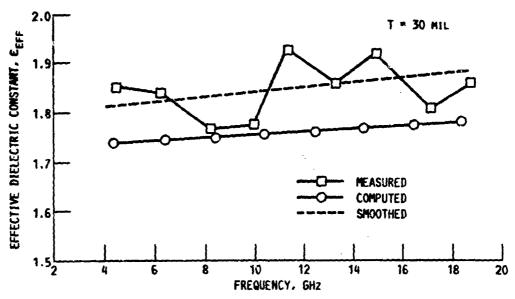
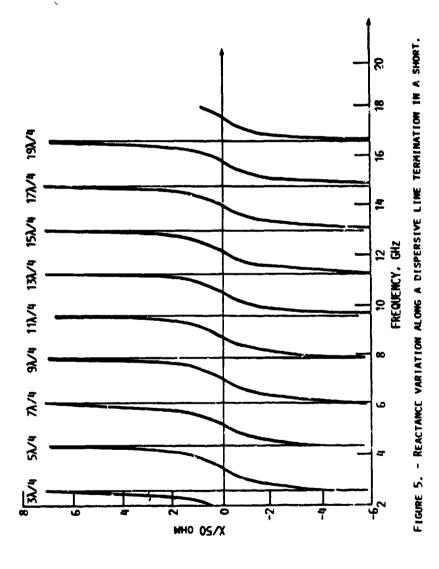


Figure 4. - Effective dielectric constant. $\epsilon_{\rm eff}$, versus frequency.



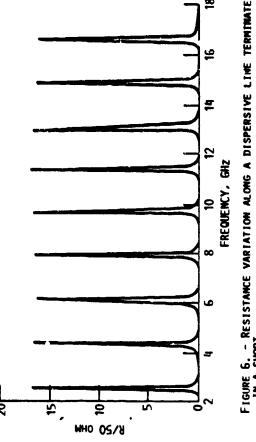


FIGURE 6. - RESISTANCE VARIATION ALONG A DISPERSIVE LIME TERMINATED IN A SHORT.

EVALUATION OF LOCALIZED INHOMOGENEITIES
IN THE REFLECTIVITY OF PLANAR ABSORBER PANELS

DIRK E BAKER AND CORNELIS A VAN DER NEUT

COUNCIL FOR SCIENTIFIC AND INDUSTRIAL RESEARCH P.O. BOX 395, PRETORIA, SOUTH AFRICA 0001

ABSTRACT

For certain applications the antenna designer may require a knowledge of the small scale, or localized, reflectivity properties of microwave absorbers. Suppliers of microwave absorbers generally quote the average absorption achieved over fairly large panels (610 mm x 610 mm) as determined by one of several free-space measurement techniques. By the nature of their construction, small samples of planar absorber panels cannot generally be evaluated directly in waveguide, particularly at X-cand and above.

This paper describes a swept-frequency, one-horn interferometer where the absorber panel is placed directly against the aperture of a well matched horn. By careful selection of waveguide components and by aperture matching an exponential horn, residual reflections within the system can be reduced to acceptably low levels (typically better than -35 dB). The measurement procedure has the advantage that fairly small areas (about the size of the horn aperture) of planar absorber panels can be evaluated without having to cut the panels to fit pieces into a sample holder.

Reflectivity measurements on a variety of planar absorber panels show that multilayer Jaumann absorbers have the greatest

inhomogeneity (reflectivity can vary by 10 or even 20 dB over a few centimeters). Some multilayer, graded dielectric absorbers show excellent homogeneity down to the -30 dB level. Honeycomb absorbers have excellent homogeneity within a panel but occasionally show variations from panel to panel when the honeycomb is excessively loaded. The technique conveniently determines the center frequency of resonant absorbers.

INTRODUCTION

For certain applications (e.g. the microwave absorber in the backing cavity of a planar spiral antenna), the reflectivity of the absorber over quite small areas (50 mm x 50 mm) can influence antenna performance¹. Small samples of absorber are sometimes measured in waveguide but this technique is not satisfactory because the physical construction of most planar panels make them poorly suited for insertion into small waveguides. small samples of absorber can ъе measured by a horn interferometer where the sample is placed a meter or so from the horn². In this case a tuner is usually used to reduce the residual reflection from the horn at each frequency of interest. Evaluation of absorbers over even modest frequency bands can be an extremely time-consuming and tedious process.

This paper describes a one-horn interferometer where the residual reflection from the horn is reduced to a low level (typically better than -35 dB) by eliminating reflections from the throat of the horn and significantly reducing reflections from the horn aperture. This is achieved by using an aperture-matched exponential horn. Because the horn can be matched over the full bandwidth of the standard waveguide bands, swept-frequency measurements can be taken over 1.5:1 frequency bands.

In order to examine relatively small samples, the planar absorber panel is placed directly against the aperture of the horn and its reflectivity compared to that of a metallic shorting plate which sets the zero dB reference level. Comparative measurements over various parts of the absorber panel can be made rapidly without having to cut samples from the panel. Measured results are presented for a variety of absorbers to illustrate some of the observed inhomogeneities in reflectivity.

MEASUREMENT PROCEDURE

The measurement system consists of an RF swept source, some means of isolating the source, 10 dB directional couplers with a minimum of 40 dB directivity, aperture-matched exponential horn, RF step attenuator and network analyser (see Figure 1). The system is configured out of components generally available in a microwave laboratory and lends itself to rapid, real time evaluation of absorber panels over comparatively broad (1.5:1) frequency ranges.

Figure 2 shows the aperture-matched horn. The aperture matching is achieved by attaching a 20 mm diameter rolled edge to all four walls of a conventional exponential horn (e.g. model 640 of the NARDA Microwave Corporation). Theoretical and experimental aspects of aperture matching are described by Burnside and Chuang³. For reasonable aperture matching the cylinder diameter should be about a wavelength at the lowest operating frequency. Experience has shown that significantly improved VSWR performance can be achieved by using even quite small cylinders (down to a quarter wavelength in diameter)⁴. By choosing 20 mm cylinders $(0.53 \ \lambda \ at \ 8 \ GHz)$, the aperture of the horn at the tangential points to the cylinders is not increased too much.

The reflection coefficient of the conventional NARDA horn is shown in Figure 3 together with that of the aperture-matched horn. Without aperture matching the reflection coefficient is about -31 dR (YSWR 1.06:1) and with aperture matching better than -37 dB (VSWR 1.03:1) over the 8.4 to 12 GHz band. The dips at about 9.1, 10.3 and 11.3 GHz result from the finite directivity (about 44 dB, in this case) of the couplers used. This effect is analogous to that observed when measuring antenna patterns in the presence of extraneous reflections and can be analyzed in the same way⁵.

The residual reflectivity (-37 dB) of the aperture-matched horn will introduce measurement uncertainty depending on the amplitude and phase of the reflected signal from the absorber. For example, a true reflected level of -25 dB from the sample could lie anywhere between -23 and -27.5 dB depending on whether it adds in or out of phase with the residual reflection. At a true -30 dB level, the residual reflectivity could cause this to be between -26.8 and -35 dB. Measured reflectivities below the -25 dB level should therefore be treated with caution.

The measurement procedure is as follows: place the metallic plate against the horn aperture to obtain a zero dB reference level (a better baseline is achieved by placing the plate at the waveguide flange between the coupler and the horn), check RF linearity and dynamic range with the RF attenuator (60 dB linear dynamic range was achieved), place the absorber panel against the horn aperture with the metallic plate behind it ensuring that the sample is firmly pressed against both the aperture and the plate. The reflection coefficient with the sample in place is the reflectivity of the absorber panel. The aperture of the horn is not free-space nor is the incident wave plane, however for

comparative measurements this is of no consequence. Measurements on known samples show that the test results for homogeneous panels do not deviate significantly from the free-space results.

3. MEASURED RESULTS

A wide variety of planar absorber panels were evaluated using the procedure of Section 2 to ascertain how homogeneous common absorber panels are when sampled over small areas (about 60 mm x 80 mm in X band) within the panels (typically 610 mm x 610 mm or 305 mm x 305 mm). The absorbers tested fall into three broad classes: (a) multilayer dielectric absorbers, (b) carbon coated honeycomb panels and (c) thin, resonant absorbers (single layer or double layer). Chapter 9 of reference 2 gives a detailed discussion of absorber types.

3.1 Multilayer dielectric absorbers

Broadband absorbers can be made by using multiple layers of resistive sheets and low dielectric constant spacers. Several of these Jaumann absorbers were evaluated, the absorber panels differing in the number of resistive sheets and spacer thicknesses but all specified to have -17 dB reflectivity in the 8 to 18 GHz frequency band.

Figure 4 shows the swept-frequency results for a three resistive layer Jaumann absorber. The two plots were taken at positions near the center of a 610 mm x 610 mm panel with the panel displaced about 100 mm between the measurements. There are localized inhomogeneities where the reflectivity differs by between 5 and 10 dB to the -25 dB level. The largest difference in reflectivity observed for any of the Jaumann absorbers tested

is shown in Figure 5 for a six sheet absorber measured over 12 to 18 GHz. A difference in reflectivity of about 20 dB was observed when the horn was moved only 50 mm. The absorber was dissected to see whether the inhomogeneity could be ascribed to mechanical defects - the spacers were all of correct thickness and the resistive layers were not damaged. The difference in performance can only be ascribed to the fact that the lossy layers are not sufficiently homogeneous and isotropic. When the absorber panels are to be used to cover large surfaces, the localized inhomogeneities in reflectivity are of no consequence since these variations will be averaged out.

A multilayer, carbon loaded, low density from absorber panel was also evaluated (see Figure 6). The three curves show the extent of variations over the 610 mm x 610 mm panel. Down to the -30 dB level, the variation is only about 4 dB which is typical of the graded from absorbers tested.

3.2 Honeycomb_absorbers

Honeycomb absorbers are made by coating the hexagonal open cell honeycomb with a resistive layer. These absorbers are often used to line antenna cavities and are thus required to have good homogeneity and, the reflectivity should be the same (or nearly so) from panel to panel of the same type. The honeycomb itself is not homogeneous, there being a series of ribbons where adjacent hexagonal cells meet. Figures 7 and 8 show the reflectivity from 8 to 12 GHz and 12 to 18 GHz, respectively. In each case there are two curves — one for the electric field parallel to the ribbon and the other for the electric field perpendicular to the ribbon direction. The two plots track each other fairly closely, the perpendicular plot being typically 1 or

2 dB better. Figures 7 and 8 were measured using different one-horn interferometers. There is excellent tracking of the reflectivities at the -20 dB level at the cross-over frequency of 12 GHz.

In general, excellent homogeneity in reflectivity was found within a sheet and several sheets of the same type tracked each other to within a dB from 8 to 12 GHz. One particular honeycomb ansorber deviated from the above. The absorber sheets were quite thin (12.7 mm) and had been heavily loaded to achieve -20 dB at X band. Figure 9 shows the difference in reflectivity between two sheets of the same type, within each sheet the homogeneity was good (about 1 dB). This particular honeycomb was odd in the sense that the absorption decreases with increasing frequency.

3.3 Thin, resonant absorbers

The spept-frequency, one horn-interferometer can be used to determine the resonant frequency of thin narrowband absorbers. Figure 10 shows the resonant frequencies of three narrowband absorbers. These measurements were taken at the center of each 305 mm x 305 mm panel. Within each panel the resonant frequency shifted by about 500 MHz as the horn was moved around. The manufacturer does not quote the center frequency for the absorber but simply states that the absorption will be better than -17 dB at 9.3 GHz. Since these absorbers generally have high dielectric constants, small changes in thickness will cause a shift in the resonant frequency.

Figure 11 shows an interesting resonant absorber where two resonances are achieved in a 4.7 mm thick panel to increase the bandwidth over that of the conventional resonant absorber of

Figure 10. The solid curve shows the typical reflectivity over about 90% of the sheet and the dashed curve shows the manufacturer's typical data which was taken using an arch far field range. The solid curve of Figure 11 shows good agreement with the arch measurements. In part, this agreement results because the sheet tested with the interferometer is quite homogeneous.

4. CONCLUSIONS

Details of a swept-frequency interferometer for making rapid, real time assessments of localized inhomogeneities in planar absorber panels have been presented. An aperture-matched, exponential horn was used to reduce residual reflections in the system to about -37 dB. This residual reflection is adequate for making comparative measurements on planar absorber panels whose reflectivities usually fall in the -15 to -25 dB range. Jaumann absorbers have the worst homogeneity, while the honeycomb absorbers generally have excellent homogeneity within a sheet and from sheet to sheet. The center frequencies of resonant absorbers were also measured using the test set-up. suitable directional couplers and aperture-matched exponential horns, the technique can easily be applied in the standard waveguide bands from 2 to 40 GHz.

ACKNOWLEDGEMENTS

The authors are indebted to the Council for Scientific and Industrial Research for permission to publish this work.

6. REFERENCES

- 1. Green, P.B. (1983) Advances in spiral antenna technology, Proceedings of the 1983 Antenna Applications Symposium, Allerton, Illinois.
- 2. Knott, E.F., Shaeffer, J.F. and Tuley, M.T. (1985) Radar Cross Section, Artech House, Dedham, MA, Chapters 9 and 10.
- 3. Burnside, W.D. and Chuang, C.W. (1982) An aperture-matched horn design, <u>IEEE Trans. Antennas Propagat</u>. AP-30 (No. 4): 790-796.
- 4. Baker, D.E. and Van der Neut, C.A. A compact, aperture-matched, balanced transmission line antenna (1985) <u>Trans.</u>
 SAIEE 76 (No. 2):62-66.
- 5. IEEE Standard Test Procedures for Antennas Std. 149 (1979), IEEE Press, New York, p. 23 and p. 55.

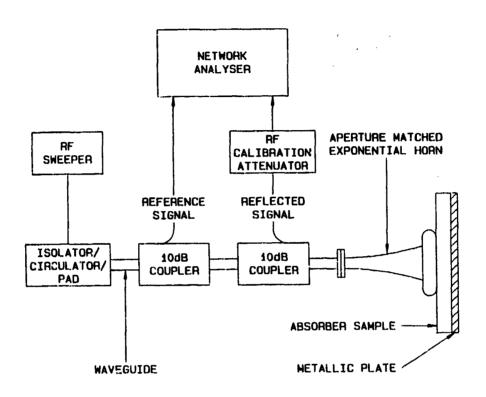


FIGURE 1 : Swept-frequency, one-horn interferometer.

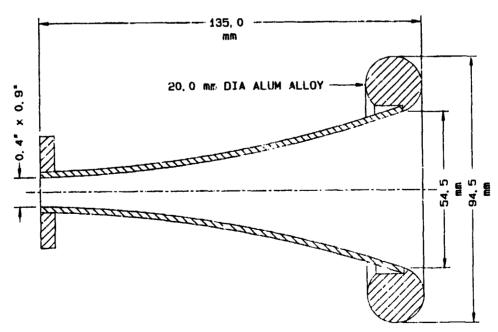
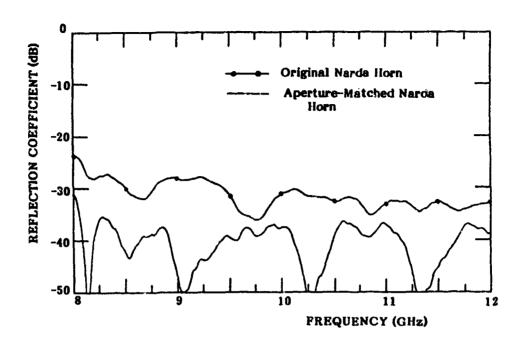


FIGURE 2 : Aperture-matched exponential horn.



 $\underline{\text{FIGURE 3}}$: Measured reflection coefficient of two exponential horns.

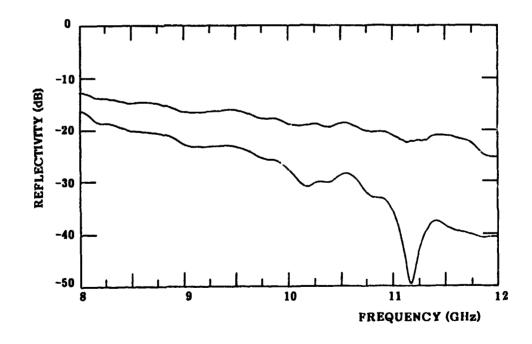


FIGURE 4: Reflectivity of 3 layer Jaumann absorber measured at points separated by 100 mm.

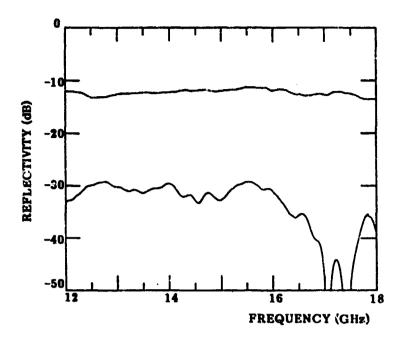


FIGURE 5: Reflectivity of 6 layer Jaumann absorber measured at points separated by 50 mm.

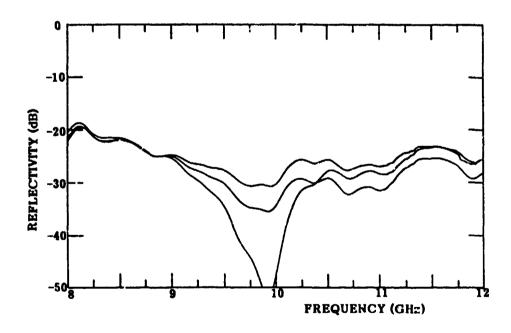


FIGURE 6 : Reflectivity of carbon loaded roam absorber showing variation over 610 mm x 610 mm sheet.

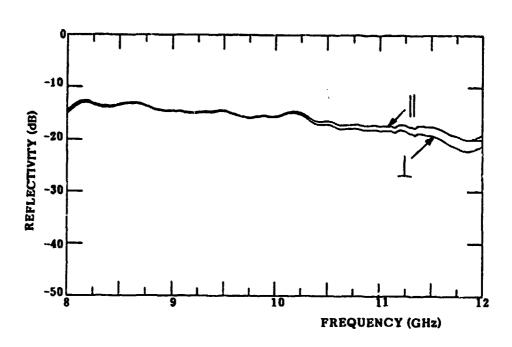


FIGURE 7: Reflectivity of honeycomb absorber with E field parallel and perpendicular to ribbon.

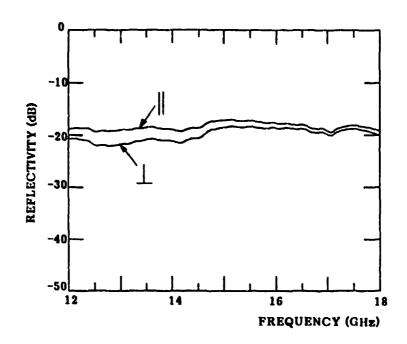
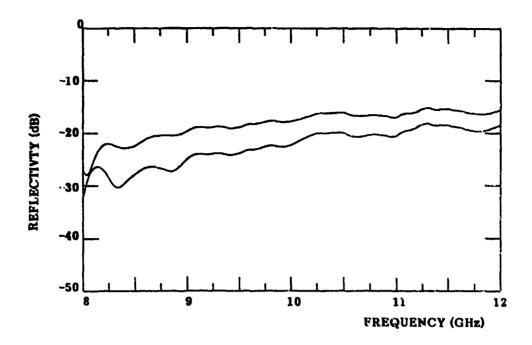


FIGURE 8: Reflectivity of honeycomb absorber with E field parallel and perpendicular to ribbon.



 $\underline{\text{FIGURE 9}}$: Reflectivity of two honeycomb absorber sheets of the same type.

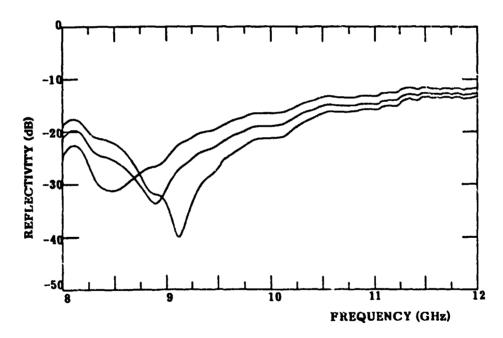


FIGURE 10 : Measured resonance frequencies of three narrowband absorber panels.

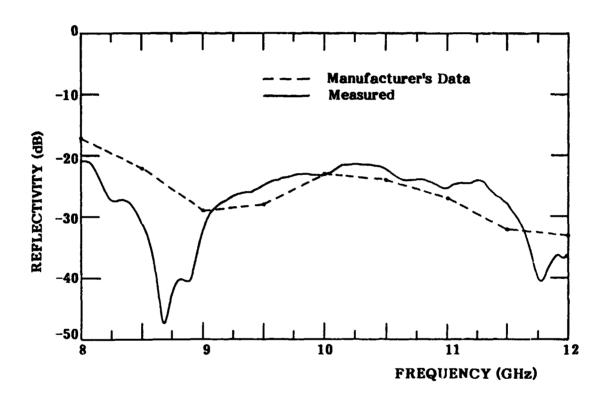


FIGURE 11 : Comparison between measured data and the typical data supplied by the manufacturer for a doubly resonant absorber panel.

RESULTS OF OPTIMIZATION OF YAGI-UDA ARRAYS OF SHAPED DIPOLES

Stephen D. Hibbard, Sharad R. Laxpati and Paul D. Wolfe Department of Electrical Engineering and Computer Science University of Illinois at Chicago P. O. Box 4348
Chicago Illinois 60680

<u>Abstract</u>

The method for maximization of the directivity of Yagi-Uda arrays of shaped dipoles as outlined by Liang and Cheng was employed to optimize a three-element array of shaped dipoles, each 1.5 wavelengths in length and 0.01 wavelengths in radius. Liang and Cheng's optimal three element array was confirmed to yield a maximum directivity of 11.8 dB using the moment method with second-order expansions as formulated by Harrington.

Two simplex minimization routines were alternately used to independently determine optimal element shapes and eliminate saddle points for a three element array of the same dipole lengths and radii, 1.5 and 0.01 wavelengths, respectively. Using this procedure, a shaped-dipole Yagi-Uda array different from Liang and Cheng's example was found to yield a maximum directivity of 12.6 dB.

This paper will also present results for optimal shapes of Yagi-Uda arrays of more than three elements.

1.Introduction

The Yagi-Uda array has important applications in the VHF/UHF frequency range due to its simplicity. A conventional Yagi-Uda array consists of a row of parallel straight cylindrical conductors, of which only one is driven by a source and all others are parasitic. Among the parasitic elements, one serves as a reflector and the rest are directors. A conventional Yagi-Uda array of three elements is pictured in Figure 1.

Methods for increasing the directive gain of this type of antenna abound. The methods include changing element spacing, element radius, element length, boom length and number of directors. Element lengths are usually on the order of one-half wavelength.

Landstorfer reasoned that for dipole elements longer than one wavelength, shaped dipoles could yield a

higher directive gain than linear ones of the same length, sinuspidal current distribution that assuming a independent of the shape or radius of the dipole. Ву experimentation. he found that a three-element Yagi-Uda array of shaped elements, each 1.5 wavelength long, could be adjusted to yield a directive gain of 11.5 dB. Cheng and Liang' proposed a numerical uptimization procedure for Yagi-Uda arrays. Each dipole was described by three parameters; dipole length and radius were held constant at 1.5 and 0.01 wavelengths, respectively, for the array. Their procedure used the method of moments and point matching to approximate the array as a multiport network, and a simplex routine to maximize the directivity of the array. Liang and Cheng achieved a maximum gain of 11.8dB, which could only be implemented with a conventional Yagi-Uda array of nine or ten linear elements.

The increase in the directivity of a shaped three element array indicates the possibility of increasing the gain or Yagi-Uda arrays of more than three elements. Thus, a study was undertaken to inverstigate shaped arrays of more than three elements. The investigation is numerical in nature and paralleled that of Liang and Cheng. The moment method numerical technique employed in

this work was verified by reproducing the results published by Liang and Cheng. When an optimization procedure was instituted with their results as a first guess, the procedure did not converge; the intermediate results indicated that there existed other optimal shapes. Based on these intermediate results it was decided to examine a three element array as well.

In this paper, the results of numerical analysis of multi-element Yagi-Uda arrays are presented. In the following the numerical moment method formulation of an axially symmetric array is presented. Also, a brief description of the optimization prucedures used in this study is provided. The results of the optimization study of optimal shapes, element spacings for three element array are described in the last section. In that section, the results of directivity and impedance for arrays of more than three elements are also included. Finally, some general conclusions are offered.

2. Formulation

As described by Liang and Cheng, each element is described by the following equation:

$$y(x) = A_i [1 - 1/(1 + B_i x^2)] + C_i$$
 (1)

where $i=1,2,3,\ldots$ N, and N is the total number of elements. The parameters A_i , B_i , and C_i are to be optimized. The relation between the total arc length L of each element and half of its projected length on the x-axis is as follows:

$$L = 2 \int_{0}^{\infty} \sqrt{\Gamma^{-}} I^{-} + (d\vec{y} 7 d\vec{x})^{r-} dx \qquad (2)$$

where x. is the x-coordinate of the end-point of the antenna element number i.

Each element is divided into segments such that one segment is centered on the y-axis. Each segment is then numbered and considered to be a port in a multi-port linear network. Following Harrington², the self and mutual impedances of each segment are given by

$$Z(m,n) = j\omega\mu \underline{al}_{n} \cdot \underline{al}_{n} + (1/j\omega\epsilon) [\psi(n^{+},m^{+}) - \psi(n^{-},m^{+}) + \psi(n^{+},m^{-}) + \psi(n^{-},m^{-})]$$
 (3)

where,

$$\psi(m,n) = (1/8\pi\alpha) \int_{-\alpha}^{\alpha} \frac{E \times P \left(-jkR_{m,n}\right)}{R_{m,n}} dz' \qquad (4)$$

j = square root of -1,
ω = frequency in radians,
μ = permeability of free space,
ε = permitivity of free space,
Δl_n = length of segment m,
2α = lΔl_n |

$$|\underline{R}_{n}| = \begin{bmatrix} \sqrt{-[p^{x}-1-(z^{x}-2^{y})^{x}]} & , & m \neq n \\ \sqrt{-[a^{x}-1-(z^{y})^{x}]} & , & m = n \end{bmatrix}$$
wire radius

The second order approximations of the scalar function of equation (4) from Harrington are used, and the geometry for determination of this function is described in Figure 2.

The directive gain for one polarization is as follows:

$$g(\theta,\phi) = \frac{\eta k^2}{4\pi} \frac{1 \left[\tilde{V}_r(\theta,\phi)\right] \left[Y\right] \left[V_s\right] I^2}{P_{in}}$$
 (5)

where,

 η = intrinsic impedance of free space, $k = 2\pi/\lambda$ = the wave number,

$$\tilde{V}_r(\theta, \phi) = \underline{E}_r \cdot \underline{d}_l$$
, $m = 1, 2, 3, \dots, N$

$$\underline{E}_{rn}(\theta, \phi) = \hat{u}_r \cdot \exp(-j\underline{k}_r \cdot \underline{r}_n).$$

Note that \widetilde{V}_r and \underline{E}_r are induced voltages and electric fields, respectively, induced on a unit dipole receiving antenna by the antenna segment m.

The input power of a source feeding the nth segment of an antenna is

$$P_{in} = Re \{ |V_n|^2 | Y(n \cdot n) \}$$
 (6)

where, V_n is the source voltage, Y(n,n) is the input admittance, n is the feed port. The current is given by the product of the admittance matrix and source voltage vectors.

$$[I] = [Y][V_8]$$
 (7)

[
$$V_8$$
] = [0, 0,..., V_n , 0,...,0]^T .

The admittance matrix is the inverse of the impedance matrix:

$$[Y] = [Z]^{-1}$$
 (8)

The above mentioned expressions were modeled on a

computer to determine the directive gain, current distribution, bandwidth, and input impedance for an axially symmetric array. This computer code was verified by checking with the known results for: a three element Yagi-Uda array of linear elements; a single linear dipole and an array of three V-shaped dipoles; and most importantly the results of Liang and Cheng for three shaped element array.

The numerical task of solving the above moment method equations is well known and will not be discussed. Suffice it to say that the code was carefully verified. In the next section, a brief discussion of the optimization procedure used in this work is provided.

3. Procedure

The optimal analysis of the Yagi-Uda arrays carried out here utilizes two different simplex routines. A simplex routine is essentially a root-finding routine for a function of N variables. It will determine the set of N values of a function of N variables which will yield a minimum value of the function. It scans the "space", the range of possible values for all the function's

variables, evaluating the function for many different sets of variable values. When a minimum is suspected, it contracts the space it is searching and conducts a more detailed search. This process is reiterated until a local minimum is found or the search proves futile (in which case it scans a much larger space and the process starts again).

For a function of N variables, if the function's inverse is found to have a minimum for a set of N values of those variables, then this same set of variables is that which will yield a maximum for the function. Usually, the minimum (or maximum for a function's inverse) is only the minimum within a certain range of values, termed a "neighborhood", of the function's variables, or constraints. This is termed a "local" minimum. A minimum value of the function for the entire range of possible values of the function is termed a "global" minimum. Different sets of values which yield different local minima that are not the global minimum are termed "saddle points" (See Priemer*).

Any effort to reduce the number of variables will greatly increase the speed of the optimization procedure.

Liang and Cheng did just that by setting one of the independent variables to equal zero (fixing the antenna configuration at a reference point) and thus reducing the number of independent variables from nine to eight.

Liang and Cheng used this procedure to determine the three sets of parameters necessary for maximum directive gain on a three-element, shaped Yagi-Uda array of element length 1.5 wavelengths and radius 0.01 wavelength. The procedure required approximately 40 minutes of CPU time on a DEC 10 computer, and yielded a set of parameters describing an antenna whose directivity is 11.8 dB, which could only be implemented with a conventional Yagi-Uda array of nine or ten dipoles.

Usually, for functions that require a very short amount of CPU time, one can allow the simplex routine to attempt to converge on the global minimum. However, for long routines such as moment method code used here, (approximately two seconds in the simplest case: three elements), one must print intermediate results in case it fails to converge.

In the numerical analysis carried out here, two

simplex routines were alternately used as follows:

"MINMUM"³: This routine has constraints defined by how much the function variables' values are varied from initial first guesses.

"ZXMWD": This routine is part of the IMSL subroutine library generally available on major mainframe computers. It uses ranges of the function variables' values as constraints.

A first run of the simplex using MINMUM with Liang and Cheng's parameters as a first guess failed to converge on a local minimum within two hours of CPU time on an IBM 3081K64 machine. This is due to the fact that even with C₁ fixed at zero, the dimension of the space was eight, and the function required approximately two seconds of CPU time for each evaluation. However, intermediate results of the optimization were printed, and they indicated a global minimum existed other than the one obtained by Liang and Cheng. Numerous saddle points (local minima) were also indicated.

ZXMWD was used to search for a local minimum

within the neighborhoods of each saddle point. This was a very costly process, requiring approximately two hours of CPU time. ZXMWD also failed to converge for the same reason as MINMUM, but it was found that the neighborhood of a saddle point could be sufficiently investigated for a local minimum within only two minutes of CPU time.

Therefore, for the case of the three-element shaped Yagi-Uda array, using Liang and Cheng's parameters as a first guess, program MINIMUM was used to scan a large neighborhood around the first guess, and ZXMWD was used to investigate the indicated saddle prints within much smaller neighborhoods.

Unfortunately, for the cases of shaped Yagi~Uda antennas of elements numbering more than three, the benefit of such an excellent first guess was not available. Therefore, it was necessary to try and find one by evaluating the function at widely spaced variable values throughout the entire range of the functions. For this purpose, to reduce the space, the A_i variables were fixed at a constant value for the entire array; the C_i values were fixed such that the interelement spacing was constant, and only the B_i parameters were varied. Thus,

for a four-element array, the search space was reduced from 12 independent variables to four. Similarly, for a five-element array, the space was reduced from 15 to five. Also, to further reduce the CPU time required for each evaluation of the function for a set of parameter values, each element was divided into 15 segments instead of the 21 used by Liang and Cheng. However, once a fruitful minima was achieved, 21 segments were used.

4. Results and Discussion

Using the above procedure each parameter was optimized independently, fixing only C_2 at 0.000. This procedure required approximately 40 minutes of CPU time on the IBM 3081K64. The following parameters were found to yield a maximum directive gain of 12.6 dB and an input impedance of 6.99 + j32.5 whms.

 $\frac{\text{Table 1}}{\text{Parameters of a Three Element Array with a Directivity of }}$

Element	Ai	Bi	C:	
Reflector	0.378	15.05	-0.162	
Active	0.393	32.11	0.000	
Director	0.362	77.69	0.151	

The parameters found in Table 1 were found separately by optimizing each parameter except C_2 .

More interesting results were found when the space was reduced by setting the value of A_i parameters equal to 0.370 and the inter-element spacing, D_i , equal to 0.160. Then C_i is given by $(i-1)D_i$. The B_i parameters were then separately optimized. The space for a three element antenna is now reduced to three, the number of B_i parameters. The results of this procedure are found in Table 2.

 $\frac{Table\ 2}{Parameters\ of\ a\ Three\ Element\ Array\ with\ a\ Directivity\ of\ 13.2\ dB.}$

Element	Bi			
Reflector	15.00			
Active	31.00			
Director	50.00			

For antennas of N elements, the above procedure was duplicated. All parameters except C_2 were optimized. Then, the B_i parameters were separately optimized together with a constant A_i equal to 0.370 and interelement spacing

of D = 0.160. The optimized B_i parameters are presented in Table 3 for N equals three to nine.

 $\begin{tabular}{lll} \hline $Table 3$ \\ \hline \end{tabular} \begin{tabular}{lll} Optimized Parameter B_i and Directive Gain for Multi-element Arrays \\ \hline \end{tabular}$

N	Bi	B ₂	B ₃	B4	Bs	B ₄	B ₇	Ba	Bo	GAIN
3	15	31	50							13.2
4	22	30	58	73						13.4
5	15	30	70	117	130					13.9
6	12	24	75	113	160	92				14.1
7	13	30	60	90	120	140	160			14.2
8	12	38	65	91	116	144	166	181		14.4
9	12	37	66	90	115	140	166	182	211	14.5

Note that the values of the B_i parameters are to two significant digits. For N equal to five through nine, A_2 is set to 0.370 and interelement spacing to 0.160.

For the procedure used in this study, it was found that the best results for directive gain is achieved when the B_i parameters are optimized again, when compared to optimization over the entire space. That is, A_2 is fixed to 0.370 and the interelement spacing is set at 0.160. It should be noted that this has been confirmed for antennas of three and four elements only.

By reducing the space over which the optimization was carried out, and by reducing the number of dimensions, the number of possible saddle points on which the optimization will attempt to converge is reduced. This also increases the chances of having any local minimum to be a global minimum; thus increasing the efficiency of the optimization.

5. Conclusions

In this paper, the results of a numerical analysis of shaped dipole Yagi-Uda arrays are presented. This analysis was performed using the method of moment and the work presented by Liang and Cheng. Their optimization was confirmed using this method. The optimization of the array presented by Liang and Cheng was refined for greater directive gain.

This was accomplished by alternately using two optimization routines. It was found that by reducing the space over which the optimization was performed greater computing efficiency was achieved and most importantly, directive gain was increased. Using Liang and Cheng's results as a first guess and optimizing over

the whole space, a directive gain of 12.6 dB was obtained. But, by fixing the inter-element spacing and one of the parameters for each element, an increase in the directive gain to 13.2 dB was achieved. The procedure was then extended to an array of four elements and a directive gain of 13.4 dB was found. The results for up to nine elements have also been presented. Specifically, the appropriate parameters and the directive gain have been tabulated.

An interesting observation that should be made that analogous to the case of a linear Yagi-Uda array, an increase in the number of director beyond the first two does not increase the directivity significantly. This observation is based on our restrictive optimization of more arrays with more than three directors (five elements) and a full optimization may produce significant change in the directive gain. However, the computational resources needed to carry out such an exhaustive analysis are significant and no attempt was made to carry out such an analysis here.

It is planned to continue this study. In particular, arrays with four and more elements will be explored further. Also an investigation into the bandwidth would be of considerable interest.

6. Acknowledgements

Authors would like to thank the use of the Computer Center facilities of the University of Illinois at Chicago. Special thanks are to Dr. Sabelli and other staff members at the Computer Center for their assistance. Use of the optimization code developed by Dr. Priemer of the Department of EECS is gratefully acknowledged.

7. References

- 1. Liang, C. H. and Cheng, D. K. (1983) Directivity optimization for Yagi-Uda arrays of shaped diploes, <u>IEEE Trans. Antennas and</u> <u>Propagat</u>. AP-31:522-524.
- 2. Harrington, R. F. (1967) Matrix methods for field problems, <u>Proc. IEEE</u>. 55:136-149.
- 3. Landstorfer, F. M. (1976) A new type of directional antenna, <u>Digest of the IEEE/APS</u>

 <u>International Symposium</u>, 169-172.

4. Priemer, R. (1986) <u>Introduction to Signal</u>
<u>Processing</u>, to be published.

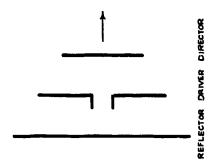


Figure 1. Conventional Three Element Yagi-Uda Array

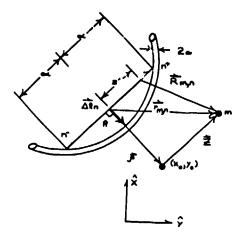


Figure 2. Geometry of Shaped Array for Impedance Expressions

RESULTS OF NUMERICAL AND PHYSICAL MODELLING OF AIRBORNE ADCOCK ARRAYS FOR VHF DF APPLICATIONS

*D.C. BAKER, **L. BOTHA, *D.A. McNAMARA and *G.W. REED

*University of Pretoria, Pretoria, South Africa **Council for Scientific and Industrial Research, Pretoria, South Africa

ABSTRACT

This paper describes an attempt to predict the received voltages on a VHF direction finding (DF) array using the geometrical theory of diffraction and the principle of reciprocity. Once the received voltages are known bearing errors can be predicted from the phase information.

The predicted receive mode radiation patterns are compared with a simple model of a C130 Hercules transport aircraft. Further comparison is made with models representing a low-wing jetliner with underwing engines. The latter aircraft models use either a blunt capped cylinder or a sectional cylinder with a hemispherical cap and a conic section. The comparison between predicted and measured results are reasonable.

It is concluded that a simplified model with a blunt cylindrical model yields acceptable results. Furthermore for underbelly mounted DF arrays the smallest bearing errors are obtained for high-wing aircraft followed by low-wing aircraft with tailmounted engines. Low-wing aircraft with underwing enginepods will yield the worst results.

1. INTRODUCTION

It is known from previous modelling of Direction Finding (DF) antennas on aircraft and ships 1,2 that reradiation from structures in the vicinity of the antennas can be a major source of errors. In this paper attempts to predict the magnitude of structural effects using standard computer techniques and to verify these predictions by model measurements are described.

The initial decision was to use a reasonably simple physical model of the Lockheed C130 (Type L100-30) Hercules transport aircraft. This aircraft is used extensively in a variety of roles. In South Africa it has been used in several longrange search and rescue operations by SAFAIR Freighters. Some of these missions are In view of the fact that frequencies at listed in Table 1. approximately 121.6, 156.8 and 243.0 MHz are designated for calling and distress use, it seemed to the authors appropriate that this aircraft would be a suitable case study for an analysis of structural scattering effects on a simple VHF DF array. The complexity of mounting appropriate antennas on the underbelly of the real aircraft in view of the low ground clearance was not considered important for the purpose of this study.

In view of the somewhat disappointing results obtained during comparison of numeric and physical modelling it was decided to extend the measurements to include a model of what could be considered a fairly typical low-wing commercial jetliner with two underwing engine pods. In order to reduce the complexity of the computer model it was also decided to investigate the use of a blunt capped cylinder for the fuselage as an alternate to a more accurate scale model.

2. THEORETICAL CONSIDERATIONS

2.1. Introduction

The principles of the method for computing the effect of an aircraft structure on the performance of an airborne DF array are described here.

Since a DF system is essentially a receiving device, the direct approach would be to consider the response of the antennas for plane waves incident from various directions (bearings). However, this would require that the fields of the incident wave at the DF system antennas be computed in the presence of the aircraft structure. That is, scattering of an incident plane wave by the aircraft structure would have to be accounted for. The latter is an extremely difficult problem. On the other hand, very efficient

TABLE 1

Summaries of Long-range search and rescue flights undertaken with Lockheed L-100 (Cl30 Hercules) aircraft by SAFAIR Freighters

Short-range search and rescue in South African Coastal Waters are normally undertaken by SAAF.

Sorties area Comments 10 area 1650 nms 3 Sorties by SAAF Shackl 6 Sorties by two USN P3C 0 rions 9 Sorties by RNAF P3B Or Vessel and crew not foun Debris found. 8 900 nms 8 Body sighted. 8 1 200 nms 8 Body sighted. 9 1 200 nms 8 Body sighted. 9 1 200 nms 8 Body sighted. 9 2 1 200 nms 8 Body sighted. 9 2 1 200 nms 8 Body sighted. 9 2 2 3 200 nms 8 Body sighted. 9 2 3 200 nms 8 Body sighted. 9 2 45 000 sq nms 8 Bobris found. 9 2 45 000 sq nms 8 Bobris found. 9 2 8 200 proposed and crew not foun				
of area area area 1650 nms 900 nms 1 200 nms 45 000 sq nms search area	Comment	3 Sorties by SAAF Shackleton 6 Sorties by two USN P3C Orions 9 Sorties by RNAF P3B Orion Vessel and crew not found. Debris found.	Dinghy found. Body sighted. Vessel and crew not found.	Debris found. One further search on prob- able track in Indian Ocean by SAFAIR. Vessel and crew not found.
Ind Country Date Sorties je-Vanga Nov 10 ay 1979 10 ien Spring July 6 in Career July 2	į į	area 1650 nms	900 nms	1 200 nms 45 000 sq nms search area
ind Country Date je-Vanga Nov iay 1979 ien Spring July ien Career July iic Career July	No Sorties		9	
und Country je-Vanga ay len Spring an	Date	Nov 1979	July 1982	July 1985
Vessel a la Rerg Norw Norw S. Gold Taiw 3. Arct	essel and Country	. Berge-Vanga Norway	. Golden Spring July Taiwan 1982	Arctic Career

methods exist ^{3,4,5,6} which enable one to compute the fields of the DF antennas if we consider them to be transmitting in the presence of the aircraft structure. Using the reciprocity theorem of electromagnetic theory, a method can be developed when aby these "transmit mode" fields are used to determine the response (receive voltages) of the DF system to incident waves, in the presence of the aircraft.

In practice it is more than reasonable to assume that the source of radiation (beacon) whose bearing the DF system is to determine, is in the far zone of the DF system, and vice versa. The beacon may then be represented as an infinitesimal electric current source. Since most beacons of the "distress" type will have electrically small omnidirectional antennas, such a representation as an infinitesimal source will usually be valid irrespective of range.

2.2 Definitions and Terminology

Consider the configuration shown in Fig 1(a) which shows schematically the n-th antenna (antenna "a") of a DF system radiating in the presence of an aircraft structure.

At location $\underline{R} = \underline{R}_S = (x_S, y_S, z_S)$ is a beacon (antenna "b") of orientation \hat{n}_S , which in the light of the preceding discussion can be considered transverse to \underline{R}_S . The beacon represents an infinitesimal electric current source of length $\Delta \ell$ and strength I_0 . Thus its current density can be written as,

$$\underline{J}_b(x,y,z) = I_0 \Delta k \delta(x-x_s, y-y_s, z-z_s) \hat{n}_s$$
 (1)

The orientation $\hat{n_s}$ selected determines the polarisation of the incident field being simulated.

The surface S_1 encloses antenna "a", while S_2 encloses both antennas "a" $\underline{\text{and}}$ the aircraft.

The fields $(\underline{E}_a,\underline{H}_a)$ are those of antenna "a" (the n-th DF antenna) when it is transmitting in the presence of the aircraft structure and the antenna "b". Thus the scattering from both the aircraft and that from antenna "b" is included. Since "b" is the infinitesimal element, its effect on $(\underline{E}_a,\underline{H}_a)$ will be negligible.

The fields $(\underline{E}_b,\underline{H}_b)$ are those of antenna "b" (the beacon) when it is transmitting in the presence of the aircraft structure and antenna "a". Thus scattering from both the aircraft and antenna "a" is included.

(E_F , H_F) represents the fields (E_a , H_a) as observed at $R = R_s$, while (E_T , H_T) represents (E_a , H_a) as observed on S_2 . Finally, (E_R , H_R) will be fields (E_b , H_b) as observed on S_2 .

2.3 Reciprocity Theorem

The general reciprocity theorems for an electromagnetic field states that 7,

$$\oint_{S} (\underline{E}_{a} \times \underline{H}_{b} - \underline{E}_{b} \times \underline{H}_{a}) \cdot \underline{dS}$$

$$= \int_{V} (\underline{E}_{b} \cdot \underline{J}_{a} - \underline{E}_{a} \cdot \underline{J}_{b} - \underline{H}_{b} \cdot \underline{M}_{a} + \underline{H}_{a} \cdot \underline{M}_{b}) dV \qquad (2)$$

where the closed surface S encloses the volume V containing two sets of electric and magnetic sources $(\underline{J}_a,\underline{M}_a)$, $(\underline{J}_b,\underline{M}_b)$ which give rise to electromagnetic fields $(\underline{E}_a,\underline{H}_a)$ and $(\underline{E}_b,\underline{H}_b)$ respectively.

The vector \underline{dS} is normal to surface S and is directed positively out of S.

2.4 Application of the Reciprocity Theorem

The reciprocity theorem given in expression (2) will now be applied in two ways, to the configuration of Fig 1(a).

First, choose the surface S in the theorem as S_1+S_2 , so that the volume V enclosed by S is a source-free region, containing neither antenna "a" or antenna "b". In such a case, the volume integral on the right hand side of equation (2) is zero. The surface integral on the left side can then be separated into two surface integrals as,

$$\oint_{S_1} (\underline{E}_a \times \underline{H}_b - \underline{E}_b \times \underline{H}_a) \cdot \underline{dS} = -\oint_{S_2} (\underline{E}_a \times \underline{H}_b - \underline{E}_b \times \underline{H}_a) \cdot \underline{dS}$$
 (3)

with dS directed positively out of V. Using the "shielded antenna", whereby surface S_1 enclosing the antenna can be considered (for the wire antenna case in Fig 1(a) and the aperture antenna case of Fig 1(b)) to coincide with conducting portions of the antenna except for an "aperture" portion S_{ap} , Collin has shown that the received voltage at antenna "a" due to source "b" is

$$V_{R} = C_{n} \oint_{S_{1}} (\underline{E}_{a} \times \underline{H}_{b} - \underline{E}_{b} \times \underline{H}_{a}) \cdot \underline{dS}$$
 (4)

where C_n is a complex constant dependent on the particular antenna type. From (3) this voltage is then also given by,

$$V_{R} = -C_{n} \oint_{S_{2}} (\underline{E}_{a} \times \underline{H}_{b} - \underline{E}_{b} \times \underline{H}_{a}) \cdot \underline{dS}$$
 (5)

If (E_T, H_T) and (E_R, H_R) on S_2 are substituted for (E_a, H_a) and (E_b, H_b) respectively, this is just

$$V_{R} = -C_{n} \oint \frac{(\underline{E}_{T} \times \underline{H}_{R} - \underline{E}_{R} \times \underline{H}_{T}) \cdot \underline{dS}}{S_{2}^{2}}$$
 (6)

Let the reciprocity theorem (2) be applied once more with volume V being the region enclosed by surface S_2 and the sphere at infinity S_{∞} . For the volume integral term on the right hand side of (2), the only source term enclosed is the beacon antenna "b", with current density J_b given by (1). It therefore integrates to $-E_F(R_S) \cdot \tilde{n}_S I_0 \Delta l$, where E_F is the field E_a as observed at R_S , as decided above. Thus expression (2) becomes,

$$\oint_{S_2+S_m} (E_a \times H_b - E_b \times H_a) \cdot dS = -E_F(R_s) \cdot \hat{n}_s I_0 \Delta R$$

But that portion of the surface integral in (7) over the infinite sphere is zero 8 . With (E_a, H_a) and (E_b, H_b) on S_2 replaced by the symbols (E_T, H_T) and (E_K, H_R) , respectively, (7) becomes

$$-\int_{S_2} (E_T \times \underline{H}_R - \underline{E}_R \times \underline{H}_T) \cdot dS = -\underline{E}_F (\underline{R}_S) \cdot \hat{n}_S I_0 \Delta t$$
 (8)

Comparison of (6) and (8) then shows that the voltage received by the n-th DF antenna, when beacon "b" is transmitting is,

$$V_R = C_n \ \underline{E}_F \ (\underline{R}_S) \cdot \hat{n}_S \ I_0 \ \Delta \ell \tag{9}$$

Note that (9) is valid for any range and orientation of the beacon.

2.5 Summary of Theoretical Result for Received Voltages

The voltage received by the n-th antenna of the DF system, when the beacon of orientation \hat{n}_S is transmitting from bearing R_S , is given by

$$V_n = A_0 \hat{n_s} \cdot \underline{E_F} (\underline{R_S})$$
 (10)

where

- (i) A_0 is a complex constant, C_n I_0 $\Delta \mathfrak{L}$, which will be of no concern in determining the relative complex values of the receive voltages of the identical DF antennas.
- (ii) $E_F(R_S)$ is the field at R_S of the n-th antenna of the DF system, when it is transmitting in the presence of the aircraft. These fields are computed using the geometrical theory of diffraction (GTD) methods 3 , 4 , 5 , 6 .

In order to evaluate the DF system, the fields $E_F(R_S)$ of each

DF antenna, with phase referred to a common reference point, are computed for a known bearing $(\hat{n}_s \mid location \mid R_s)$. Then the voltages V_n are computed for each antenna using (10) and used in the particular DF system algorithm to find the predicted bearing. The bearing error is then the difference between the known and predicted bearings. This is repeated for each direction of incidence of interest.

3. NUMERICAL PREDICTION

3.1 Introduction

The GTD is ideal for studying antennas in a complex environment as only the most basic features of a very complex structure need to be modelled. The components of the fields incident on, reflected by and diffracted by the various structures are determined by using ray optical techniques. Components of the fields are found by summing the Geometrical Optics (GC) terms with the diffracted terms in the far field. The diffraction terms can be found by using the GTD solutions for the individual rays incident on structural elements such as edges and corners. The rays from any one structural element tend to interact with other structural elements and cause various higher order terms. By tracing all the possible rays and evaluating only the dominant terms an accurate and efficient code can be created 3,4,5,6.

3.2 Implementation

A short description of how the GTD is implemented in the code used is now given. The code allows the model used to include a finite elliptical cylinder and a set of flat plates. The cylinder may be capped with a flat plate which may be at any angle relative to the cylinder in the vertical plane ". The plates must be flat and each plate may have up to six corners.

The following terms are included in the code:

direct field field reflected from a plate field doubly reflected by plates field diffracted by plates field reflected by a plate then diffracted by a plate field diffracted by a plate then reflected by a plate

field scattered by the cylinder field reflected by an end cap field diffracted by an end cap rim field reflected by a plate then scattered by the cylinder field scattered by the cylinder then reflected by a plate field reflected by the cylinder then diffracted by a plate field diffracted by a plate then reflected by the cylinder

Scattered by cylinder means that the fields scattered by the cylinder includes both reflected and diffracted (creeping) rays.

The code uses the method discussed in the previous section to determine receive voltages of the DF antennas in the presence of the aircraft. As such the code is a transmitting antenna code and it computes the transmit radiation pattern of the antennas mounted on the structure.

The code allows more than one antenna to be mounted on the structure at any one time. The free space radiation pattern of each antenna on the structure must be known a priori. Recause of the simplicity of expressions for the radiation patterns of dipole (monopole) and slot antennas and the fact that their fields have the required ray optical form, they are used in the code.

To compute the radiation pattern of a two antenna DF system, the program is used in the transmit mode and both antennas are transmitting simultaneously with a phase difference of 180 degrees. The total radiation pattern of the two antennas is thus found for comparison with measurements.

To compute the errors introduced in a DF system the transmit radiation pattern is found for each antenna. The method described above is then used to compute the receive voltages of each antenna from its transmit fields with amplitude and phase information preserved. The receive voltages of each of the antennas can then be fed into the DF algorithm used to compute the errors introduced because of the distortion of the receiving patterns. The algorithm of a four antenna system described by Gething has been included to supplement the code. This enables direct calculation of DF errors for an interferometric system.

In order to establish that the GTD method described correctly preserves the phase information so essential for application to interferometric DF applications, a DF array of two antennas mounted on a box was first modelled. Rearing errors were then calculated in two ways. First the GTD was used to find the transmit fields and the bearing errors found. Then the method of moments was used to find the transmit fields and the bearing errors found. The results were, for all intents and purposes, identical. In what follows only the GTD has been used in the computations.

3.3 The Numerical Aircraft Models

The models under consideration have been built-up by using a circular cylinder with capped ends for the fuselage. The wings were modelled with one flat plate each and the tail was modelled with a set of plates. The modelling of the engines was done using one of two methods. The first engine model was a vertical plate hanging from the wing. This model will have the correct shadowing properties but does not have the correct diffraction effects of a real engine. For a more realistic model of the engine three plates were used. Recause the number of plates that may be used in the code is limited to 14, not all the engines of the Hercules C130 could be modelled in this way.

4. EXPERIMENTAL PROCEDURE

4.1 Description of Models

4.1.1 Lockheed C130 Type L100-30

The choice of scale was determined by the availability of aluminium tubing which happened to have a diameter of 220 mm. Flat plate with a thickness of 3 mm was used for all wing surfaces. Small cylinders were mounted underneath the wings to model the engine pods. For convenience a 20:1 scale factor was used. Details of the model are given in Table 2 together with the positions of the Adcock arrays. A hemisphere was used for the nose section. The upwards tapered tail section of the C130 was approximated by a conic section, the base of which had been cut at a slight angle to provide the necessary upward slope. All slots formed were taped with aluminium tape. Five possible configurations were considered. These were:

- Fuselage only
- (2) Fuselage + Tailplane
- (3) Fuselage + Wings + Tailplane
- (4) Fuselage + Wings + Tailplane + Inner Engine Pods
- (5) full model (excluding rudder)

These configurations are adequately described by the stick model shown on the polar diagrams. Polar diagram measurements were performed for two antenna positions (1 or 2) with the Adcock array mounted circumferentially (C) or axially (A) along the centre line on the underbelly. The mounting designations are shown on the diagrams as 1A, 1C, 2A or 2C.

A photo of the model and one of the authors (G.W.R.) is shown in Figure 2. For the measurements the model was mounted upside down

TABLE 2

Construction details of C130 Type L100-30 Hercules aircraft model

2-4-1

Scale	20:1 (approximate)		
Fuselage :	Total length Nose section (hemisphere) Central section (cylinder) Tail section (cone with base cut at angle) Diameter	94 50	cm cm cm
Wings:	Total span Chord length at tip Chord length at root Length central untapered section Distance of leading edge from nose	24.5 61	CM
Tailplanes:	Total Span Chord length at tip Chord length at root Distance of leading edge from nose	9	cm cm cm
Engines(4):	Length of cylinders Diameter of cylinders Protrusion ahead of wing Propellor length (fixed vertically for maximum scattering effect)	3.7 11.5	
Engines fitt	ed directly to the wing: Distance between centres of inner cylinders Distance between centres of outer	50	cm
	cylinders	100	CM
Adcock array	: Position 1 (from nose) Position 2 (from nose)		cm
Aluminium us	ed throughout		

on the antenna positioner. A bottom view line-drawing is shown in Figure 3a.

4.1.2 The Low Wing Jetliner

A 2.2 m length of the aluminium tubing was left over after fabrication of the Cl30 model. This was used to make a basic model of a low-wing jetliner. The dimensions are shown in Table 3 together with the Adcock array positions. Two cylinders were attached directly to and underneath the wings to model the engine pods.

After completion of the series of measurements, portions of the fore and after sections were cut off and replaced by a hemisphere and a conic section so that the model fuselage would resemble an actual fuselage more closely. A new tailplane with the same overall dimensions was made to cater for the wing root at the conic section. The overall length of the improved model was the same as that of the basic cylindrical model and a bottom view is shown in Figure 3b. These mode is are designated as I and B for improved and basic respectively. As before, the Adcock arrays were mounted in two positions either circumferentially or axially along the central line on the underbelly. This model was also mounted upside down for the measurements. During the course of measurements it was found that the welded bracket supporting the model was slightly off centre. This resulted in the port and starboard wings making dihedral angles of 5° and 7° respectively. As for the C130 model a number of configurations were possible.

4.2 The Adcock Array

The basic Adcock array consisted of two short monopoles fed via 6 dR attenuators to the inputs of a 180° hybrid to form sum or difference patterns.

The probes were two pins soldered into the central conductors of bulkhead mounted SMA connectors. The pins projected through holes in the fuselage approximately 2.5 mm in diameter. For the frequency range above 1,6 GHz the projecting length was 1 cm. Below this frequency the projecting length was 2 cm. The spacing between the probes was kept fixed at 3 cm. This was the minimum practical value in view of the fact that the SMA connectors and other hardware were fitted inside the cylinder. Allowance had to be made for connecting the 180° hybrids with very short lengths of relatively inflexible coaxial cable. The gain of the individual elements was not expected to affect the overall results provided sufficient signal to noise ratios could be obtained. For future reference the gains of the elements were

TABLE 3

Construction details of model to represent a low-wing jetliner

Scale:	20:1 (approximately)	
Fuselage:	Rasic model (designation R) Cylinder length (Ends blocked with metal disks)	220 cm
Fuselage:	Improved model (designation I) Total length Nose section (hemisphere) Tail section (cone) Central cylindrical section	220 cm 11 cm 50 cm 159 cm
Diameter of	both models:	22 cm
Wings:	Length each wing Chord length at tip Chord length at root Fitted to give total span of Sweep at leading edge Dihedral angle Distance of leading edge from nose	107 cm 14.2 cm 47.5 cm 222 cm 37° 6° 79 cm
Tailplanes:	Length Chord length at tip Chord length at root Sweep at leading edge Distance of leading edge from nose	24 cm 10 cm 25 cm 43° 195 cm
Engines(2):	Length of cylinders Diameter of cylinders Distance between centres of cylinders Protrusion ahead of wing Fitted directly to the wing	26 cm 8.5 cm 100 cm 17 cm
Adcock array	Position 1 (from nose)	60 cm
	Position 2 (from nose)	45 cm
Aluminium us	sed throughout	

measured at 1,6 GHz with the 6 dB attenuator pads in place. The gains were found to be -20 dBi and -24 dBi for the 2 cm and 1 cm probes respectively.

All interconnections were made with RG 142 B/U cable terminated in SMA connectors. In order to minimise phase errors the electrical lengths were checked using a Hewlett Packard 2-18 GHz Network Analyser. Appropriate cable pairs were selected for the closest possible match.

The 180° hybrid couplers were a MARDA Model 4343 covering the range 2-8 GHz and an ANZAC Model H-183-4 covering the range 30 to Measurements were made between 2 and 3 GHz using both couplers to obtain an overlap of results. The amplitude and phase imbalance for the NARDA Hybrid are given as ±0.5 dB max and ±7 degrees max respectively with an isolation of 17 dB. amplitude and phase imbalance of the ANZAC hybrid are given as ± 0.4 dB and 7.5 degrees max from 100 to 1500 MHz rising to 15 degrees max from 1500 to 3000 MHz respectively. The isolation was given as 20 dB min for the ANZAC hybrid. Both hybrids were checked using the HP network analyser and found to be well within specification. The worst phase imbalance measured did not exceed approximately 7.5 degrees. This implies that broadside null depths in excess of 17 to 20 dB should be treated with caution. In general the null depths exceeded 20 dB.

The 6 dB attenuators ensured that the mismatch between the inputs of the hybrids and the probes would not exceed an SWR of 2:1.

The probes were mounted on the rounded cylindrical surface as is. No attempt was made to provide a flat groundplane in the vicinity of the array. In the circumferential position this meant that the maximum surface height between the probes due to base curvature for the array was 1 mm higher than the line interconnecting the holes through which the probes project. This was not believed to be detrimental to the measurements and simplifies the numerical model.

Access to the bulkhead mounted SMA connectors, attenuators and hardware was through a hatch measuring 25 cm axially and 12 cm circumferentially on the opposite side of the cylinder from the array itself. A single cable carrying the difference signal was led through a small cutout in the hatch.

4.3 The Antenna Test Facility

All measurements were performed at the National Antenna Test Facility operated by the National Institute for Telecommunications Research of the South African Council for Scientific and Industrial Research. This facility operates in the ground reflection mode and is situated approximately 30 km Northeast of Pretoria. It is described fully in the reports by Baker 10 11 .

The antenna positioner is mounted on a concrete mast at the control room. The total height from the ground to the model was approximately 12 m. Down range slope for the ground reflection mode was 1.4 degrees. The source tower is 500 m away. Source antenna heights can be adjusted from 0,3 m to a maximum of 11 m depending on the frequency. The source positioning system allows adjustment of polarisation, azimuth and elevation pointing angle. A range of dish antennas is used to cover various frequency ranges. Range instrumentation allows operation from 500 MHz to 18 GHz.

For frequencies above 1 GHz a wideband mixer must be used. Signals with frequencies less than this couple directly to the receiver.

5. RESULTS

All measured results discussed here were digitised in one degree increments in order to display them on the same polar plots as the predicted values.

Figures 4 and 5 show a sequence of measured polar diagrams with increasing model complexity for the C130 Hercules aircraft at 2 and 6 GHz. The configurations are adequately described by the line drawings. Only results for a basic Adcock array mounted axially along the fuselage are shown. The nulls are thus broadside to the fuselage. Also plotted are the results predicted by the modified GTD code.

At 2 GHz there is an obvious bulge in the polar diagram in the direction of the tail. This is ascribed to diffraction effects and creeping waves along the conical section of the fuselage. The fact that the Adcock array is positioned near the nose and the fact that this effect was observed at other frequencies suggests that the bulge cannot be ascribed to constructive interference of diffracted and direct fields alone. A more pronounced effect in the direction of the nose would have been expected. The effect of increasing model complexity is surprisingly little as can be seen by comparing Figure 4(a) and 4(d). Some increase in pattern ripple is noticeable.

The predicted results show an anomaly towards the nose from +15 to -15 degrees as well as one in the direction of the tail. It is

expected that the addition of one further GTD ray term to the summation could correct this. Of interest is the prediction of the increasing bulge in the polar diagram in the direction of the tail. The numerical model predicts somewhat greater effects for the presence of wings and engine pods. These effects are not obvious in the measured results. The agreement is regarded as fair.

At 6 GHz the measured pattern is remarkably clean with very little ripple effect as can be seen in Figures 5(a) to (d). Agreement between the patterns for the fuselage alone and the full model is generally within 1 dB or better. The ripple effect is considerably less pronounced than for the 2 GHz case. The effects of wings and engine pods should have appeared between 110° and 140° as measured from the nose but are not evident.

The agreement between predicted and measured results is satisfactory except for the same anomalous behaviour towards the nose and tail as was the case at 2 GHz.

From the point of view of having scattering or diffraction effects for purposes of checking the code these results were somewhat disappointing and gave rise to the next series of measurements on a model representing a low-wing jetliner with two underwing engine pods.

For purposes of illustration the sequence of measurements with the basic (blunt cylinder) model at 7 GHz are shown in Figure 6 for an Adcock array mounted circumferentially in position 1. From other measurements it was clear that the tailplanes had minimal effect and this sequence illustrates the effect of wings and engine pods A slight wing effect appears to be evident in the top half of the polar diagram in Figure 6(c) about 130° from the nose direction. Reference was made earlier to the unequal dihedral This difference was found to account for considerable angles. asymmetry in many of the measurements. In Figure 6(d) the effect of engine pod shadowing and diffraction can be clearly seen in the same direction noted previously and to a lesser extent in the lower half. It was generally found that the amount of ripple in the polarplot was substantially higher than in the case of the C130 model.

Finally Figure 6(f) shows a comparison of measured results for the complete model with the blunt cylinder and the improved cylindrical body as fuselage. Apart from what appears to be a 2 degree offset (due to misalignment of the models) and a slippage in the positions of ripples the overall agreement is regarded as good. Note that the points of normalisation for the two curves are not

the same. Asymmetry in the individual curves can be ascribed to the model asymmetry and imbalance in the 180 degree hybrids.

There is some discrepancy between the measured and predicted results as shown in Figures 6(a) and 6(b) and agreement is regarded as fair. There is far worse agreement between the curves shown in Figure 6(c) and considerable asymmetry in the predicted results. Time did not permit a check of the numeric model used although it is suspected that there may be an error concerning one of the wing's data. Figure 6(d) shows that the numerical model predicts the effects of the enginepods in approximately the correct position.

It was found that using a flat vertical plate or a combination of three plates attached to the wing to form a box section made very little real difference to the predicted results.

On the strength of these results the expected DF errors for the configurations shown were calculated assuming that the DF system was of the interferometric type.

The predicted DF errors are shown in Figure 7 for the C130 model and Figure 8 for the low-wing jetliner model. Many of the spikes can be attributed to irregularities which could arise from the lack of a sufficient number of GTD terms rays in the numeric solution. It would appear though that the high-wing C130 would make a better DF platform than a low-wing aircraft. Further work is however needed torefine the numerical model for the analysis of DF systems on aircraft.

6. CONCLUSIONS

DF arrays mounted on top of aircraft fuselages suffer greater induced errors from stabiliser effects than those mounted on the underbelly. For the latter case the DF errors are least for aircraft with high wing mountings and the error appears to decrease with frequency due to decreased distortion of the basic Adcock array patterns by scattered fields. For low-wing aircraft the DF errors will be less for those with the engines mounted in the tail than for those with underwing pods.

The results obtained from numerical modelling are encouraging. It is believed that further work will yield in predictions which are sufficiently accurate for the evaluation of the performance of DF arrays on various aircraft as well as the optimum positioning of such arrays on specific aircraft.

The relatively good agreement between the basic model using a

cylindrical fuselage and the improved model using a hemispherical nosecap and a conical tailsection suggests considerable simplification in the physical and numerical model of an aircraft in the VHF range.

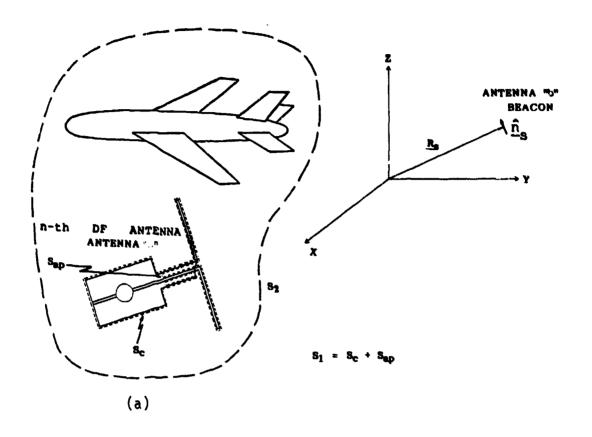
ACKNOWLEDGEMENTS

The authors gratefully acknowledge the assistance of the National Institute for Telecommunications Research, Johannesburg which made the National Antenna Test Facility at Paardefontein available free of charge for this unfunded research work.

REFERENCES

- 1. Kunachowicz, K.J. (1975) Model testing of airborne VHF direction finding antenna system, Antennas for Aircraft and Spacecraft, IEE Conference publication No 128:223-227.
- 2. Mönich, G. (1983) Prediction of bearing errors of vehicular DF antennas by fast measurements on models, Third Intennational Conference on Antennas and Propagation, IEE Conference Publication No 219:101-104.
- 3. Burnside, W.D., Wang, W. and Pelton E.L. (1980) Near-field pattern analysis of airborne antennas, IEEE Trans. Antennas and Propagation, Vol. AP-28:318-327.
- 4. Burnside, W.D. and Marhefka, R.J. (1984) Applications of edge diffraction, Vol II of the notes for the Short Course on the Modern Geometrical Theory of Diffraction, Department of Electrical Engineering, Ohio State University, Columbus, Ohio.
- 5. Burnside, W.D., Gilreath, M.C., Marhefka, R.J. and Yu, C.L. (1975) A Study of KC-135 Aircraft Antenna Patterns, IEEE Trans. on Antennas and Propagation, Vol AP-23: 309-316.
- 6. Yu, C.L., Burnside, W.D. and Gilreath, M.C. (1975) Volumetric Pattern Analysis of Airborne Antennas, IEEE Trans. on Antennas and Propagation, Vol AP-26:636-641.
- 7. Harrington, R.F. and Villeneuve A.T. (1958) Reciprocal relations for gyrotropic media, IRE Trans. Microwave Theory and Tech. Vol MTT-6:308-310.
- 8. Collin R.E. and Zucker F.J. (1969) Antenna Theory, Part I, McGraw-Hill New York.

- 9. Gething, P.J.D. (1978) Radio Direction-Finding, Peter Peregrinus Ltd, London.
- 10. Baker, D.E. (1983) Development of the Microwave Antenna Test Range of the National Antenna Test Facility at Paardefontein, Proceedings of the Antennas and Propagation Symposium of the South African Institute of Electrical Engineers, Pretoria, 16-18 May 1983:FF-1 to FF-10.
- 11. Baker, D.E. (1984), Development and Evaluation of the 500 m Ground-reflection Antenna Test Range of the CSIK, Pretoria, South Africa, Proceedings of the Annual Conference of the Antenna Measurement Techniques Association, San Diego, California, 2-4 October 1984, pp 5A4-1 to 5A4-16.



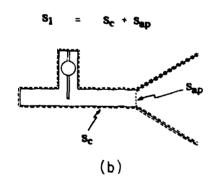
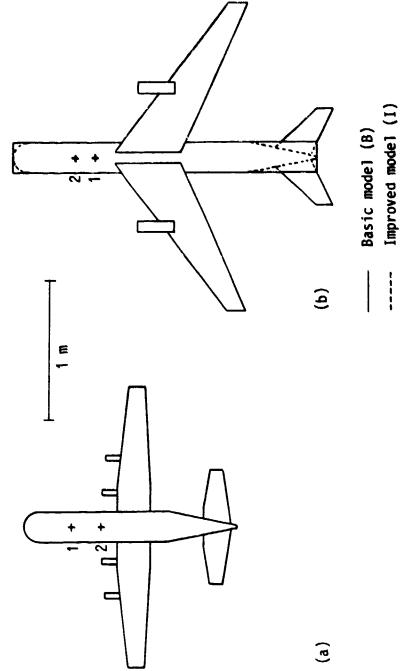


FIGURE 1. (a) Geometry for the derivation of the expression for receive voltages on a DF array. (Wire antenna case)

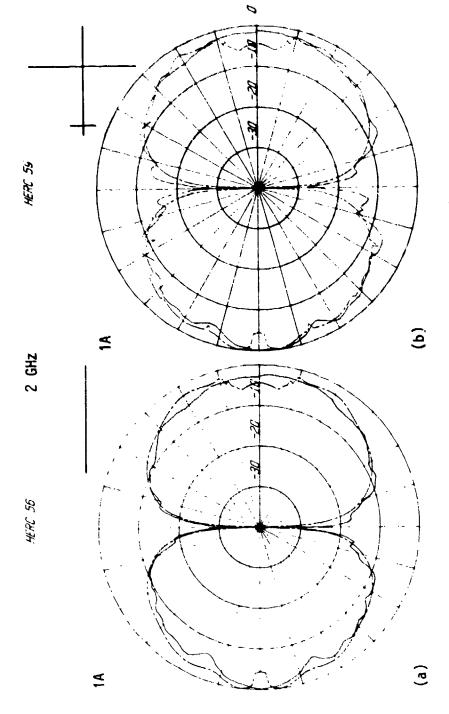
(b) Surface of integration for aperture type antenna.



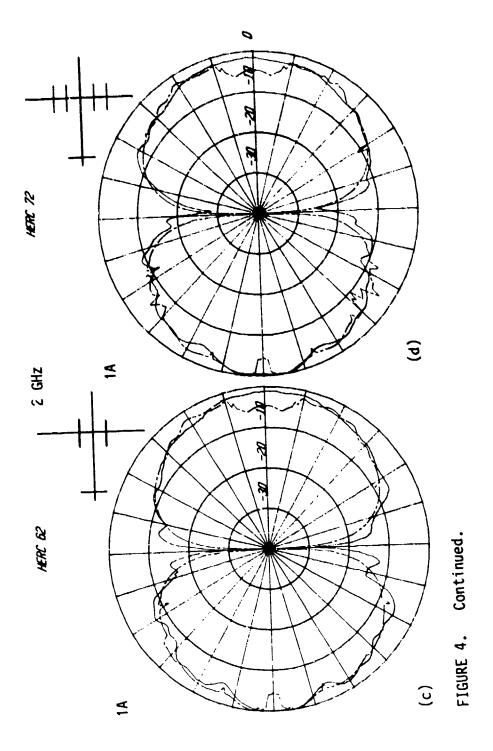
FIGURE 2. Une of the authors (G.W.R.) with the model of the C130 Hercules.

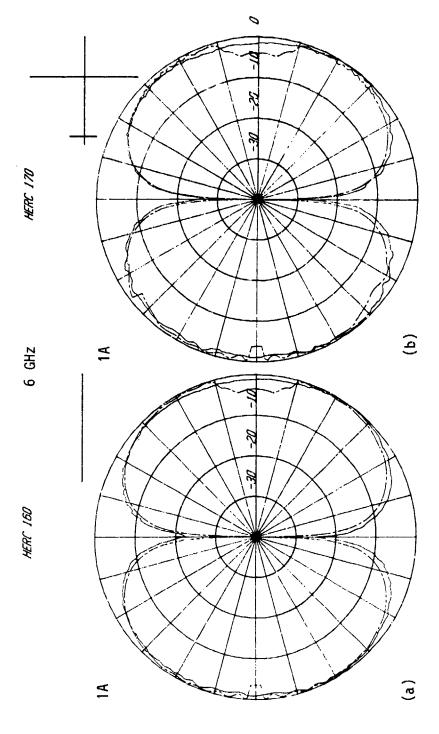


positions 1 or 2 either axially (A) along the fuselage or circumferentially (C) across it. Line drawings showing bottom views of (a) the Lockheed C130 Hercules mudel and (b) a model representing a low-wing jetliner. The diagrams are approximately to scale. The basic Adcock arrays were fixed at FIGURE 3.



Measured (solid line) and predicted (broken line) receive mode polar diagrams at 2 GHz of a simple Adcock array mounted axially at position 1 on the underbelly of a 20:1 scale model of a C130 Hercules transport aircraft. The configurations are represented by the stick drawings. FIGURE 4.





Measured (solid line) and predicted (broken line) receive mode polar diagrams at 6 GHz of a simple Adcock array mounted axially at position on the underbelly of a 20:1 scale model of a C130 Hercules transport aircraft. The configurations are represented by the stick drawings. FIGURE 5.

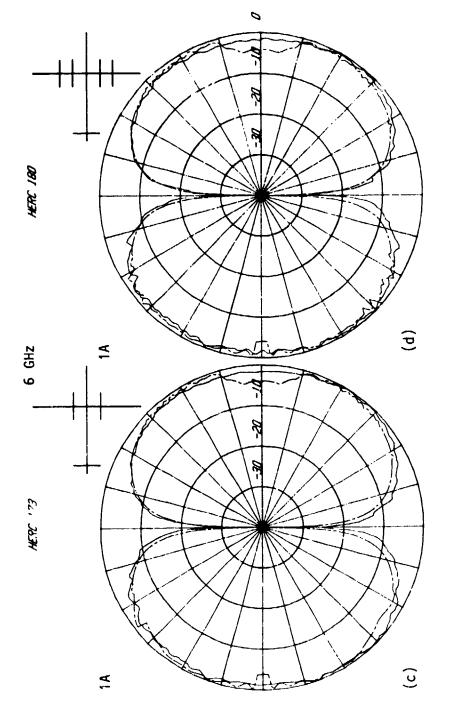
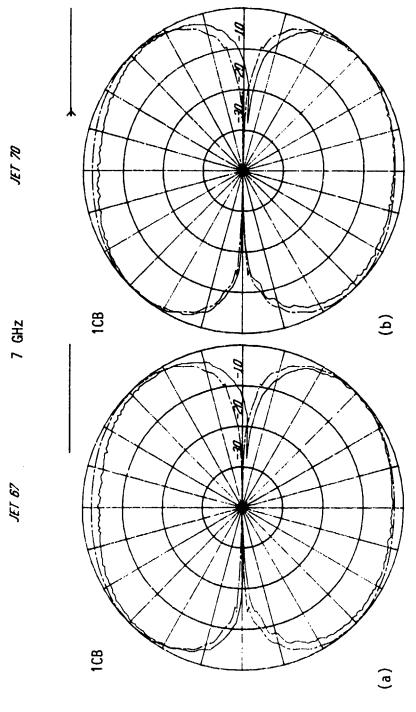


FIGURE 5. Continued.



0

Measured (solid line) and predicted (broken line) receive mode polar diagrams at 7 GHz of a simple Adcock array mounted circumferentially in position 1 on the underbelly of a 20:1 scale model representation of a low-wing jetliner with two underwing engines. The configurations are represented by the stock drawings. A blunt cylinder was used for the fuselage. FIGURE 6 (a) - (e).

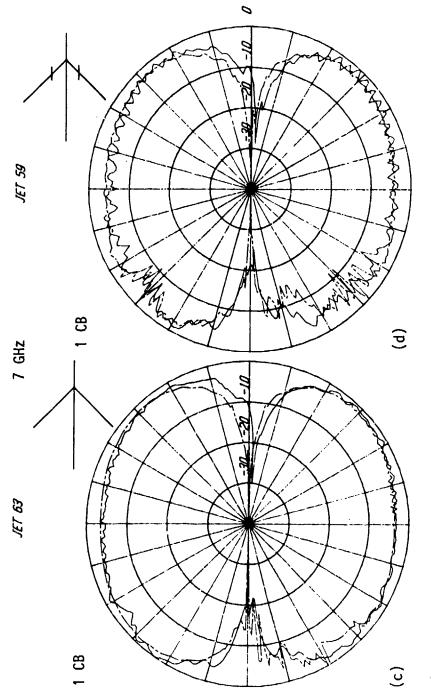
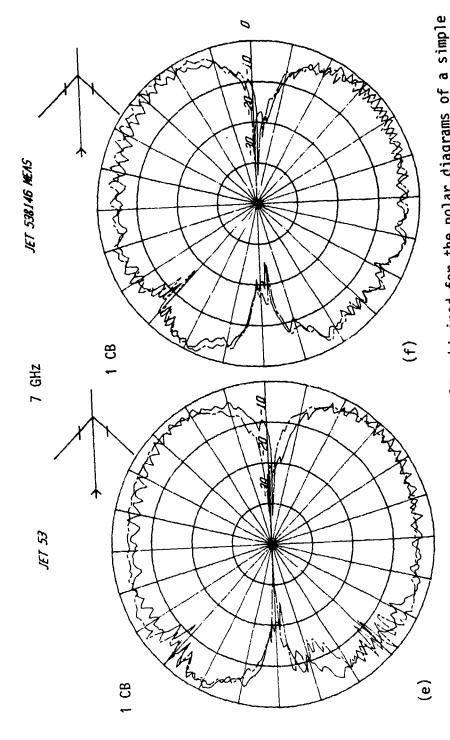


FIGURE 6. Continued.



Comparison of results obtained for the polar diagrams of a simple Adcock array at 7 GHz for the full model of a low-wing jetliner with a blunt cylinder (solid line) and a sectional cylinder with hemispherical nose-cap and conical tail-section (broken line) for the fuselage. FIGURE 6 (f) only.

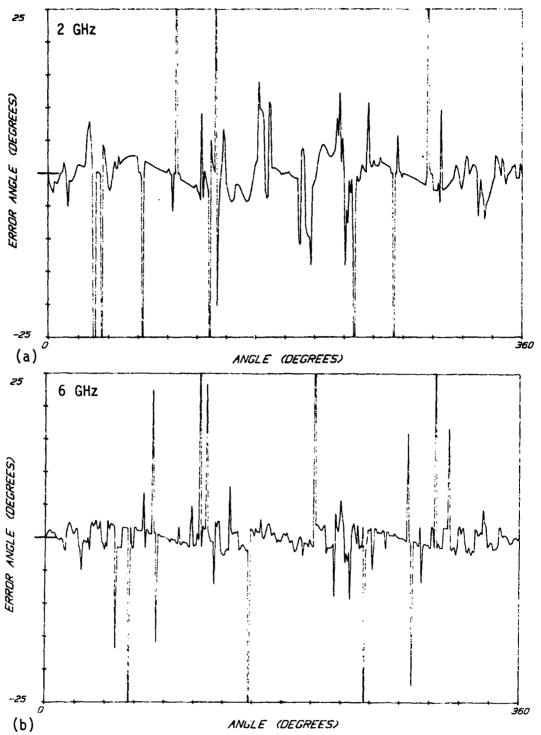


FIGURE 7. Predicted DF errors for the Hercules transport model aircraft at 2 (a) and 6 (b) assuming an interferometric DF system.

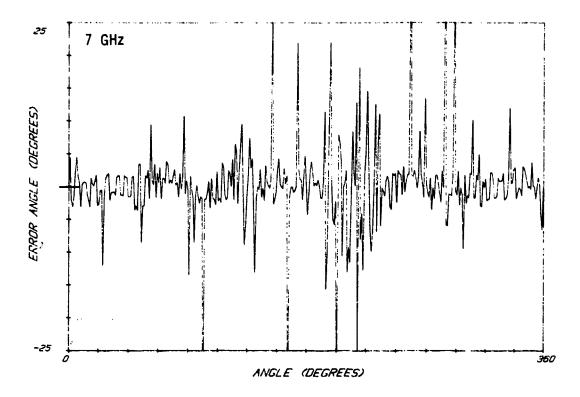


FIGURE 8. Predicted νF errors for the model low-wing jetliner at 7 GHz.



MATRIX FORMULATION OF VECTOR OPERATIONS IN ELECTROMAGNETICS ANALYSIS

Feng Chang Chang

Antenna Systems Laboratory

TRW Electronic Systems Group

Redondo Beach, California

ABSTRACT

The manipulation of vector quantities is unavoidable in the study of electromagnetic fields. An efficient technique is developed to simplify the evaluation of vector algebraic and differential operations by simply converting the vector operations into matrix operations. This matrix formulation is especially useful when there are mixed coordinate basis involved in the vector operations. Applications to some antenna analysis problems will demonstrate the merit of the technique presented.

MATRIX FORMULATION

In analysis it is usually more efficient to work with matrix operations than to deal with vector operations.

In vector operation, components and basis of a vector are inseparate and must work together; whereas in matrix operation, components and basis can be dealt with separately and usually only the vector components are involved.

Therefore, most vector operations can be handled more efficiently by simply converting them into matrix operations.

In matrix formulation, a vector $\overrightarrow{\mathbf{A}}$ is expressed as a column matrix with components (A₁, A₂, A₃) where it is understood that it has ($\hat{\mathbf{u}}_1$, $\hat{\mathbf{u}}_2$, $\hat{\mathbf{u}}_3$) as its basis. Four basic conversions are required to relate vector to matrix expressions:

- (1) a scalar quantity as a diagonal matrix,
- (2) a vector or gradient operator as a column matrix,
- (3) a dot-product or divergent operator as a row matrix,

TABLE 1. MATRIX FORMULATION OF VECTOR ALGEBRAIC

AND DIFFERENTIAL OPERATORS

VECTOR OPERATORS	CARTESIAN COORDINATES
Vector Ä	$(\vec{A}^{\circ}) = \begin{bmatrix} A_{X} \\ A_{Y} \\ A_{Y} \end{bmatrix}$
Dot-Product X •	$\{\vec{A}^c\} = \begin{bmatrix} A_X & A_Y & A_E \end{bmatrix}$
Cross-Product Â×	$\begin{bmatrix} \vec{A}^{C} \end{bmatrix} = \begin{bmatrix} 0 & -A_{Z} & A_{Y} \\ A_{Z} & 0 & -A_{X} \\ -A_{Y} & A_{X} & 0 \end{bmatrix}$
Gradient ▼	$(\Delta_C) = \begin{bmatrix} \frac{9\pi}{9} \\ \frac{9\pi}{9} \end{bmatrix}$
Divergence V.	$\{\nabla^{c}\} = \begin{bmatrix} \frac{\partial}{\partial x} & \frac{\partial}{\partial y} & \frac{\partial}{\partial \overline{z}} \end{bmatrix}$
Curl ▼×	$[\nabla^{C}] = \begin{bmatrix} 0 & -\frac{\partial}{\partial x} & \frac{\partial}{\partial y} \\ \frac{\partial}{\partial x} & 0 & -\frac{\partial}{\partial x} \\ -\frac{\partial}{\partial y} & \frac{\partial}{\partial x} & 0 \end{bmatrix}$
Scalar Laplacian V² = V • V	$\{\nabla^{c}\}(\nabla^{c}) = \left[\Delta^{c}\right],$ $\Delta^{c} = \frac{\delta^{2}}{\delta x^{2}} + \frac{\delta^{2}}{\delta y^{2}} + \frac{\delta^{2}}{\delta z^{2}}$
Vector Laplacian V ² = V V• - V× V×	$= \begin{bmatrix} 0 & 0 & \nabla_{c} \\ 0 & \nabla_{c} & 0 \\ \nabla_{c} & 0 & 0 \end{bmatrix}$ $(\Delta_{c})\{\Delta_{c}\} - [\Delta_{c}][\Delta_{c}]$

TABLE 1. (CONTINUED)

CYLINDRICAL COORDINATES	SPHERICAL COORDINATES
$\begin{pmatrix} \vec{A}d \end{pmatrix} = \begin{pmatrix} A_{\rho} \\ A_{\psi} \\ A_{\chi} \end{pmatrix}$	$(\vec{\Lambda}^0) = \begin{bmatrix} A_\theta \\ A_\phi \\ A_T \end{bmatrix}$
$\{\vec{A}^d\} = \begin{bmatrix} A_p & A_{\varphi} & A_{\Xi} \end{bmatrix}$	$\{\vec{A}^0\} = \begin{bmatrix} A_\theta & A_\phi & A_\Gamma \end{bmatrix}$
$\begin{bmatrix} \vec{A}d \end{bmatrix} = \begin{bmatrix} 0 & -A_z & A_{\varphi} \\ A_z & 0 & -A_{\varphi} \\ -A_{\varphi} & A_{\varphi} & 0 \end{bmatrix}$	$\begin{bmatrix} \vec{A}^{3} \end{bmatrix} = \begin{bmatrix} 0 & -A_{r} & A_{\phi} \\ A_{r} & 0 & -A_{\theta} \\ -A_{\phi} & A_{\theta} & 0 \end{bmatrix}$
$(\forall d) = \begin{bmatrix} \frac{\partial}{\partial \rho} \\ \frac{1}{\rho} \frac{\partial}{\partial \nu} \\ \frac{\partial}{\partial z} \end{bmatrix}$	$(\nabla^3) = \begin{bmatrix} \frac{1}{r} & \frac{\delta}{\delta \theta} \\ \frac{1}{r \sin \theta} & \frac{\delta}{\delta \theta} \\ \frac{\delta}{\delta r} \end{bmatrix}$
$\{\nabla d\} = \begin{bmatrix} \frac{1}{\rho} \frac{\partial}{\partial \rho} \rho & \frac{1}{\rho} \frac{\partial}{\partial \nu} & \frac{\partial}{\partial z} \end{bmatrix}$	$\{ \nabla^{\mathbf{S}} \} = \left[\frac{1}{\operatorname{rsin}\theta} \frac{\partial}{\partial \theta} \operatorname{sin}\theta - \frac{1}{\operatorname{rsin}\theta} \frac{\partial}{\partial \phi} - \frac{1}{\operatorname{r}^2} \frac{\partial}{\partial r} r^2 \right]$
$\begin{bmatrix} \nabla d \end{bmatrix} = \begin{bmatrix} 0 & -\frac{\partial}{\partial z} & \frac{1}{\rho} \frac{\partial}{\partial \varphi} \\ \frac{1}{\rho} \frac{\partial}{\partial \varphi} & \frac{1}{\rho} \frac{\partial}{\partial \rho} \rho & 0 \end{bmatrix}$	$[\nabla^{\mathbf{s}}] = \begin{bmatrix} 0 & -\frac{1}{r}\frac{\partial}{\partial r}r & \frac{1}{r\sin\theta}\frac{\partial}{\partial \varphi} \\ \frac{1}{r}\frac{\partial}{\partial r}r & 0 & -\frac{1}{r}\frac{\partial}{\partial \theta} \\ -\frac{1}{r\sin\theta}\frac{\partial}{\partial \varphi} & \frac{1}{r\sin\theta}\frac{\partial}{\partial \theta}\sin\theta & 0 \end{bmatrix}$
$\{\nabla d\}(\nabla d) = [\Delta^d],$	$\{\nabla^{S}\}(\nabla^{S}) = [\Delta^{S}],$
$\Delta^{\mathbf{d}} = \frac{1}{\rho} \frac{\partial}{\partial \rho} \rho \frac{\partial}{\partial \rho} + \frac{1}{\rho^2} \frac{\partial^2}{\partial \phi^2} + \frac{\partial^2}{\partial z^2}$	$\Delta^{S} = \frac{1}{r^{2} \sin \theta} \frac{\partial}{\partial \theta} \sin \theta \frac{\partial}{\partial \theta} + \frac{1}{r^{2} \sin^{2} \theta} \frac{\partial^{2}}{\partial \varphi^{2}} + \frac{1}{r^{2}} \frac{\partial}{\partial r} r^{2} \frac{\partial}{\partial r}$
	$ \left\{ \begin{array}{lll} \left\{ \nabla^{\mathbf{S}} \right\} \left\{ \nabla^{\mathbf{S}} \right\} - \left[\nabla^{\mathbf{S}} \right] \left[\nabla^{\mathbf{S}} \right] \\ & = \begin{bmatrix} \Delta^{\mathbf{S}} - \frac{1}{r^{1} \sin^{2} \theta} & -\frac{2 \cos \theta}{r^{1} \sin^{2} \theta} \frac{\partial}{\partial \phi} & \frac{2}{r^{1}} \frac{\partial}{\partial \theta} \\ & \frac{2 \cos \theta}{r^{2} \sin^{2} \theta} \frac{\partial}{\partial \phi} & \Delta^{\mathbf{S}} - \frac{1}{r^{1} \sin^{2} \theta} & \frac{2}{r^{1} \sin \theta} \frac{\partial}{\partial \phi} \\ & -\frac{2}{r^{2} \sin \theta} \frac{\partial}{\partial \theta} \sin \theta & -\frac{2}{r^{1} \sin \theta} \frac{\partial}{\partial \phi} & \Delta^{\mathbf{S}} - \frac{2}{r^{1}} \end{bmatrix} $

Also included in Table 1 are Laplacian operators defined as

 $\nabla^2 f = \nabla \cdot \nabla f$ and $\nabla^2 \vec{F} = \nabla \nabla \cdot \vec{F} - \nabla \times \nabla \times \vec{F}$ where $f = f(\vec{r})$ is a scalar function and $\vec{F} = \vec{F}(\vec{r})$ is a vector function. Except for the Cartesian coordinates, the derivation of ∇^2 is very involved through the conventional formulas [1]. Applying the matrix formulation technique will greatly reduce the derivation to matrix multiplication and partial differentiation.

Matrix formulation is especially useful when there are mixed coordinate basis involved in the vector operation. The basic transformations in changing from one basis to another are given in Table 2. It should be noted that $\nabla^V = \nabla^U$ in the vector operation does not give (∇^V) = (∇^U) in the matrix operation, unless v = u is in the same basis. It does imply (∇^V) = [$^VT^U$] (∇^U), where [$^VT^U$] is a coordinate transformation matrix relating the u-coordinates to the v-coordinates. Employing the technique of coordinate transformation flowchart [2], any transformation matrix among the coordinate systems can readily be determined.

The following applications to the reflector antenna analysis will demonstrate the merit of matrix formulation of vector operations in the mixed coordinate basis.

TABLE 2. TRANSFORMATIONS OF COORDINATE BASIS

	ABC	VECTOR ALGEBRAIC OPERATORS		
Vector	χ" -	<u>Y</u> a	$(\vec{\lambda}^{V}) - [^{V}\vec{\tau}^{U}] (\vec{\lambda}^{U})$	
ot-Product	₹	χu.	$\{\vec{\lambda}^{\mathbf{v}}\} = \{\vec{\lambda}^{\mathbf{u}}\} [\mathbf{u}_{\mathbf{v}^{\mathbf{v}}}]$	
Cross-Product	ĀV× -	Ã ^u ×	$\begin{bmatrix} \vec{A}^{V} \end{bmatrix} = \begin{bmatrix} \nabla^{U} \end{bmatrix} \begin{bmatrix} \vec{A}^{U} \end{bmatrix} \begin{bmatrix} u^{T^{V}} \end{bmatrix}$	
	VRCTN	DR DIPPERS	NTIAL OPERATORS	
Gradient	A^ -	Ψu	$(\Delta_{A}) = (\Delta_{B}) (\Delta_{B})$	
		•		
	A A. •	j	$\{ \Delta_{\underline{A}} \} = \{ \Delta_{\overline{B}} \} [\underline{n} \Delta_{\underline{A}}]$	

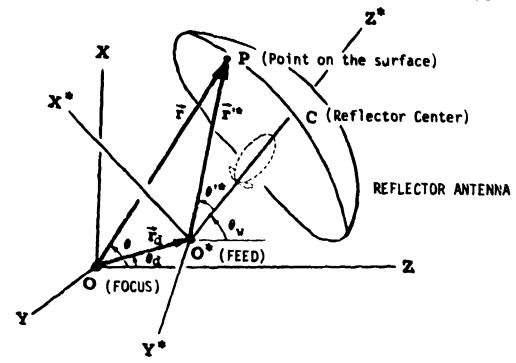


Figure 1. Reflector (Non-Starred) and Feed (Starred) Systems

APPLICATIONS

In constructing a physical optics radiation integral to determine the vector potential, the induced current on the reflector surface illuminated by a positioned feed source must be first determined. As shown in Figure 1, the induced surface current $\vec{J}(\vec{r})$ at a point $\vec{r}(\theta, \phi, r)$ on the reflector surface $F(\vec{r}) = 0$ can be derived by

$$\vec{J}(\vec{r}) = \frac{2}{\eta} \hat{n}(\vec{r}) \times \hat{r}'' \times \vec{E}(\vec{r}''')$$

The feed system (starred system) and the reflector system (non-starred system) are related through both the origin translation along the feed location vector \vec{r}_d (Θ_d , ϕ_d , r_d) and the three axsis rotations about the feed's positioned angles (Θ_w , ϕ_w , ψ_w). The radiated field \vec{E} (\vec{r}'') is generally given in the spherical coordinates (Θ''' , Φ''' , r''') of the feed system. If the normal vector \hat{n} (\vec{r}) = ∇ F / $|\nabla$ F| to the reflector surface \vec{r} (\vec{r}) = 0 is expressed in the spherical coordinates (Θ , Φ , r) of the reflector system, and the desired surface current distribution \vec{J} (\vec{r}) in the Cartesian coordinates (x, y, z), then

$$\vec{J}^{C} = \frac{2}{\eta} \hat{n}^{S} \times \hat{r}'^{S'^{*}} \times \hat{E}^{S'^{*}}$$

All the quatities in the right-hand side of the equation are either known or can be derived from the given quantities [2].

However, the direct execution of this mixed basis crossproduct equation is usually not so easy. The computation can be greatly simplified, if it is converted into matrix expression:

$$(\vec{J}^{C}) = \frac{2}{n} [^{C}T^{S}] [\hat{n}^{S}] [^{S}T^{S'^{*}}] [\hat{r'}^{S'^{*}}] (\vec{E}^{S'^{*}})$$

The coordinate transformation matrices [CTS] and [STS'*] can be readily obtained from the coordinate transformation flow chart [2], therefore, the evaluation of the induced current distribution becomes mere a direct and straightforward matrix multiplications.

When a vector potential is obtained, the magnetic field can be determined by $\vec{H} = \nabla \times \vec{A}$. If a vector potential \vec{A} (θ , ϕ , r) is given as a function of variables in the spherical coordinates but with three components in the Cartesian coordinates, and the desired field \vec{H} (θ , ϕ , r) is to be determined with three components in the spherical coordinates, then

$$\vec{H}$$
S = $\overset{\rightarrow}{\nabla}$ S \vec{X} \vec{A} C

Converting it into matrix form, we have

$$(\vec{H}^{S}) = [\nabla^{S}][^{S}T^{C}](\vec{A}^{C})$$

Or explicitly,

$$\begin{bmatrix} H_{\Theta} \\ H_{\phi} \end{bmatrix} = \begin{bmatrix} 0 & -\frac{1}{r} \frac{\delta}{\delta r} r & \frac{1}{r \sin \theta} \frac{\delta}{\delta \phi} \\ \frac{1}{r} \frac{\delta}{\delta r} r & 0 & -\frac{1}{r} \frac{\delta}{\delta \theta} \\ -\frac{1}{r \sin \theta} \frac{\delta}{\delta \phi} & \frac{1}{r \sin \theta} \frac{\delta}{\delta \theta} \sin \theta & 0 \end{bmatrix}$$

$$\begin{bmatrix} \cos\theta\cos\phi & \cos\theta\sin\phi & -\sin\theta \\ -\sin\phi & \cos\phi & 0 \\ \sin\theta\cos\phi & \sin\theta\sin\phi & \cos\theta \end{bmatrix} \begin{bmatrix} A_{\chi} \\ A_{\gamma} \\ A_{z} \end{bmatrix}$$

In the similar manner, the electric field \vec{E} (θ , ϕ , r) is determined by

$$\stackrel{+}{E}^{S} = -j \omega \mu \ (1 + \frac{1}{k^2} \nabla^{S} \nabla^{S} \cdot) \stackrel{+}{A}^{C}$$

Or in the matrix form

$$(E^{S}) = -j\omega\mu [\Gamma^{S}][ST^{C}](\overline{A}^{C})$$

where

$$[\Gamma^{S}] = \langle 1 \rangle + \frac{1}{k^{2}} (\nabla^{S}) \{\nabla^{S}\}$$

Both the magnetic field and electric field can therefore be obtained simply by direct matrix multiplication and partial differentiation.

Quite often a vector potential is found to be in the form of

$$\vec{A}$$
 (θ , ϕ , r) = G (r) \vec{A}_0 (θ , ϕ)

where

$$G(r) = \frac{e^{-jkr}}{4\pi r}$$

then the differential operators at the far field become

$$-\frac{1}{jk} [\nabla^{S}] G (r) \xrightarrow{r >> \lambda} G (r) \begin{bmatrix} 0 & -1 & 0 \\ 1 & 0 & 0 \\ 0 & 0 & 0 \end{bmatrix}$$

$$[\Gamma^{S}] G (r) \xrightarrow{r >> \lambda} G (r) \begin{bmatrix} 1 & 0 & 0 \\ 0 & 1 & 0 \\ 0 & 0 & 0 \end{bmatrix}$$

CONCLUSION

Derivation of compact matrix formulas for both vector algebraic operations and vector differential operations has been presented in detail. The simple technique is especially useful when there are mixed coordinate basis involved in the vector operations.

No claim is made that the matrix formulations presented are superior to those conventional formulas appeared in most of vector analysis textbooks. Rather it is hoped that these matrix formulas will become more popular and may be used as alternatives for those conventional formulas.

For any curvilinaer coordinate system (u_1 , u_2 , u_3) with scale factors (h_1 , h_2 , h_3), the following table may be useful.

TABLE 3. MATRIX FORMULATIONS OF CURVILINEAR COORDINATES

	VECTOR ALGEBRAIC OPERATORS		
Scalar	8	\s\= s or [s] or [s s]	
Vector	Ã	$\begin{pmatrix} \widetilde{A} \end{pmatrix} = \begin{pmatrix} A_1 \\ A_2 \\ A_2 \end{pmatrix}$	
Dot-Product	Ā •	$\{\vec{A}\} = \begin{bmatrix} A_1 & A_2 & A_3 \end{bmatrix}$	
Cross-Product	Ā×	$\begin{bmatrix} \vec{A} \end{bmatrix} = \begin{bmatrix} 0 & -A_3 & A_2 \\ A_3 & 0 & -A_1 \\ -A_2 & A_1 & 0 \end{bmatrix}$	
VECTOR DIFFERENTIAL OPERATORS			
Gradient	▼	$(v) = \begin{bmatrix} \frac{1}{h_1} \frac{\delta}{\delta u_1} \\ \frac{1}{h_2} \frac{\delta}{\delta u_2} \\ \frac{1}{h_3} \frac{\delta}{\delta u_3} \end{bmatrix}$	
Divergence	▼•	$\{ v \} = \left[\frac{1}{h_1 h_2 h_3} \frac{\delta}{\delta u_1} h_2 h_3 \frac{1}{h_1 h_2 h_3} \frac{\delta}{\delta u_2} h_3 h_1 \frac{1}{h_1 h_2 h_3} \frac{\delta}{\delta u_3} h_1 h_2 \right]$	
Curl	٧×	$ \begin{bmatrix} 0 & -\frac{1}{h_3 h_2} \frac{\delta}{\delta u_3} h_2 & \frac{1}{h_2 h_3} \frac{\delta}{\delta u_2} h_3 \\ \frac{1}{h_3 h_1} \frac{\delta}{\delta u_3} h_1 & 0 & -\frac{1}{h_1 h_3} \frac{\delta}{\delta u_1} h_3 \\ -\frac{1}{h_2 h_1} \frac{\delta}{\delta u_2} h_1 & \frac{1}{h_1 h_2} \frac{\delta}{\delta u_1} h_2 & 0 \end{bmatrix} $	

REFERENCES

- Arfken, G.(1970) <u>Mathematical Method for Physicists</u>,
 2nd ed. Academic, New York, pp.178-184.
- 3. Chang, F.C. (1984) Novel coordinate transformations for antenna applications, IEEE Trans. Antenna Propag. (Vol.AP-32): 1292-1297.